Title
Seismic Performance Enhancement of Structures Using Protective Devices and Rocking Components

Author
Peng, Yi

Publication Date
2021

Peer reviewed|Thesis/dissertation

UNIVERSITY OF CALIFORNIA

Los Angeles

Seismic Performance Enhancement of Structures Using Protective Devices and Rocking Components

A dissertation submitted in partial satisfaction

of the requirements for the degree

Doctor of Philosophy in Civil Engineering

by

Yi Peng

2021

ABSTRACT OF THE DISSERTATION

Seismic Performance Enhancement of Structures Using Protective Devices and Rocking Components

by

Yi Peng
Doctor of Philosophy in Civil Engineering
University of California, Los Angeles, 2021
Professor Jian Zhang, Chair

Significant structural damages (even collapses) have been observed in past earthquakes. Seismic protective devices and innovative structural systems can be used to improve the responses and post-earthquake serviceability. This study aims to derive the optimal design of protective devices for structures and evaluate the promises of rocking components to effectively improve the structural performance and mitigate the earthquake hazards.

First, the hybrid simulation framework is adapted and validated to enable nonlinear structural control of inelastic structures with protective devices. The structure is modeled in OpenSees while the protective devices and control algorithms are modeled in MATLAB. Subsequently, guided by the actively controlled responses, the study provides different optimization procedures to identify the optimal design parameters of equivalent passive protective devices. Demonstrated by an eight-story inelastic building, the equivalent passive design yields much improved structural performance, comparable to actively controlled response.

Second, the hybrid simulation scheme is further modified to incorporate multi-support excitations, often observed in bridges due to significant soil-structure interaction effects. The methodology is applied to a benchmark highway bridge where base isolation and supplemental energy dissipation are used. Active control algorithms (either linear or nonlinear) are implemented and optimal parameters for base isolators and damping devices are derived to mimic the actively controlled responses. The robustness of active controls and optimal passive controls is further demonstrated by comparing various control schemes under different bridge systems and motion inputs.

Third, rocking components are evaluated as an innovative structural system that can be incorporated along with conventional lateral force resisting systems. Several numerical models are evaluated and improved to account for complex dynamic behavior of rocking components in flexible structures. A probabilistic seismic demand model (PSDM) is also proposed as an alternative way to capture the uncertainties in predicting individual rocking responses. A new finite element-based rocking model is implemented in OpenSees, which consists of a zero-length rocking element with a Dirac-delta type impact model. Finally, a nine-story rocking wall-frame building is designed and analyzed. Nonlinear time history analysis results demonstrated that both strength and deformation demands are reduced, and the structural damage is controlled when rocking motion is activated.

The dissertation of Yi Peng is approved.

Ertugrul Taciroglu

Henry Burton

Yousef Bozorgnia

Jian Zhang, Committee Chair

University of California, Los Angeles

2021

To my parents, Chaobo Peng and Lina Luo

my husband, Xinwei Chen

for their love and support.

TABLE OF CONTENTS

LIST OF FIGURES

LIST OF TABLES

ACKNOWLEDGMENTS

First and foremost, I am grateful to my Ph.D. advisor, Professor Jian Zhang, for her invaluable advice, continuous support, and encouragement during my Ph.D. study. Her immense knowledge and ample experience have enlightened me in my academic research and daily life. She is an academic advisor and a life mentor who profoundly influenced me with her personality charm. I learned from her the enthusiasm for life, the diligence for work, the attitude towards questioning, and persistence for academic pursuit.

I would like to thank the members of my doctoral committee, Professor Ertugrul Taciroglu, Professor Henry Burton, and Professor Yousef Bozorgnia, for their splendid education on each subject and their thoughtful suggestions on this research. Special thanks to Professor Michalis F. Vassiliou for his help on the research topic of numerical simulation of rocking behavior.

Many thanks to Dr. Wang Xi, Dr. Yazhou Xie, Dr. Dong Wang, Dr. Jianian Wen and Zhenlei Jia for their help and collaboration on my research. My appreciation also goes to my friends at UCLA, Dr. Zhan Shu, Xitong Zhou, Henan Mao, Dr. Xingquan Guan, Dr. Zhenxiang Yi, Dr. Han Sun, Dr. Wenyang Zhang, Dr. Pengyu Chen, and many others, who have offered support and help to me in the past years.

I want to express my gratitude to my parents and my husband. Without their tremendous understanding and encouragement in the past few years, it would be impossible for me to complete my study. In particular, I am grateful to my husband, Xinwei, for providing me the financial stability and the spiritual support. I would not be a wife and pursue my academic dream without his hard-working, endless love for our family and me.

Lastly, my appreciation goes out to financial support in the form of university fellowship and tuition waiver from the Department of Civil and Environment Engineering.

VITA

EDUCATION

M.S. in Engineering Mechanics, Xiamen University, Xiamen, China 2013-2014
B.E. in Civil Engineering, Xiamen University, Xiamen, China 2008-2012

ACADEMIC EXPERIENCE

Teaching Fellow, University of California, Los Angeles 2016-2021
Graduate Student Researcher 2016-2021

PROFESSIONAL EXPERIENCE

Internship, Nabih Youssef Associates Structural Engineers, Los Angeles 2019
Internship, Hordor Design Group, Xiamen, China 2011

PUBLICATIONS

Gu Q, Peng Y. A new framework for response sensitivity analysis of soil-structure interaction (SSI) systems., Fifth Asian-Pacific Symposium on Structural Reliability and its Applications (APSSRA2012), Singapore, May 23-25, 2012.

Gu Q, Zona A, Peng Y, Dall'Asta A. Effect of buckling-restrained brace model parameters on seismic structural response. Journal of Constructional Steel Research, 2014, 98:100-113.

Peng Y. Finite element response sensitivity and reliability analyses of structures and soil-structure interaction systems. Master's degree thesis, 2015, Xiamen University, China.

Gu Q, Yang ZH, Peng Y. Parameters affecting laterally loaded piles in frozen soils by an efficient sensitivity analysis method. Cold Regions Science and Technology, 2016, 121:42-51.

Peng Y, Zhang J, Wu G. Seismic performance enhancement of structures using rocking components. 2021, in preparation.

Peng Y, Zhang J, Xi W. Structural control of inelastic structures with energy dissipation devices through hybrid simulation. 2021, in preparation.

Peng Y, Xie YZ, Xi W, Dyke S, Zhang J. Optimal passive control design of the benchmark highway bridge based on hybrid simulation. 2021, in preparation.

Wang D, Zhang J, Peng Y. A Data-driven Seismic Damage Assessment Framework of Regional Highway Bridges. 2021, in preparation.

REPORT

Peng Y, Wen JN, Jia ZL, Xie YZ, Zhang J. PEER Blind Prediction Contest of Shaking Table Tests for the Seismic Response of a Rocking Podium Structure, PEER Blind Prediction (BP) Contest, 2019.

1. INTRODUCTION

1.1 BACKGROUND

In conventional seismic design, buildings expect beams, columns, and walls to exhibit inelastic responses under strong earthquakes. Energy is dissipated through structural damping and plastic hinge development at a specific location. However, damage to the structure due to plastic hinge development may require expensive and time-consuming retrofit efforts, thus, lead to long-term loss of building functionality post earthquake. Moreover, irreparable structural damages, even collapses in the region close to the epicenter, have been observed after a number of strong earthquakes, which have resulted in significant deaths and economic losses (Han et al., 2009; Wang, 2008). For example, the 2008 Wenchuan earthquake (Ms 8.0) in Sichuan Province, China, has resulted in more than 68,858 deaths and losses in the hundreds of billions RMB. Figure 1.1 (a) and (b) shows the complete destruction of four buildings of the Dongqi Middle School, which resulted in hundreds of students losing their lives, and bridge damage caused by the fell of abutments during the Wenchuan earthquake. Besides, highway bridges are one of the most critical links in the transportation network that are susceptible to earthquake damage (Chang et al., 2000; Jennings & Wood, 1971; Tarakji, 1997; Xie, 2017). The 1995 Kobe earthquake in Japan resulted in the collapse of 9 highway bridges and catastrophic damages to 16 bridges. Figure 1.1 (c) and (d) show the RC column shear failure and flexural failure, which caused the collapse occurred at an 18-span viaduct of Hanshin Expressway.

During the past several decades, many practical and research efforts have been made to better understand the seismic performance of structures and protect structures against strong earthquakes. To maintain post-earthquake serviceability, promising technologies including the use

of innovative seismic energy-dissipating structural systems (Anastasopoulos et al., 2014; Gelagoti et al., 2012; Hajjar et al., 2013; Palermo et al., 2007), the use of column retrofit measures (Kim & Shinozuka, 2004; Padgett & DesRoches, 2008), innovative materials (DesRoches & Delemont, 2002), and seismic protective devices (Housner et al., 1997; Spencer & Nagarajaiah, 2003; Xi, 2014; Xie & Zhang, 2017, 2018; Zhang & Huo, 2009), etc. are widely studied. Under this background, this research substantially extends the previous studies (Xi, 2014; Xie, 2017) in seismic modeling, optimal control, and design of buildings and highway bridges equipped with seismic protective devices and rocking components.

(a) Complete destruction of four buildings

(b) Abutments fell

(c) Column shear failure

(d) Column flexural failure

Figure 1.1. Structure and bridge failures observed in case histories (Wang, 2008; Xie, 2017)

1.2 ACTIVE AND PASSIVE CONTROL OF INELASTIC STRUCTURES

1.2.1 Pros and Cons of Different Seismic Protective Devices

Based on the control mechanism, seismic protective devices can be classified into passive, active/hybrid, and semi-active systems (Housner et al., 1997). To date, passive devices, such as base isolators, viscoelastic dampers, and tuned mass dampers have been widely implemented in civil structures because they are relatively easy to install, and do not need external power or energy to sustain the control effect, thus it is easy to operate and reliable during natural hazards (Constantinou et al., 1998; Kunde & Jangid, 2003; Reinhorn et al., 1995; Soong & Dargush, 1997; Soong & Spencer, 2002; Symans et al., 2008), as shown in Figure 1.2. However, restricted by their mechanical characteristics, passive devices are not sufficiently adaptive to structural changes and the ever-varying external excitations (Christopoulos et al., 2006; Spencer & Nagarajaiah, 2003). For example, a tuned mass damper is only effective for the structure with a pre-designed dominant mode. Namely, passive control may not reach the intended performance objectives resulting in the need of effective optimal design of supplemental mass, stiffness, or damping parameters.

Conversely, active control systems consist of sensors and actuators that can capture structural responses in time and generate appropriate external forces along with the time history of the ground excitation. Active control strategies to dynamically reduce the structural responses caused by earthquakes have been studied in many previous research and implemented on practical structures (Soong & Costantinou, 2014). Although active structural control is achievable by using active protective devices, the solution to deliver large active control forces is needed before the wide use of this technology in civil structures. First, active control strategies have demand of significant external power supply and colossal force generation equipment. Second, it is vulnerable to power supply outage as a severe earthquake can damage not only the structural members but

also the power supply system. Furthermore, the actuators have harmful potentials such as destabilization of the structure if, unfortunately, the actuator control computer has malfunctioned.

(a) LRB base isolation system used for Hanshin Expressway

(b) Viscous fluid damper on 91/5 Overcrossing

(c) MR dampers installed on Dongting Lake Bridge

Figure 1.2. Seismic protection devices (Xi, 2014).

Semi-active systems, such as magnet-orheological (MR) dampers (Spencer & Nagarajaiah, 2003), include smart mechanical and material components whose physical parameters can be modified in real-time through switching or on-off operations. They are becoming a promising technology for seismic hazard mitigation of civil engineering structures. As a hybrid between passive and active control, a semi-active control system maintains the adaptive ability of active control to the vibration nature of both structural response and external excitation. While it only requires a small power supply such as batteries, which is a great advantage when the primary power source in the structure or control computer fails during seismic events. At the same time, it

inherits the pros of the passive control system of easy to manufacture and reliable to operate. However, the control capacity of a semi-active system is still limited as it can only operate within the capacity of the corresponding passive devices on which it is based. Besides, the finite element (FE) model of semi-active devices has not been addressed in typical finite element analysis software because structural control methods are needed to realize the semi-active control behavior.

1.2.2 Structural Control of Inelastic Structures

Considering the pros and cons of different protective devices, it will be a substantial improvement if an equivalent passive control system that can provide the same control effects of the active/semi-active control system could be identified. To do so, structural control of inelastic structures needs to be performed first. Then multiple optimization procedures need to be developed to determine the design parameters of passive devices based on actively controlled response.

For structures exhibiting nonlinearity, although current finite element software typically has various elements and materials for modeling complex nonlinear structural components, the structural control task cannot be easily conducted within the typical finite element analysis program. Instead, the structural controls were often executed on simplified or reduced-order structural models generated in the same simulation platform for control algorithms. For example, Gluck et al. (Gluck et al., 1996) and Yang et al. (Yang et al., 1995) proposed linear quadratic regulator (LQR) theory and sliding mode control (SMC) to control the responses for simple elastic or hysteretic multistory structures; Ohtori and Agrawal had made efforts to develop benchmark control problems and reduced-order structural model that was exclusively built in the program of MATLAB/Simulink to allow for a platform to compare various control strategies (Agrawal et al., 2009; Ohtori et al., 2004).

Nevertheless, the ability to use advanced structural models with realistic geometry and

nonlinearity in conjunction with structural control is currently lacking, thus also limits the adoption of structural control. The purpose of this study is to utilize a hybrid simulation scheme to overcome the modeling difficulties of inelastic structures with multiple control technologies. Then move forward in a similar direction as these recent studies to present an effective optimal design procedure of various nonlinear protective devices.

1.2.3 Hybrid Simulation Methodology

Hybrid simulation is a method for examining the seismic response of structures using a hybrid model comprised of either physical and numerical sub-structures or numerical sub-structures only (Saouma & Sivaselvan, 2008). This alternative way of physical testing or numerical modeling of an entire system allows for numerical simulations of complex coupled systems performed separately on different computational platforms, offers a feasible means to link control algorithms with realistic structural models. In this study, a novel approach utilizing the hybrid simulation is proposed to take advantage of the nonlinear modeling ability of existing finite element software programs and perform the structural control task simultaneously. As shown in Figure 1.3, a complex inelastic structure can be modeled in any existing finite element software, such as OpenSees, ABAQUS, etc. Meanwhile, the seismic protective devices such as base isolators, viscous fluid dampers, MR dampers, or active controllers are simulated in other software, such as MATLAB, where the control algorithms can be easily formulated and implemented using the built-in toolboxes. The main inelastic structure and the control devices, as two substructure parts, can communicate with each other by transferring force and displacement information through a platform designed for hybrid simulation: UI-SIMCOR (Kwon et al., 2007).

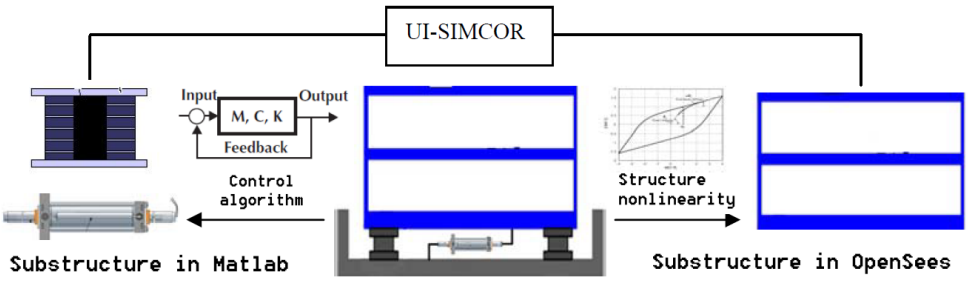

Figure 1.3. Hybrid numerical simulation scheme (Xi, 2014)

By utilizing hybrid simulation methodology, different control algorithms can be easily formulated and implemented in MATLAB to get the optimal structural responses, which furthermore guides the derivation of optimal design parameters of seismic protective devices. In this study, an eight-story inelastic structure equipped with nonlinear viscous dampers, MR dampers, or base isolators is studied using the hybrid simulation scheme. The active structural control tasks are executed, and the equivalent passive parameters are derived for this eight-story building to verify the proposed hybrid numerical simulation scheme in efficiently developing seismic protection strategies for inelastic structures. Moreover, the optimal active and passive control of a benchmark highway bridge is also evaluated to investigate the control efficiency more thoroughly.

1.2.4 Optimal Passive Design Based on Control Theory

After obtaining the actively controlled responses, an optimal passive design can be identified through different model identification techniques. Gluck et al. (Gluck et al., 1996) presented a method for designing supplemental linear passive viscous or viscoelastic devices based on optimal linear control theory. The stiffness and damping parameters of equivalent passive control are approximated using the transformed gain matrix or truncated gain matrix. The main advantage of this method is that the procedure is non-iterative and not computationally demanding,

and it does not need to compute the structural response. Still, the disadvantage is that it can only be applied to linear structures. Cimellaro and Retamales (Cimellaro & Retamales, 2007) adopted Gluck's work to determine the optimal stiffnesses and capacities of softened stories and dampers placed in a shear-type building. Lavan et al. (Lavan et al., 2008) presented an alternative methodology for determining the optimal location and amount of weakened structural components and the added linear viscous damping devices in inelastic structures. Extended from previous studies, this study provides new optimization and model identification methods to find the optimal design of nonlinear damping devices and base isolations of inelastic structures.

1.3 SYSTEMS EXHIBITING ROCKING BEHAVIOR

The synopsis of Hajjar et al. (Hajjar et al., 2013) provided a large number of examples related to modeling, analysis, and experiments of seismic energy-dissipating structural systems. These systems consist of self-centering systems, systems exhibiting rocking behavior, and systems with energy-dissipating fuse elements. During the last decade, it's worth noting that there were a series of publications (Ajrab et al., 2004; Deng et al., 2012; Gajan & Kutter, 2008; Harden et al., 2006; Hung et al., 2011), which bring the attention of engineers to the unique advantages associated with allowing structures to rock. In this class of publications, the basic concept is the intentional generation of uplifting mechanism in traditional moment-resisting systems, either at the bottom of shear walls or even at the foundation level, by allowing appreciable rotations of the footings, such as frame – rocking shear wall structure and rocking column-foundation system. The series of systematic studies on the dynamic response and stability of rocking structures gradually led to rocking isolation -- a unique seismic protection strategy for large, slender structures at the limit-state and the operational state.

As shown in Figure 1.4, once the uplift mechanism is activated, rocking motion can reduce

the seismic loading and ductility demands by forcing structural behavior to remain in the elastic range or mildly inelastic range. Besides, given the inherent negative stiffness, a rocking frame neither amplifies nor resonates with any frequency content of the input ground motion. Moreover, re-centering of the rocking system is achieved unconditionally through gravity, thus eliminating any permanent displacement. However, although rocking isolation has good seismic performance, their practical design aspects have not been fully addressed in the literature due to the difficulties in modeling rocking behaviors.

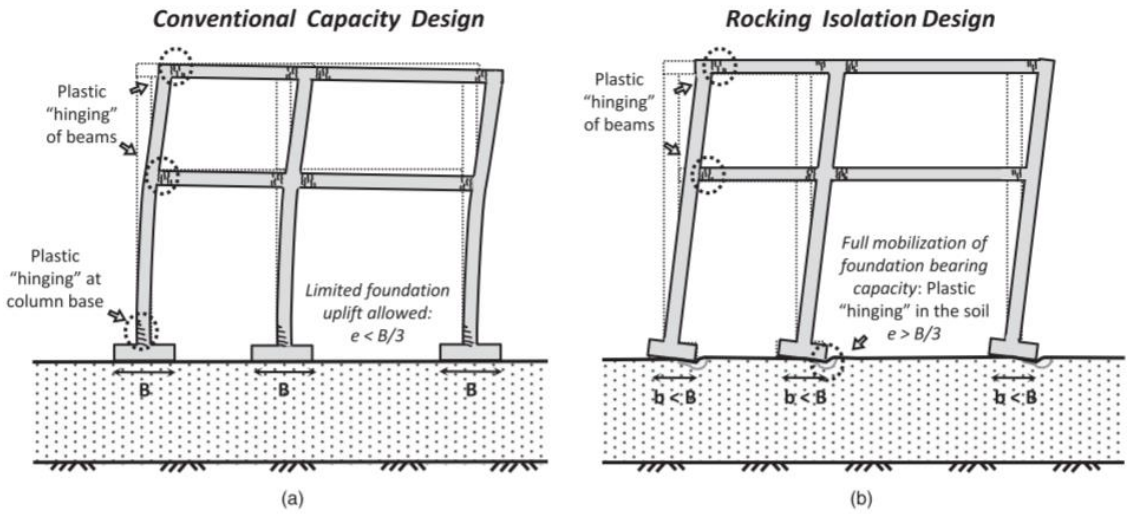

Figure 1.4. (a) Conventionally designed frame compared to (b) rocking-isolation design (Anastasopoulos et al., 2014)

1.3.1 Analytical Modeling

The development of the analytical model of rocking behavior is a long history based on extensive observation in experiments and real earthquakes. As early as 1885, Mine presented analytical studies on the seismic response of slender, free-standing blocks in an effort to estimate levels of ground shaking (Milne, 1885). Four decades after Milne's work, Kirkpatrick (1927) presented the first minimum-acceleration overturning spectrum and brought two essential key

quantities other than the peak ground acceleration that affect the stability of a slender, free-standing column: (a) the size of the column; and (b) the duration of the period of the excitation. In the late 1940s to 1960s, a series of studies by Ikegami & Kishinouye (1947) discovered that the dynamic response of a rocking column is governed by a negative stiffness. Therefore, its free-vibration response is described by hyperbolic sines and cosines rather than harmonic. Housner (1963) offered a qualitative explanation of the size-frequency scale effect and made it famous for earthquake engineering.

Following Houser's study, a large number of studies have been conducted to further explain the complex dynamics of the free-standing rigid blocks (Makris & Konstantinidis, 2003; Makris & Vassiliou, 2013; Psycharis & Jennings, 1983; Zhang & Makris, 2001). Zhang and Makris (2001) investigated in depth the overturning potential of free-standing rigid blocks under pulse-like excitations and discovered two modes of overturning: (1) by exhibiting one or more impacts; and (2) without exhibiting any impact. Makris and Konstantinidis (2003) presented the above results in the form of rocking spectra. Subsequently, several researches are conducted to study the practical applications of rigid structures design for rocking, such as overturning of anchored rocking motion and damped rocking motion (Dimitrakopoulos & DeJong, 2012; Makris & Zhang, 2001; Vassiliou & Makris, 2015), rigid blocks with isolated bases (Vassiliou & Makris, 2012), and multiple aligned free-standing rigid columns (Makris & Vassiliou, 2013), theoretical work on the three-dimensional rocking response of free-standing column (Konstantinidis & Makris, 2007) and wobbling 3D frame (Vassiliou, 2018), etc.

However, compared with research on the analytical model of rigid rocking blocks, additional research efforts should be made to address the complexity associated with influences of flexibility and impact mechanisms on rocking behaviors. Relevant studies have been conducted to

investigate the transient drift and rocking responses of the rocking system by deriving and solving the equations of motion, and developing discontinuous impact mechanisms (Acikgoz & DeJong, 2012, 2016; Chopra & Yim, 1985; Oliveto et al., 2003; Vassiliou et al., 2015; Zhang et al., 2019). Through these studies, it has been found that fundamental discrepancies exist if the foundation is designed for rocking in contrast to the fixed-base condition. Particularly, geometric nonlinearity and the rocking impact must be considered to accurately predict the dynamic performance of the system.

1.3.2 Numerical Modeling

The physical constructions, analysis methods used to describe the seismic response, and practical design methodologies of two classes of rocking structures -- post-tensioned and free-standing rocking -- are quite different since the free-standing rocking structures have negative stiffness. In contrast, the post-tensioned structures have positive stiffness (Makris & Konstantinidis, 2003). To develop the practical design method of systems with rocking components, numerical models to quantify the seismic response of rocking structures (post-tensioned and free-standing rocking; rigid and deformable), simultaneously at the level of rocking connections, structural elements, and the entire rocking structure are needed. It would be advantageous if those models were consistent with existing finite element simulation frameworks.

Although some finite element simulations of the rocking system are already available, the significant difficulties in numerical modeling of rocking behavior cannot be ignored. First, the energy dissipation mechanism in impact is instantaneous and discontinuous, which is very much ideologically incompatible with the energy dissipating mechanisms commonly incorporated in the time integration procedures employed in conventional finite element programs. For example, rocking structures generally be modeled as nonlinear-elastic viscously-damped systems (Nazari et

al., 2017; Vassiliou et al., 2014) using ordinary FEM software, such as ABAQUS (Qu et al., 2012) and OpenSees (Vassiliou et al., 2017). However, since the principal energy dissipation mechanism of impact is instantaneous and discontinuous, the use of viscous damping cannot be predicted as a priori (Chopra & McKenna, 2016; Hall, 2006; Petrini et al., 2008; Truniger et al., 2015; Wiebe et al., 2012).

Secondly, the pure rocking problem is a stiff and geometrically nonlinear problem, which requires an iterative solution process considering the structure's displaced geometry at all times. Furthermore, the boundary conditions for a rocking problem are nonlinear. Therefore, the response of the structure with rocking behavior is very much history-dependent, and errors are consequently cumulative (Ma et al., 2005). Hence, it is essential to precisely determine the intermittent contact events in the time domain for an accurate analysis. Therefore, the computation costs are increased much more due to the tiny timestep size, and it took much effort to avoid the convergence problem.

Lastly, impact events associated with the complexity of rocking system, especially with the influences of flexibility of rocking system, is another practical obstacle for the implementation of rocking problem within FEM. It remains challenging to simulate both the large deformation effect and the non-continuous energy loss during instantaneous rocking impacts. Relatively few studies have been conducted to develop finite element models for the deformable rocking systems (Barthes, 2012; Vassiliou et al., 2014, 2017). In sum, further research needs to be done to develop numerical models that accurately predict the rocking behavior, then provide applicable references in developing practical design methodologies.

1.4 ORGANIZATION

The objective of this research is to investigate seismic performance enhancement by using protective devices and rocking components. To accomplish such a goal, this research work focuses

on modeling and seismic response analysis of two structural systems: one is inelastic structures and bridges with protective devices, the other is structures with rocking components.

This dissertation starts with the modeling and optimal design of the inelastic structure with seismic protective devices. In Chapter 2, a hybrid simulation method is utilized for accurate simulations of inelastic structures and bridges with linear/nonlinear protective devices and control algorithms. First, the modeling of seismic protective devices is implemented into the existing hybrid simulation platform, UI-SIMCOR (Kwon et al. 2007). Then both classical linear control algorithm (LQR) and nonlinear control algorithm (sliding mode control, SMC) are integrated into the hybrid simulation framework. Finally, an optimal passive control design method derived from active control responses is proposed to find the optimal design of protective devices and improve the seismic behavior. The optimal design of an eight-story inelastic building with nonlinear viscous dampers is provided as an example.

The previous optimal passive design method is extended to find optimal passive control of a benchmark highway bridge in Chapter 3. The multi-support excitation scheme and modified integration and iteration scheme are integrated into the hybrid simulation framework to enable the nonlinear time history analysis of bridges including soil-structure interaction elements. Both active and passive control responses are evaluated and compared to show the effectiveness of improving the seismic performance of a bridge and demonstrate the influence of different isolation systems and ground motion inputs on optimal design.

Chapters 4 and 5 focus on the analytical and numerical simulation of rocking systems. In Chapter 4, an analytical 2D model is derived for the evaluation of a deformable rocking column-foundation system. Various existing finite element models for rocking behavior are examined in depth. The emphasis is to understand the difficulties and find appropriate methods of modeling the

flexible rocking structures. Furthermore, a finite element-based rocking model is implemented in OpenSees, consisting of a zero-length rocking element with a Dirac-delta type impact model. By comparing both analytical and experimental results, the FEM rocking element is validated. In addition, a probabilistic seismic demand model is also proposed as an alternate way to account for the uncertainties in predicting individual rocking responses.

In Chapter 5, the seismic responses of buildings with rocking components are examined through nonlinear time history analyses. A nine-story rocking wall-frame building is developed and analyzed. It is demonstrated that the strength and deformation demands of this prototype building are reduced, and the structural damage is controlled when rocking components are used.

Finally, a summary and discussion are presented in Chapter 6.

2. STRUCTURAL CONTROL OF INELASTIC STRUCTURES WITH SEISMIC PROTECTIVE DEVICES THROUGH HYBRID SIMULATION

This chapter provides an optimal passive design procedure based on hybrid simulation and structural control methodologies. The proposed approach is applied to investigate a seismically protected eight-story inelastic structural model whose main structure is modeled in OpenSees. At the same time, the seismic protective devices and the control algorithms are implemented in MATLAB. First, the hybrid simulation scheme for inelastic structures with seismic protective devices and linear/nonlinear structural control methods is developed and validated. Through hybrid simulation, the responses and structural control of the inelastic structure are conducted. An equivalent damping parameter set is derived through linear and nonlinear control results for this nonlinear building, and it shows much improved structural performance.

2.1 HYBRID SIMULATION PLATFORM: UI-SIMCOR

This study builds on an existing hybrid simulation platform: UI-SIMCOR, and implements changes to consider various nonlinear seismic protective devices and structural control algorithms. The UI-SIMCOR was initially developed to facilitate geographically distributed pseudo-dynamic (PSD) hybrid simulation. It has been widely used for PSD hybrid simulation and multi-platform simulation with OpenSees, MATLAB, ABAQUS, etc. (Kwon et al., 2008). The simulation can be either all experiments, a combination of experiments and numerical analyses, or all numerical analyses. This study's hybrid simulation scheme is all numerical analyses, i.e., modeling the main nonlinear structure in a major finite element software while modeling the seismic protective devices in another computational platform.

The UI-SIMCOR program solves the equation of motion (EOM) of a dynamic system

generated by static condensation (Kwon et al., 2007). The degree of freedoms (DOFs) that have no mass defined or are not of interest are condensed out. UI-SIMCOR only solves the EOM with these remaining DOFs in analysis, and they are referred as 'effective DOFs.' After defining the effective DOFs, the mass matrix and damping are easily formulated. At the same time, the condensed stiffness matrix can be determined by applying a pre-specified displacement to each effective DOFs and measuring reaction forces. Due to limited space, a detailed generation of condensed EOM is not provided herein but can be found in Kwon et al. (2008). Nevertheless, the time integration method and its modifications made in UI-SIMCOR to accommodate new requirements associated with the active and passive control problems are described in the following sections.

2.2 TIME INTEGRATION METHOD ADOPTED IN UI-SIMCOR

An explicit integration algorithm of the Newmark family, called the α operator splitting (α−OS) method (Nakashima, 1990), is adopted in UI-SIMCOR to solve the condensed EOM in a time-stepping manner. The EOM of a structure with nonlinear restoring force can be expressed as:

$$\mathbf{Ma}(t) + \mathbf{Cv}(t) + \mathbf{r}(t) = \mathbf{f}(t) \tag{2.1}$$

where $\mathbf{M}$ and $\mathbf{C}$ are mass and structural damping matrix; $\mathbf{a}(t)$ and $\mathbf{v}(t)$ are acceleration and velocity vector; $\mathbf{f}(t)$ is the external excitation and $\mathbf{r}(t)$ is the nonlinear restoring force. Rewrite Equation (2.1) in discrete time form and apply the α operator, the EOM becomes:

$$\mathbf{Ma}_{n+1} + (1+\alpha)\mathbf{Cv}_{n+1} - \alpha\mathbf{Cv}_n + (1+\alpha)\mathbf{r}_{n+1} - \alpha\mathbf{r}_n = (1+\alpha)\mathbf{f}_{n+1} - \alpha\mathbf{f}_n \tag{2.2}$$

where n denotes the time step. The equilibrium in Equation (2.2) is solved according to:

(i) A predictor step:

$$\begin{aligned}\tilde{\mathbf{d}}_{n+1} &= \mathbf{d}_n + \Delta t\mathbf{v}_n + \frac{\Delta t^2}{2}(1-2\beta)\mathbf{a}_n \\ \tilde{\mathbf{v}}_{n+1} &= \mathbf{v}_n + \Delta t(1-\gamma)\mathbf{a}_n\end{aligned} \tag{2.3}$$

and (ii) A corrector step:

$$\begin{aligned}\mathbf{d}_{n+1} &= \tilde{\mathbf{d}}_{n+1} + \Delta t^2\beta\mathbf{a}_{n+1} \\ \mathbf{v}_{n+1} &= \tilde{\mathbf{v}}_{n+1} + \Delta t\gamma\mathbf{a}_{n+1}\end{aligned} \tag{2.4}$$

where parameter $\beta = (1-\alpha^2)/4$ and $\gamma = (1-2\alpha)/2$, $\alpha \in \left[-\frac{1}{3}, 0\right]$ allows the tuning of numerical damping of the method. To solve the equilibrium in Equation (2.2) without iteration, the unknown nonlinear term $\mathbf{r}_{n+1}$ is replaced by:

$$\mathbf{r}_{n+1}(\mathbf{d}_{n+1}) \approx \tilde{\mathbf{r}}_{n+1}(\tilde{\mathbf{d}}_{n+1}) + \mathbf{K}^{\mathrm{I}}(\mathbf{d}_{n+1} - \tilde{\mathbf{d}}_{n+1}) \tag{2.5}$$

which is the predicted restoring force $\tilde{\mathbf{r}}_{n+1}(\tilde{\mathbf{d}}_{n+1})$ corrected by a linear force term that is related to the system initial stiffness matrix $\mathbf{K}^{\mathrm{I}}$. Based on this assumption and substituting Equation (2.3) ~ (2.5) into Equation (2.2), the EOM becomes:

$$\hat{\mathbf{M}}\mathbf{a}_{n+1} = \hat{\mathbf{f}}_{n+1} \tag{2.6}$$

where:

$$\begin{aligned}\hat{\mathbf{M}} &= \mathbf{M} + \gamma\Delta t(1+\alpha)\mathbf{C} + \beta\Delta t^2(1+\alpha)\mathbf{K}^{\mathrm{I}} \\ \hat{\mathbf{f}}_{n+1} &= (1+\alpha)\mathbf{f}_{n+1} - \alpha\mathbf{f}_n + \alpha\tilde{\mathbf{r}}_n - (1+\alpha)\tilde{\mathbf{r}}_{n+1} + \alpha\mathbf{C}\tilde{\mathbf{v}}_n - (1+\alpha)\mathbf{C}\tilde{\mathbf{v}}_{n+1} + \alpha\left(\gamma\Delta t\mathbf{C} + \beta\Delta t^2\mathbf{K}^{\mathrm{I}}\right)\mathbf{a}_n\end{aligned} \tag{2.7}$$

Finally, the acceleration at time t_{n+1} can be solved by Equation (2.8):

$$\mathbf{a}_{n+1} = \hat{\mathbf{M}}^{-1}\hat{\mathbf{f}}_{n+1} \tag{2.8}$$

Then $\mathbf{a}_{n+1}$ is substituted into Equation (2.4) to update displacement and velocity at time t_{n+1}.

The α−OS time integrator is written in the MATLAB subprogram of UI-SIMCOR for solving the equation of motion and is ready to be modified by users. Due to this open-source

property, UI-SIMCOR can accommodate different integration schemes that are fit for hybrid simulation models in this study. Moreover, it is noted that the above integration scheme is linearly implicit and does not need iteration. This is beneficial for performing physical hybrid tests because the repeated or potentially cyclic loading for a single time step may damage the experimental specimen. It is also essential in this study because a noniterative optimization is achievable by implementing structural control methods into UI-SIMCOR, while the optimization remains highly iterative process in previous studies (Parcianello et al., 2017; Tubaldi & Kougioumtzoglou, 2015; Xie et al., 2018).

2.3 IMPLEMENTATION OF SEISMIC PROTECTIVE DEVICES IN UI-SIMCOR

The goal of implementing seismic protective device elements in a hybrid numerical simulation framework is to accurately analyze the dynamic response of nonlinear structures equipped with seismic protective devices, such as base isolation bearings, linear/nonlinear viscous dampers, and MR dampers, etc. Using the numerical hybrid simulation scheme in UI-SIMCOR, the nonlinear structures can be accurately modeled with well-developed finite element software, such as OpenSees, ABAQUS, etc. Meanwhile, the seismic protective devices, which are usually highly nonlinear, can be modeled separately on another computational program. In this study, MATLAB is used to formulate computational elements for seismic protective devices.

Considering a structure with seismic protective devices installed, the original EOM in Equation (2.1) is modified to contain the additional resisting forces, as shown below:

$$\mathbf{Ma}(t)+\mathbf{Cv}(t)+\mathbf{r}(t)+\mathbf{f}^{\text{protective}}(t)=\mathbf{f}(t) \tag{2.9}$$

where $\mathbf{f}^{\text{protective}}(t)$ is the nonlinear force of seismic protective devices, such as bearing force $\mathbf{f}^{\text{b}}(t)$ if base isolators are installed, damper force $\mathbf{f}^{\text{d}}(t)$ if passive or semi-active dampers are installed.

By setting vector components in $\mathbf{f}^{\mathrm{b}}(t)$ and $\mathbf{f}^{\mathrm{d}}(t)$ to be zero, the locations where bearings and dampers are installed can be adjusted accordingly. Due to the nonlinear behavior of seismic protective devices and their roles in the equation of motion, the computational elements that model them are implemented in terms of additionally defined MATLAB function or direct modification of integration scheme in UI-SIMCOR, as introduced as follows.

2.3.1 Hybrid Simulation for Structure with Isolators

Considering a structure with base isolators installed, the EOM in Equation (2.9) can be written in time discrete form:

$$\mathbf{M}\mathbf{a}_{n+1}+(1+\alpha)\mathbf{C}\mathbf{v}_{n+1}-\alpha\mathbf{C}\mathbf{v}_{n}+(1+\alpha)\mathbf{r}_{n+1}-\alpha\mathbf{r}_{n}+(1+\alpha)\mathbf{f}^{\mathrm{b}}_{n+1}-\alpha\mathbf{f}^{\mathrm{b}}_{n}=(1+\alpha)\mathbf{f}_{n+1}-\alpha\mathbf{f}_{n} \quad (2.10)$$

where the only additional unknown variable compared to the original equation of α−OS method, Equation (2.2), is $\mathbf{f}^{\mathrm{b}}_{n+1}$, which is the bearing force at time t_{n+1}. Similar to the approximation of nonlinear restoring force $\mathbf{r}_{n+1}$ in Equation (2.5), the predicted bearing force $\tilde{\mathbf{f}}^{\mathrm{b}}_{n+1}$ can be first evaluated by the predictor displacement of base isolation devices $\tilde{\mathbf{d}}^{\mathrm{b}}_{n+1}$, i.e., $\tilde{\mathbf{f}}^{\mathrm{b}}_{n+1}=\tilde{\mathbf{f}}^{\mathrm{b}}_{n+1}\left(\tilde{\mathbf{d}}^{\mathrm{b}}_{n+1}\right)$. Then $\tilde{\mathbf{f}}^{\mathrm{b}}_{n+1}$ is corrected by a linear term that is related to the initial stiffness of base isolation devices $\mathbf{K}^{\mathrm{I}}_{\mathrm{b}}$ to approximate the true bearing force:

$$\mathbf{f}^{\mathrm{b}}_{n+1}\left(\mathbf{d}^{\mathrm{b}}_{n+1}\right)\approx\tilde{\mathbf{f}}^{\mathrm{b}}_{n+1}\left(\tilde{\mathbf{d}}^{\mathrm{b}}_{n+1}\right)+\mathbf{K}^{\mathrm{I}}_{\mathrm{b}}(\mathbf{d}^{\mathrm{b}}_{n+1}-\tilde{\mathbf{d}}^{\mathrm{b}}_{n+1}) \quad (2.11)$$

After the additional unknown force $\mathbf{f}^{\mathrm{b}}_{n+1}$ is formulated, the response of whole structure with base isolation devices can be solved by the α−OS scheme explained before. Within this linear integration scheme, a new element that can evaluate the bearing force $\tilde{\mathbf{f}}^{\mathrm{b}}_{n+1}$ of a given predictor displacement $\tilde{\mathbf{d}}^{\mathrm{b}}_{n+1}$ is needed. Therefore, a MATLAB function is written based on classical

plasticity theory to model the kinematic hardening behavior of base isolation devices, such as Bouc-Wen model (Wen, 1976). This element takes in predictor displacement of base isolator and returns bearing force to UI-SIMCOR to proceed the time integration scheme explained from Equation (2.9) ~ (2.11).

2.3.2 Hybrid Simulation for Structure with MR Damper

There are two types of methods for modeling MR dampers. One is a clipped-optimal control strategy based on structural response feedback, consisting of a linear control method to identify the desired voltage to the current driver associated with saturation of the magnetic field in the MR damper to provide optimal force into the structure (Xi, 2014). This method is proper when the hybrid simulation is either all experiments or a combination of experiments and analyses. The other is a simple mechanical model of the MR damper, which is preferred for pure numerical analysis in this study. As shown in Figure 2.1, Spencer and his co-workers (Dyke et al., 1996; Spencer et al., 1997) proposed a modified Bouc-Wen model with spring and dashpot in parallel, and additional dashpot and spring elements were introduced to portray force-velocity characteristics of MR damper more accurately. The simple mechanical idealizations of the MR damper depicted in Figure 2.1 have been shown to predict the behavior of the prototype MR damper over a broad range of inputs accurately (Spencer et al., 1997).

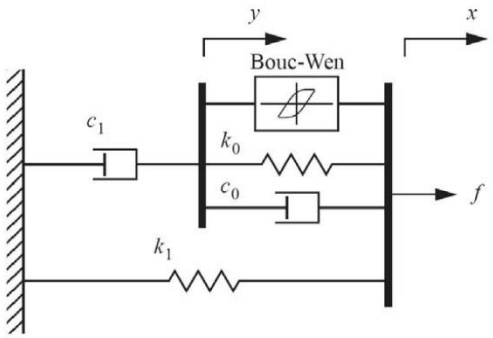

Figure 2.1. Modified Bouc-Wen model of MR damper (Dyke et al., 1996)

The modified Bouc-Wen model can be expressed mathematically as:

$$f^{\mathrm{d}} = c_1\dot{y} + k_1\left(x - x_0\right) \tag{2.12}$$

$$\dot{y} = \frac{1}{c_0 + c_1}\left[\alpha z + c_0\dot{x} + k_0\left(x - y\right)\right] \tag{2.13}$$

$$\dot{z}\left(t\right) = -\gamma\left|\dot{x} - \dot{y}\right|z\left|z\right|^{n-1} - \beta\left(\dot{x} - \dot{y}\right)\left|z\right|^{n} + A\left(\dot{x} - \dot{y}\right) \tag{2.14}$$

where f^{d} is the applied MR damper force; α, γ, β, A and n are the parameters for the built-in Bouc-Wen model, which control the shape of the hysteresis loops for the yielding element; c_0, c_1, k_0 and k_1 are coefficients for the linear dashpots and springs in the model, which control the stiffness and force-velocity loop at different stage; x_0 is the initial displacement of spring and x is the displacement of where the MR damper is placed. Since UI-SIMCOR adopts a time-stepping integration scheme with timestep Δt, elements that model history-dependent behavior should be discretized in the time domain. To work compatibly with the UI-SIMCOR integration scheme, the above equations are converted into the incremental form by Euler's method, as written as follows:

$$f_{N+1}^{d} = c_1\dot{y}_{N+1} + k_1\left(x_{N+1} - x_0\right) \tag{2.15}$$

$$\dot{y}_{N+1} = \frac{1}{c_0 + c_1}\left[\alpha z_{N+1} + c_0\dot{x}_{N+1} + k_0\left(x_{N+1} - y_{N+1}\right)\right] \tag{2.16}$$

$$z_{N+1} = z_N + \Delta t\left[-\gamma\left|\dot{x}_N - \dot{y}_N\right|z_N\left|z_N\right|^{n-1} - \beta\left(\dot{x}_N - \dot{y}_N\right)\left|z_N\right|^{n} + A\left(\dot{x}_N - \dot{y}_N\right)\right] \tag{2.17}$$

$$y_{N+1} = y_N + \Delta t\left\{\frac{1}{c_0 + c_1}\left[\alpha z_N + c_0\dot{x}_N + k_0\left(x_N - y_N\right)\right]\right\} \tag{2.18}$$

A MATLAB function based on Equation (2.15) ~ (2.18) is developed as an element that provides the MR damper behavior presented in Figure 2.1. Note that the damper force at time t_{N+1} is essentially a function of the damper's displacement x_{N+1} and velocity $\dot{x}_{N+1}$, which can be

estimated by the predictor quantities in Equation (2.3). Then the error is compensated with the α−OS integration process in UI-SIMCOR. Namely, this element takes in predicted displacement and velocity of MR damper as input and returns the updated MR damper force. Before further applying this element, a numerical MR damper model based on the ODE solver of MATLAB is developed and used to verify the accuracy of the presented approach. The calibrated parameters of modified Bouc-Wen model for MR damper and harmonic excitation can be found in Table 4.11 of Xi (2014). Figure 2.2 shows that the implemented MR damper element yields the same results as the ODE solver method, which validates the modeling approach.

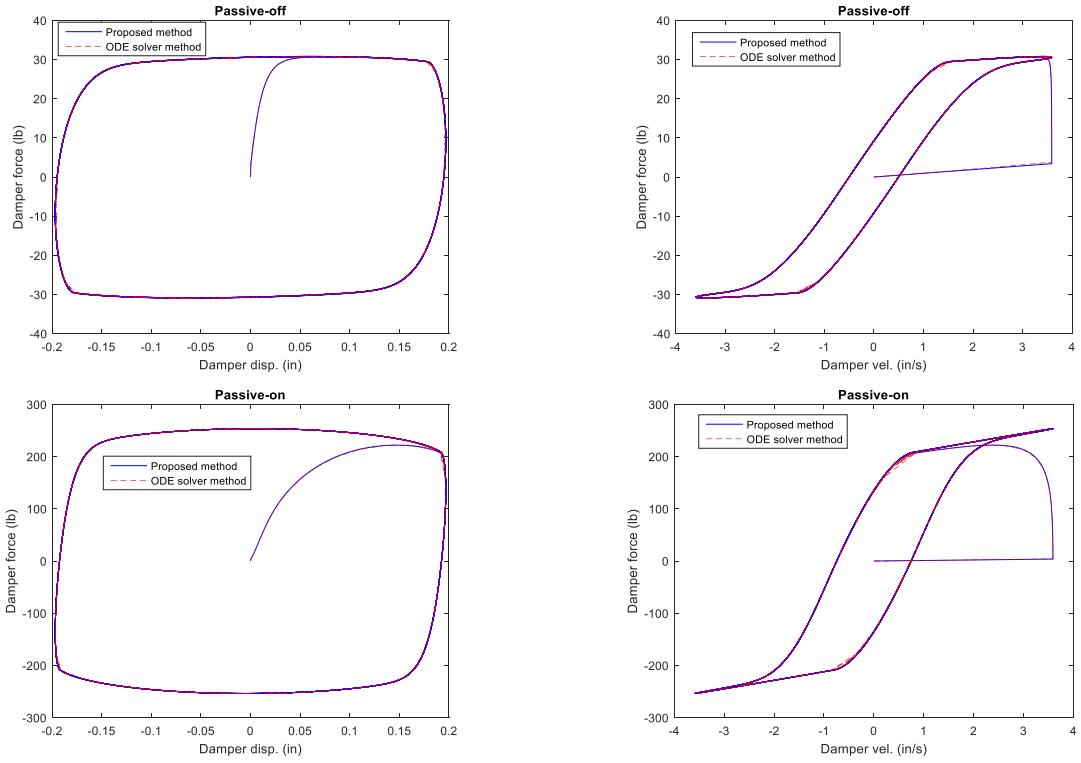

(a) Force-displacement (b) Force-velocity

Figure 2.2. Verification of proposed MR damper element with ODE solver in MATLAB

2.3.3 Hybrid Simulation for Structure with Isolators and Nonlinear Dampers

For hybrid simulation of structure with base isolators and nonlinear viscous dampers

installed, after defining the computational element of base isolators as shown in section 2.3.1, the computational element that models nonlinear viscous dampers is incorporated in the time integration section of UI-SIMCOR according to their role in the equation of motion. The modification of the built-in α−OS method is shown in the following to model nonlinear viscous dampers.

First, the displacement and velocity vectors $\mathbf{d}_{n+1}$ and $\mathbf{v}_{n+1}$ can be solved by the same predictor and corrector steps defined in Equations (2.3) & (2.4). Then $\mathbf{a}_{n+1}$ needs to be solved iteratively from the time discretized form of Equation (2.19) as following:

$$\mathbf{F}\left(\mathbf{a}_{n+1}\right)=\mathbf{M}\mathbf{a}_{n+1}+\mathbf{C}\mathbf{v}_{n+1}(t)+\mathbf{r}_{n+1}\left(\mathbf{a}_{n+1}\right)+\mathbf{f}_{n+1}^{\mathrm{b}}\left(\mathbf{a}_{n+1}\right)+\mathbf{f}_{n+1}^{\mathrm{d}}\left(\mathbf{a}_{n+1}\right)-\mathbf{f}_{n+1}=0 \tag{2.19}$$

In general, a nonlinear viscous damper can be modeled by:

$$f^{d}=c_{\mathrm{d}}\left|v_{\mathrm{d}}\right|^{\alpha_{\mathrm{d}}}\operatorname{sign}\left(v_{\mathrm{d}}\right) \tag{2.20}$$

where c_{d} is the damping coefficient, v_{d} is the velocity of the nonlinear damper and α_d is a constant that controls the force-displacement loop of the damper. For a N-DOF system equipped with nonlinear dampers and bearings on each DOF, the damper forces are in the vector form:

$$\mathbf{f}^{\mathbf{d}}=\begin{bmatrix} f^{\mathrm{d}1} & f^{\mathrm{d}2} & \cdots & f^{\mathrm{d}i} & \cdots & f^{\mathrm{d}N}\end{bmatrix}^{\mathrm{T}} \tag{2.21}$$

Approximating the restoring force term $\mathbf{r}_{n+1}$ and $\mathbf{f}_{n+1}^{\mathrm{b}}$ as shown in Equations (2.5) and (2.11) respectively, the derivative of Equation (2.19) about $\mathbf{a}_{n+1}$ is given by:

$$\mathbf{F}'\left(\mathbf{a}_{n+1}\right)=\mathbf{M}+\mathbf{C}\frac{\partial\mathbf{v}_{n+1}}{\partial\mathbf{a}_{n+1}}+\frac{\partial\mathbf{r}_{n+1}}{\partial\mathbf{a}_{n+1}}+\frac{\partial\mathbf{f}_{n+1}^{\mathrm{b}}}{\partial\mathbf{a}_{n+1}}+\frac{\partial\mathbf{f}_{n+1}^{\mathrm{d}}}{\partial\mathbf{v}_{n+1}}\frac{\partial\mathbf{v}_{n+1}}{\partial\mathbf{a}_{n+1}} \tag{2.22}$$

where $\frac{\partial\mathbf{f}_{n+1}^{\mathrm{d}}}{\partial\mathbf{v}_{n+1}}$ is a $N\times N$ vector, $\frac{\partial\mathbf{v}_{n+1}}{\partial\mathbf{a}_{n+1}}=\Delta t\gamma\mathbf{I}$, $\frac{\partial\mathbf{r}_{n+1}}{\partial\mathbf{a}_{n+1}}=\Delta t^{2}\beta\mathbf{K}^{\mathrm{I}}$, and $\frac{\partial\mathbf{f}_{n+1}^{\mathrm{b}}}{\partial\mathbf{a}_{n+1}}=\Delta t^{2}\beta\mathbf{K}_{\mathrm{b}}^{\mathrm{I}}$. For the i^{th} nonlinear damper, the derivative of damper force about velocity is given by:

$$\frac{\partial f^{\mathrm{d}i}}{\partial v_{\mathrm{d}i}} = \alpha_{\mathrm{d}i} c_{\mathrm{d}i} \left| v_{\mathrm{d}i} \right|^{\alpha_{\mathrm{d}i}-1} \tag{2.23}$$

where the velocity across of the i^{th} nonlinear damper $v_{\mathrm{d}i}$ can be related to global velocity vector $\mathbf{v}$ according to the two DOFs it is installed to. Once $\mathbf{F}'\left(\mathbf{a}_{n+1}\right)$ is obtained, Newton's iteration can be applied to obtain the converged solution for $\mathbf{a}_{n+1}$:

$$\mathbf{a}_{n+1}^{k+1} = \mathbf{a}_{n+1}^{k} - \mathbf{F}'\left(\mathbf{a}_{n+1}^{k}\right)\mathbf{F}\left(\mathbf{a}_{n+1}^{k}\right) \tag{2.24}$$

The displacement and velocity vectors can then be obtained by Equation (2.4) once the acceleration vector $\mathbf{a}_{n+1}$ is solved.

2.4 VALIDATION OF HYBRID NUMERICAL SIMULATION SCHEME

To validate the hybrid numerical simulation scheme proposed above, a three-story nonlinear frame structure, as shown in Figure 2.3, is considered for numerical simulation and verification hereafter. This model represents a test structure located in Harbin Institute of Technology, China, which was tested for validating the hybrid numerical simulation scheme experimentally. A detailed description of the experimental structure can be found in Xi (2014). Four energy dissipation strategies are adopted to investigate the structural responses under earthquake excitation: (a) base isolators are installed at the base level; (b) MR damper is installed between the first floor of the structure and outside fixture; (c) Nonlinear viscous dampers are installed between floors; (d) base isolators are installed at the base level, and a nonlinear damper is installed between the first floor of the structure and outside fixture. Figure 2.3 illustrates the above control strategies for the structure to be analyzed.

In this study, OpenSees is chosen as the FE software to model the nonlinear main structure, and MATLAB is used to model the seismic protective devices as stated in Section 2.3. The beams

and columns in the frame are modeled by beam-column elements with bilinear force-displacement material property in OpenSees (Mazzoni et al., 2006). The model parameters of base isolators and nonlinear damper are shown in Table 2.1. In contrast, other structural properties and identified parameters of the modified Bouc-Wen model for MR damper can be found in Xi (2014). In implementing the hybrid simulation scheme for this structure, two horizontal DOFs are selected as effective DOFs corresponding to each floor and base layer, namely, six effective DOFs in total for case (b) and (c) while eight effective DOFs in total for case (a) and (d). The equation of motion is solved with the modified integration algorithm in UI-SIMCOR described in Section 2.3.

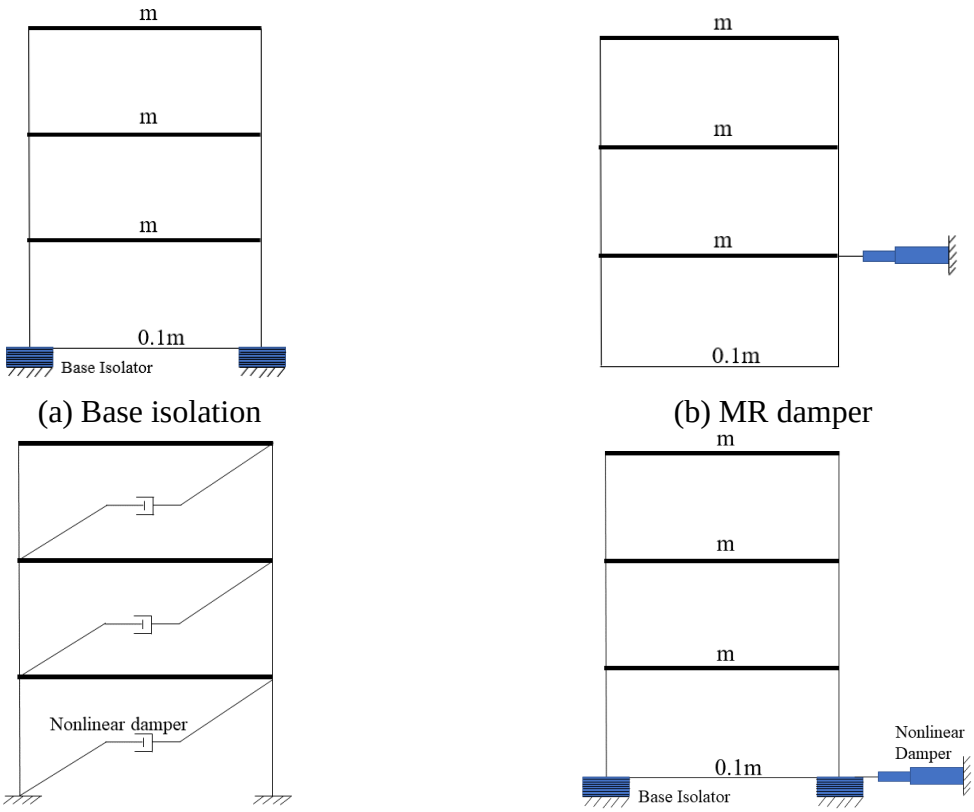

(a) Base isolation (b) MR damper

(c) Interstory nonlinear damper (d) Base isolation & nonlinear damper

Figure 2.3. Structural control strategies for numerical simulation and verification

Table 2.1. Modeling parameters for protective devices

Nonlinear damper	c = 300N*s/m	α = 0.5					
Bouc-Wen model parameters for base isolator (Wen, 1976)	K = 131.35N/m	α = 0.1	Dy = 0.25m	γ = 0.5	β = 0.5	n = 20	A=1

The 1940 El-Centro earthquake record (North-South component, Peknold version) is used as the input ground motion for all cases. This motion was used in the experimental program of the testing structure at HIT (Xi, 2014). For control strategies (a), (c), and (d), the dynamic structural responses from the hybrid numerical simulation are compared with those of the whole OpenSees model, whose both main structure and control devices are modeled in OpenSees. For control strategy (b), results solved from ODE solver in MATLAB are used to verify the structural control by MR damper. Figure 2.4 to Figure 2.7 compares the structural response and force-displacement curves of protective devices under different control strategies using the hybrid simulation and the whole model. As can be seen, not only the peak values but also the time histories of the inter-story drift, the floor acceleration, and force-displacement loops of protective devices are well captured by using the proposed hybrid simulation scheme. Namely, the proposed hybrid numerical simulation framework can accurately analyze the dynamic response of nonlinear structures equipped with seismic protective devices, thus builds a solid foundation for finding the optimal design of seismic protective devices to minimize the structural responses.

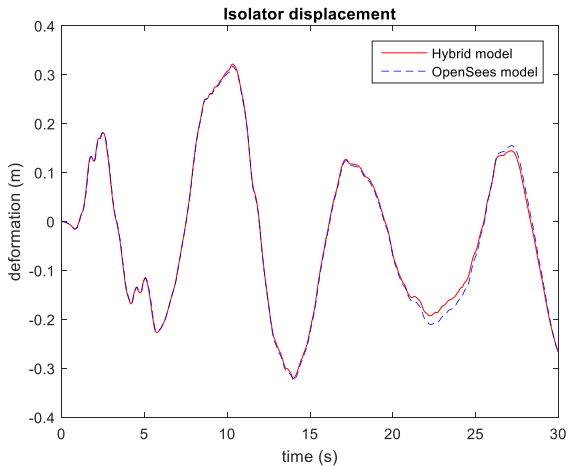

(a) Isolator displacement history

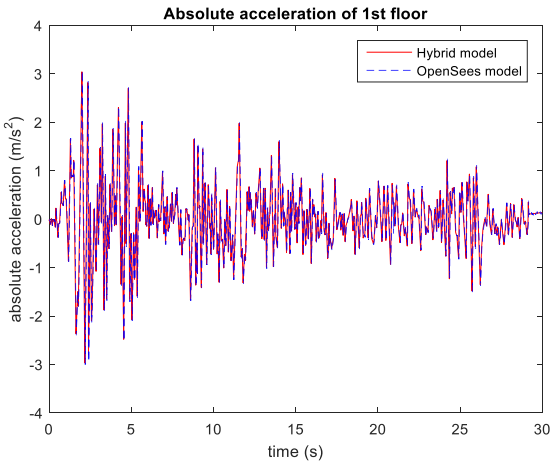

(b) Isolator acceleration history

Figure 2.4. Comparison of structural response under control by base isolation

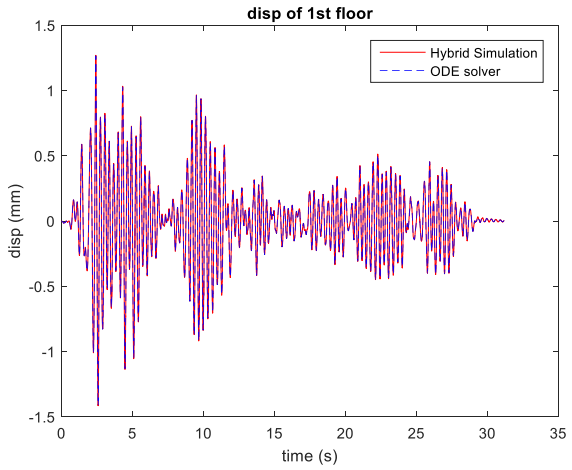

(a) 1st floor displacement history

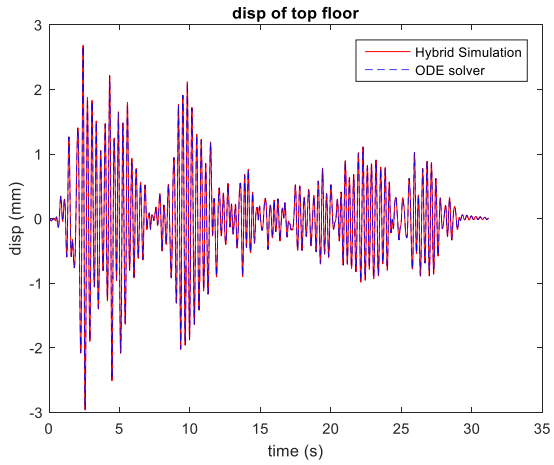

(b) Top floor displacement history

Figure 2.5. ODE solver verification of hybrid numerical simulation for MR dampers

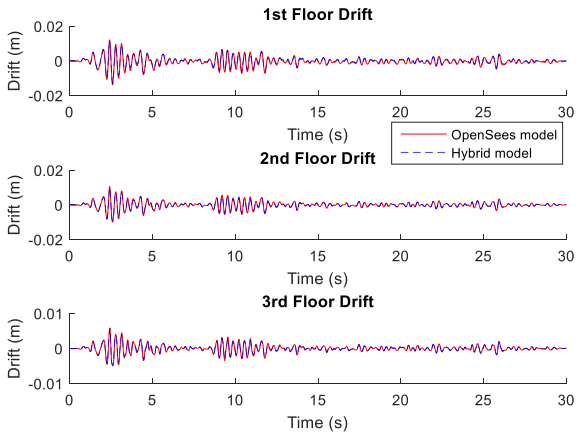

(a) Story drift comparison

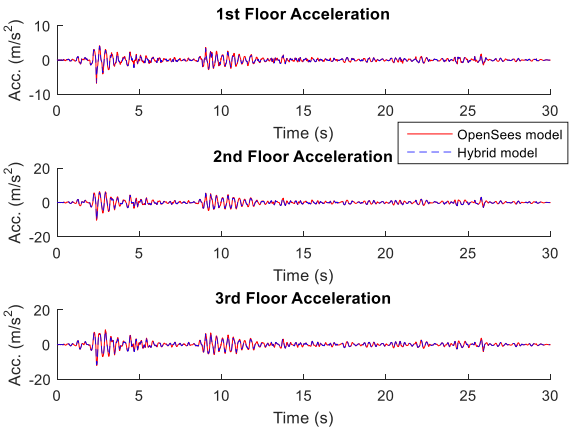

(b) Story acceleration comparison

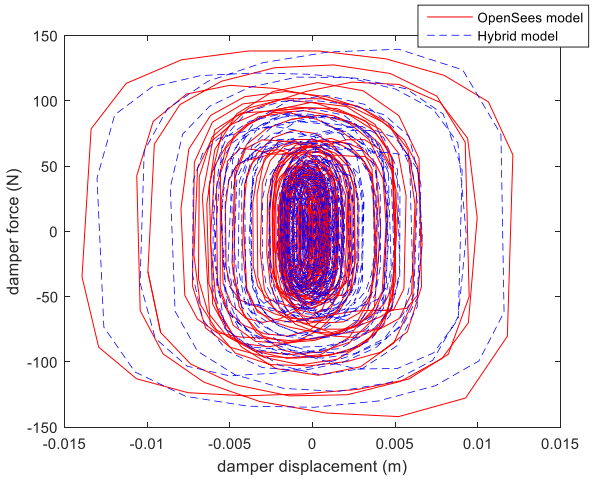

(c) Force-displacmemt loop of nonlinear damper at 1st floor

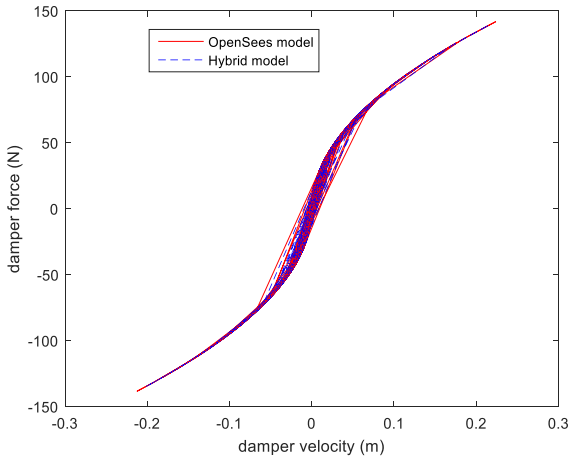

(d) Force-velocity loop of nonlinear damper at 1st floor

Figure 2.6. Verification of hybrid simulation for structure under control by nonlinear viscous dampers

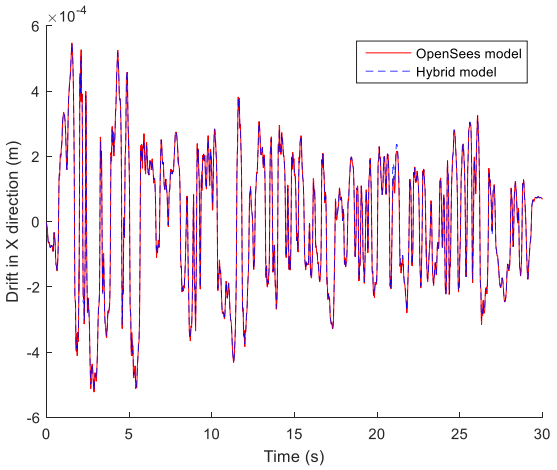

(a) 1st floor drift

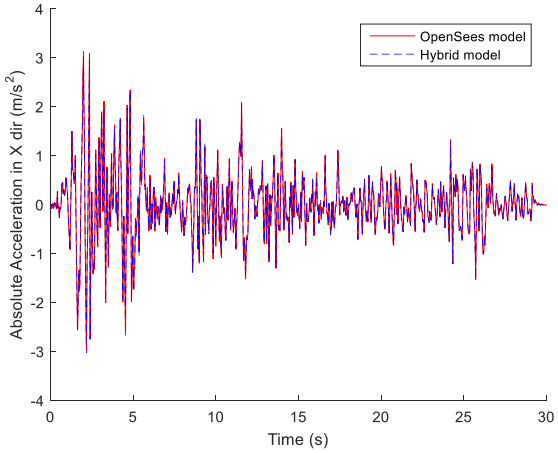

(b) 1st floor acceleration

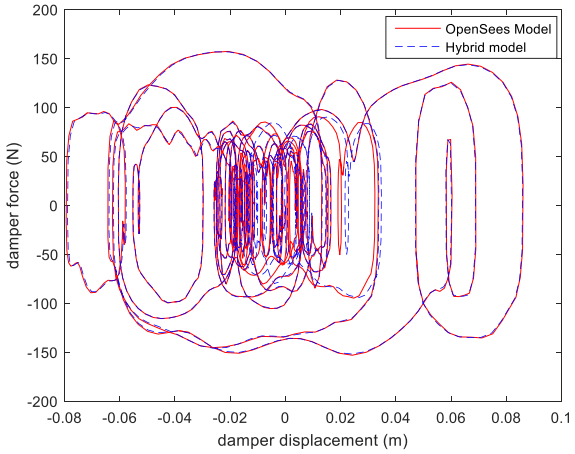

(c) Nonlinear damper force-displacement loop

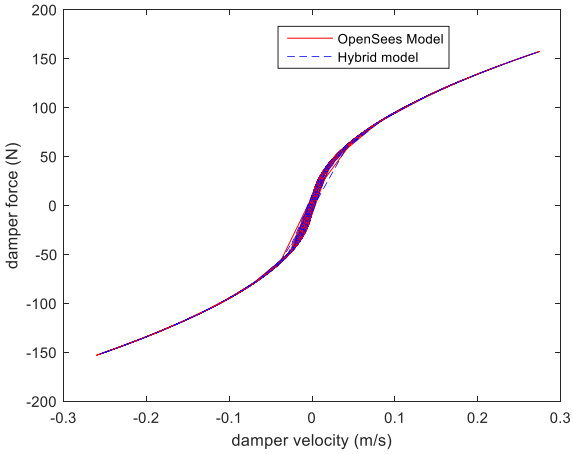

(d) Nonlinear damper force-velocity loop

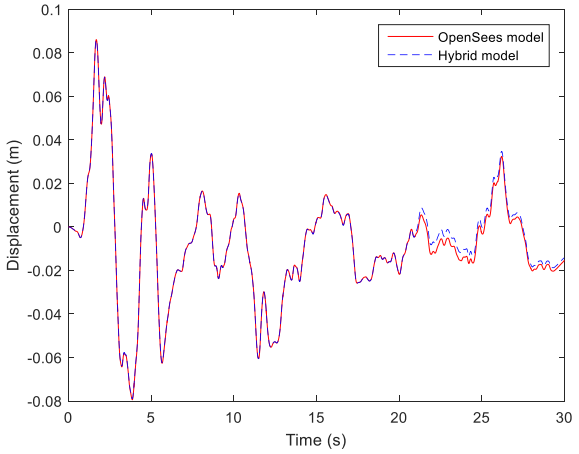

(e) Displacement of base isolator

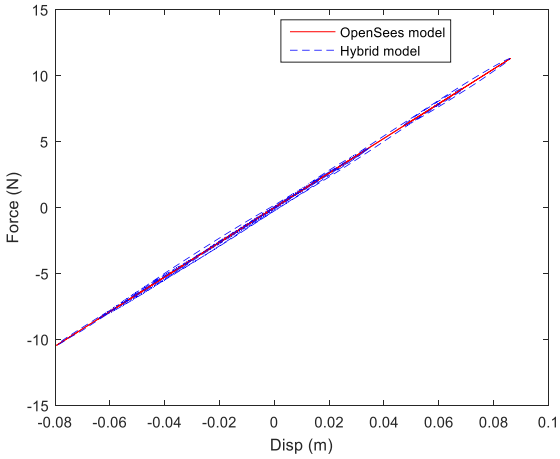

(f) Force-displacement loop of base isolator

Figure 2.7. Verification of hybrid simulation for structure under control by base isolation & nonlinear damper

2.5 STRUCTURAL CONTROL IN HYBRID SIMULATION FRAMEWORK

In the hybrid simulation scheme stated above, the control devices are modeled separately in MATLAB, which make it convenient to apply control algorithms to obtain optimized structural responses. Classical linear control theory (such as linear quadratic regulator, LQR) is easy to be developed and works perfectly for linear systems. Nevertheless, nonlinear control methods (such as sliding mode control, SMC) are presented for better applications to nonlinear and hysteretic civil engineering structures under seismic loading (Utkin, 2013; Yang et al., 1995; Young, 1993; Zhou & Fisher, 1992). The previous study shows that the SMC method has a specific ability to construct robust control systems concerning structure's parametric uncertainties and to stabilize nonlinear systems by using continuous state feedback laws. Therefore, two active control algorithms, LQR (Gluck et al., 1996) and SMC (Yang et al., 1995), are implemented and compared in a hybrid simulation scheme herein.

2.5.1 Classical Linear Optimal Control Theory

The LQR method is incorporated in the time integration section of UI-SIMCOR according to its role in the equation of motion. Consider an actively controlled n-DOF inelastic structure subjected to earthquake ground acceleration, the equation of motion with control forces is given by:

$$\mathbf{M}\ddot{\mathbf{x}}(t)+\mathbf{C}\dot{\mathbf{x}}(t)+\mathbf{F}_{\mathrm{s}}\left[\mathbf{x}(t)\right]=\mathbf{F}_{\mathrm{e}}(t)+\mathbf{H}\mathbf{U}(t) \tag{2.25}$$

where $\mathbf{M}$, $\mathbf{C}$, $\mathbf{K}$ are mass, structural damping and stiffness related to the displacements $\mathbf{x}(t)=\left[x_1, x_2, \cdots, x_n\right]^{\mathrm{T}}$ at various degrees of freedom; $\mathbf{F}_{\mathrm{e}}(t)$ is a vector representing external force caused by ground excitation; $\mathbf{U}(t)=\left[u_1(t), u_2(t), \cdots, u_n(t)\right]^{\mathrm{T}}$ is the control forces at locations

indicated by matrix $\mathbf{H}$; $\mathbf{F}_s[\mathbf{x}(t)]$ is the restoring force vector which can be written as:

$$\mathbf{F}_s[\mathbf{x}(t)] = \tilde{\mathbf{K}}\mathbf{x}(t) + \tilde{\mathbf{H}}\mathbf{f}[\mathbf{x}(t)] \tag{2.26}$$

where linear elastic stiffness of structure will appear in the $\tilde{\mathbf{K}}$ matrix of Equation (2.26), the nonlinear portion of hysteretic restoring force is $\mathbf{f}[\mathbf{x}(t)] = [f_1, f_2, \cdots, f_n]^T$.

If whole model of structure is built in MATLAB, the hysteretic restoring force of ith story unit can be modeled as (Yang et al., 1992):

$$f_{si} = \varepsilon_i k_i x_i(t) + (1-\varepsilon_i) k_i D_{yi} z_i \tag{2.27}$$

where ε_i is the ratio of the post-yielding to pre-yielding stiffness k_i; D_{yi} is the yield deformation; z_i is hysteretic variable with $|z_i| \le 1$. A detailed description of this hysteretic modeling is not provided herein and can be found in Yang et al. (Yang et al., 1992) due to limited space. While for hybrid modeling in UI-SIMCOR framework, $\mathbf{F}_s[\mathbf{x}(t)]$ can be directly returned from OpenSees module after applying the predict displacement, therefore, stiffness $\tilde{\mathbf{K}}$ is essentially the initial stiffness $\mathbf{K}^I$ that can be returned from OpenSees module.

To apply LQR method, the equation of motion needs to be simplified in the following state space form by considering only the initial elastic force vectors:

$$\dot{\mathbf{z}}(t) = \mathbf{A}\mathbf{z}(t) + \mathbf{B}\mathbf{U}(t) + \mathbf{E}\mathbf{F}_e(t) \tag{2.28}$$

where $\mathbf{z}(t) = [\mathbf{x}(t), \dot{\mathbf{x}}(t)]^T$ is the structural response in state space. $\mathbf{A}$ is the system matrix. $\mathbf{B}$ and $\mathbf{E}$ are location matrices which respectively specify the locations of the control forces and external excitations in the state space, as shown in Equation (2.29):

$$\mathbf{A} = \begin{bmatrix} \mathbf{0} & \mathbf{I} \\ -\mathbf{M}^{-1}\tilde{\mathbf{K}} & -\mathbf{M}^{-1}\mathbf{C} \end{bmatrix} \quad \mathbf{B} = \begin{bmatrix} \mathbf{0} \\ \mathbf{M}^{-1}\mathbf{H} \end{bmatrix} \quad \mathbf{E} = \begin{bmatrix} \mathbf{0} \\ \mathbf{M}^{-1} \end{bmatrix} \tag{2.29}$$

In classical linear optimal control (Gluck et al., 1996), the control force $\mathbf{U}(t)$ is chosen in such a way that a performance index J is minimized:

$$J = \int_0^{t_f} \left[\mathbf{z}^{\mathrm{T}}(t)\mathbf{Q}\mathbf{z}(t) + \mathbf{U}^{\mathrm{T}}(t)\mathbf{R}\mathbf{U}(t) \right] \mathrm{d}t \tag{2.30}$$

where $\mathbf{Q}$ and $\mathbf{R}$ are referred as weighting matrices, whose magnitudes are assigned according to the relative importance attached to the state variables and control forces. The optimal control force is given by:

$$\mathbf{U}(t) = \mathbf{G}\mathbf{z}(t) \tag{2.31}$$

where $\mathbf{G}$ is the gain matrix which given by:

$$\mathbf{G} = -\frac{1}{2}\mathbf{R}^{-1}\mathbf{B}^{\mathrm{T}}\mathbf{P} \tag{2.32}$$

and $\mathbf{P}$ is the solution of the Ricatti equation shown below:

$$\mathbf{A}^{\mathrm{T}}\mathbf{P} + \mathbf{P}\mathbf{A} - \frac{1}{2}\mathbf{P}\mathbf{B}\mathbf{R}^{-1}\mathbf{B}^{\mathrm{T}}\mathbf{P} + 2\mathbf{Q} = 0 \tag{2.33}$$

For the whole model in MATLAB, the EOM can be solved by using ODE solver once control force $\mathbf{U}$ is solved. While for hybrid modeling in UI-SIMCOR framework, by rewriting control force $\mathbf{U}(t) = \mathbf{G}\mathbf{z}(t) = \mathbf{G}_x\mathbf{x}(t) + \mathbf{G}_{\dot{x}}\dot{\mathbf{x}}(t)$ from LQR and plugging $\mathbf{U}(t)$ into Equation (2.25), the dynamic response of actively controlled inelastic structure can be solved by modifying Equation (2.7) of the original α-OS integrator to the following:

$$\begin{aligned}
\hat{\mathbf{M}} &= \mathbf{M} + \gamma\Delta t(1+\alpha)\bar{\mathbf{C}} + \beta\Delta t^2(1+\alpha)\left(\bar{\mathbf{K}} + \mathbf{K}^{\mathrm{I}}\right) \\
\hat{\mathbf{f}}_{n+1} &= (1+\alpha)\mathbf{f}_{n+1} - \alpha\mathbf{f}_n + \alpha\left(\tilde{\mathbf{r}}_n + \bar{\mathbf{K}}\tilde{\mathbf{d}}_n\right) - (1+\alpha)\left(\tilde{\mathbf{r}}_{n+1} + \bar{\mathbf{K}}\tilde{\mathbf{d}}_{n+1}\right) + \alpha\bar{\mathbf{C}}\tilde{\mathbf{v}}_n - (1+\alpha)\bar{\mathbf{C}}\tilde{\mathbf{v}}_{n+1} \\
&\quad + \alpha\left[\gamma\Delta t\bar{\mathbf{C}} + \beta\Delta t^2\left(\bar{\mathbf{K}} + \mathbf{K}^{\mathrm{I}}\right)\right]\mathbf{a}_n
\end{aligned} \tag{2.34}$$

where $\bar{\mathbf{K}} = -\mathbf{H}\mathbf{G}_x$, $\bar{\mathbf{C}} = \mathbf{C} - \mathbf{H}\mathbf{G}_{\dot{x}}$; force $\mathbf{r}$ denotes the nonlinear restoring force $\mathbf{F}_{\mathrm{s}}[\mathbf{x}(t)]$ returned from OpenSees module; force $\mathbf{f}$ denotes the external force $\mathbf{F}_{\mathrm{e}}(t)$.

2.5.2 Sliding Mode Control (SMC)

The SMC method is also incorporated in the time integration section of UI-SIMCOR framework to provide design control forces in the equation of motion. When using SMC on the inelastic structural model in MATLAB, the nonlinear portion of restoring force in the EOM is maintained, thus state-space Equation (2.28) becomes:

$$\dot{\mathbf{z}}(t) = \mathbf{A}\mathbf{z}(t) - \tilde{\mathbf{B}}\mathbf{f}(\mathbf{z}) + \mathbf{B}\mathbf{U}(t) + \mathbf{E}\mathbf{F}_{\mathrm{e}}(t) \tag{2.35}$$

where $\tilde{\mathbf{B}}$ is the location matrices specifying the locations of the nonlinear portion of hysteretic restoring force:

$$\tilde{\mathbf{B}} = \begin{bmatrix} \mathbf{0} \\ \mathbf{M}^{-1}\tilde{\mathbf{H}} \end{bmatrix} \tag{2.36}$$

The sliding mode control theory is to design controllers to drive the response trajectory into a designed sliding surface, where the motion is minimized and stable on the sliding surface. Namely, there are two fundamental steps: (1) design of sliding surfaces, where the system exhibits the designed behavior; (2) design of controllers, which guarantees the reaching of the designed sliding mode. Generally, the sliding surface is a nonlinear function of the state vector. As described by Utkin (Utkin, 2013), in cases where one controller is installed for each nonlinear element, the sliding surface becomes a linear combination of the state vector and can be written as:

$$\mathbf{S} = \mathbf{P}\mathbf{z} = 0 \tag{2.37}$$

where $\mathbf{S} = \begin{bmatrix} S_1 & S_2 & \dots & S_r \end{bmatrix}^{\mathrm{T}}$ is a vector denoting a r-dimensional linear sliding surface, with r denoting the number of controllers installed in structure. $\mathbf{P}$ is a matrix to be determined such that the motion on the sliding surface is stable and minimized. According to Yang et al. (1995), the design matrix $\mathbf{P}$ of the sliding surface is obtained by converting the state equation of motion (2.37) into the so-called “regular form”, then minimizing the integral of the quadratic function of the state

vector:

$$J = \int_0^\infty \mathbf{z}^{\mathrm{T}}(t)\mathbf{Q}\mathbf{z}(t)\,\mathrm{d}t \tag{2.38}$$

where $\mathbf{Q}$ is a $(2n \times 2n)$ positive definite weighting matrix. Details about the procedure to design the sliding surface for a nonlinear shear-type building can be found in Yang et al. (1995). The main steps of computing design matrix $\mathbf{P}$ are shown in Appendix for the sake of completion.

Based on the obtained sliding surface, the controller which drive the state trajectory into the sliding surface is achieved by using Lyapunov direct method. Detail procedures of designing controller can be found in Yang et al. (1995) and is not repeated here for simplicity. According to Yang et al. (1995), a continuous saturated controller which do not have possible chattering effects is presented as:

$$u_i(t) = \begin{Bmatrix} \alpha_i^* G_i - \delta_i \lambda_i; & \text{if } \left|\alpha_i^* G_i - \delta_i \lambda_i\right| \le \bar{u}_{i\max} \\ \bar{u}_{i\max}\,\mathrm{sgn}\left(\alpha_i^* G_i - \delta_i \lambda_i\right); & \text{otherwise} \end{Bmatrix} \tag{2.39}$$

where $0 \le \alpha_i^* \le 1$; $\pm\bar{u}_{i\max}$ $(i = 1, 2, \cdots r)$ are the upper and lower bounds of the control force u_i; $\boldsymbol{\lambda} = \mathbf{S}'\mathbf{P}\mathbf{B}$; $\mathbf{G} = -(\mathbf{P}\mathbf{B})^{-1}\mathbf{P}\left(\mathbf{A}\mathbf{z} - \tilde{\mathbf{B}}\mathbf{f} + \mathbf{E}\mathbf{F}_{\mathrm{e}}\right)$; sliding margin $\bar{\boldsymbol{\delta}}$ is a $(r \times r)$ diagonal matrix with diagonal elements $\delta_i \ge 0$. The controllers presented in Equation (2.39) are referred as the saturated controllers because the control effort $u_i(t)$ is saturated at $\pm\bar{u}_{i\max}$. Design parameters α_i^* and $\bar{u}_{i\max}$ can be specified by the designer to make a trade-off between the control effort and the structural response.

The following modifications are made to make sliding mode control work compatibly with UI-SIMCOR integration process. First, to extend the presented SMC method to structure with existing protective devices, the state-space equation of motion is modified as:

$$\dot{\mathbf{z}}(t) = \mathbf{A}\mathbf{z}(t) - \tilde{\mathbf{B}}\mathbf{F}_s(\mathbf{z}) - \hat{\mathbf{B}}\mathbf{f}^p(\mathbf{z}) + \mathbf{B}\mathbf{U}(t) + \mathbf{E}\mathbf{F}_e(t) \tag{2.40}$$

where $\mathbf{f}^p(\mathbf{z})$ is nonlinear restoring force provided by any protective devices implemented in UI-SIMCOR at locations indicated by matrix $\hat{\mathbf{B}}$. Since inelastic restoring forces $\mathbf{F}_s(\mathbf{z})$ is returned from main structure in OpenSees, it can have any nonlinearity that comes from materials, sections or elements defined in OpenSees module. Therefore, there is no need to separate the restoring forces to linear and nonlinear parts as shown in Equation (2.26), which results in the system matrix $\mathbf{A}$ becomes $\begin{bmatrix} \mathbf{0} & \mathbf{I} \\ \mathbf{0} & -\mathbf{M}^{-1}\mathbf{C} \end{bmatrix}$, location matrix $\tilde{\mathbf{B}}$ becomes $\begin{bmatrix} \mathbf{0} \\ \mathbf{M}^{-1} \end{bmatrix}$. The sliding surface and controller are the same as before except the matrix $\mathbf{G}$ becomes $-(\mathbf{PB})^{-1}\mathbf{P}\left(\mathbf{Az} - \tilde{\mathbf{B}}\mathbf{F}_s - \hat{\mathbf{B}}\mathbf{f}^p + \mathbf{E}\mathbf{F}_e\right)$. Then substituting the obtained control forces into equation of motion in time stepping method, the structural responses can be solved by using time integration methods implemented in UI-SIMCOR. Namely, during the α operator splitting process at current time step t_{n+1}, obtain control force $\mathbf{U}_{n+1}$ and $\mathbf{U}_n$ using Equation (2.39), then put them into the equivalent external force $\hat{\mathbf{f}}_{n+1}$ and solve the structural responses.

2.5.3 Validation of Structural Control Methods in UI-SIMCOR Framework

An eight-story structure, as shown in Figure 2.8 (Xie et al., 2018), is adopted and analyzed here to verify the implemented structural control methods. The floor mass and elastic stiffness of each story are given in Table 2.2. The story height of the building is taken as 3.05 m (10 feet). The yielding displacement of all eight floors is 0.02 m, and the post-yielding stiffness ratio is 0.1. For simplicity, the inherent viscous damping of the structure is not considered. Both LQR and SMC models are evaluated for applying active control force U at each story. All weight matrices in LQR

and sliding mode control are considered to be identity matrices for simplicity. To provide an effective controller in SMC, $\alpha_i^* = 0.9$ and the maximum control force $|\bar{u}_{i\max}| = 8500kN$, a sliding margin of $\delta_i = 10^6 kN \cdot t \cdot m/s$ with $i = 1 \sim 8$ are considered in this study. The fault normal component of El Centro Array no. 5, during the 1979 Imperial Valley earthquake is used as the input.

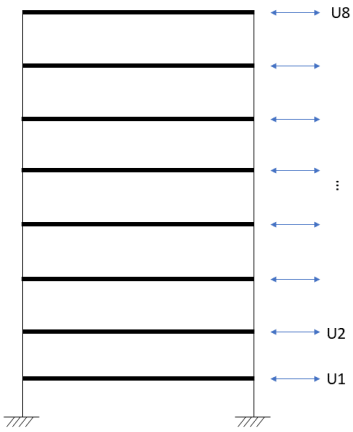

Figure 2.8. Eight story inelastic structure

Table 2.2. Structural properties of the sample 8DOF structure (Xie et al., 2018)

Story #	1	2	3	4	5	6	7	8
Story mass m_i (ton)	345.6	345.6	345.6	345.6	345.6	345.6	345.6	345.6
Story stiffness k_i ($\frac{10^5 kN}{m}$)	3.4	3.2	2.85	2.69	2.43	2.07	1.69	1.37

In order to verify the implemented control methods in UI-SIMCOR, for both the LQR method and SMC method, two equivalent models of this controlled eight-story building are developed and evaluated: (1) MATLAB model whose main structure and control algorithm are both simulated in MATLAB; (2) UI-SIMCOR model whose main structure is in OpenSees and control algorithm is implemented in MATLAB. The structural responses and control forces are

compared in Figure 2.9. It shows that the hybrid actively controlled model in UI-SIMCOR can provide the same results compared with the MATLAB model, which means the implemented active control methods are correct and ready for use in other structural control cases. The results from active control study provide the guidance needed for finding equivalent passive control cases in Section 2.6.

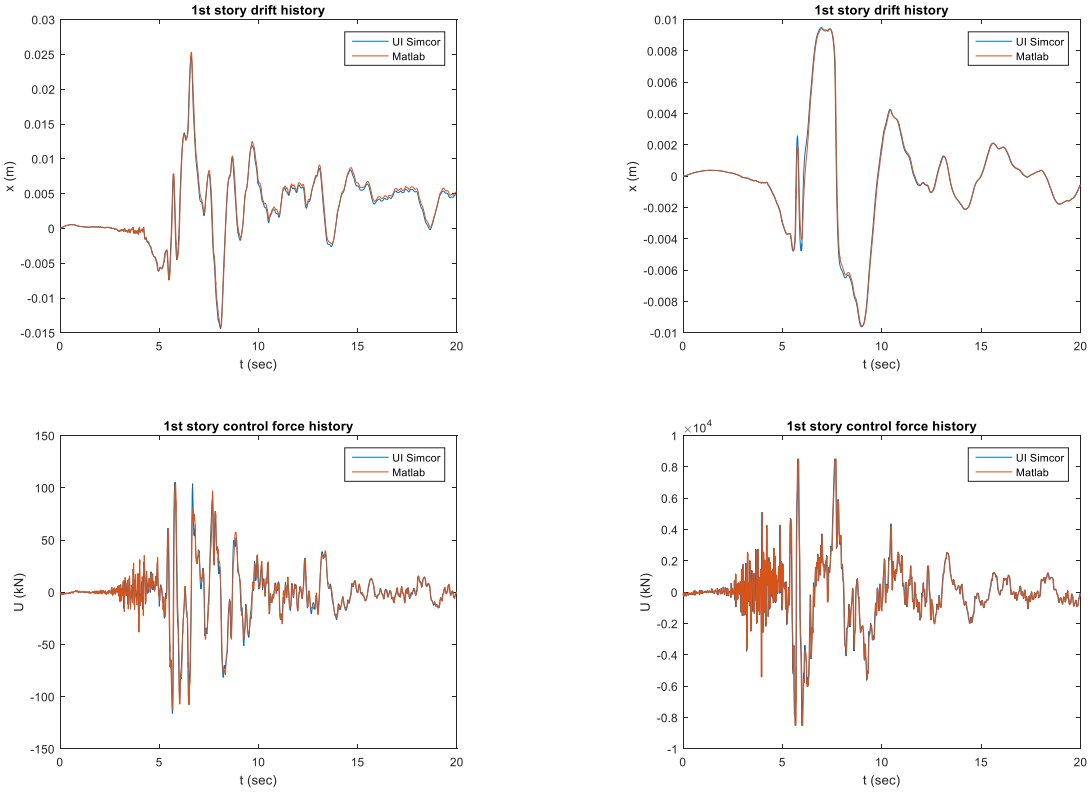

(a) Linear control method (b) SMC method

Figure 2.9. Comparison of actively controlled structural responses: MATLAB v.s. UI-SIMCOR

The effectiveness of the two control methods is examined by comparing the actively controlled structure with two additional cases: (1) the uncontrolled case where the structure is fully fixed at the base and (2) the passively controlled case with non-optimally designed nonlinear viscous dampers at each story. For each story, nonlinear viscous dampers are considered to have the total damping coefficient, $\mathbf{c}_d$, equals 20 MN $(s/m)^{0.5}$, and the velocity exponent, α, equals 0.5.

The peak responses at each story are listed in Table 2.3.

Table 2.3. Response comparisons of various design cases

	Drift (cm)				Total acceleration(m/s^2)			
Story (1)	Uncontrolled (2)	Passive (3)	LQR (4)	SMC (5)	Uncontrolled (6)	Passive (7)	LQR (8)	SMC (9)
1	4.77	2.33	2.53	0.94	6.39	2.88	3.56	3.83
2	3.66	2.11	2.03	0.95	4.88	2.55	3.63	3.93
3	3.17	2.08	1.86	1.24	4.56	2.73	3.87	3.10
4	2.08	1.87	1.77	0.95	4.79	3.01	4.11	3.25
5	2.41	1.68	1.70	0.90	5.64	3.35	4.36	3.27
6	4.14	1.46	1.65	0.83	7.35	3.74	3.97	3.25
7	3.46	1.11	1.51	0.69	5.91	4.11	3.84	3.25
8	1.80	0.55	1.08	0.42	8.02	4.29	4.80	3.25

By comparing columns (2) and (6) with other columns, it was found that passive viscous dampers and active control methods can substantially reduce both the story displacements and accelerations. This observation is reasonable since the structural damping of uncontrolled structure is ignored. By comparing columns (3) and (7) with columns (5) and (9), it indicates that the SMC method can find an optimal design with nearly 40% smaller story drifts and roughly the same accelerations compared with the passive control case. To get the same story drifts as the SMC case, more damping should be added in the passive control case. However, the provided passive force from the damper cannot be sufficiently adaptive, which results in much more significant

acceleration. This phenomenon verifies that SMC is a robust control method that can efficiently minimize deformation and acceleration at the same time. On the other hand, columns (4) and (8) indicate that LQR can simultaneously decrease story drift and acceleration compared with the uncontrolled case. Nevertheless, the LQR method has no benefits when compared with the passive control case. Namely, the same reduction effects can be achieved by randomly assign consistent damping at each floor rather than putting effort into using the LQR method. Therefore, LQR is not as effective as the SMC method when applying to control of the inelastic structure.

2.6 OPTIMAL PASSIVE CONTROL DESIGN

Although active structural control is achievable using active seismic protective devices, the solution to deliver large dynamic control forces is needed before the wide use of this technology in civil structures. Therefore, an equivalent passive control system that can provide the similar control effects as an active control system should be identified. To do so, multiple optimization procedures need to be developed to identify the passive parameters of seismic protective devices based on the actively controlled response obtained in the previous section. Additional gradient-based optimization procedures or model updating techniques can be easily implemented in the proposed hybrid simulation scheme in the UI-SIMCOR platform. The goal is to obtain the stiffness and/or damping coefficients of the protective devices added to the structure to provide the response reduction effect closest to that of the active control method. In this study, an optimal design of nonlinear viscous dampers of the previous eight-story inelastic structure is explained as an example.

2.6.1 Noniterative Optimization Procedure

According to Lavan et al. (2008), the active control effect obtained from the above structural control methods can be realized by weakening the structure and adding additional

damping. The locations and magnitudes of weakening and damping need to be calculated such that the passively controlled structure will have a similar response history to that of the actively controlled structure. Under this assumption, an error vector is formulated as the difference between the sum of control forces and restoring forces acting upon each DOF in the actively controlled structure to the sum of damping forces and restoring forces in the weakened and damped structure. Then, this error vector is minimized such that the total forces acting upon each DOF would be similar in the two cases, leading to similar response histories throughout the structure.

However, the linear damper is considered as supplemental energy dissipation devices in Lavan's paper (Lavan et al., 2008). To extend the optimization procedure to a system with nonlinear viscous dampers, modifications are made in the following steps. First, the error vector can be written as:

$$\mathbf{Err}\left(\mathbf{F}_w, \mathbf{F}_d, t\right) = \left\{-\mathbf{HU}\left(t\right) + \mathbf{T}_s\mathbf{F}_s\left[\mathbf{x}(t), \dot{\mathbf{x}}(t)\right]\right\} - \left\{\mathbf{T}_s\mathbf{F}_w\left[\mathbf{x}(t), \dot{\mathbf{x}}(t)\right] + \mathbf{F}_d\left[\dot{\mathbf{x}}(t)\right]\right\} \tag{2.41}$$

where $\mathbf{T}_s\mathbf{F}_s\left(t\right)$ and $\mathbf{HU}\left(t\right)$ are restoring forces and the active control forces acting on the DOFs in the actively controlled structure, respectively. $\mathbf{T}_s\mathbf{F}_w\left(t\right)$ and $\mathbf{F}_d\left(t\right)$ are restoring forces and nonlinear damping forces acting on the DOFs in the passively controlled structure, respectively. Consider that the weakening and softening of each element are proportional, i.e., the strength and stiffness of the element are reduced at the same ratio (Lavan et al., 2008), the restoring force provided by the weakened structure is:

$$\mathbf{F}_w\left[\mathbf{x}(t), \dot{\mathbf{x}}(t)\right] = \mathrm{diag}\left(\boldsymbol{\beta}\right)\mathbf{F}_s\left[\mathbf{x}(t), \dot{\mathbf{x}}(t)\right] \tag{2.42}$$

where $\boldsymbol{\beta}$ is a vector of coefficients for weakening and softening in the different structural elements. $\mathrm{diag}\left(\mathbf{v}\right)$ is an operator that generates a diagonal matrix with diagonal elements equals to elements of a given vector $\mathbf{v}$. Damping force of nonlinear viscous dampers distributed in the structure can

be written as:

$$\mathbf{F}_d\left[\dot{\mathbf{x}}(t)\right] = \mathbf{T}_d^T \operatorname{diag}\left(\mathbf{c}_d\right)\left\{\left|\mathbf{T}_d\dot{\mathbf{x}}(t)\right|^{\alpha_d} \cdot \operatorname{sign}\left[\mathbf{T}_d\dot{\mathbf{x}}(t)\right]\right\} \tag{2.43}$$

where $\mathbf{T}_d$ is the transform matrix whose element $T_{d,ij}$ is the contribution of velocity j to the damper i. $\mathbf{c}_d$ is a vector of coefficients whose element $c_{d,i}$ is the damping coefficient of *i*th damper added to structure. α_d is a constant that controls the force-displacement loop of the damper. Substituting Equation (2.42) and (2.43) into Equation (2.41), the error vector can be written as:

$$\begin{aligned}\mathbf{Err}\left(\mathbf{F}_w, \mathbf{F}_d, t\right) = &\left\{-\mathbf{HU}\left(t\right) + \mathbf{T}_s\mathbf{F}_s\left[\mathbf{x}(t), \dot{\mathbf{x}}(t)\right]\right\} \\ &-\left\{\mathbf{T}_s \operatorname{diag}\left(\boldsymbol{\beta}\right)\mathbf{F}_s\left[\mathbf{x}(t), \dot{\mathbf{x}}(t)\right] + \mathbf{T}_d^T \operatorname{diag}\left(\mathbf{c}_d\right)\left\{\left|\mathbf{T}_d\dot{\mathbf{x}}(t)\right|^{\alpha_d} \cdot \operatorname{sign}\left[\mathbf{T}_d\dot{\mathbf{x}}(t)\right]\right\}\right\}\end{aligned} \tag{2.44}$$

For any two vectors $\mathbf{v}$ and $\mathbf{u}$ of the same dimensions, $\operatorname{diag}\left(\mathbf{v}\right)\mathbf{u} = \operatorname{diag}\left(\mathbf{u}\right)\mathbf{v}$, therefore the error vector can be written as:

$$\begin{aligned}\mathbf{Err}\left(\boldsymbol{\beta}, \mathbf{c}_d, t\right) = &\left\{-\mathbf{HU}\left(t\right) + \mathbf{T}_s\mathbf{F}_s\left[\mathbf{x}(t), \dot{\mathbf{x}}(t)\right]\right\} \\ &-\left\{\mathbf{T}_s \operatorname{diag}\left(\mathbf{F}_s\left[\mathbf{x}(t), \dot{\mathbf{x}}(t)\right]\right)\boldsymbol{\beta} + \mathbf{T}_d^T \operatorname{diag}\left(\left|\mathbf{T}_d\dot{\mathbf{x}}(t)\right|^{\alpha_d} \cdot \operatorname{sign}\left[\mathbf{T}_d\dot{\mathbf{x}}(t)\right]\right)\mathbf{c}_d\right\}\end{aligned} \tag{2.45}$$

which can be written in a compact linear form as the following:

$$\mathbf{Err}\left(\mathbf{y}, t\right) = \mathbf{A}\left(t\right)\mathbf{y} - \mathbf{b}\left(t\right) \tag{2.46}$$

where $\mathbf{y}$ is vector of unknown variables, $\mathbf{A}\left(t\right)$ and $\mathbf{b}\left(t\right)$ are known matrix and vector varying with time defined as follows:

$$\begin{aligned}\mathbf{A}\left(t\right) &= -\left[\mathbf{T}_s \operatorname{diag}\left(\mathbf{F}_s\left[\mathbf{x}(t), \dot{\mathbf{x}}(t)\right]\right) \quad \mathbf{T}_d^T \operatorname{diag}\left(\left|\mathbf{T}_d\dot{\mathbf{x}}(t)\right|^{\alpha_d} \cdot \operatorname{sign}\left[\mathbf{T}_d\dot{\mathbf{x}}(t)\right]\right)\right] \\ \mathbf{b}\left(t\right) &= -\left\{-\mathbf{HU}\left(t\right) + \mathbf{T}_s\mathbf{F}_s\left[\mathbf{x}(t), \dot{\mathbf{x}}(t)\right]\right\} \\ \mathbf{y} &= \left[\boldsymbol{\beta} \quad \mathbf{c}_d\right]^{\mathrm{T}}\end{aligned} \tag{2.47}$$

Once the error vector has been established as a linear function of the design variables, an

optimization problem can be easily formulated by using many scalar functions of this error vector as a measure of the error between actively controlled system and passively controlled system. For example, in Lavan's paper (Lavan et al., 2008), a weighted least squares error could be formulated as:

$$err(\mathbf{y}) = \int \mathbf{Err}^{\mathrm{T}}(\mathbf{y},t)\mathbf{W}(t)\mathbf{Err}(\mathbf{y},t)\,\mathrm{d}t \tag{2.48}$$

where $\mathbf{W}(t)$ is a diagonal matrix of positive weights for different unknown variables at each time step. Taking into account that the unknown variable $\mathbf{y}$ is not a function of time since it's a set of constant design variables of structural properties and supplemental dampers, the optimization problem can be formulated by substituting Equation (2.46) into Equation (2.48) and minimizing the weighted least square:

$$\min err(\mathbf{y}) = \mathbf{y}^{\mathrm{T}}\mathbf{\Psi}\mathbf{y} - 2\mathbf{d}^{T}\mathbf{y} + \mathrm{const} \tag{2.49}$$

where $\mathbf{\Psi} = \int \mathbf{A}^{\mathrm{T}}(t)\mathbf{W}(t)\mathbf{A}(t)\,\mathrm{d}t$, $\mathbf{d} = \int \mathbf{A}^{\mathrm{T}}(t)\mathbf{W}(t)\mathbf{b}(t)\,\mathrm{d}t$. The weighted least square can be minimized by using gradient based optimization methodology, which could be easily adopted and solved with any available optimization program. In the proposed hybrid simulation scheme, a built-in optimization toolbox in the MATLAB library is used to minimize the scalar error, subject to constraints on the variables if desired. Finally, the optimal values of the vector $\mathbf{y}$ yields to the best values for the design parameters. In reality, the location of weakening and damping is also represented by the value of $\boldsymbol{\beta}$ and $\mathbf{c}_d$. If $\beta_i = 1$, it is expected that weakening is not required for element i; If $\beta_i = 0$, it means that element i needs to be removed; If $c_{d,i} = 0$, it indicates that additional damper is not required at that location.

2.6.2 Equivalent Average Optimization Procedure

Instead of solving one set of design variables $\mathbf{y}$ throughout the entire integration time, the maximum likelihood estimator of the previous linear model can be used to find different sets of optimal design parameters $\mathbf{y}(t)$ at each time step. For general linear model as shown in Equation (2.46), $\mathbf{y}(t)$ at each time step t can be calculated by using closed form solution of maximum likelihood estimator $\hat{\mathbf{y}}(t)$,

$$\hat{\mathbf{y}}(t) = \left(\mathbf{A}'(t)\mathbf{A}(t)\right)^{-1}\mathbf{A}'(t)\mathbf{b}(t) \tag{2.50}$$

An equivalent average design variable $\overline{\mathbf{y}}$ can be easily established as follows:

$$\overline{\mathbf{y}} = \frac{\int_{t_{start}}^{t_{end}} \hat{\mathbf{y}}(t)}{\Delta t} \tag{2.51}$$

where t_{start} and t_{end} are selected integral time period. To fit the peak value of structural response, the integral time period can be specified by designer to ensure that several peak structural response cycles appear in the integration.

2.6.3 Example of Optimization Procedure

To verify the effectiveness of implemented optimization procedures in identifying passively controlled design from actively controlled results, structural responses and control forces obtained from the eight-story structure used in Section 2.5.3 are adopted and analyzed here. For each story, nonlinear viscous dampers are considered to have the total damping coefficient, $\mathbf{c}_d$, ranges from 0 to 50 MN $(s/m)^{0.5}$, and the velocity exponent, α, equals 0.5. Both LQR and SMC models are evaluated to get the optimal value of $\mathbf{c}_d$.

(1) Noniterative optimization versus equivalent average optimization

To compare the accuracy and efficiency of optimization procedures, the peak inter-story drift ratio and peak floor acceleration of actively controlled structure, as well as responses of passively controlled structures identified from two optimization procedures, are plotted as shown in Figure 2.10. It shows that: (i) When comparing the "Sliding Mode Control" curve with the "Noniterative opt." curve, namely, when using noniterative optimization procedure, peak floor acceleration of passive control structure matches well with that of active control structure. In contrast, peak inter-story drift of passive control structure is overall 50% larger than that of active control structure; (ii) When comparing "Sliding Mode Control" with "Equivalent average opt.", namely, when using average optimization procedure and do the integration for whole time history, both inter-story drift and floor acceleration are way off from actively controlled responses.

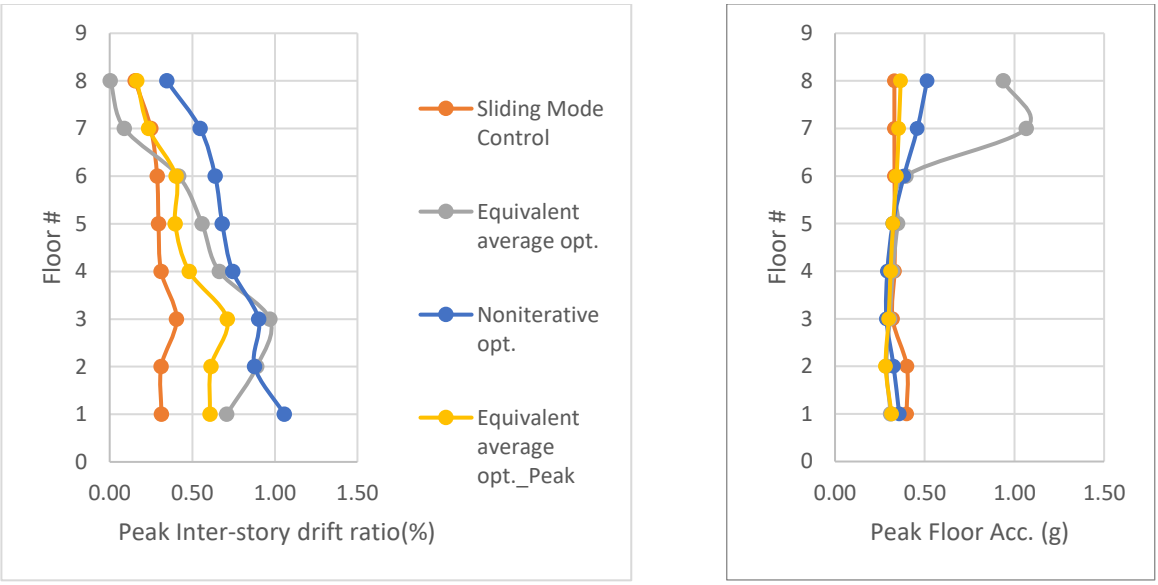

(a) Peak inter-story drift ratio (b) Peak floor acceleration

Figure 2.10. Comparison of actively controlled and passively controlled structural responses

However, by carefully selecting the integrating peak cycles of structural response (i.e., for "Equivalent average opt._Peak" curve), the fitting of both inter-story drift ratio and acceleration are improved and reaches a better fitting compared with the noniterative optimization procedure. These phenomena are reasonable because a weighted least squares error is minimized in obtaining

one set of design parameters using the noniterative optimization procedure. Nevertheless, accurate responses can only be approached when errors at each time step are minimized, which requires different sets of design parameters at each time step. Besides, the damping force provided by nonlinear viscous dampers has a solid physical relationship with structural responses and its modeling parameters, so it is hard to reproduce an arbitrary active control force with high accuracy. In sum, the passively controlled structure can produce similar structural responses to the actively controlled model, which means the proposed optimal design procedures are applicable.

(2) Linear control versus nonlinear control

By comparing the actively controlled responses (i.e., "Linear control" and "Sliding Mode Control" curve) and passively controlled structural responses (i.e., "Passive control from LC" and "Passive control from SMC" curve) of different control methods with the uncontrolled response, as shown in Figure 2.11, it can be concluded that: for both active and passive control cases, sliding mode control can get better optimal responses than linear control. Because LQR only produces control force that is generated by considering the linear part of restoring force of inelastic structural element, while SMC has a saturated controller which generated by the whole nonlinearity of the structure. Moreover, besides of weighting matrix, the SMC controller has additional parameters (α_i^* and $\bar{u}_{i\max}$) to make a trade-off between the control effort and the structural response, thus leads to a much more robust control system. In conclusion, the SMC method is more effective not only in actively controlling the structural response of the inelastic structure, but also in identifying passively controlled responses.

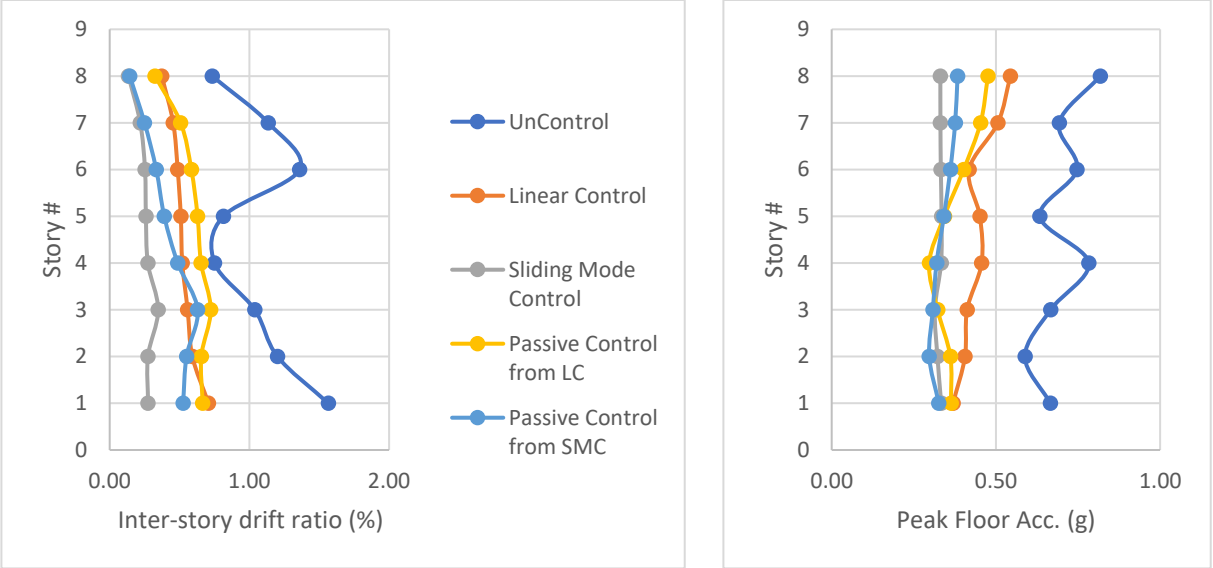

(a) Peak inter-story drift ratio (b) Peak floor acceleration

Figure 2.11. Comparison of LQR and SMC methods

(3) Proposed optimal design versus hybrid genetic method

In order to verify the efficiency of identified optimal design parameters in controlling the structural response, the optimal design parameters and controlled structural responses are compared with those of the hybrid genetic method presented in Xie et al. (2018), as shown in Table 2.4 and Figure 2.12. From Figure 2.12, it can be concluded that: (i) Passively controlled structural responses identified from LQR and SMC fits well with the optimal responses from the hybrid genetic method, which means the proposed active control methods and optimization procedure can provide effective optimal design parameters and accurate prediction of structural response; (ii) Peak inter-story drift ratio optimized from SMC method is smaller than that of LQR method and hybrid genetic method. Meanwhile, the passive model identified from the SMC method has smaller peak accelerations compared with the passive LQR model and hybrid genetic method. Therefore, the passive model identified from the SMC method is most effective when considering the simultaneous minimization of story drift and floor acceleration.

The identified optimal design parameters and dimensionless damping coefficients are

shown in Table 2.4. One can observe that: (i) the passive model identified from the SMC method and hybrid genetic method has a more considerable damping cost than the passive model identified from the LQR method. It is because the LQR method only controls the linear deformation of the inelastic structure, which leads to a smaller supplemental damping coefficient but larger structural responses. (ii) When comparing the passive model identified from SMC and hybrid genetic model, the dimensionless damping index and equivalent damping ratio are very close, but peak inter-story drifts and peak floor accelerations of the passive SMC model are smaller along with the story height. It means that the passive SMC model can provide an optimal design to achieve better optimized structural responses by using the same cost of additional damping.

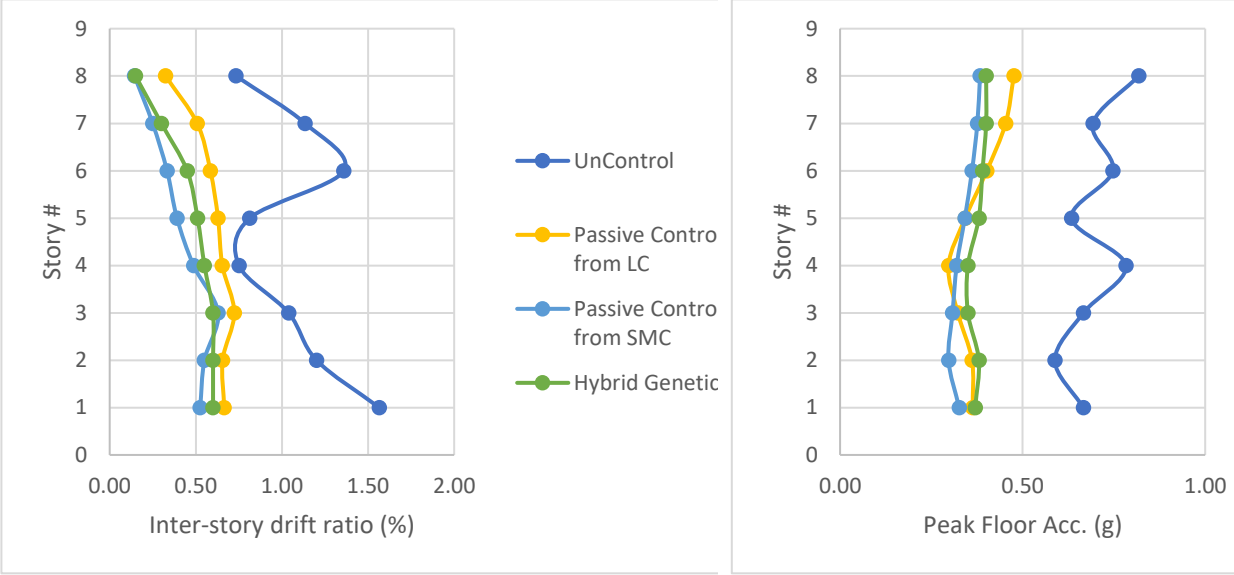

(a) Peak inter-story drift ratio (b) Peak floor acceleration

Figure 2.12. Comparison of different optimal design methods

Table 2.4. Optimal design damping coefficients identified from different methods

Optimization Method	**Optimal Design [MN(s/m)$^{0.5}$]**									
	1	**2**	**3**	**4**	**5**	**6**	**7**	**8**	$\Pi_{\xi,n}$*	ξ_d*
Passive Control LC	5.5	5.8	5.0	4.4	2.9	1.7	1.0	0.6	0.10	0.20
Passive Control SMC	13.3	9.6	5.1	8.5	9.9	8.9	7.7	5.4	0.24	0.56
Hybrid Genetic*	12.4	9.7	7.9	7.1	6.5	6.4	8.3	8.0	0.23	0.56

*Hybrid Genetic results are obtained from reference paper. (Xie et al., 2018)

(4) Sensitivity test of SMC method

To apply this implemented SMC method to other cases, it should be verified that the SMC method is not sensitive to structural properties. To doing so, 10% disturbance is applied to the initial stiffness and yield displacement of the first floor. It is shown in Figure 2.13 that the orange curve and yellow curve are lapped together. Namely, the actively controlled response for original structure and disturbed structure are almost the same, which means the SMC method is stable and can be used in other cases. Besides, it is observed that both peak inter-story drift ratio and peak floor acceleration of the SMC method can be 20% ~ 50% less than those of the hybrid genetic method. This will be a significant benefit if active control is achievable for a specific type of structure.

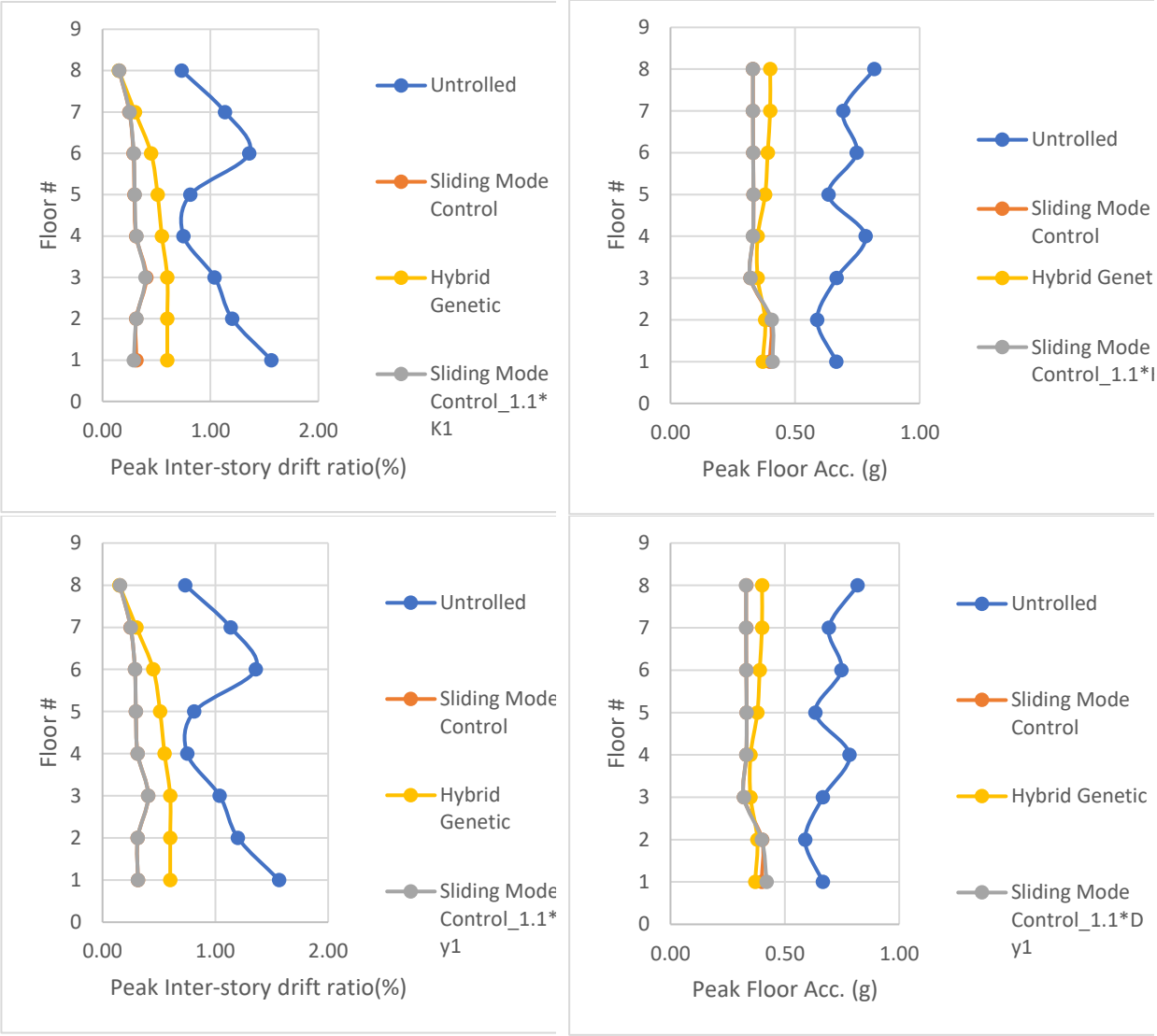

(a) Peak inter-story drift ratio (b) Peak floor acceleration

Figure 2.13. Original structure versus disturbed structure

2.7 CONCLUDING REMARKS

This chapter explores using of the proposed hybrid numerical simulation scheme to conduct structural control of nonlinear structures so as to derive the optimal passive stiffness and damping values to mimic the actively controlled devices. In order to achieve this objective, an existing hybrid simulation software (UI-SIMCOR) is adopted and modified to enable the integration algorithm to include nonlinear seismic protective devices such as nonlinear dampers,

base isolation devices and MR dampers. While the realistic behavior of nonlinear structures can be modeled separately in current finite element analysis software package (e.g. OpenSees, ABAQUS etc.), the nonlinear seismic protective devices can be modeled in MATLAB and pieced together through hybrid simulation to produce the most realistic overall structural responses. Using a numerical model of a real test structure equipped with various protection devices, the study demonstrated the accuracy and versatility of the hybrid numerical simulation scheme.

Furthermore, this leads to the easy application of different control algorithms, such as classical linear optimal control and nonlinear sliding mode control, under this framework. Subsequently, it yields the optimal selection of stiffness and damping values for control devices in design. The optimal design of an eight-story inelastic structure with nonlinear viscous damper is evaluated to validate the proposed structural control based optimal design procedure. The following conclusions can be drawn from this study:

1. The developed hybrid simulation framework can provide accurate assessment of seismic behavior of inelastic structure with energy dissipation devices.

2. The developed hybrid simulation framework possess convenience in integrating advanced structural model with different seismic protective devices, structural control methods and optimization procedures. It has ability to use inelastic structural models in conjunction with nonlinear structural control, thus overcomes the limits in the adoption of structural control.

3. The equivalent passive control structure obtained from optimization procedure can produce similar structural responses to the active control model, which means the proposed active control methods in conjunction with optimization procedure can provide effective optimal design parameters of protective devices. The equivalent passive control provides comparable response reduction effect compared with active control but has stability and less cost.

4. The eight-story inelastic structure study case demonstrates that SMC method has robust ability in controlling the structural response of inelastic structure. Moreover, the implemented SMC method is not sensitive to structural properties thus can be used in other cases.

In summary, this chapter offers effective means to analyze and optimize seismic protective devices for inelastic structures. The structural control and hybrid simulation methodology-based optimization procedure can be further extended to optimal design of protective devices for other advanced inelastic system. The obtained nonlinear structural response and optimal design parameters provide a valuable guidance to evaluate and design the seismic protective devices. The main contents in Chapter 2 are under preparation in a journal publication (Peng et al. 2021a).

3. OPTIMAL PASSIVE CONTROL OF THE BENCHMARK HIGHWAY BRIDGE BASED ON HYBRID SIMULATION

3.1 INTRODUCTION

In Chapter 2, this study provides a hybrid simulation scheme to enable the structural control for inelastic structures. This chapter further extends that scheme to implement structural control techniques to improve the seismic performance of highway bridges. A benchmark problem was defined for the 91/5 highway overcrossing, which is a two-span prestressed concrete box girder bridge with base isolators and fluid dampers installed at end abutments (Agrawal et al., 2009; Makris & Zhang, 2004; Zhang, 2002). In the past studies, considering that the structural control task cannot be directly conducted in finite element programs, the dynamics of the bridge in the benchmark problem were represented by a reduced-order model that was exclusively built in the program of MATLAB/Simulink. Therefore, the active control algorithms and bridge dynamics could be modeled in one platform so that the state space information of the bridge at each time step can be available for performing structural control. Various control strategies and devices have been implemented and compared under this benchmark framework (Nagarajaiah et al., 2009; Tan & Agrawal, 2009), where active and semi-active controls were discovered as promising strategies to protect highway bridges (Ali & Ramaswamy, 2009; Nagarajaiah et al., 2009).

However, the typical layout of highway bridges, namely two-to-four spans of girder deck supported by center bents and end abutments, in together with the commonly short span length renders that highway bridges are subjected to multiple soil-structure interaction (SSI) effects (Xie et al., 2017; Xie et al., 2018; Zhang & Makris, 2002b). On the other hand, inherent structural nonlinearity has to be considered because the use of protective devices cannot guarantee that the

structure's elastic limit is not exceeded (Makris & Zhang, 2004; Palermo et al., 2013). As a result, it remains questionable whether active control can still be effective if SSI effects and nonlinearities of protective devices and bridge columns are rationally incorporated. To this end, the MATLAB framework developed for the benchmark problem is somewhat deficient because a much-simplified bridge model was considered therein. The current study is motivated by the need to couple active control algorithms with the advanced finite element model (FEM) of highway bridges to investigate the control efficiency more thoroughly.

Hybrid simulation, originally developed as a tool to combine physical testing with numerical modeling, offers a feasible means to link control algorithms with realistic structural models (Kwon et al., 2005; Schellenberg & Mahin, 2006; Yang et al., 2017). Large coupled systems can be analyzed in parallel on different software platforms by maintaining the displacement compatibility and force equilibrium at the interface. In this chapter, the benchmark bridge control problem is readdressed using the hybrid simulation scheme proposed in Chapter 2. As an example depicted in Figure 3.1, the bridge structure and SSI effects are modeled using the finite element program of OpenSees (Mazzoni et al., 2006), while supplemental protective devices and control algorithms are implemented in MATLAB. The sub-models in OpenSees and MATLAB are coupled by sharing forces and displacements at common nodes through the hybrid simulation platform UI-SIMCOR (Kwon et al., 2008; Kwon et al., 2007). Modifications have been made in UI-SIMCOR to account for multi-support excitation, the SSI effects, and solving nonlinear system equations of motion. The proposed hybrid simulation methodology is verified against the complete finite element model of the as-built case of the benchmark bridge. This study concludes that both linear and nonlinear active controls can effectively improve the seismic performances of the benchmark bridge when the associated SSI effects and structural

nonlinearities are considered.

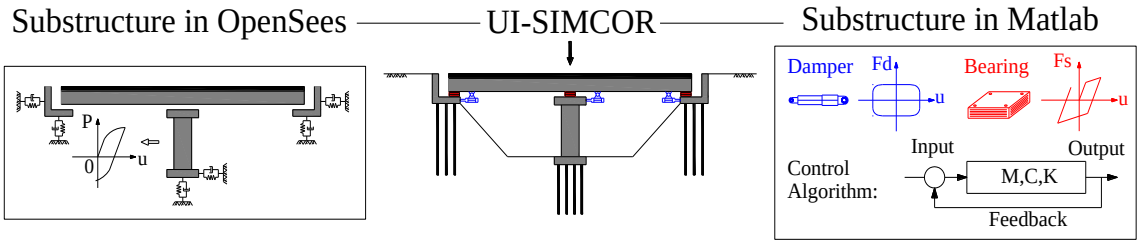

Figure 3.1. Hybrid simulation scheme for controlled highway bridges

Furthermore, an equivalent passive control system that can provide the similar control effects as the active control system is identified. To do so, an optimization procedure needs to be developed to determine the design parameters of passive protective devices based on actively controlled response. In this study, equivalent stiffness and damping coefficients of the protective devices added to the structure are derived based on the energy dissipating curve obtained in the active control process. An optimal design of the base isolator and linear viscous dampers of the benchmark bridge is derived and explained as an example.

3.2 HYBRID SIMULATION SCHEME AND VALIDATION FOR HIGHWAY BRIDGES

3.2.1 Multi-support Excitation Scheme

Previous studies have recognized that kinematic responses of approach embankments would notably amplify the free-field motions(Maroney et al., 1990; Zhang & Makris, 2002a). This embankment motion amplification effect leads to distinct input motions at end abutments and pier foundations, which will alter the bridge responses significantly (Rahmani et al., 2016; Xie et al., 2017; Xie et al., 2018; Zhang & Makris, 2002b). Therefore, multi-support excitation needs to be considered when solving the dynamic responses of the bridge. As shown in the Figure 3.2, for the

analysis of system under multi-support excitation, the displacement vector should be extended to include the degrees of freedom at the supports. Namely, $\mathbf{X}(t) = [\mathbf{X}_s(t) \quad \mathbf{X}_g(t)]^T$ is the total displacement vector, where $\mathbf{X}_s(t)$ includes the N DOFs of the superstructure, $\mathbf{X}_g(t)$ contains the N_b components of support displacement.

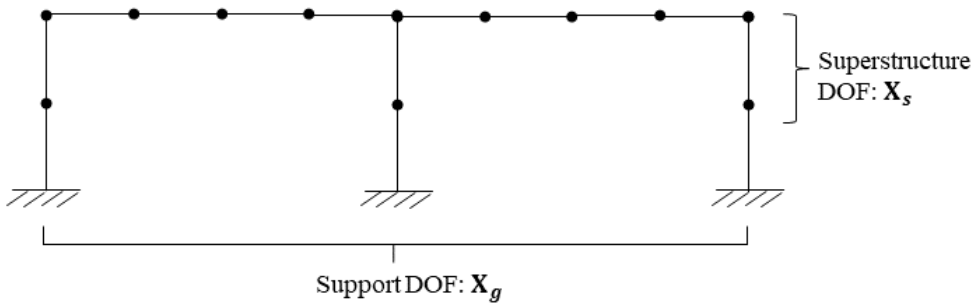

Figure 3.2. Definition of superstructure and support DOFs

Equation (3.1) provides the partitioned form of the equation of motion for all the DOFs:

$$\begin{bmatrix} \mathbf{M}_{ss} & \mathbf{M}_{sg} \\ \mathbf{M}_{gs} & \mathbf{M}_{gg} \end{bmatrix} \begin{Bmatrix} \ddot{\mathbf{X}}_s(t) \\ \ddot{\mathbf{X}}_g(t) \end{Bmatrix} + \begin{bmatrix} \mathbf{C}_{ss} & \mathbf{C}_{sg} \\ \mathbf{C}_{gs} & \mathbf{C}_{gg} \end{bmatrix} \begin{Bmatrix} \dot{\mathbf{X}}_s(t) \\ \dot{\mathbf{X}}_g(t) \end{Bmatrix} + \begin{bmatrix} \mathbf{K}_{ss} & \mathbf{K}_{sg} \\ \mathbf{K}_{gs} & \mathbf{K}_{gg} \end{bmatrix} \begin{Bmatrix} \mathbf{X}_s(t) \\ \mathbf{X}_g(t) \end{Bmatrix} = \begin{Bmatrix} \mathbf{0} \\ \mathbf{p}_g(t) \end{Bmatrix} \tag{3.1}$$

As given in Equation (3.1), $\mathbf{M}_{ss}$, $\mathbf{C}_{ss}$, and $\mathbf{K}_{ss}$ are the system matrices that consist of superstructure DOFs, and $\mathbf{M}_{gg}$, $\mathbf{C}_{gg}$, and $\mathbf{K}_{gg}$ are the system matrices composed by the support DOFs. The rest matrix parts (e.g., $\mathbf{M}_{sg}$, $\mathbf{K}_{sg}$, and $\mathbf{C}_{sg}$) are composed by the connecting elements. $\mathbf{p}_g(t)$ is the support force. The support DOFs are numbered with the highest values such that they are in the bottom rows of the system matrices. Hence, support DOFs and input vectors can be extracted and moved to the right-hand side of Equation (3.1), and combined as an external force vector. Namely, expanding the first block row of the Equation (3.1), one obtains:

$$\mathbf{M}_{ss}\ddot{\mathbf{X}}_s(t) + \mathbf{C}_{ss}\dot{\mathbf{X}}_s(t) + \mathbf{K}_{ss}\mathbf{X}_s(t) = -\mathbf{M}_{sg}\ddot{\mathbf{X}}_g(t) - \mathbf{C}_{sg}\dot{\mathbf{X}}_g(t) - \mathbf{K}_{sg}\mathbf{X}_g(t) \tag{3.2}$$

where $\ddot{\mathbf{X}}_s(t)$ and $\dot{\mathbf{X}}_s(t)$ are structural acceleration and velocity vectors, $\ddot{\mathbf{X}}_g(t)$ and $\dot{\mathbf{X}}_g(t)$ are

input acceleration and velocity vectors at support DOFs. Equation (3.2) turns out to be the modified system equation of motion that can incorporate different input values at each support DOF. As such, distinct motion inputs are considered.

Note that the superstructure responses $\mathbf{X}_s(t)$ here are absolute or total displacements. The benefit of solving responses in absolute coordinates is that it is straightforward when solving the new EOM, Equation (3.2), in the integrator in UI-SIMCOR. Namely, we only need to replace the original system matrices with condensed system matrices and generate new external force $-\mathbf{M}_{sg}\ddot{\mathbf{X}}_g(t)-\mathbf{C}_{sg}\dot{\mathbf{X}}_g(t)-\mathbf{K}_{sg}\mathbf{X}_g(t)$. However, it requires both ground displacement and velocity, which cannot be easily obtained from typical seismic instrumentations. Therefore, a relative EOM approximation might be used, as discussed in Li et al. (2012). In this study, the ground displacement and velocity are obtained using integration with baseline correction, so that we can directly solve EOM in absolute coordinate instead of using relative EOM approximation.

3.2.2 Modified Integration and Iteration Schemes

In this study, multi-support excitations are realized by reformatting the system matrices in UI-SIMCOR. First, the condensed system matrices $\mathbf{M}_{ss}$, $\mathbf{C}_{ss}$, and $\mathbf{K}_{ss}$ are used instead of the original system matrices returned from the OpenSees subprogram to account for multi-support excitation effects. To easily facilitate such operation, the support DOFs are numbered with the highest values in UI-SIMCOR such that they are located in the bottom rows of the system matrices. Besides, a new excitation force $-\mathbf{M}_{sg}\ddot{\mathbf{X}}_g(t)-\mathbf{C}_{sg}\dot{\mathbf{X}}_g(t)-\mathbf{K}_{sg}\mathbf{X}_g(t)$ should be used instead of the original external excitation force $-\mathbf{M}\ddot{\mathbf{X}}_g(t)$.

To account for the nonlinear forces of the bridge structure and controllers, the integration scheme in UI-SIMCOR needs to be modified to incorporate passive and active controllers for the

benchmark problem. The majority of the work has been done in Chapter 2 for active and passive control of inelastic structures with seismic protective devices. In this chapter, the α-OS integration scheme in UI-SIMCOR is combined with Broyden's method to converge the nonlinear force vectors (Broyden, 1965). Instead of completely composing the Jacobian matrix at each iteration step, Broyden's method computes the approximate inverse of the Jacobian matrix. As shown in Equation (3.3), the acceleration vector at the $(k+1)^{\text{th}}$ iteration step can be expressed as:

$$\mathbf{a}_{n+1}^{k+1} = \mathbf{a}_{n+1}^{k} - \left[\mathbf{B}_{n+1}^{k}\right]^{-1} \mathbf{F}(\mathbf{a}_{n+1}^{k}) \tag{3.3}$$

where $\mathbf{a}_{n+1}^{k}$ is the acceleration vector of the k^{th} iteration step; $\mathbf{F}(\mathbf{a}_{n+1}^{k})$ is the system force vector; and $\mathbf{B}_{n+1}^{k}$ is the approximate Jacobian matrix that has the general form as:

$$\mathbf{B}_{n+1}^{k}(\mathbf{a}_{n+1}^{k} - \mathbf{a}_{n+1}^{k-1}) = \mathbf{F}(\mathbf{a}_{n+1}^{k}) - \mathbf{F}(\mathbf{a}_{n+1}^{k-1}) \tag{3.4}$$

Note that multiple solutions of $\mathbf{B}_{n+1}^{k}$ exist by solving Equation (3.4), whereas an appropriate choice of $\mathbf{B}_{n+1}^{k}$ is a minor modification of $\mathbf{B}_{n+1}^{k-1}$ (Broyden, 1965):

$$\mathbf{B}_{n+1}^{k} = \frac{(\Delta\mathbf{F}_{n+1}^{k} - \mathbf{B}_{n+1}^{k-1}\mathbf{h}_{n+1}^{k})(\mathbf{h}_{n+1}^{k})^{T}}{(\mathbf{h}_{n+1}^{k})^{T}\mathbf{h}_{n+1}^{k}} + \mathbf{B}_{n+1}^{k-1} \tag{3.5}$$

where $\mathbf{h}_{n+1}^{k}$ and $\Delta\mathbf{F}_{n+1}^{k}$ are the incremental force vectors that can be calculated as $\mathbf{h}_{n+1}^{k} = \mathbf{a}_{n+1}^{k} - \mathbf{a}_{n+1}^{k-1}$ and $\Delta\mathbf{F}_{n+1}^{k} = \mathbf{F}(a_{n+1}^{k}) - \mathbf{F}(a_{n+1}^{k-1})$, respectively. With the initial guesses of $\mathbf{a}_{n+1}^{1}$, $\mathbf{a}_{n+1}^{2}$, and $\mathbf{B}_{n+1}^{1}$, the approximate Jacobian matrix can be determined at each iteration step, from which converged $\mathbf{a}_{n+1}$ can be obtained by using Equation (3.3). Then the nonlinear system equation of motion in the general framework as shown in Chapter 2 can be solved. Especially, the use of Broyden's method avoids a dramatic change in the system Jacobian matrix, which solves the convergence issue.

3.2.3 Numerical Validation of the Hybrid Simulation Scheme

The as-built case of the benchmark bridge (i.e., the 91/5 Overcrossing) is utilized to verify the proposed hybrid simulation scheme. As shown in Figure 3.3(a), 91/5 Overcrossing is a continuous two-span prestressed concrete box-girder bridge supported by an outrigger beam at mid-span. The bridge is installed with four elastomeric bearings and fluid dampers at each end abutment (Makris & Zhang, 2004). As the reference for validation, the complete FEM of the bridge (Figure 3.3(b)) is built in OpenSees, where modeling considerations of each component are based on the study of Zhang et al. (Zhang et al., 2004). Note, the modeling scheme considered for the complete FEM has been well-documented and discussed in previous studies (Xie & Zhang, 2017, 2018; Zhang & Makris, 2002a, 2002b; Zhang et al., 2004). Especially, the modeling considerations of SSI effects and structural nonlinearity have been validated by comparing the numerical responses against the recorded counterparts of two instrumented bridges in California (Zhang & Makris, 2002b). SSI effects are captured through macro dashpots and springs attached at foundation nodes to quantify soil damping and stiffness, respectively. Using a shear-wedge model, the dynamic stiffness of the approach embankment is estimated through an iteration process that calculates the appropriate level of dynamic shear strains under earthquakes (Zhang & Makris, 2002a). The dynamic stiffnesses of a pile group are computed by superposing the dynamic stiffnesses of single piles, initially developed for static loads by Poulos (1968) and later justified for dynamic loads by Kaynia and Kausel (1980) and Roesset (1984). The low-frequency values of the dynamic stiffnesses for both approach embankments and pile groups are used to develop the frequency-independent macro dashpots and springs (Zhang et al., 2004). Further, the shear-wedge model yields estimates for the motion amplification functions of typical embankments, which are subsequently used to obtain the amplified motion inputs at end abutments (Zhang & Makris,

2002a).

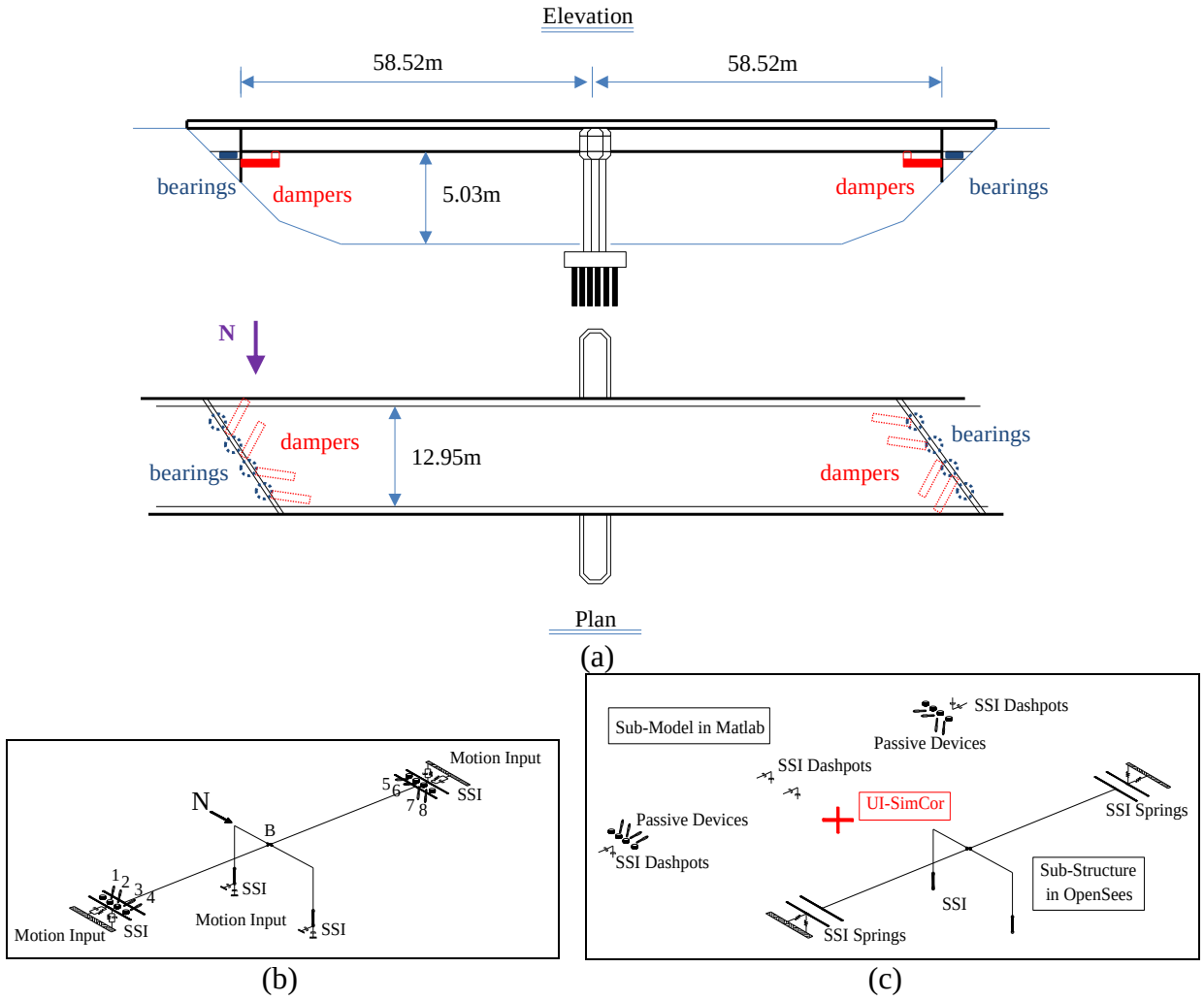

Figure 3.3. Numerical validation scheme of the benchmark highway bridge: (a) benchmark highway bridge of 91/5 Overcrossing; (b) complete OpenSees model; and (c) hybrid UI-SIMCOR model

Modeling parameters of isolation bearings and fluid dampers are selected based on the material properties, device sizes, and test results of the devices that have been designed and installed on the 91/5 highway overcrossing (Zhang et al., 2004). Isolation bearings are considered as a perfectly plastic material with an elastic stiffness of 5 MN/s and the yielding displacement of 0.06 m. The nonlinear fluid dampers installed at bridge ends are modeled through a nonlinear

dashpot (as given in Equation 2.20) with the damping coefficient C_α = 1.09 MN(s/m)$^{0.35}$ and the fractional exponent α_d = 0.35. Nonlinear beam-column elements are used to model bridge columns, whose moment-curvature relationship regresses as a bilinear curve. The bridge deck is simulated by the elastic beam elements, whereas transverse rigid components are modeled to preserve the skew geometry and connect the deck with columns and end abutments. Based upon the complete FEM, the UI-SIMCOR model (Figure 3.3(c)) is modified by decoupling the as-built bridge into two substructures. Namely, the OpenSees substructure consists of the bridge structure and the SSI springs, and the MATLAB substructure consists of isolation bearings, fluid dampers, and SSI dashpots.

Seismic responses of the benchmark bridge are simulated when subject to the Newhall motion record under the 1994 Northridge earthquake. Figure 3.4 presents the acceleration time history of the Newhall record at free field and the amplified motion at end abutments. For validation purposes, responses of four critical components are examined, such as bridge deck, bridge columns, isolation bearings, and fluid dampers. Figures 3.5(a) compares the deck total acceleration responses at the bridge center (i.e., node B shown in Figure 3.3(b)), whereas Figure 3.5(b) presents the drift responses of the southern column. As shown in both figures, not only the peak values but also the time histories of the bridge deck and columns are well captured by using the hybrid simulation scheme. In addition, Figures 3.5(c) and 3.5(d) compare the force-displacement curves of one sample bearing and two sample dampers, respectively (bearings and dampers are numbered in Figure 3.3(b)). As can be seen, minor discrepancies exist in the force-displacement loops, resulting from that: (1) different nonlinear solvers have been used in the complete FEM and the hybrid model; and (2) the initial stiffness matrix is used to obtain the nonlinear restoring force in the hybrid model. However, the overall trends and peak values

calculated from the hybrid model are generally consistent with those from the complete model. Figure 3.5 confirms that the hybrid simulation method effectively predicts the benchmark bridge's seismic responses.

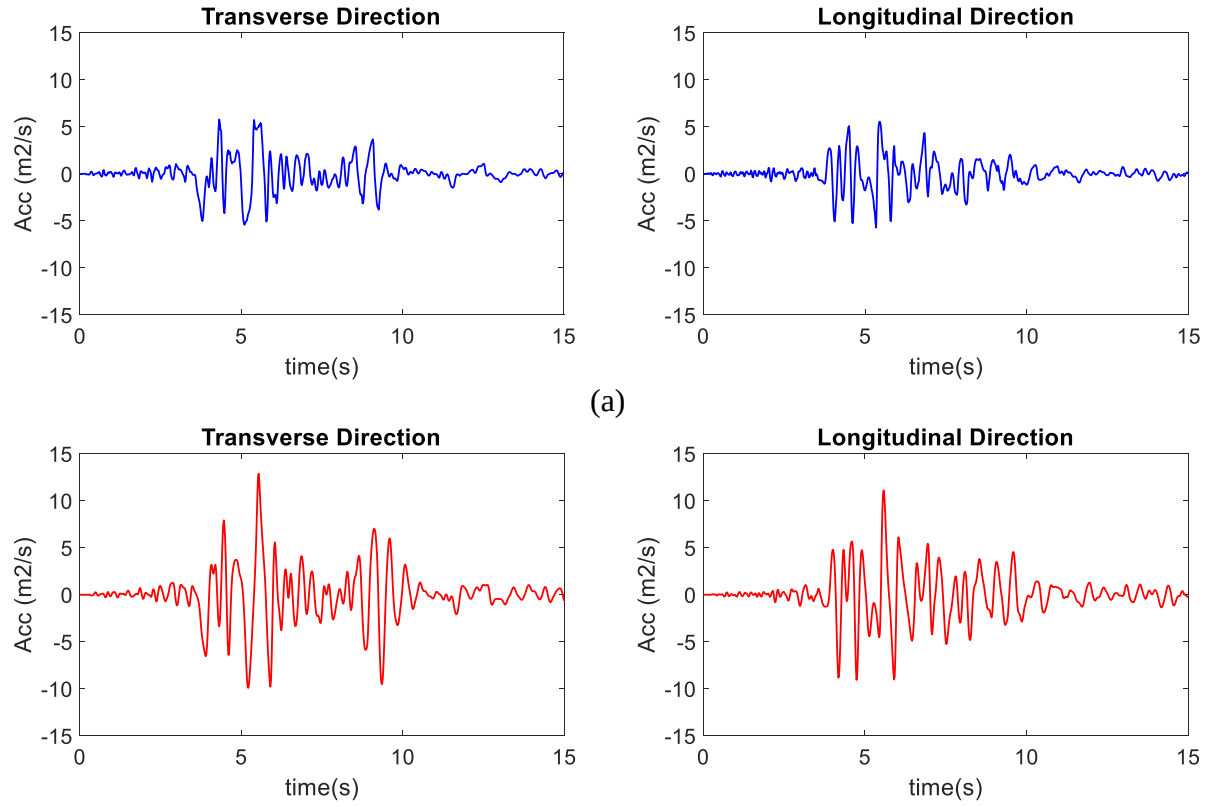

Figure 3.4. Acceleration time histories of the Newhall record at (a) free field and (b) end abutments

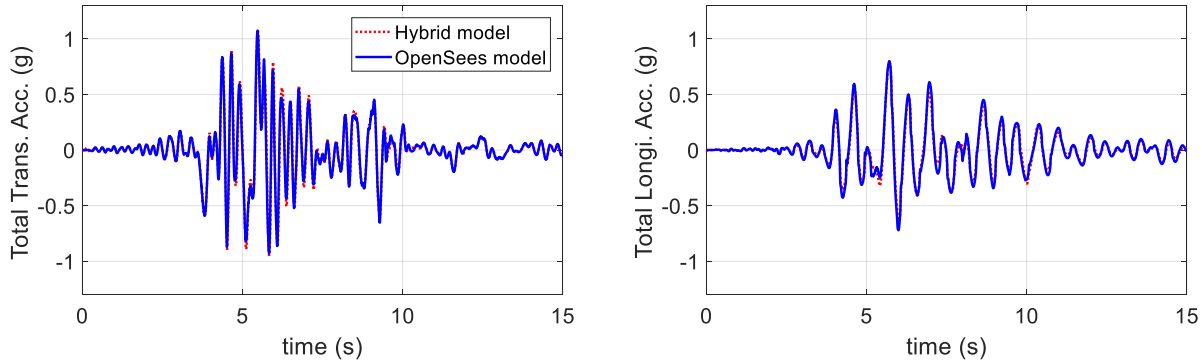

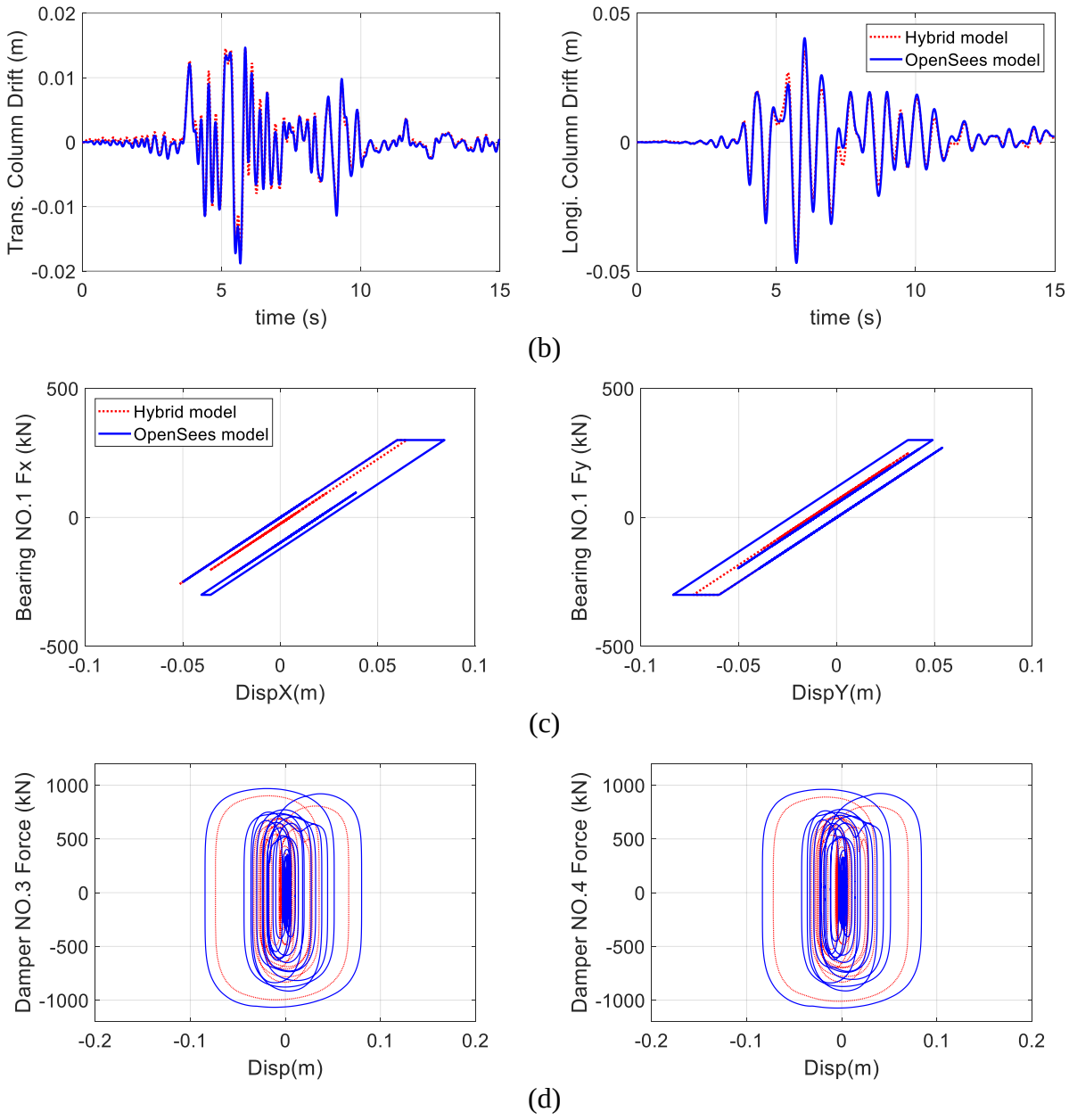

Figure 3.5. Response comparisons of the hybrid model and the complete OpenSees model: (a) total acceleration comparisons at bridge center; (b) column drift comparisons of the southern column; (c) force-displacement relationship comparisons of bearing No.1; and (d) force-displacement relationship comparisons of dampers No.3 and No.4

3.3 ACTIVE CONTROL OF BRIDGE MODEL IN HYBRID SIMULATION SCHEME

3.3.1 Controller Design

The second phase of the benchmark problem is considered hereafter as the testbed for active and optimal passive control designs (Nagarajaiah et al., 2009). To this end, two additional bearings are installed at the top of the columns to fully isolate the bridge. As shown in Figure 3.6, the active design of the benchmark highway bridge consists of ten base isolators and twenty orthogonal actuators, all of which are installed at the marked locations.

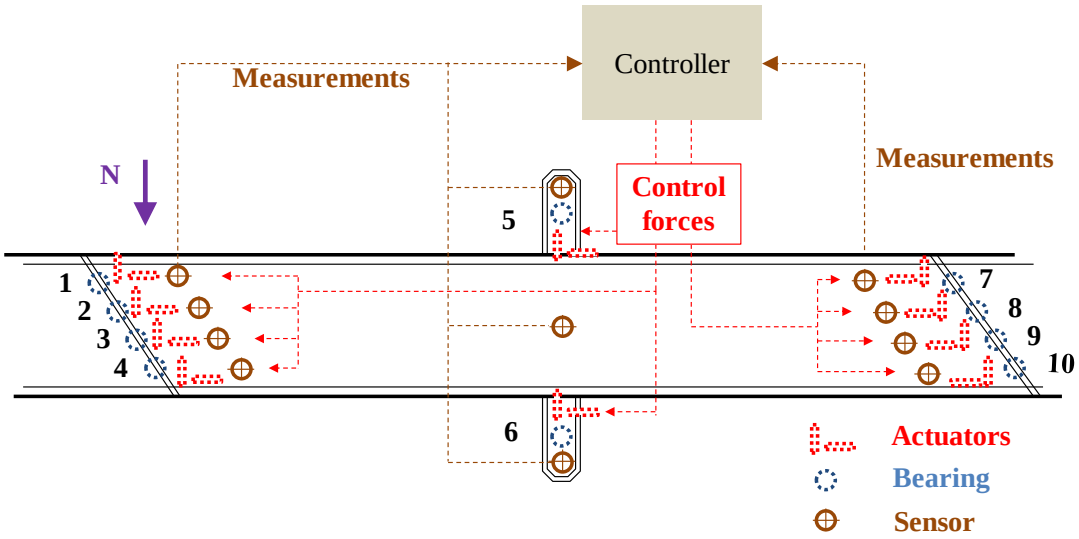

Figure 3.6. Active control system of the benchmark highway bridge

As introduced in Chapter 2, LQR and SMC control methods are applied to observe the effectiveness of active control in the bridge model. Since there are numerous nodes and DOFs in the bridge model, it is impossible to control the responses of all DOFs. Instead, a control target vector **y**(t), also known as the measurement output vector, can be formed as:

$$\mathbf{y}(t) = \mathbf{C}_m \mathbf{z}(t) + \mathbf{D}\mathbf{U}(t) + \mathbf{H}\mathbf{F}_e(t) \tag{3.6}$$

where $\mathbf{z}(t)$ is the structural responses vector in state space; $\mathbf{U}(t)$ is the active control force; $\mathbf{F}_e(t)$ is the external force; $\mathbf{C}_m$, $\mathbf{D}$ and $\mathbf{H}$ are coefficient matrices that can be determined on the basis of

the components in **y**(t). The measurement vector **y**(t) of the LQR method should be designed to capture the overall seismic performance of the benchmark bridge. In this study, the vector **y**(t) measures the peak acceleration demand of the deck at the bridge center and peak bearing deformations, as shown in Equation (3.7).

$$\mathbf{y(t)}=\begin{bmatrix}\text{Acceleration demand of the deck at bridge center}\\ \text{Peak deformations of all the bearings}\end{bmatrix} \tag{3.7}$$

The peak acceleration demand of the deck at the bridge center is positively correlated to the base shears and drift demands of columns, while the peak bearing deformations controls the damage of isolation bearings. It is worth mentioning that bearing deformation and deck acceleration in general conflict with each other. To wit, a stronger (i.e., more rigid) connection between the deck and the column would decrease the bearing deformation but increase the deck acceleration, and vice versa. As such, the proposed measurement vector **y**(t) captures the correlations between critical bridge components. It also reflects the overall seismic performance of the benchmark bridge. As shown in Figure 3.6, twenty string potentiometers are used to measure the bearing displacements at each marked location in both transverse and longitudinal directions, whereas two accelerometers are used at the middle center of the bridge deck to measure the longitudinal and transverse accelerations at this location.

Correspondingly, the quadratic performance index *J* of the LQR method can be formed as:

$$J=\int_0^{t_f}[\mathbf{y}(t)^T\mathbf{Q}\mathbf{y}(t)+\mathbf{U}(t)^T\mathbf{R}\mathbf{U}(t)]dt \tag{3.8}$$

where **Q** and **R** are weighting matrices that can be determined based on the relative importance of the state variables and control forces. The weighting matrices are chosen as:

$$\mathbf{Q}=\begin{bmatrix}\mathbf{q_a I} & \mathbf{0}\\ \mathbf{0} & \mathbf{q_d I}\end{bmatrix};\ \mathbf{R}=\mathbf{I}_{nd\times nd} \tag{3.9}$$

where $\mathbf{q_a} = 10^3$ weights the total acceleration at bridge center and $\mathbf{q_d} = 10^6$ weights the bearing deformations, **R** is chosen to be the $nd \times nd$ identical matrix, where *nd* is the number of control devices. These two weighting matrices are determined through a trial-and-error process to ensure that (1) no unstable bridge response has occurred and (2) the active control force at each location stays within the range of 0-2500 kN.

Similarly, a trial and error process is conducted to determine the SMC sliding surface, where the associated weighting matrix contains (1) 750 to weight the transverse displacements of bearing No.5 and No.6, (2) 1×10^7 to weight the transverse displacements of all other bearings, (3) 1×10^8 to weight the longitudinal displacements of all the bearings, (4) 100 to weight the transverse displacement of the deck at bridge center, (5) 1×10^4 for the longitudinal displacements of the deck at multiple locations, (6) 100 to weight the longitudinal velocities of the deck at multiple locations, and (7) 1 for all other parameters. A sliding margin of δ_i = 100 kN·kg·m/s with i = 1-20 is considered in this study. The coefficient α^* is chosen appropriately such that the maximum control force is around 2500 kN at each location.

3.3.2 Active Control Results

The effectiveness of the two active control designs is examined by comparing the actively controlled bridge with two additional cases: (1) the uncontrolled case where the bridge is fully isolated by ten isolation bearings, and (2) the initial passive design case with each numbered location in Figure 3.6 equipped with isolation bearings and two orthogonal fluid dampers. Existing protective devices (i.e., bearings with the elastic stiffness of 5 MN/m and the yielding displacement of 0.06 m, dampers with C_α = 1.09 MN(s/m)$^{0.35}$ and α_d = 0.35) are considered for the uncontrolled and initial passive design cases. Table 3.1 lists the response comparisons of various control cases when subject to the aforementioned Newhall motion record. Because isolation bearings at the same

locations (i.e., west ends, east ends, and pier tops) yield similar responses, the mean displacement values at each location are listed in the table. By comparing column (5) in the table with other columns, it can be found that passive viscous dampers are able to substantially reduce the bearing displacement. However, the provided passive forces from the dampers are not sufficiently adaptive, which in turn generates much larger deck accelerations. This phenomenon verifies that bearing deformation and deck acceleration are two conflicting demand parameters, and a robust control shall efficiently minimize these two parameters at the same time. On the other hand, columns (7) and (8) in Table 3.1 indicate that both LQR and SMC can simultaneously decrease bearing displacements and deck accelerations compared with the uncontrolled case. Although active controls deliver less reductions of bearing displacements than the initial passive design case, significant decreases in deck accelerations can be achieved. As such, the active controls are more rational in a way that both columns and bearings will have smaller and more balanced responses. Conversely, the initial passive design case is somewhat inappropriate by viewing that bridge deck (or equivalently, bridge columns) will dominant the seismic response of the bridge.

Figure 3.7 compares the acceleration time histories at the deck center between the initial passive design, the LQR design, and the SMC design. As is depicted, the main acceleration pulses experienced in the initial passive control are significantly diminished when active controls are used. Force displacement curves of the base isolators are also compared in Figure 3.8 between the uncontrolled case and two active control designs. For brevity, one bearing at each location is compared (i.e., bearing No.1 at the west end, bearing No.5 at pier tops, and bearing No.9 at the east end). Evidently, bearing deformations in the transverse direction are decreased through the implementation of active controls.

Table 3.1. Response comparisons of various design cases under the Newhall record

Direction	Demand	Location	Uncontrolled	Initial Passive	Optimal Passive	LQR	SMC
(1)	(2)	(3)	(4)	(5)	(6)	(7)	(8)
Transverse	Δu^*(m)	West end	0.47	0.12	0.51	0.36	0.21
		Pier top	0.47	0.11	0.50	0.33	0.21
		East end	0.49	0.20	0.49	0.35	0.24
	a_m^* (m^2/s)	Deck center	4.17	7.25	1.19	1.61	3.35
	Performance Index *J**		**1.00**	**1.03**	**0.67**	**0.56**	**0.63**
Longitudinal	Δu^* (m)	West end	0.21	0.12	0.16	0.18	0.17
		Pier top	0.20	0.13	0.14	0.17	0.16
		East end	0.20	0.09	0.14	0.16	0.14
	a_m^*(m^2/s)	Deck center	1.15	4.46	0.81	0.85	0.99
	Performance Index *J**		**1.00**	**2.22**	**0.72**	**0.79**	**0.81**

*Δu is the peak bearing displacement, and a_m is the peak deck total acceleration at bridge center.

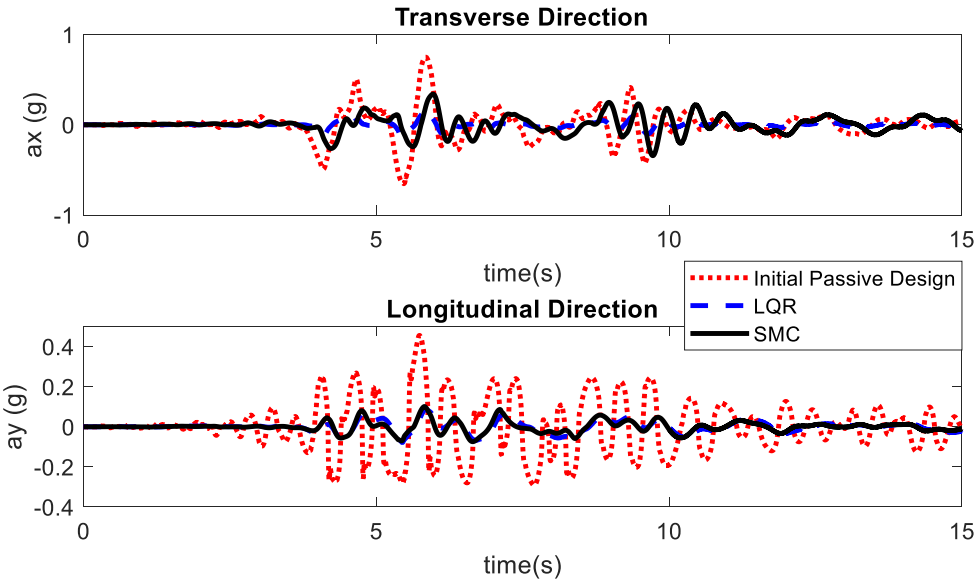

Figure 3.7. Response histories of deck total accelerations at bridge center with different control schemes

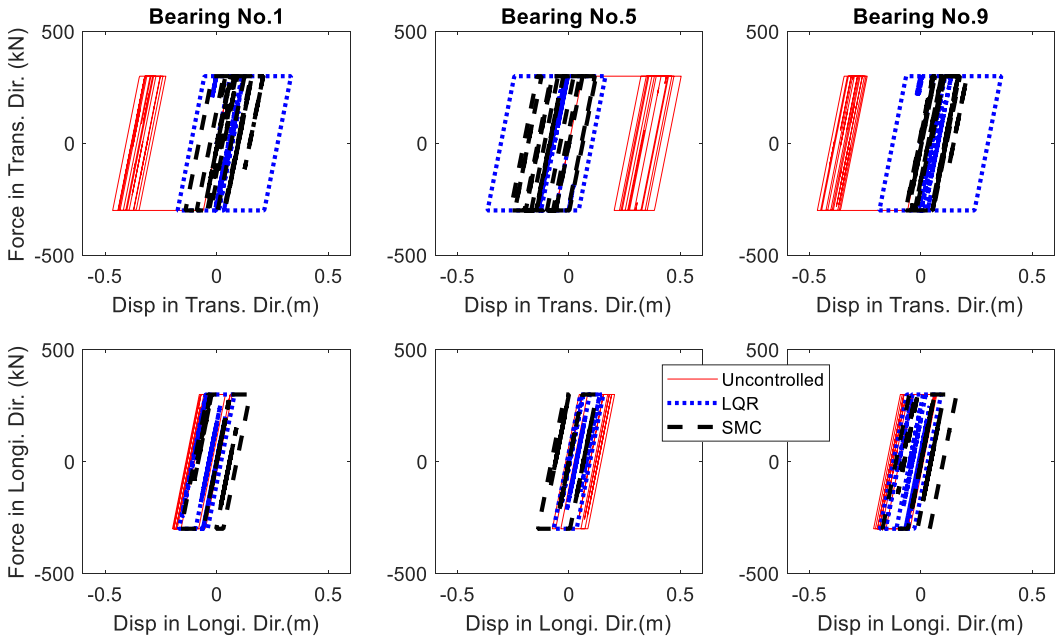

Figure 3.8. Base isolator force displacement loops with different control schemes

3.4 OPTIMAL PASSIVE CONTROL DESIGN

3.4.1 Optimal Passive Control Design and Results

After verifying the effectiveness of active control design and obtaining actively controlled responses, we can find the optimal passive design to mimic the behavior exhibited by active control roughly. The optimal passive design of the benchmark highway bridge consists of ten base isolators and twenty orthogonal fluid linear dampers, all of which are installed at the same marked locations, as shown in Figure 3.6. The key is how to design the optimized stiffness of bearings and damping coefficients of additional dampers to achieve optimal performance, which depends on the characteristics of structures and ground motions.

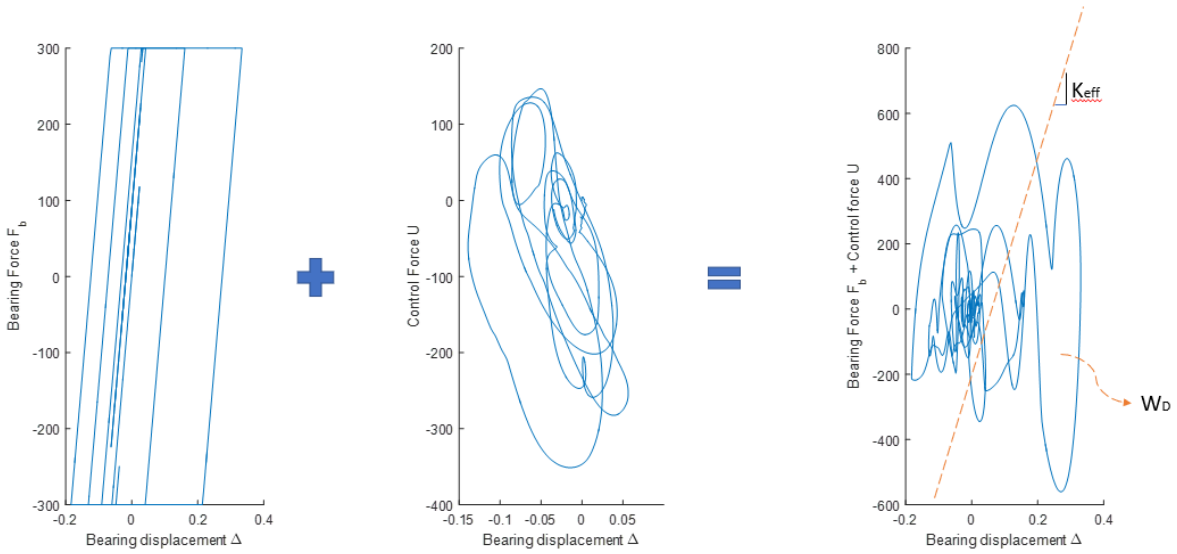

Figure 3.9. Method of the optimal passive control design

As shown in Figure 3.9, an optimal design of effective stiffness of isolator and additional damping at each controlling location can be identified based on active control force and bearing's response at that location. After conducting an active control analysis, the force and displacement of each bearing, as well as active control forces can be recorded. Then, based on the energy dissipating curve, which is bearing's displacement versus total resisting force generated from bearing and active control, an equivalent effective stiffness k_{eff} and additional damping $C(\Omega)$ can be derived using Equations (3.10) and (3.11):

$$k_{eff} = \frac{F^+ - F^-}{\Delta^+ - \Delta^-} = \frac{|F^+| + |F^-|}{|\Delta^+| + |\Delta^-|} \tag{3.10}$$

$$C(\Omega) = \frac{4W_D}{\pi\Omega\left(|\Delta^+| + |\Delta^-|\right)^2} \tag{3.11}$$

where F is total bearing force plus total active control force at each controlled location. Δ is the relative displacement of the top and bottom of isolation. At abutment, relative displacements at each bearing location might not be the same if there is out-of-plane rotation, so average

displacement is used for $\Delta.\Omega$ is the dominant frequency of ground motions identified after transforming ground motion records from the time domain to frequency domain. To this end, an optimal passive control design is achieved by providing the optimized stiffness k_{eff} of bearings and damping coefficient $C(\Omega)$ of additional linear viscous dampers.

The aforementioned active control responses are used to identify optimal passive control design, as shown in Table 3.2. Due to the different control effects of two active control methods, two different optimal designs are obtained accordingly. When focusing on controlling results in the transverse direction in Table 3.1, it is observed that SMC controls bearing displacement better than acceleration, namely, 50% reduction of bearing displacement and only 20% reduction of total acceleration of deck center. Therefore, the optimal passive design identified from SMC has linear dampers with relatively larger damping coefficients work along with strengthened bearings at pier tops and softened bearings at abutments, as shown in Table 3.2. In contrast, LQRY control can yield much less acceleration but provide less benefit in controlling bearing displacement, namely, almost 60% reduction of total acceleration and only 30% reduction of bearing displacement. Thus, the optimal passive design identified from LQRY has linear dampers with relatively small damping coefficients work along with softened isolation bearings. By comparing column (6) and column (7) in Table 3.1, it can be found that the equivalent passive design identified from LQRY can provide a good approximation of the behavior exhibited by active control. The bearing deformation in the transverse direction and deck acceleration in both directions are well approximated, while the bearing deformations in the transverse direction are less accurate.

It should be noted that the controlling effect of deformation and acceleration can be tuned by changing active controller design in section 3.3.1 to get new active control behavior then find the equivalent passive design accordingly. For better quantifying the conflicting responses of

critical components, a performance index that combines bearing deformations and deck acceleration is proposed in this study as:

$$J^* = \frac{1}{2N}\sum_{i=1}^{N}\frac{|\Delta u_i|}{\Delta u_0} + \frac{|a_m|}{2a_0} \tag{3.12}$$

where N is the total number of the bearings, which is ten in this study, $|a_m|$ is the deck total acceleration demand at bridge center, $|\Delta u_i|$ is the bearing displacement demand at location i in Figure 3.6, and Δu_0 and a_0 are the mean value of bearing demands and acceleration demand at deck center for the uncontrolled case, respectively. Note that the proposed performance index equals unity for the uncontrolled case, which serves as a reference value to compare the effectiveness of different control schemes. The choices of performance index can be modified based on the needs. Besides, we can go one step further, which is to relate the response quantities to repair cost of bridge. Then a probabilistic repair cost ratio developed in an earlier study (Xie & Zhang, 2018) can be utilized to provide more direct indication about the performance.

As is calculated in Table 3.1, the initial passive design amplifies the performance index by inappropriately changing the two demand parameters. Taking the bridge's longitudinal responses as an example, the initial passive control reduces the bearing displacement from an already tiny number at the cost of increasing the deck acceleration from 1.15 m/s^2 to 4.46 m/s^2, which in turn is reflected by a 122% increase of the final performance index. In contrast, the LQR successfully reduces the performance index by 44% and 21% in the transverse and longitudinal directions, respectively. Likewise, 33% and 28% reductions can be expected using optimal passive control in transverse and longitudinal directions, respectively. Similarly, SMC successfully reduces the performance index by 37% and 19% in the transverse and longitudinal directions, respectively.

Table 3.2. Response comparisons of active control and optimal passive control designs

	Optimal passive design from LQRY		Optimal passive design from SMC	
	C [kN(s/m)]	K_{eff} [kN /m]	C [kN(s/m)]	K_{eff} [kN /m]
South Pier (transverse)	250	3569	820	11760
South Pier (longitudinal)	212	3107	544	9934
North Pier (transverse)	251	3561	861	12401
North Pier (longitudinal)	250	4113	515	9807
Est end (transverse)	76	956	176	3038
Est end(longitudinal)	155	2490	172	3337
West end(transverse)	49	582	216	3614
West end(longitudinal)	119	2112	147	2990

3.4.2 Influence of Different Isolation Systems

The effectiveness of active control and optimal passive control is further investigated when various bridge systems are considered. The dynamic characteristic of the fully isolated benchmark bridge is highly contingent on the isolation designs. To this end, three additional bearing designs are considered to vary the bridge's natural periods. Isolation bearings are assumed to possess a perfectly plastic behavior with a yielding displacement of 0.06 m. Three elastic stiffness values of 2500 kN/m, 10000 kN/m, and 15000 kN/m are assigned to each of the additional three bridge cases. Note that the change of elastic stiffness also changes the yielding strength of the bearing, which will alter the dynamic characteristic of each bridge (Xie & Zhang, 2017). For brevity, location variance is not considered here, namely, bearings at different locations are assumed to have identical parameters.

Figure 3.10 compares the performance indices of different bridge systems under the

Newhall record during the 1994 Northridge earthquake. The initial passive control uses the viscous dampers with the same design parameters as the benchmark model. The optimal passive control uses the optimized design parameters of bearings and dampers identified from LQR and SMC. As is depicted, both LQR and SMC can substantially decrease the performance index no matter which isolation design is considered. Specifically, the LQR design yields an average performance reduction of 38% in the transverse direction and 18% in the longitudinal direction. Likewise, the SMC design can decrease the performance objective by 26% and 16% in the transverse and longitudinal directions, respectively. Conversely, the initial passive control using the existing design of viscous dampers amplifies the performance index for most cases. For the case with a strong base isolation effect (e.g., when the bearing elastic stiffness is 2500 kN/m), initial passive control will sharply increase the already very small deck acceleration, resulting in a much higher performance index, i.e., an 84% increase in the transverse direction and 265% increase in the longitudinal direction. However, the amplified performance due to initial passive control can be well controlled after conducting the proposed optimal passive control design to identify their optimal design parameters. Similar to active control, the optimal passive control is able to substantially decrease the performance index in both directions except isolation design with Ks=1500kN/m.

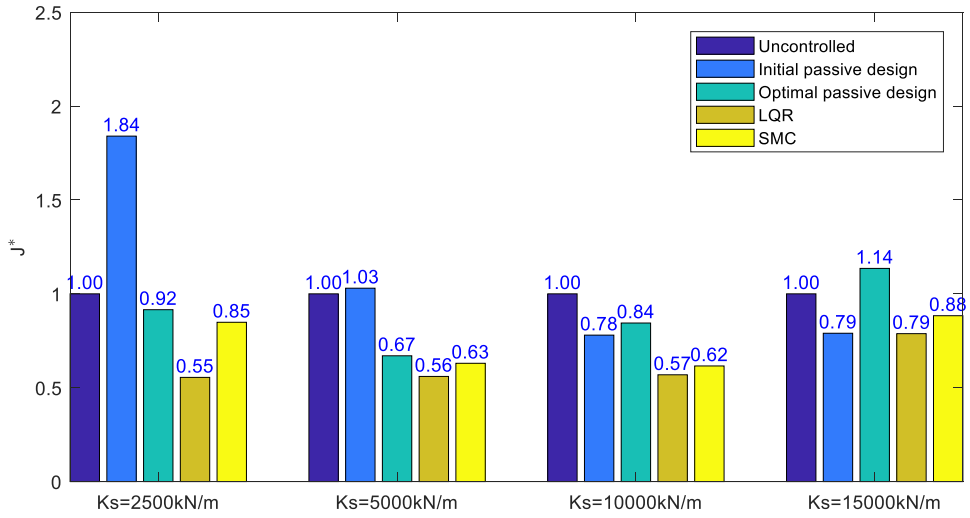

(a)

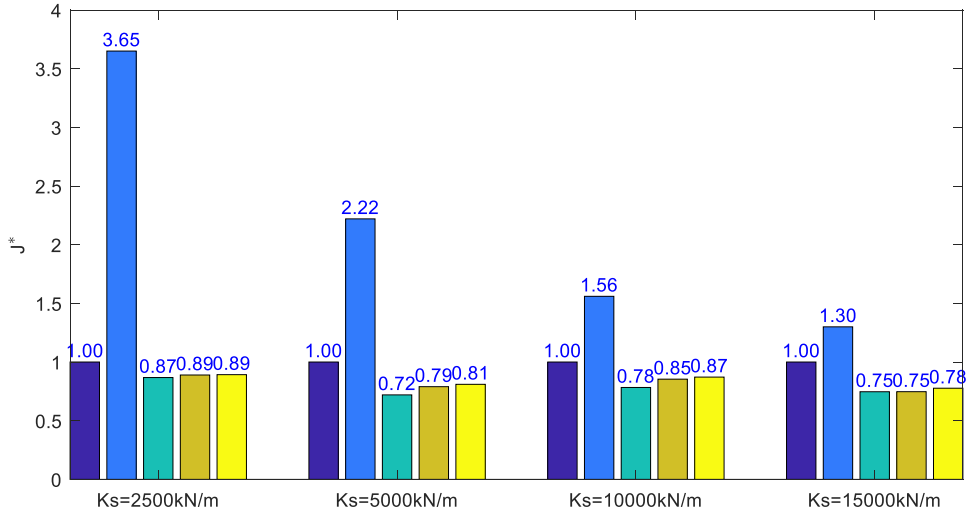

(b)

Figure 3.10. Performance index comparisons with different bridge systems in (a) transverse direction and (b) longitudinal direction

3.4.3 Influence of Different Ground Motions

Ground motion uncertainty is another factor that will affect the control efficiency. In this regard, three additional near-fault ground excitations, as given in Table 3.3, are used as the ground motion inputs. The fault normal component of each motion is exerted in the transverse direction

of the bridge, whereas the fault parallel component is applied in the longitudinal direction.

Table 3.3. Strong earthquake records selected for various control designs

Record Station	Earthquake	Magnitude	Fault distance	Peak acceleration* (g)
Cape Mendocino	1992 Petrolia	7	3.8	1.50 (1.04)
Rinaldi	1994 Northridge	6.7	9.9	0.89 (0.39)
Sylmar	1994 Northridge	6.7	12.3	0.73 (0.60)

* The peak accelerations of the fault parallel component are offered in parentheses. Values outside the parentheses are peak accelerations of the fault normal component.

Figure 3.11 compares the performance indices of the benchmark bridge when subject to these three strong motions. Promisingly, the two active control designs and optimal passive design are demonstrated to be able to improve the bridge performance under all three motions in both directions. The LQR and SMC controls bear average reductions of 37% and 23% in the transverse direction, respectively, and 27% and 28% in the longitudinal direction, respectively. The optimal passive design can provide a very similar response reduction. Therefore, it is proven that the proposed active control schemes and optimal passive control design are robust when ground motion uncertainty is taken into account. On the other hand, the initial passive control still amplifies the bridge response due to its inadaptability to adjust when facing different ground excitations.

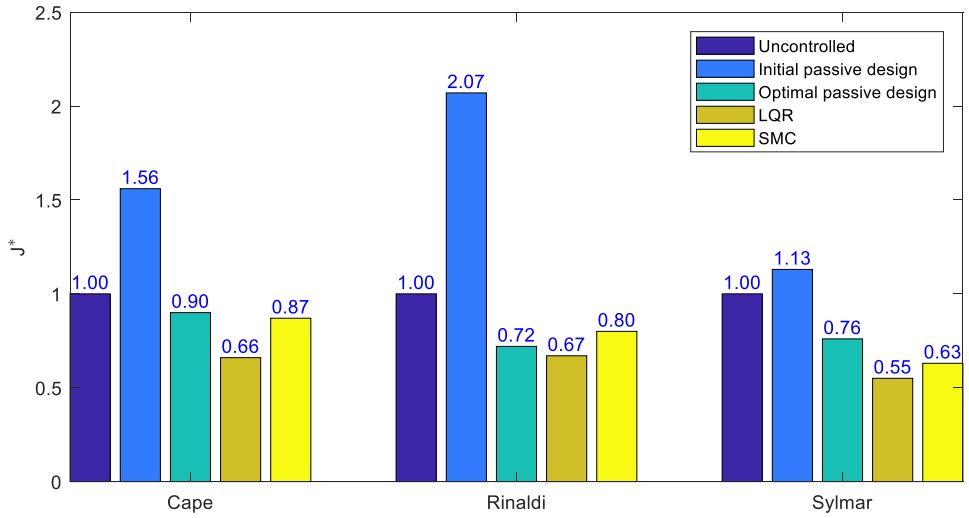

(a)

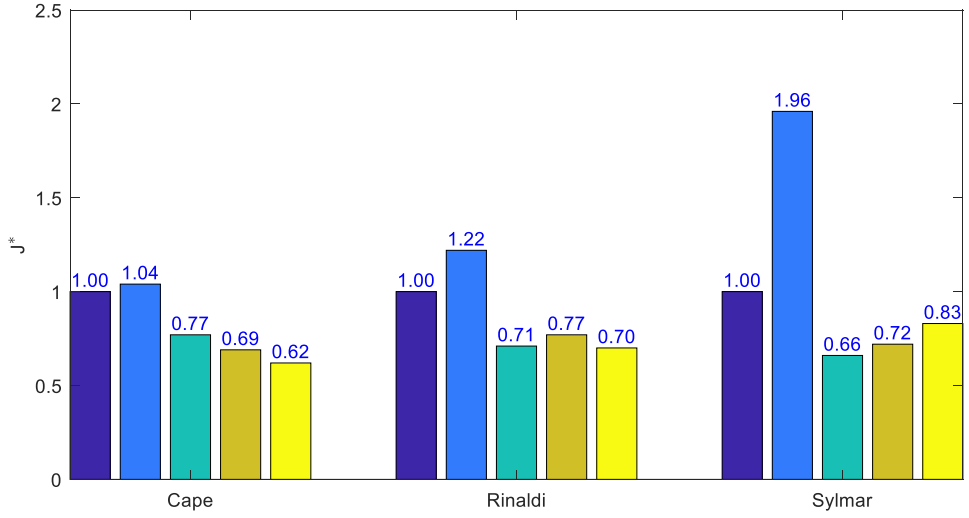

(b)

Figure 3.11. Performance index comparisons with different ground motion records in (a) transverse direction and (b) longitudinal direction

3.5 CONCLUDING REMARKS

The benchmark seismic control problem of highway bridges is revisited in this chapter using hybrid simulation that couples control algorithms with the realistic seismic model of the bridge. Two active control methods are shown to effectively improve the seismic performance of

the benchmark bridge when subject to a variety of bridge systems and ground motions. Optimal passive control designs are then delivered to approach the same effective improvement as the active controls. Our study concludes the following:

1. The hybrid simulation platform of UI-SIMCOR with the modifications made to accommodate the unique requirements associated with the benchmark control problem can reliably predict the bridge's seismic performance when validated against the complete finite element model. The hybrid model considers SSI effects and nonlinearities of both bridge columns and protective devices.

2. Initial passive control using viscous fluid dampers reduces bearing displacements at the cost of substantially increasing the deck acceleration. Bridge's system-level performance index indicates that initial passive control remains unattractive in some instances by inappropriately redistributing deck and bearing responses. Much amplified responses of the bridge's critical components such as deck and columns can be expected if the mechanical parameters of the passive viscous dampers are not optimally designed.

3. The proposed two classic active controls, the LQR method and the SMC method, are able to provide superior seismic performance for the benchmark bridge problem.

4. The optimal passive control identified from active controls can provide similar seismic performance for the benchmark problem among various active control schemes. The optimal passive design offers an appealing way to improve the bridge performance in general. Such improvement stays when the benchmark bridge has a different isolation design and subjects to different ground motion inputs.

In summary, this study develops a hybrid simulation framework to verify that active control can be considered an effective technique to alleviate the shaking of highway bridges when the

bridges' seismic responses are rationally simulated. The proposed optimal passive design can achieve the similar control effects and overcome related issues of active control, such as reliability of the power supply system, hydraulic noise, and time delays in the process of sensing. The main contents in Chapter 3 are under preparation in a journal publication (Peng et al. 2021b).

4. ANALYTICAL AND FINITE ELEMENT MODELING OF ROCKING BEHAVIORS

4.1 INTRODUCTION

Aiming at precisely predict the seismic responses of rocking structures subjected to seismic shaking and assess the efficiency of using the free-standing rocking components to enhance the seismic performance of structures, the objectives of the current study could be classified into the following items:

(1) To validate the prediction of rocking behavior by using different FE models. (Comparing with analytical models and experimental data).

(2) To compare the accuracy, efficiency, and limitations of different FE models for both rigid and deformable rocking structures.

(3) To assess the benefits of the free-standing rocking components for enhancing the seismic behavior of structures.

This chapter is devoted to introducing both analytical and numerical models for rocking simulation. For analytical modeling, two analytical models for a free-standing block and deformable rocking column-foundation are evaluated to investigate the influence of flexibility on impact mechanism during rocking motion. Both models can be solved by using the ordinary differential equation (ODE) solver in MATLAB. It also presents three existing finite element rocking models, i.e., nonlinear-elastic viscously damped spring model (SM), the deformable rocking body (DRB) model, and the augmented DRB model. All three models are verified for both rigid rocking and deformable rocking cases by comparing their results with those of the analytical models and experimental data. The comparison of accuracy, efficiency, and limitations for

different models are concluded. Suggestions for obtaining a better behavior of these FE models are also provided. A probabilistic seismic demand model (PSDM) is proposed to capture the uncertainties in predicting individual rocking responses from numerical models. Finally, a modified zero-length impact rocking model is proposed and implemented in OpenSees to provide more accurate and stable numerical solutions.

4.2 ANALYTICAL MODEL OF ROCKING BEHAVIOR

In this section, an analytical model of a free-standing block (Zhang & Makris, 2001) and an analytical model of deformable column-foundation are introduced, respectively. For a free-standing block, the equation of motion can be derived from the dynamic moment equilibrium since it only has one variable, i.e., the uplift angle θ. The kinetic energy dissipation at impact is considered by the value of the coefficient of restitution r (Housner, 1963) given from the conservation of angular momentum. For deformable column-foundation, the analytical model becomes more complicated since the system has two variables, the uplift angle θ and the column drift u. Besides, it experiences a distinct impact mechanism because of the additional vibrational mode that comes from the column flexibility. Following Lagrange formulation, the nonlinear equations of motion of the system excited by horizontal near-fault ground motions are derived and solved numerically. The kinetic energy dissipation at impact is derived differently under two different impact mechanisms: first, it is assumed that the system will stay full contact on the ground after each impact; Second, it is assumed that after each impact, the system will either remain full contact on the ground, or immediately uplift about the new pivot and continue to rock. For both impact mechanisms, if the post-impact kinematic energy is larger than the pre-impact one, the post-impact horizontal velocity is given by considering the loss of vertical pre-impact kinematic.

Both analytical models for rigid and deformable rocking can be easily solved using ODE solvers in MATLAB and can be used to validate the numerical models presented in this study.

4.2.1 The Rocking Response of a Free-Standing Block

(1) Equation of motion

Consider a free-standing rigid block as shown in Figure 4.1 with a size $R = \sqrt{b^2 + h^2}$, a slenderness $\alpha = \tan^{-1}(b/h)$, a mass m, a moment of inertia I_o about the pivot point O. The block will oscillate about the centers of O and O' when it is set to rocking. It is assumed that the coefficient of friction is sufficiently large, so there will be no sliding between the block and the base.

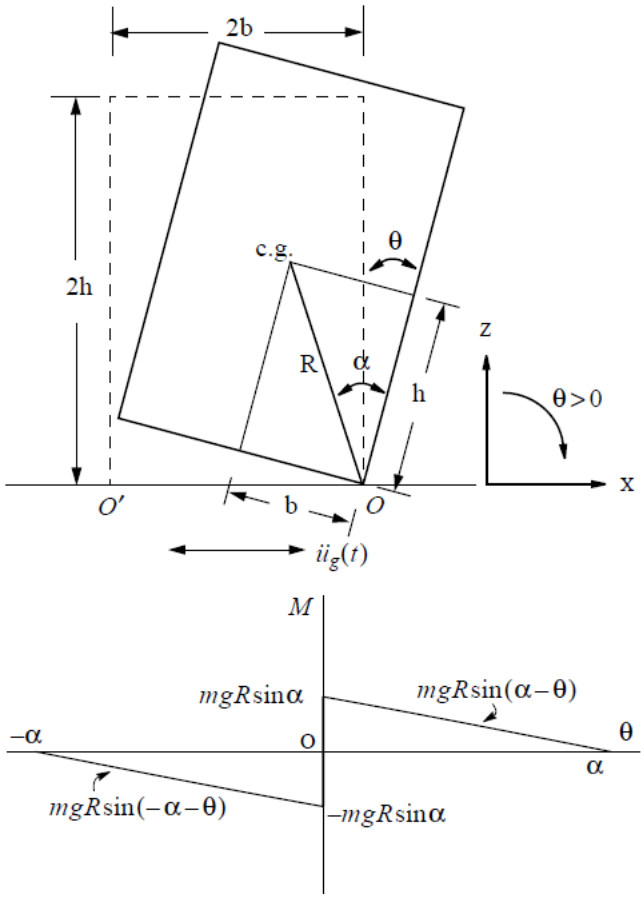

Figure 4.1. Schematic of a free-standing block in rocking motion (Zhang & Makris, 2001)

Under a negative horizontal ground acceleration $\ddot{u}_g$, as shown in Figure 4.1, the block will initially rotate with a positive rotation, $\theta > 0$. If it does not overturn, it will eventually rotate with a negative rotation, and so forth. When the block is rotated through a positive angle θ, the weight of the block will exert a restoring moment $mgR\sin(\alpha - \theta)$, then the equation of motion is:

$$I_0\ddot{\theta}(t) + mgR\sin\left[\alpha - \theta(t)\right] = -m\ddot{u}_g(t)R\cos\left[\alpha - \theta(t)\right], \quad \theta > 0 \tag{4.1}$$

when the block is rotated through a negative angle θ,

$$I_0\ddot{\theta}(t) + mgR\sin\left[-\alpha - \theta(t)\right] = -m\ddot{u}_g(t)R\cos\left[-\alpha - \theta(t)\right], \quad \theta < 0 \tag{4.2}$$

For rectangular blocks, $I_0 = \frac{4}{3}mR^2$, Equation (4.1) and (4.2) can be expressed in a compact form:

$$\ddot{\theta}(t) = -p^2\left\{\sin\left[\alpha\,\mathrm{sgn}\left[\theta(t)\right] - \theta(t)\right] + \frac{\ddot{u}_g}{g}\cos\left[\alpha\,\mathrm{sgn}\left[\theta(t)\right] - \theta(t)\right]\right\} \tag{4.3}$$

where $p = \sqrt{\frac{3g}{4R}}$ is the frequency parameter of the block. The larger the block (larger R), the smaller p. According to the literature (Housner, 1963), the oscillation frequency of a rigid block under free vibration is not constant because it strongly depends on the vibration amplitude. Nevertheless, the quantity p can still be used as a measure of the dynamic characteristics of the block.

(2) Uplift condition

Figure 4.1 (bottom) shows the moment-rotation relationship during the rocking motion of the free-standing block. Uplift of the block happens when the seismic demand (overturning moment) $m\ddot{u}_g h$ reaches the seismic resistance (re-centering moment) $mgR\sin\alpha$. Namely, the system has infinite stiffness until the magnitude of the applied moment reaches $mgR\sin\alpha$.

Therefore, the uplift condition can be determined as:

$$\left|\ddot{u}_g\right| > g\tan\alpha \tag{4.4}$$

Once the rocking motion is initiated, the restoring moment of the block decreases monotonically, then reaches zero when $\theta = \alpha$. Notice that, the moment-rotation curves follow the curve in Figure 4.1 (bottom) without enclosing any area during the oscillatory rocking motion. Energy is dissipated only during the impact when the rotation angle reverses.

(3) Impact mechanism

Energy loss of free-standing rigid block during the rocking impact was originally addressed by Houser (Housner, 1963). It is assumed that the impact is inelastic thus there is no bouncing. The pivot point switches smoothly from point O to O' as shown in Figure 4.2, and the moment of momentum about O' is conserved.

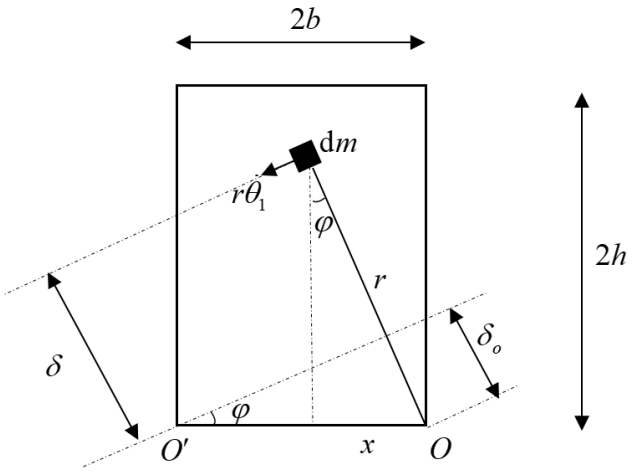

Figure 4.2. Rocking impact when the base pivot changes from O to O'

Momentum of $\mathrm{d}m$ can be written as $\mathrm{d}J = r\dot{\theta}_1\mathrm{d}m$. Its moment of momentum about point O' before impact is:

$$\mathrm{d}\Lambda = \mathrm{d}J\cdot\delta = \rho r\dot{\theta}_1\delta\mathrm{d}x\mathrm{d}y \tag{4.5}$$

where $\delta = r - \delta_o = r - \frac{x}{r} \cdot 2b$. By substituting it to Equation (4.5), the moment of momentum of the rigid block before impact is:

$$\Lambda = \int_A \mathrm{d}\Lambda = I_o \dot{\theta}_1 - m\dot{\theta}_1 2bR\sin\alpha \tag{4.6}$$

Then the conservation of momentum about point O' just before the impact and right after the impact gives:

$$I_o \dot{\theta}_1 - m\dot{\theta}_1 2bR\sin\alpha = I_o \dot{\theta}_2 \tag{4.7}$$

The reduction of kinetic energy during the impact is defined as:

$$r = \frac{\dot{\theta}_2^2}{\dot{\theta}_1^2} \tag{4.8}$$

which means that the angular velocity after the impact is $\sqrt{r}$ times the angular velocity before the impact. Combining of (4.7) and (4.8) gives:

$$r = \left[1 - \frac{m2R^2\sin^2\alpha}{I_o}\right]^2 \tag{4.9}$$

Given $I_0 = \frac{4}{3}mR^2$ for rectangular block, the coefficient of restitution is given by:

$$r = \left[1 - \frac{3}{2}\sin^2\alpha\right]^2 \tag{4.10}$$

Note that, the value of the coefficient of restitution given by (4.10) is the upper limit of r for a rigid block undergo rocking motion. When considering additional energy lost due to interface mechanism, the true value of the coefficient of restitution, r, will be less than the one computed using Equation (4.10).

By combining the condition of rocking initiation, the equation of motion of block during rocking, and the coefficient of restitution, the analytical solution of rocking response can be

derived using the technique of solving differential equations, such as rocking response of rigid blocks under near-source ground motions (Makris & Roussos, 2000; Zhang & Makris, 2001). In this study, the ordinary differential equation (ODE) solver in MATLAB is utilized to solve the rocking response.

4.2.2 Analytical Modeling of the Deformable Column-Foundation

(1) Equation of motion

Figure 4.3 shows a rocking column-foundation system supported on the rigid surface. The system has a detached rocking interface at the bottom of the shallow foundation, which facilitates the foundation to uplift and re-center when subjected to horizontal ground excitations. As shown in Figure 4.3, considering that the self-weight of the column is much less than the participating weight from the deck and foundation, the system can be idealized as a two degree of freedom system when foundation rotates along the pivot points of the base. Namely, the dynamics of the system can be defined as the uplift angle denoted as θ and the column drift denoted as u. The column-foundation has a mass of deck m, a mass of foundation m_b, a moment of inertia of the base around pivot point I_{bc}, a height of H, a base width of $2b$, an elastic stiffness of E_cI_c, and a damping coefficient of C.

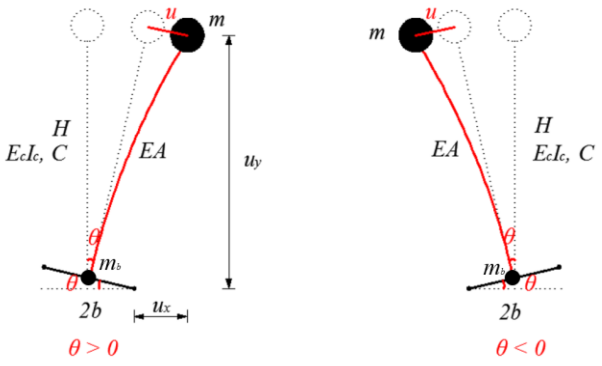

Figure 4.3. Schematic of the flexible rocking column-foundation system

The kinematics of the mass point m when rotates along the pivot are:

$$\left\{\begin{array}{l} u_x = -\mathrm{sgn}(\theta) b\cos\theta + H\sin\theta + u\cos\theta \\ u_y = \mathrm{sgn}(\theta) b\sin\theta + H\cos\theta - u\sin\theta \end{array}\right\} \tag{4.11}$$

where u_x and u_y are the relative displacements of the mass point to the pivot point in the horizontal and vertical directions, respectively. The sign of θ is used to consider the rotates direction. Therefore, the kinematic energy of the mass point m and m_b can be calculated as:

$$\begin{aligned} T &= \frac{1}{2} I_{bc}\dot{\theta}^2 + \frac{1}{2} m\left(\dot{u}_x^2 + \dot{u}_y^2\right) \\ &= \frac{1}{2} I_{bc}\dot{\theta}^2 + \frac{1}{2} m\left[\left(H^2 + b^2 + u^2 - \mathrm{sgn}(\theta) 2bu\right)\dot{\theta}^2 + \dot{u}^2 + 2H\dot{u}\dot{\theta}\right] \end{aligned} \tag{4.12}$$

The potential energy of the mass point m and m_b that comes from gravity and the D'Alembert force, and the column strain energy can be summarized as:

$$\begin{aligned} V &= mgu_y + \mathrm{sgn}(\theta) m_b gb\sin\theta + m\ddot{u}_g u_x + m_b\ddot{u}_g\left[-\mathrm{sgn}(\theta) b\cos\theta\right] + \frac{3E_c I_c}{2H^3}u^2 \\ &= \mathrm{sgn}(\theta) m_b gb\sin\theta + mg\left[\mathrm{sgn}(\theta) b\sin\theta + H\cos\theta - u\sin\theta\right] \\ &\quad + m_b\ddot{u}_g\left[-\mathrm{sgn}(\theta) b\cos\theta\right] + m\ddot{u}_g\left[-\mathrm{sgn}(\theta) b\cos\theta + H\sin\theta + u\cos\theta\right] \\ &\quad + \frac{3E_c I_c}{2H^3}u^2 \end{aligned} \tag{4.13}$$

where $\ddot{u}_g$ is the acceleration magnitude of the input ground motion. The Lagrange's equation shall be satisfied during the rocking motion:

$$\left\{\begin{array}{l} \dfrac{\mathrm{d}}{\mathrm{d}t}\dfrac{\partial(T-V)}{\partial\dot{\theta}} - \dfrac{\partial(T-V)}{\partial\theta} = 0 \\ \dfrac{\mathrm{d}}{\mathrm{d}t}\dfrac{\partial(T-V)}{\partial\dot{u}} - \dfrac{\partial(T-V)}{\partial u} = -C\dot{u} \end{array}\right\} \tag{4.14}$$

Substituting the equations (4.12) and (4.13) into equation (4.14) gives the equations of motion of the rocking system:

$$
\begin{aligned}
&I_{bc}\ddot{\theta}+m\ddot{\theta}\left[H^2+b^2-\operatorname{sgn}(\theta)2bu+u^2\right]+mH\ddot{u}-2m\dot{\theta}\dot{u}\left[\operatorname{sgn}(\theta)b-u\right]\\
&+m_b g\operatorname{sgn}(\theta)b\cos\theta-mg\left[H\sin\theta-\operatorname{sgn}(\theta)b\cos\theta+u\cos\theta\right]\\
&=-m_b\ddot{u}_g\operatorname{sgn}(\theta)b\sin\theta-m\ddot{u}_g\left[H\cos\theta+\operatorname{sgn}(\theta)b\sin\theta-u\sin\theta\right]
\end{aligned}
\tag{4.15}
$$

$$
\ddot{\theta}H+\ddot{u}+2\xi w_n\dot{u}+\dot{\theta}^2\left[\operatorname{sgn}(\theta)b-u\right]-g\sin\theta+w_n^2u=-\ddot{u}_g\cos\theta \tag{4.16}
$$

where $w_n=\sqrt{3E_cI_c/mH^3}$ is the vibration natural frequency of the column, $\xi=\frac{C}{2}\sqrt{\frac{H^3}{3E_cI_cm}}$ is the associated damping ratio. It's noted that when $\ddot{\theta}=\dot{\theta}=\theta=0$, Equation (4.16) turns out to be the equation of motion during full contact, i.e.,

$$
\ddot{u}+2\xi w_n\dot{u}+w_n^2u=-\ddot{u}_g \tag{4.17}
$$

(2) Uplift condition

Like the uplift condition of rigid block, uplift happens when the overturning moment, $M_o=\mp m\left(\ddot{u}_g+\ddot{u}\right)H$, due to external loads exceeds the resisting moment, $M_r=\left(m+m_b\right)gb\mp mgu$, that provided by gravity. Namely, uplift happens when:

$$
\mp m\left(\ddot{u}_g+\ddot{u}\right)H>\left(m+m_b\right)gb\mp mgu \tag{4.18}
$$

By substituting $\ddot{u}_g+\ddot{u}$ in Equation (4.17) to Equation (4.18), the uplift condition can be determined as:

$$
\pm\left(2\xi w_n\dot{u}+w_n^2u\right)H>g\left(\frac{m+m_b}{m}b\mp u\right) \tag{4.19}
$$

For undamped system and assume $u\ll b$, $m_b\ll m$ the above uplift condition can be further simplified to (Acikgoz & DeJong, 2012; Vassiliou et al., 2015):

$$
|u|>\frac{gb}{w_n^2H} \tag{4.20}
$$

(3) Different impact mechanisms

Because of the additional vibration mode that comes from column flexibility, the deformable rocking column-foundation shall experience a distinct impact mechanism when compare with the rigid block case (Housner, 1963). In previous studies (Acikgoz & DeJong, 2012; Oliveto et al., 2003), it was assumed that after each impact, the system will either stay full contact on the ground, or immediately uplift about the new pivot point and continue to rock, and the state with less total energy will govern. In the recently completed experiment study (Truniger et al., 2015), the post-impact velocity is calculated by assuming the column remains full contact after each impact and system's kinematic energy associated with vertical velocity components is lost during the impact. In the study of Zhang et al. (2019), they considered that the full contact condition will follow each rocking impact, thus, the post-impact horizontal velocity is the only variable that needs to be determined by forcing the conservation of momentum. It is possible that the post-impact kinematic energy is larger than the pre-impact one (Vassiliou et al., 2015), which is not physically meaningful. Therefore, in the study of Zhang et al. (2019), the conservation of momentum is abandoned when the previous physically unmeaningful situation happens. Instead, the equilibrium of kinematic energy is calculated by considering the pre-impact vertical kinematic energy is lost (Chopra & Yim, 1985).

To evaluate different impact energy dissipation mechanisms, two impact mechanisms -- full contact mechanism and check uplift mechanism -- are proposed and evaluated in this study.

(a) "Full contact" impact mechanism

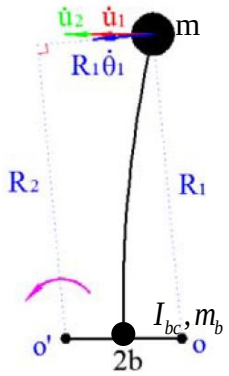

Figure 4.4. Rocking impact when the base pivot changes from point O to O'

Considering that the full contact condition will follow each rocking impact (Zhang et al., 2019), consequently, there will be zero post-impact rocking angle and angular velocity of base, i.e., $\theta_2 = \dot{\theta}_2 = 0$. Since the impact is instantaneous, it is reasonable to assume pre-impact horizontal displacement and post-impact horizontal displacement are the same, i.e., $u_1 = u_2$. As shown in Figure 4.4, the conservation of angular moment of momentum around point O' leads to:

$$m\dot{u}_2 H = m\left(R_1\dot{\theta}_1\right)R_2 + m\dot{u}_1 H + \left(I_{bc} - 2m_b b^2\right)\dot{\theta}_1 \tag{4.21}$$

where $R_1 = \sqrt{H^2 + \left(b-u\right)^2}$ and $R_2 = \dfrac{H^2 + u^2 - b^2}{\sqrt{H^2 + \left(b-u\right)^2}}$ are the distances from the pre-impact rotational velocity tensor to the pivot O and O' respectively. $\dot{\theta}_1$ is the pre-impact angular velocity of the base, $\dot{u}_1$ and $\dot{u}_2$ are the pre-impact and post-impact horizontal velocities respectively. By substituting R_1 and R_2 into equation (4.21), the post-impact horizontal velocity can be solved as:

$$\dot{u}_2 = \frac{I_{bc} - 2m_b b^2 + m\left(H^2 + u^2 - b^2\right)}{mH}\dot{\theta}_1 + \dot{u}_1 \tag{4.22}$$

The system kinetic energy of the rocking phase and full contact phase are defined as:

$$E_r = \frac{1}{2}I_{bc}\dot{\theta}^2 + \frac{1}{2}m\left[\left(b^2 + H^2 + u^2 \pm 2bu\right)\dot{\theta}^2 + \dot{u}^2 + 2H\dot{\theta}\,\dot{u}\right] \tag{4.23}$$

$$E_f = \frac{1}{2} m\dot{u}^2 \tag{4.24}$$

If the post-impact energy $E_{2,f}$ is larger than the pre-impact energy $E_{1,r}$, use vertical velocity energy lost (VVEL) model (Chopra & Yim, 1985; Zhang et al., 2019) instead, leading to:

$$\dot{u}_2 = H\dot{\theta}_1 + \dot{u}_1 \tag{4.25}$$

(b) "Check uplift" impact mechanism

Assume that the either full contact or immediately rocking will follow each rocking impact, the uplift condition (4.19) needs to be checked at each impact. If the uplift condition is not satisfied, i.e., full contact phase happens after impact and $\theta_2 = \dot{\theta}_2 = 0$, $u_1 = u_2$, use the conservation of angular moment of momentum to compute post-impact horizontal velocity $\dot{u}_2$, as shown in Equation (4.22). If the uplift condition is satisfied, i.e., immediate rocking after impact results in $\theta_2 = 0$, $u_1 = u_2$. Assume $\dot{u}_1 = \dot{u}_2$ (Acikgoz & DeJong, 2012), applying conservation of angular momentum around the impacting corner gives:

$$\dot{\theta}_2 = \frac{I_{bc} - 2m_b b^2 + m\left(H^2 + u^2 - b^2\right)}{I_{bc} + m\left(H^2 + u^2 + b^2 \pm 2bu\right)} \dot{\theta}_1 \tag{4.26}$$

After checking the uplift condition and calculating the post-impact response, if the system energy post-impact is larger than the energy pre-impact, then use vertical velocity energy lost (VVEL) model (Chopra & Yim, 1985; Zhang et al., 2019), which leads to:

$$\dot{u}_2 = H\dot{\theta}_1 + \dot{u}_1,\ \theta_2 = \dot{\theta}_2 = 0,\ u_1 = u_2 \tag{4.27}$$

By combining the uplift condition, the equation of motion, and the impact mechanism, the analytical solution of the rocking response can be derived using the technique of solving differential equations. In this study, the ODE solver in MATLAB is utilized to solve the rocking response for deformable rocking structures. The effectiveness of these two impact mechanisms is

examined by applying them to predict (1) the dynamic response of deformable cantilevers rocking on a rigid surface under pulse like ground motion input (i.e., forced vibration case); (2) Free vibration of rigid and deformable bridge pier on a shallow foundation. The comparison with experimental results and impact mechanisms from previous studies (Zhang et al., 2019) are shown in the following section. It is found that the introduced model is more consistent with the experimental results that were presented in the literature (Truniger et al., 2015).

4.2.3 Comparation with Shaking Table Test

(1) Prediction of rocking behavior under forced vibration

First, an experiment of deformable cantilevers rocking on a rigid surface from Truniger et al. (Truniger et al., 2015) is adopted to examine the different impact mechanisms. A specimen consists of a steel base plate, two columns made using steel threaded rods, and a steel weight at the top (shown in Figure 4.5). The specimen configuration is deliberately similar to the configuration of the model of a deformable rocking column utilized in this study. Two horizontal stiffeners were mounted between the two columns, as shown in Figure 4.5, to increase the out-of-plane horizontal stiffness and, thus, impede out-of-plane movement. Different column diameters are used to make specimens with different fixed-base natural frequencies. Specimen with 1Hz and 2 Hz are considered in this study. In addition, base plates with widths of 15 cm (short base case) and 30 cm (long base case) were used to investigate the influence of the specimen slenderness on the response. Dimensions and masses, together with values of the slenderness α and rocking parameter p as well as the measured fixed-base natural frequencies and damping ratios of the eight specimens, can be found in Table I of the original paper (Truniger et al., 2015).

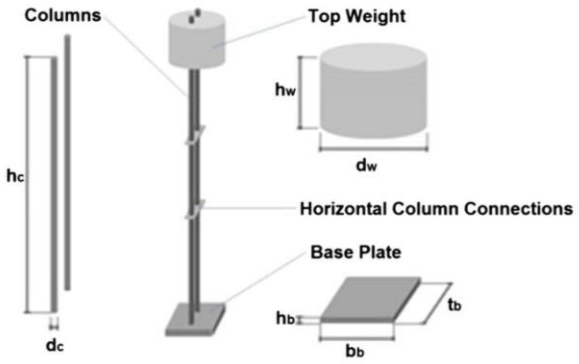

Figure 4.5. Sketch of deformable cantilever structure (Truniger et al., 2015)

The rocking response of a specimen was induced by dynamics excitation at its support. Each specimen was tested under pulse-type ground motions. A Ricker wavelet approximates the main pulse of pulse-type ground motions (Ricker, 1943). The acceleration amplitude, ap, and period, Tp, of a Ricker wavelet are discussed further in Vassiliou and Makris (2012). The Ricker wavelets used in this study had the pulse periods Tp=0.5s, 1.0s, and the acceleration amplitudes ap = 0.16 g to 0.24 g. For the forced vibration case, as shown in Figure 4.6, it can be concluded that both models with different impact mechanisms yield good predictions in the dynamic response of these deformable cantilevers.

However, it's hard to say which one works better. For the 1Hz case, the model with the "check uplift" impact mechanism works better; For the 2Hz case, the model with the "full contact" impact mechanism works better. Since the flexibility of structure coupled with rocking behavior in the experiments, the vibration of structure could either increase or decrease the energy loss at the impact. To further quantify the influence of impact mechanisms on energy dissipation, the kinetic energy responses of different models are plotted in Figure 4.7. Quantities α, the slenderness of the rocking system, u_{cr}, the relative displacement of the elastic column when uplift occurs, E_{ref}, the reference energy, are defined in Vassiliou et al. (2015). It is observed that the energy dissipated at impact is different when using different impact mechanisms. However, it is impossible to predict

which impact mechanism will always dissipate more energy due to the complexity of flexibility coupled with the rocking of structure. Thus, we can only say that the one with similar energy dissipation with experimental data works better. More research should be done to obtain the real energy dissipation curve in experiments.

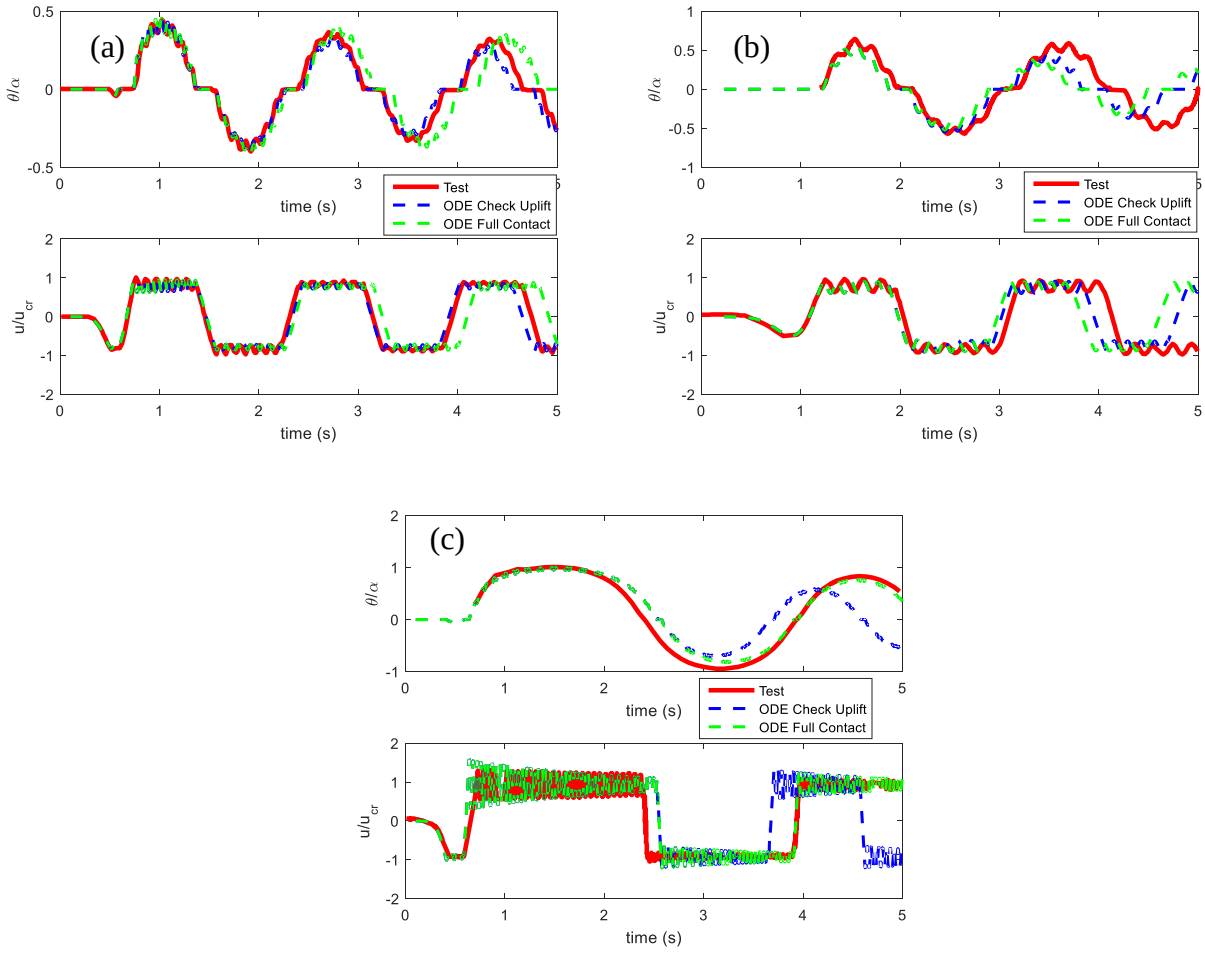

Figure 4.6. Dynamic response of deformable cantilevers (a) 1Hz short case; (c)1Hz long base case; (c) 2Hz short base case

Figure 4.8 shows the impact behavior of different models, i.e., the changing of rocking angle during impact. For model with "check uplift" impact mechanism, as shown in Figure 4.8 (a), "double impact" could happen. Which means, at current time immediate rocking will happen after the impact. Then structure goes into a small rocking phase and reached the second impact.

However, in the recently experiment study (Truniger et al., 2015), it's discovered that the "double impact" doesn't exist during the impact. Therefore, the model with the "full contact" impact mechanism is selected as the analytical solution when verifying the FE models in the following sections.

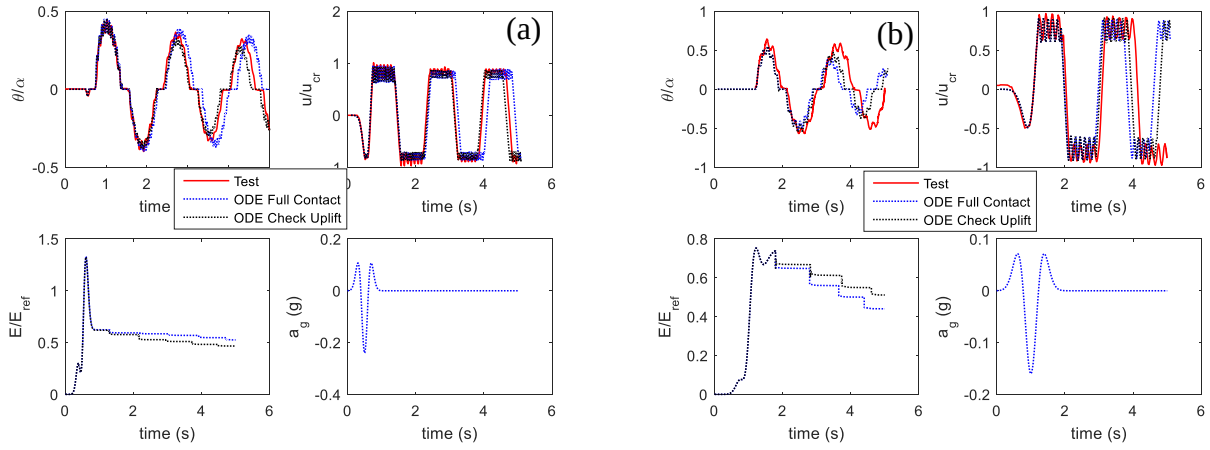

Figure 4.7. Dynamic response of deformable cantilevers (a) 1Hz short case; (c)1Hz long base case

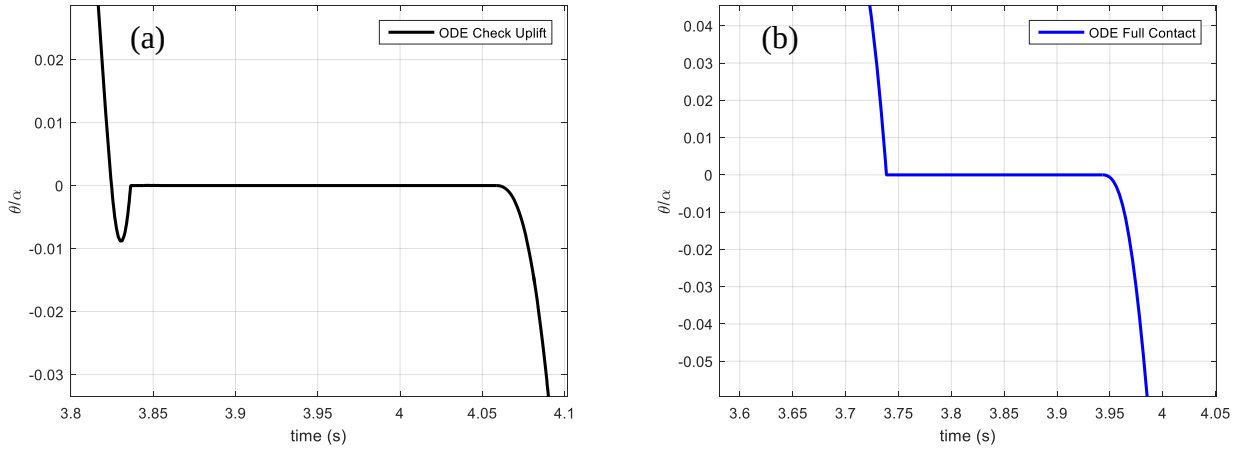

Figure 4.8. Impact mechanism of 1Hz long base case

(2) Prediction of rocking behavior under free vibration

Secondly, the free vibration of a prototype of the experimental model of a bridge pier on a shallow foundation, as shown in Figure 4.9 (a) (Chen, 2017), is used to observe the proposed analytical model. The reinforced concrete pier has a height of 3.32m and a diameter of 0.53m. The deck can be simulated as a lumped mass of 95 tons. The bridge is fixed on a shallow foundation. The shallow foundation has a width of 1.6 m and a mass of 17.6 tons. The fundamental frequency of the structure with a fixed-base assumption is 1.47Hz. The slenderness $\alpha = 13.5^{o}$. The details about the similitude of an uplift structure between the prototype and physical model are performed in the literature (Chen, 2017). The experimental model was scaled down by a factor of 4, as shown in Figure 4.9 (b). Secondary beams were installed to limit out-of-plane and torsional motion during uplift. A fundamental frequency of 2.94 Hz has been achieved, which satisfies the similitude in model scaling.

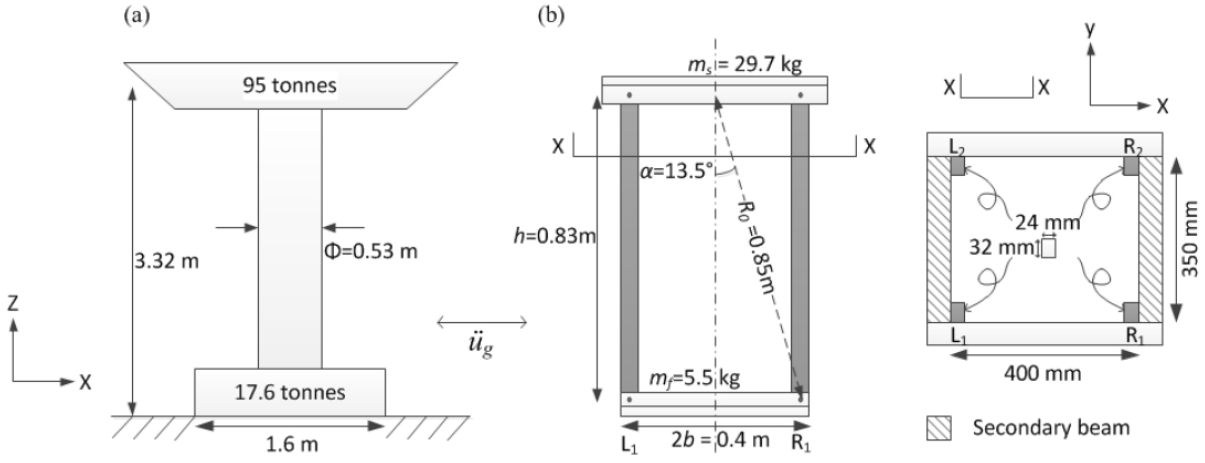

Figure 4.9. Prototype (a) and dimensions of the physical model (b) (Chen, 2017)

Strain gauges were glued on the columns near the supports to measure the bending moment. Two displacement transducers were placed on both the edges of the footing to measure the vertical displacement. As shown by R1, R2, L1, and L2 in Figure 4.9 (b), four load cells were fixed under the columns beneath the footing to measure the contact forces. Sandpaper was attached at the

contact surface to increase the friction so that sliding is minimized. For simulation of a rigid structure, light-weight aluminum cross braces were added. A fundamental frequency of 20.5 Hz has been determined experimentally for the rigid structure.

An initial vertical footing displacement was first applied to the system by lifting one side of the footing. Then, the model is suddenly released from the initial vertical displacement and started free vibration. The structure overturns once the center of mass lies beyond the center of rotation, i.e., $\theta > \alpha$. Therefore, six initial vertical footing displacements, which provided an initial footing rotation within 10-20% of the maximum footing rotation α , are considered for the structure to avoid overturning. The initiation of free vibrations was carried out twice on each side.

Due to the excellent behavior of the ODE model with "full contact" impact mechanism, it is used to predict the free vibration of a previous rigid/deformable bridge pier on a shallow foundation, as shown in Figure 4.10. It's observed that the rocking responses of this model match well with the experimental data for rigid structure. However, there are discrepancies between the analytical solution and experimental data for the flexible case. It shows that structural flexibility has a more significant influence on the coupled free vibration and rocking behavior than coupled forced vibration and rocking behavior, resulting in the inaccurate analytical model.

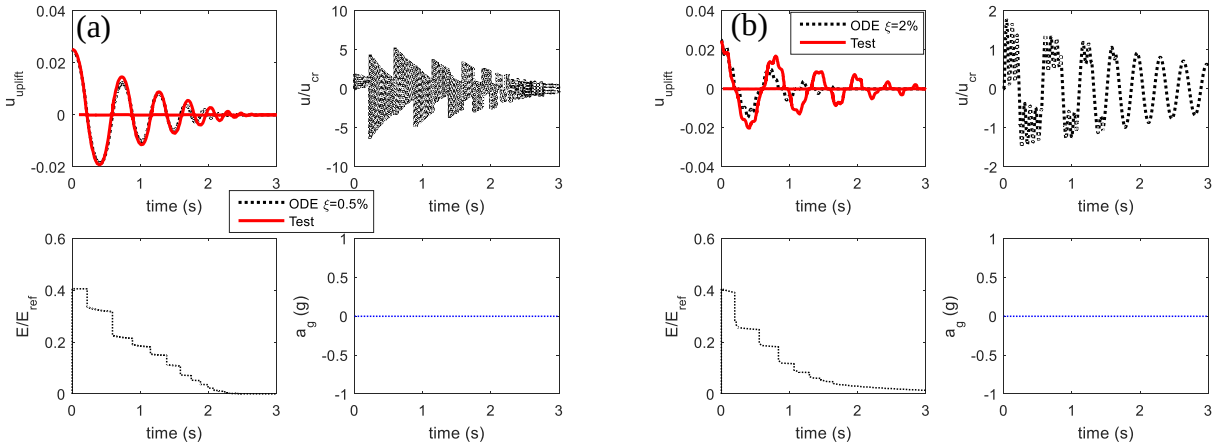

Figure 4.10. Free vibration of (a) rigid and (b) deformable bridge pier on a shallow foundation

4.3 FINITE ELEMENT MODEL OF ROCKING BEHAVIOR

As described in section 4.2, the dynamic response of a solitary rigid block or deformable column-foundation can be easily solved by using any numerical computing package, e.g., MATLAB, to solve differential equations. However, the equations of motion of more complex rocking structures become much more complicated, and their solution becomes cumbersome. Therefore, a finite element model of rocking which can be directly used in commercial finite element software is needed. The following three FE models that can be modeled in OpenSees are selected in the current study.

4.3.1 Introduction of Existing FE Models

The first FE model is a non-linear elastic viscously damped zero-length spring rocking (SM) model for the rigid and deformable body (Vassiliou et al., 2014). A zero-length rotational spring with classical damping is used to simulate the rocking behavior. The real strength of this proposed SM rocking model is: (1) The properties of the rocking body can entirely determine the value of variables of SM; (2) it can be directly used in commercial finite element software, OpenSees. If any criticism were to be leveled at the SM model, it would be to note that: First, the vertical displacements do not match the analytical solution. This behavior may limit the use of the SM to model rocking structures post-tensioned using vertical pre-stressing tendons. Second, a too simplistic method is used to capture the impact mechanism using a viscous damping ratio, which works not that well for a rocking body with less slenderness. Since the principal energy dissipation mechanism of impact is instantaneous and discontinuous, the use of viscous damping cannot be predicted as a priori (Chopra & McKenna, 2016; Hall, 2006; Petrini et al., 2008; Truniger et al., 2015; Wiebe et al., 2012). Moreover, without verification, it is further assumed that the energy

dissipated through rocking impact does not depend strongly on the flexibility of the rocking body.

To overcome the difficulties mentioned above, i.e., modeling the instantaneous and discontinuous energy dissipation mechanism using viscous damping, Vassiliou et al. (Vassiliou et al., 2017) presented a deformable rocking body (DRB) model to quantify the in-plane rocking response of system consisting of either rigid or deformable rocking bodies. Unlike the SM rocking model, the energy dissipation of the DRB model during rocking motion is modeled using a numerically dissipative time step integration scheme instead of using equivalent viscous damping ratio c. Namely, no damping is associated with the rocking body model and rocking surface model. Since the viscous damping coefficient, which is derived from the coefficient of restitution (Housner, 1963), is only valid for an ideally rigid case and can cause increasing of energy dissipation grossly (Truniger et al., 2015), the dissipative time-stepping integration procedure is a better approach by damping out high-frequency shock waves during the rocking impact. The other difference between the SM model and DRB model is that the rocking surface of DRB is modeled using the zero-length fiber cross-section element instead of using rotational spring. Therefore, it has a more accurate prediction of vertical displacement and can be used for post-tension rocking bodies.

As the rocking body becomes more deformable, the frequency of the generated shock wave during the impact decreases, causing the amount of energy numerically dissipated by dissipative time-stepping integration procedures to diminish. The presence of undamped high-frequency components of motion causes the divergence of the solution predicted by the DRB model. To overcome this unwanted divergence, the DRB model is augmented by creating an alternate energy dissipation path to avoid the generation of shock waves in the rocking body. Namely, using a set of springs and dashpots rather than using a fixed finite element model node to model the stiff

ground on which the body is rocking.

In summary, these three FE models reveal a typical research process in the modeling of rocking behaviors. Although there might be more or less flaws in each model, their union should indicate a good picture of numerical simulation of rocking behaviors. In this section, the details of these FE models are introduced and validated by comparing the numerical dynamic response analysis with the analytical model and experimental data (Chen, 2017). Suggestions are provided to make each model works better under different situation.

4.3.2 Evaluation of Existing FE Models

(1) Nonlinear-elastic Viscously Damped Spring Model (SM)

As shown in Figure 4.11, the equivalent nonlinear-elastic viscously-damped Spring Model (SM) (Vassiliou et al., 2014) consists of a cantilever column connected to a nonlinear damped rotational spring. The cantilever column, whose cross-section and height are identical to the cross-section and height of the rocking block, is used to simulate the geometric behavior of the block. The rotational spring has a rigid-plastic moment-rotation response envelope, as shown in Figure 4.12, right. It has a yield moment equal to the seismic resistance (re-centering moment) $mgR\sin(\alpha)$ of the block, i.e., rocking motion is initiated only when the moment demand of rotational spring reaches the yield moment. After the initiation of rocking, there is no stiffness in the spring, and the moment unloads along the loading path during the rocking. This model does not involve explicit modeling of rocking body impact. The energy dissipation of body impact is captured by a viscous damper, which is added in parallel with the nonlinear elastic spring, with damping coefficient c. Sliding on the rocking surface is not permitted.

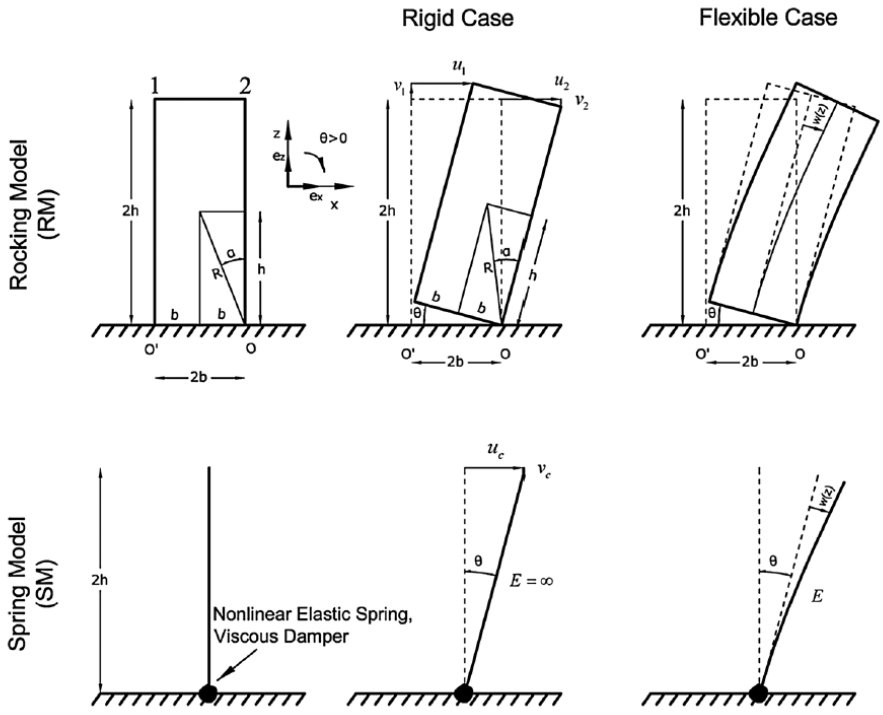

Figure 4.11. Rocking Model (top) and the Spring Model (bottom) (Vassiliou et al., 2014)

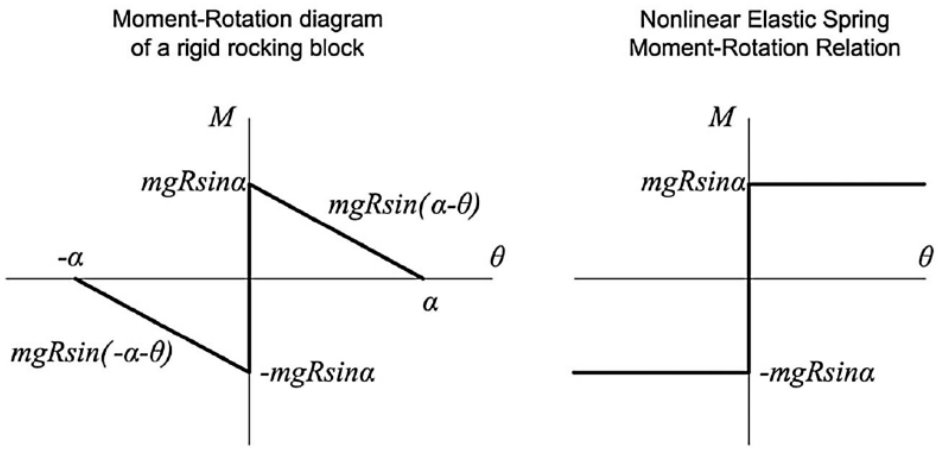

Figure 4.12. Moment relationship for a rigid block with slenderness α and size R (left) and a nonlinear elastic spring of the SM (right) (Vassiliou et al., 2014)

The equation of motion of the SM is given as:

$$I_o^{'}\ddot{\theta}(t) + mgR\left(\sin\alpha\,\mathrm{sgn}\,\theta - \cos\alpha\sin\theta\right) = -m\ddot{u}_g R\cos\alpha\cos\theta \tag{4.28}$$

where $I_o^{'} = \frac{4}{3} mR^2 \cos^2 \alpha$. Comparing with the EOM of a free-standing block introduced in Section 4.2.1, it is reasonable to assume that the differences between the two models come from the difference in the moments of inertia of the two models (Vassiliou et al., 2014). Namely, the rigid block's rotational inertia, $I_o = \frac{4}{3} mR^2$, refers to rotation about the corner of the rigid block and accounts for the shape of the rocking body (here, the body has a rectangular shape, it could be a different shape). While the rotational inertia of the SM model, $I_o^{'} = \frac{4}{3} mR^2 \cos^2 \alpha$, refers to rotation about the mid-point of the base, i.e., the endpoint of the cantilever column, and does not account for the shape of the rocking body. For this reason, the SM model was modified by evenly distributing the rotational inertia difference, $\Delta I_o = \frac{4}{3} mR^2 \left(1 - \cos^2 \alpha\right)$, among the rotational degrees of freedom (DOF) of the nodes used to model the column. Namely, a rotational mass equal to $\frac{\Delta I_o}{nnod}$ is added to the rotational DOF of each node in the finite element model.

The restitution factor r (Housner, 1963) is adopted to describe the energy dissipation ratio E / E_o per cycle for free rocking of the SM:

$$\frac{E}{E_o} = r^2 = \left(1 - \frac{3}{2} \sin^2 \alpha\right)^4 \tag{4.29}$$

where E is the energy at the end of one complete cycle, and E_o is the energy at the beginning of that cycle with initial conditions $\theta(0) = \theta_o$, $\dot{\theta}(0) = 0$. The viscous damping in the SM utilizes a viscous damper with a damping coefficient c associated with the angular velocity at the base of the column to capture the equivalent per-cycle energy loss ratio, r_{eq}^2 , which is defined as:

$$\frac{E}{E_o} = r_{eq}^2 = \varphi\left(\frac{\theta_o}{\alpha}, \alpha, \bar{c}\right) \tag{4.30}$$

where $\bar{c} = \dfrac{c}{mg^{0.5}R^{1.5}}$. As shown in Figure 4.13 (Vassiliou et al., 2014), Equation (4.30) is plotted for $\tan\alpha$ equals to 0.1, 0.2 and 0.3, $\bar{c}$ equals to 0.02, 0.08 and 0.18, and $0 < \theta_o / \alpha < 1$.

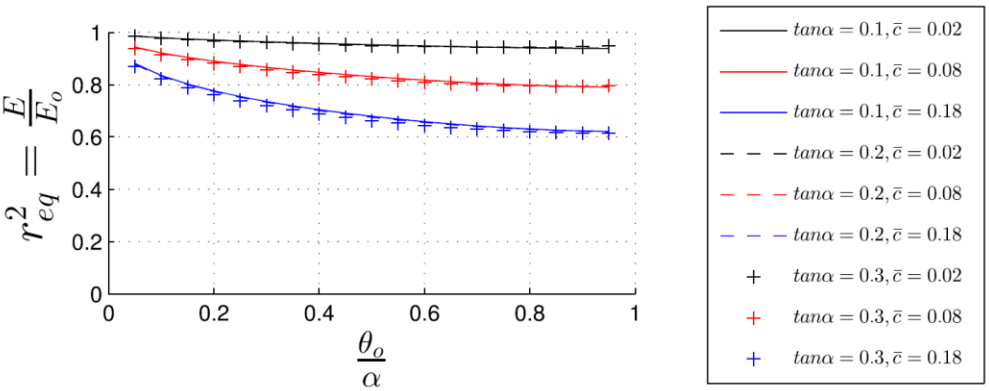

Figure 4.13. Equivalent per-cycle energy loss ratio, r_{eq}^2 (Vassiliou et al., 2014)

Based on the data in Figure 4.13, for $\theta_o / \alpha > 0.5$ and $\tan\alpha < 0.3$, a relationship between $\bar{c}$ and α can be established such that the energy dissipation during a free rocking cycle in the analytical model of rocking block and SM are the same. Then, the equivalent damping coefficient for the rotational damper in SM can be defined as a function of the body mass, size, and slenderness:

$$c = 0.02\left(\frac{\alpha}{0.1}\right)^2 mg^{0.5}R^{1.5} \tag{4.31}$$

The SM is implemented in the FEM software framework OpenSees (OpenSees, 2017). The rigid rocking body is modeled by using elastic beam-column elements. The rotational spring is modeled as a zero-length element, which has the nonlinear-elastic material with yield moment $mgR\sin(\alpha)$ in rotational DOF, parallel with the other zero-length element, which has the viscous material with equivalent damping ratio c in rotational DOF.

Rocking responses of an 8m tall block ($\tan\alpha = 0.25$), subjected to a Type-A pulse (one-cycle sinusoidal pulse) excitation with amplitude $a_p = 0.45g$, are computed using the SM model, as shown in Figure 4.15. While, the rocking response of a 25.6m tall block ($\tan\alpha = 0.36$), subjected to a Type-A pulse excitation with amplitude $a_p = g$, are computed using the SM model, as shown in Figure 4.16. The Young's modulus, E, of the material of elastic beam-column is set to a tremendous value such that the column is quasi-rigid. It is observed that both the rotation and angular velocity computed using SM match well with the analytical solution when $\tan\alpha = 0.25 < 0.3$, while the SM is not as good when $\tan\alpha = 0.36 > 0.3$ because the equation of equivalent damping ratio is derived based on data of $\tan\alpha \le 0.3$. The damping dissipation is underestimated for $\tan\alpha > 0.3$, thereby, the amplitude of rotation is overestimated. The period of free rocking depends on the amplitude of the motion; hence, errors of amplitude lead to an error of the phase of the motion.

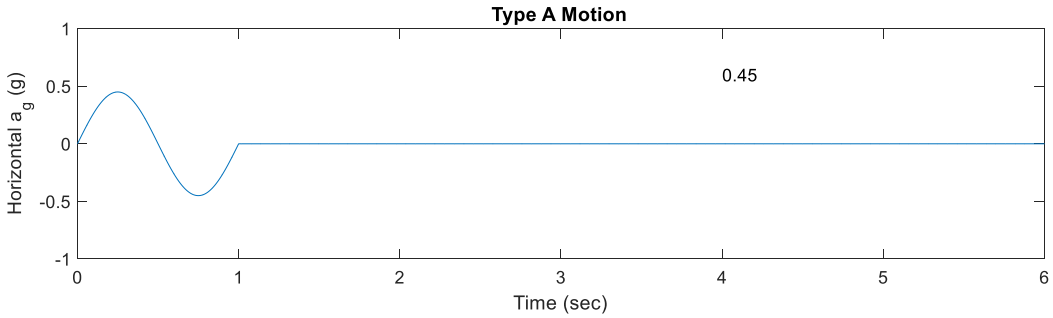

Figure 4.14. Type-A pulse excitation

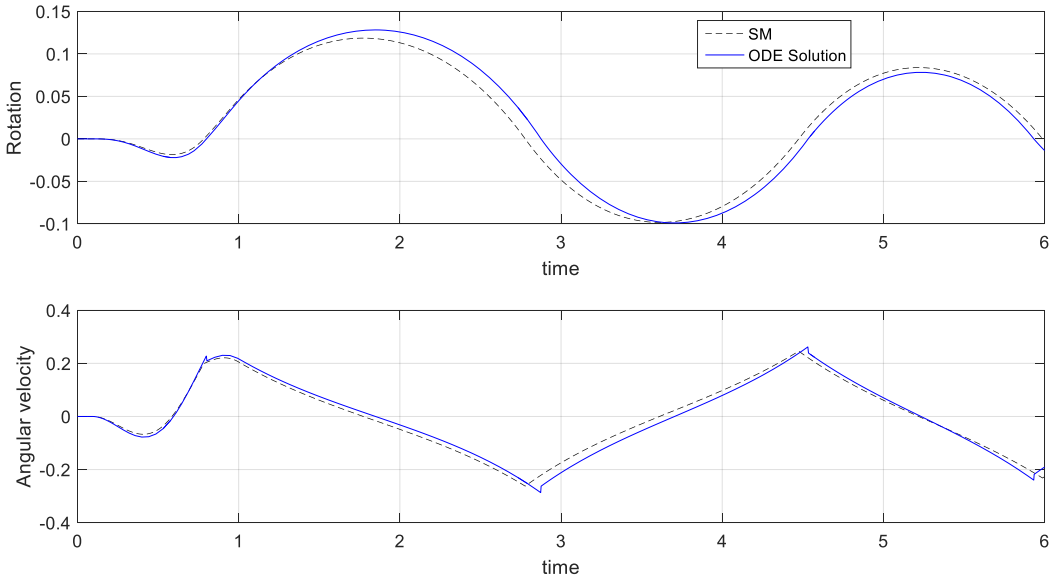

Figure 4.15. The rocking response of an 8m tall block with the slenderness $\tan\alpha = 0.25$ to a Type-A pulse excitation computed using the SM model and analytical model

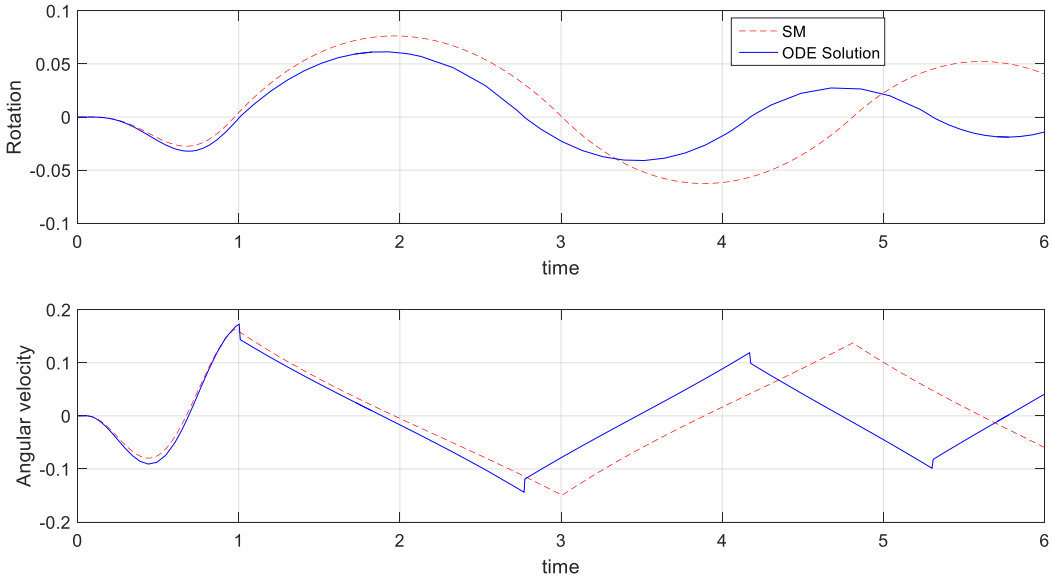

Figure 4.16. The rocking response of an 25m tall block with the slenderness $\tan\alpha = 0.36$ to a Type-A pulse excitation computed using the SM model and analytical model

(2) The deformable rocking body (DRB) model

As shown in Figure 4.17, the rocking body of DRB model is modeled using beam-element finite elements. The linear elastic beam-column is used for a rigid block; however, other beam-column finite elements are also valid for different cases. To represent the rocking of a rigid body, the values of Young's Modulus E_b should be set to sufficiently large. As mentioned before, rigid block's rotational inertia, $I_o = \frac{4}{3}mR^2$, refers to rotation about the corner of the rigid block and accounts for the rectangular shape of the rocking body. While the rotational inertia of the DRB, $I_o^{'} = \frac{1}{3}mR^2\cos^2\alpha + mR^2$, refers to rotation about the endpoint of the fiber section and does not account for the shape of the rocking body. Therefore, the DRB was modified by evenly distributing the rotational inertia difference $\Delta I_o = \frac{1}{3}mR^2\left(1-\cos^2\alpha\right)$ among the rotational DOF of the nodes used to model the column following an approach similar to the one describes in the SM model. Namely, a rotational mass equal to $\frac{\Delta I_o}{nnod}$ is added to the rotational DOF of each node in the finite element model.

The rigid rocking surface is modeled using the zero-length fiber cross-section element placed between node i and node j. If only considering the in-plane rocking motion, one row of fibers is sufficient to simulate the rocking surface. The fiber material is an elastic-no tension material, with an elastic response in compression and no resistance in tension to capture the uplift motion. Note that the stiffness of fibers, E_f, needs to be selected wisely. First, E_f is not numerically comparable to Young's modulus E_b of the beam-column element. E_f has units of [force]/[length]^3, while E_b has units of [force]/[length]^2. To simulate rocking of a rigid body on a

rigid surface, both E_f and E_b should be set to sufficiently large values. Secondly, E_f should be selected that increasing the stiffness of the rocking surface does not result in appreciable changes in the computed results. Lastly, the relative values of E_f and E_b should be selected that the impact forces deform the rocking body, not the rocking surface.

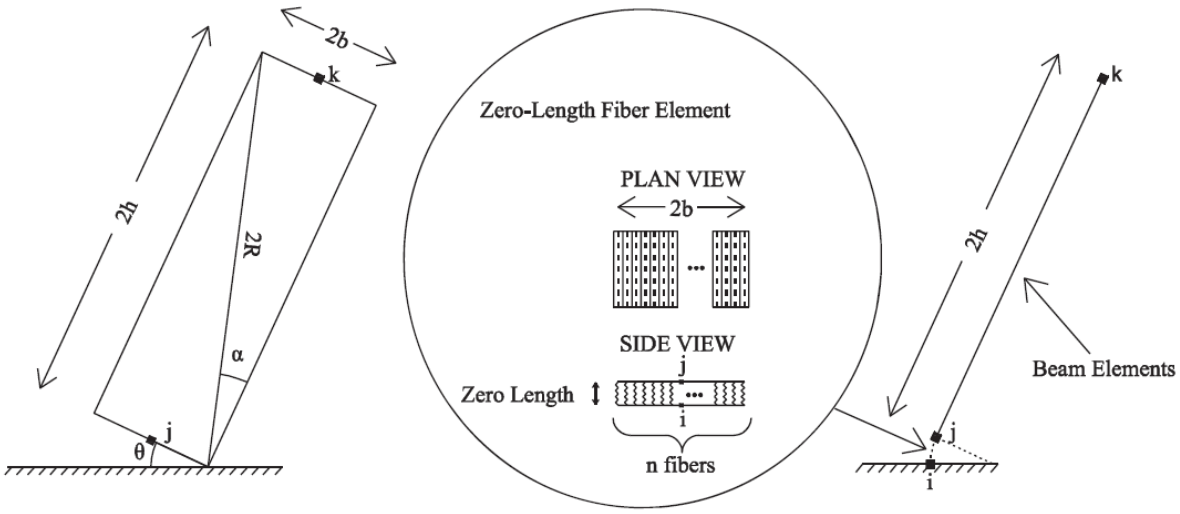

Figure 4.17. A solitary rigid block in rocking motion (left) and the DRB model (right) (Vassiliou et al., 2017)

The Corotational Coordinate Transformation (Argyris et al., 1964) is used for the DRB at each time step to account for the effect of large displacements and rotations that may occur during the rocking. A dissipative time-stepping integration procedure is used to numerically damp out the shock waves in the beam-column element to approximate energy dissipation caused by impact. The two most widely used dissipative time-stepping integration procedures are selected in this study. One is the Hilber-Hughes-Taylor (HHT) algorithm, and the other is the Newmark method. The HHT algorithm damps out the unwanted high-frequency components of the computed response without markedly affecting the low-frequency components, thus increasing the amount of numerical damping without degrading the order of accuracy (Hilber et al., 1977). Numerical

damping of the HHT is controlled by a dissipation factor α_d and the time integration step dt. For the Newmark method, numerical damping is controlled by factor γ, factor β, and the time integration step dt. However, numerical damping of Newmark also affects the lower modes and reduces the accuracy of the integration scheme from second order to first order.

Both HHT and Newmark integration algorithms are available in OpenSees. Note that, for the HHT algorithm, the dissipation factor α_d is defined differently in Hilber's paper (Hilber et al., 1977). $\alpha_d = \alpha_d' - 1$, where α_d is the dissipation factor used in the OpenSees implementation of the HHT integration algorithm, α_d' is that used in Hilber's paper. $\alpha_d = 1.0$ corresponds to the Newmark method and α_d should be between 0.67 and 1.0. The smaller the α_d the greater the numerical damping. For the Newmark algorithm, $\gamma > \frac{1}{2}$ results in numerical damping proportional to $\gamma - \frac{1}{2}$. The method is second-order accurate if and only if $\gamma = \frac{1}{2}$. The method is conditionally stable for $\beta >= \frac{\gamma}{2} >= \frac{1}{4}$. Achieving a good match in the rocking response time history requires that the energy dissipation calculated in the numerical integration in DRB model perfectly matches the analytical model.

As shown from Figure 4.19 to Figure 4.22, the rocking responses of a solitary free-standing block with $2b \times 2h = 4m \times 12m$ and material density of 25 ton/m^3 are computed using the analytical model in MATLAB, as well as the DRB model in OpenSees with different integration algorithms, timestep sizes and mech sizes. A recorded ground motion excitation, the Takatori 090 ground motion from the 1995 Kobe earthquake, is plotted in Figure 4.18. According to Vassiliou's paper (Vassiliou et al., 2017), $E_f = 30 \times 10^9$ kN/m^3 and $E_b = 30 \times 10^9$ kPa are selected to simulate rigid

body rocking on the rigid surface.

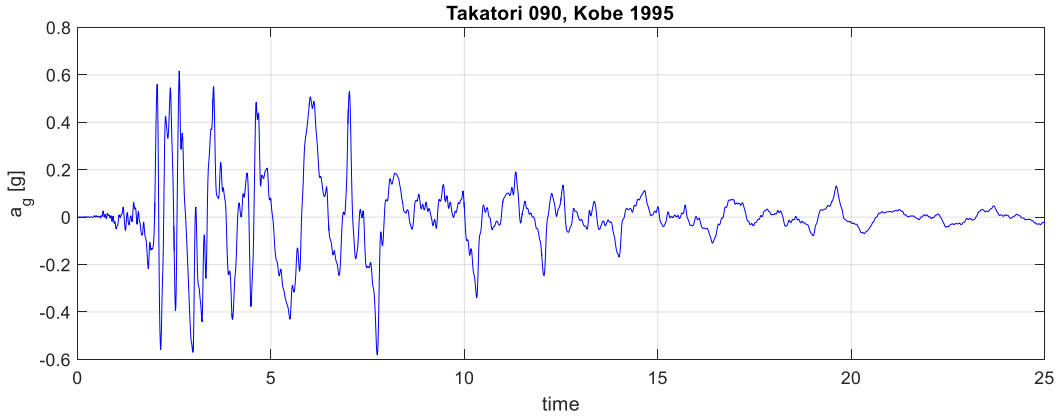

Figure 4.18. The Takatori 090 ground motion from the 1995 Kobe earthquake

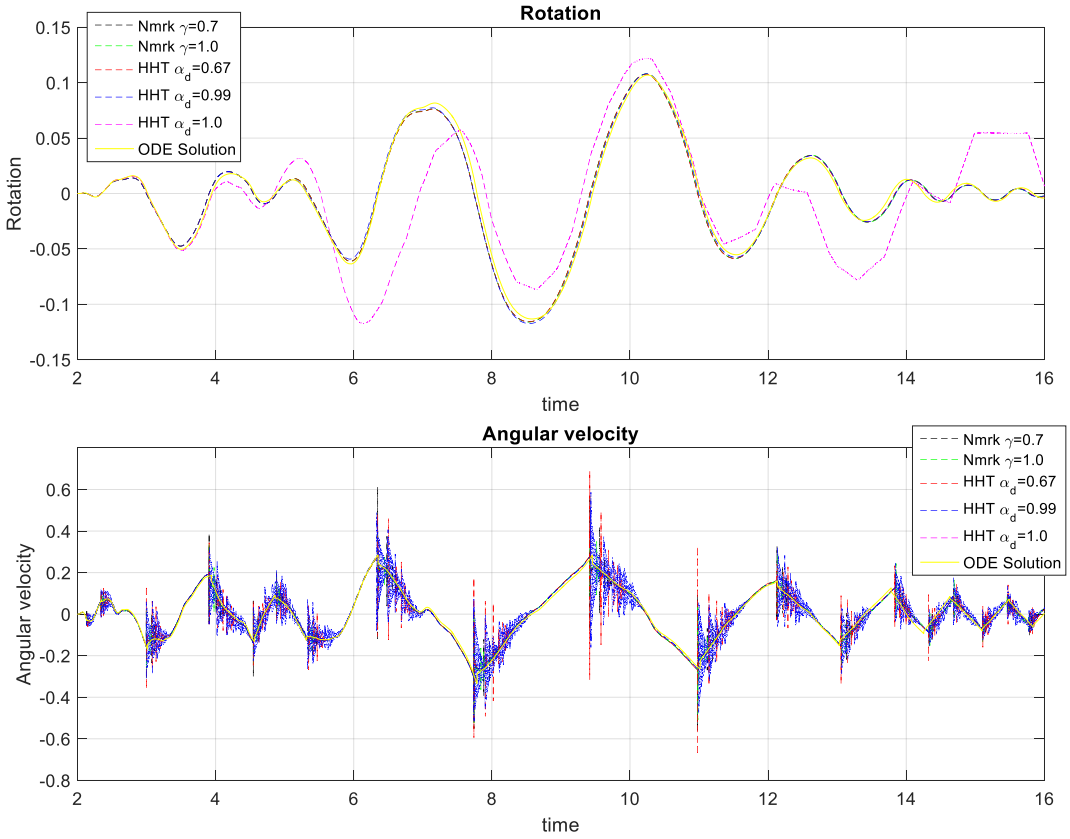

Figure 4.19. Demonstration of convergence for a recorded ground motion excitation (Takatori 090, Kobe 1995) for different time-stepping integration algorithm

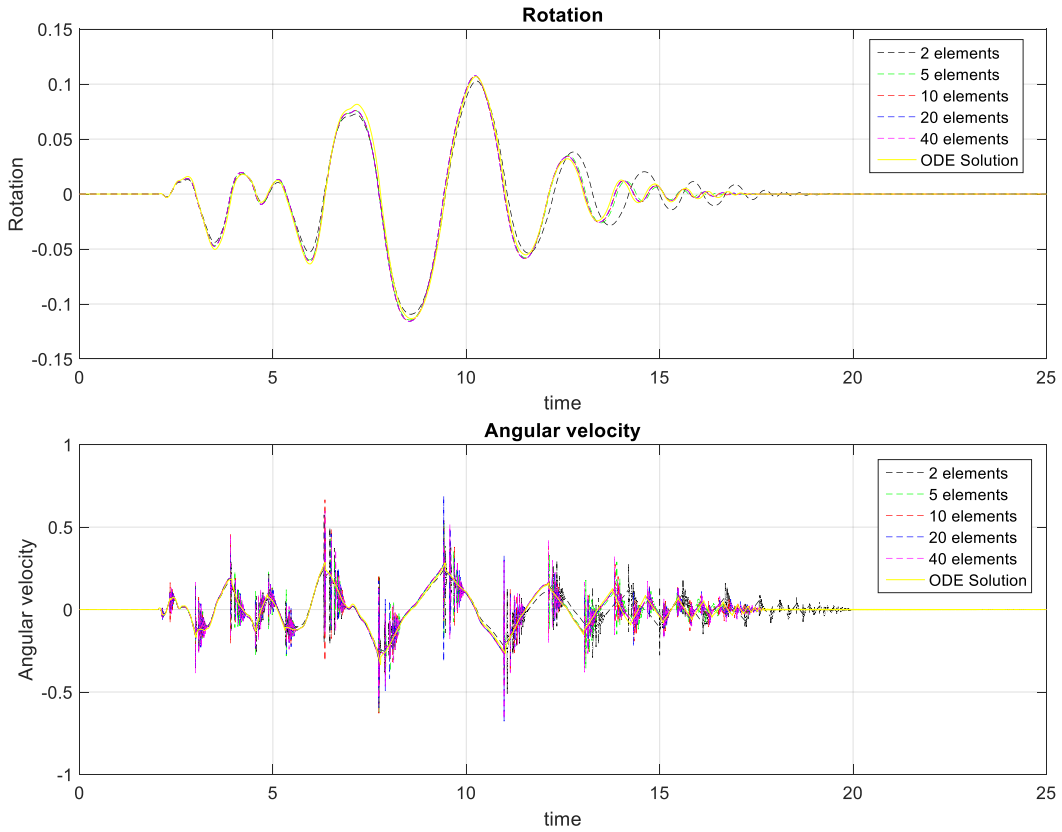

Figure 4.20. Demonstration of convergence for a recorded ground motion excitation (Takatori 090, Kobe 1995) for different element sizes

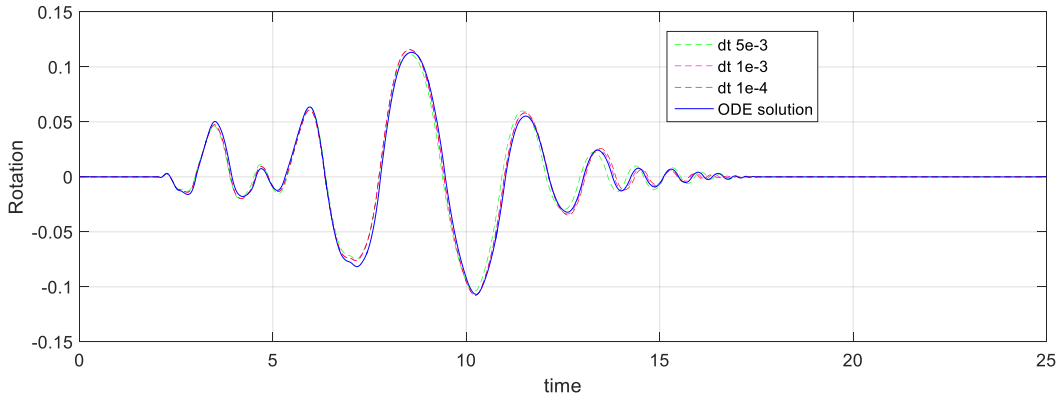

Figure 4.21. Convergence of rotation for a recorded ground motion excitation (Takatori 090, Kobe 1995) for different timestep sizes

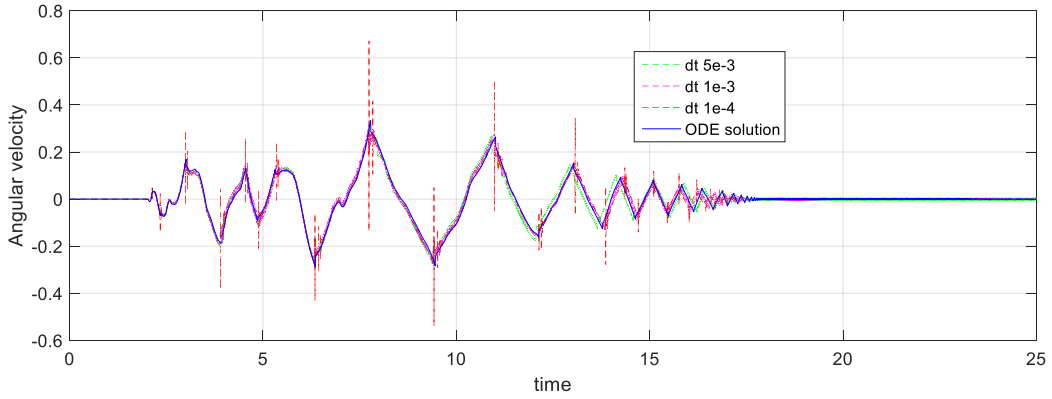

Figure 4.22. Convergence of angular velocity for a recorded ground motion excitation (Takatori 090, Kobe 1995) for different timestep sizes

From Figure 4.19, it can be concluded that: (1) both Newmark and HHT algorithm works well in this case; (2) the DRB model is not sensitive to the selected OpenSees numerical dissipation factor values for HHT if they are below 1.0. Results in Figure 4.20 reveals that the DRB model is not sensitive to the number of beam-column elements used to model the rocking body, which will save much more computation costs and make it possible to use DRB model in large scale structures. In this example, using five or more elements produces an essentially identical response. Figure 4.21 and Figure 4.22 indicate that the DRB model is not sensitive to the variation of the integration time step if it is reasonably short with the periods of the dominant motion components. A smaller time step size also saves much more computation costs.

As shown from Figure 4.24 and Figure 4.25, the parameter sensitivity analysis is conducted for the same DRB model excited by PEER strong motion database record, El Centro array #12, 140 (USGS station 931) with an amplification factor equals to 5, as shown in Figure 4.23. From Figure 4.24, it can be concluded that: (1) results for two different earthquakes reveal that the DRB works well for different earthquake; (2) both Newmark and HHT algorithm works well in this case; (3) different from the previous case, the DRB model is not sensitive to the selected OpenSees numerical dissipation factor values for HHT if they are below 0.95. From Figure 4.25, it can be

concluded that using five or more elements produces an essentially identical response.

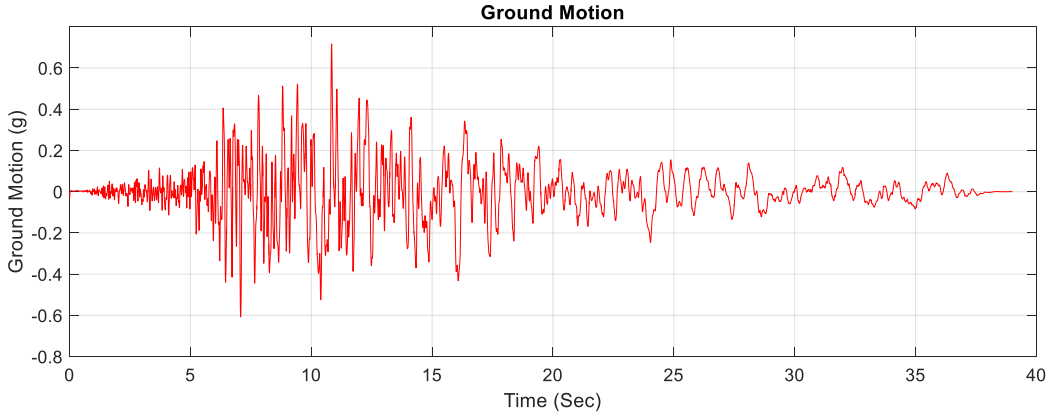

Figure 4.23. The PEER strong motion database record, El Centro array #12, 140 (USGS station 931) with an amplification factor equals to 5

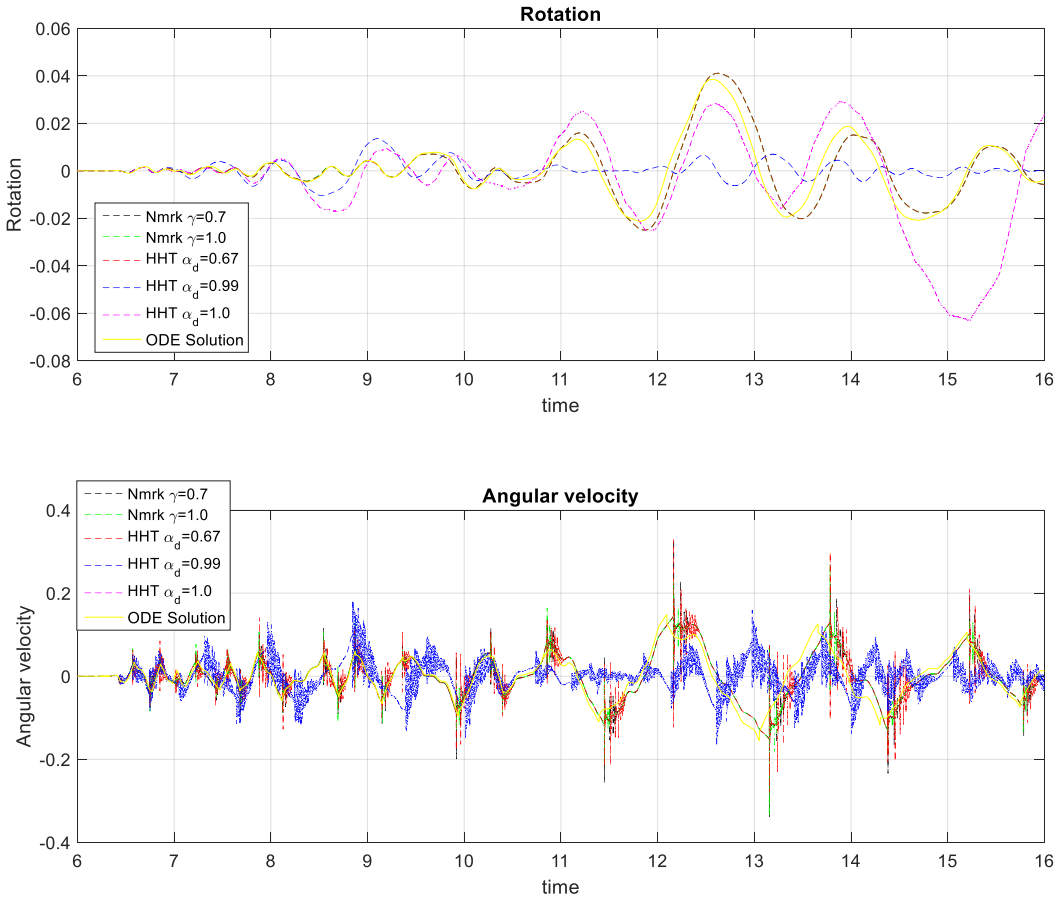

Figure 4.24. Demonstration of convergence for a recorded ground motion excitation (El Centro array #12) when using different time-stepping integration algorithm

Although the DRB model can provide a good prediction for rigid rocking responses without limitation of slenderness, the FE response is more sensitive to the model parameters than the SM model. First, the modulus of fiber material and beam-column elements need to be carefully selected. Second, tests on the value of numerical damping and the number of elements should be conducted to ensure the rocking response is converged.

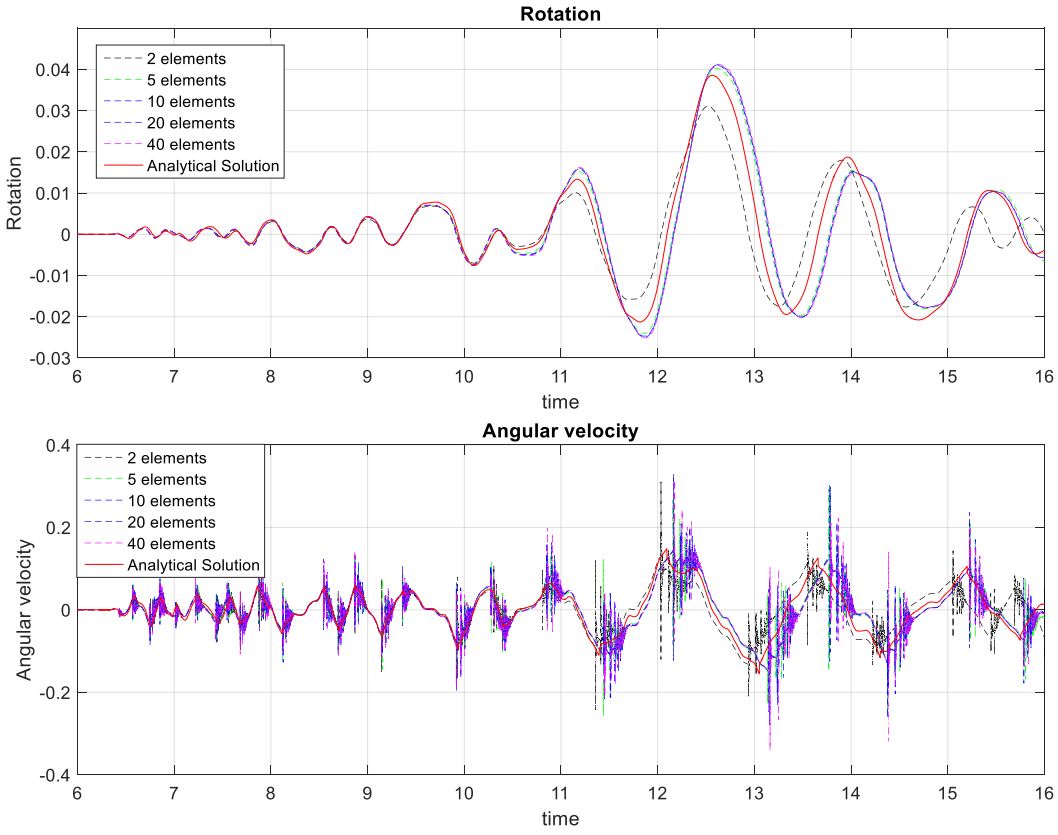

Figure 4.25. Demonstration of convergence for a recorded ground motion excitation (El Centro array #12) when using different element sizes

(3) Augmented DRB model for deformable rocking structures

As the rocking body becomes softer, the frequency of the generated shock waves during the impact will decrease. Thus, the amount of energy numerically damped by the dissipative time-stepping integration algorithms will diminish. Although the accuracy of the predicted rocking response will not be considerably affected when the deformations of the rocking body are still

small enough, the solution will diverge due to the presence of the undamped high-frequency components of motion. Namely, increasing the number of elements and decreasing the integration time step does not lead to a unique solution, as observed in Vassiliou's paper (Vassiliou et al., 2017).

To overcome the problem mentioned before, the DRB model is augmented by creating an alternate energy dissipation path, namely, considering the energy radiated into the ground under the rocking surface. The rocking body and rocking surface are preserved. At the same time, the supporting ground is modeled as a rigid massless foundation slab that rests on a stiff and dissipative ground (soil) surface, which is represented by a horizontal, vertical and rotational support, as shown in Figure 4.26 (left). An elastic spring and a viscous dashpot in each support are arranged in parallel. The rigid foundation slab does not uplift. Besides, sliding between the rocking body and foundation is not allowed. The finite element model of the augmented DRB model is shown in Figure 4.26 (right). Instead of using a fixed node of finite element model to model the stiff ground, a zero-length element with stiff springs and dashpots arranged in parallel in vertical, horizontal, and rotational directions is used to create an alternate energy dissipation path. Note, modeling of a rocking body on soft soil lies beyond the scope of this study, namely, the supporting ground (soil) is still stiff.

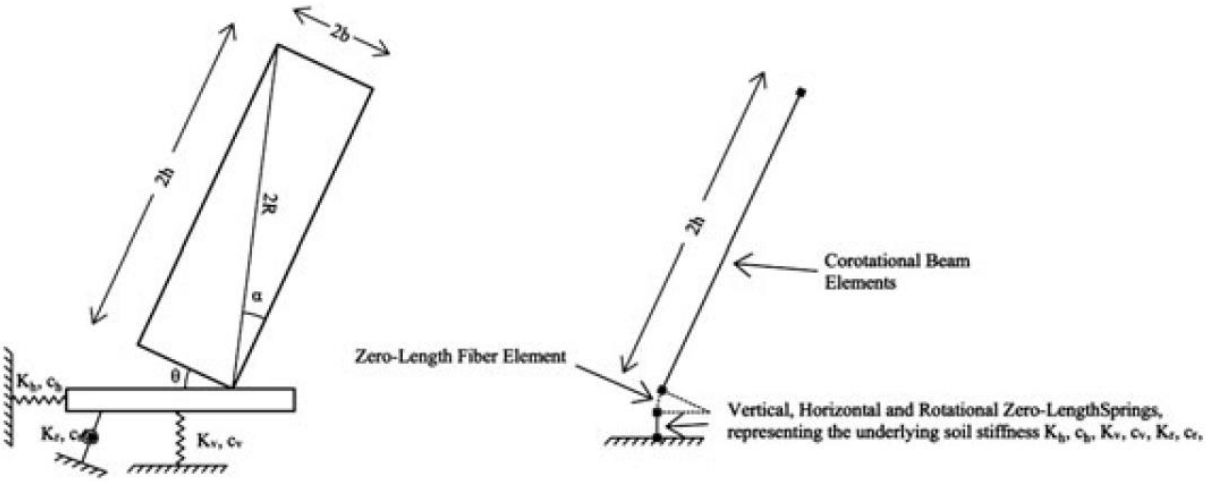

Figure 4.26. A rigid or deformable body rocking on a massless foundation supported by spring-dashpot support (left) and the augmented DRB model (right) (Vassiliou et al., 2017)

The spring stiffness K and dashpot damping coefficient C are determined according to machine vibration theory (Gazetas, 1983). Since the underlying ground is assumed stiff, the stiffness should be selected that increasing its value further does not change the natural vibration periods and modes of the structure. As verified in Vassiliou's paper (Vassiliou et al., 2017), for hard soils and structures as tall as 80m, the computed rocking response is insensitive to the values of damping coefficient of dashpot. Besides, that paper pointed out that increasing of the ground stiffness could be realized by increasing the shear wave velocity of the supporting ground, Vs, thus leading to convergence of the time history of column rotation. However, the column base moment may not be reliable.

(4) Evaluation of existing FE models

In order to evaluate the modeling of existing FE models, the results from the FE models are compared with the experimental data and analytical results. In this section, the SM, DRB and augmented DRB models (Vassiliou et al., 2014, 2017) are used to simulate the same rigid/ flexible bridge pier (Chen, 2017) with footing uplift described before. The experimental model is idealized

as a two degree-of-freedom system with mass concentrated at the top node, as shown in Figure 4.27. For FE models, $2b = 1.6\text{m}$, $2h = 3.32\text{m}$, the vibrational natural frequency of the column $w_n = 1/1.47\text{Hz}$, the Rayleigh damping ratio $\xi = 0.5\%$. The rocking column is modeled using 20 elastic beam column elements with area $A = \pi r^2$, second moment of area about the local z-axis $I_z = \frac{\pi r^4}{4}$, Young's modulus $E_b = \frac{K(2h)^3}{3I_z}$. The mass of the beam column elements is concentrated to the top node, as shown in Figure 4.27.

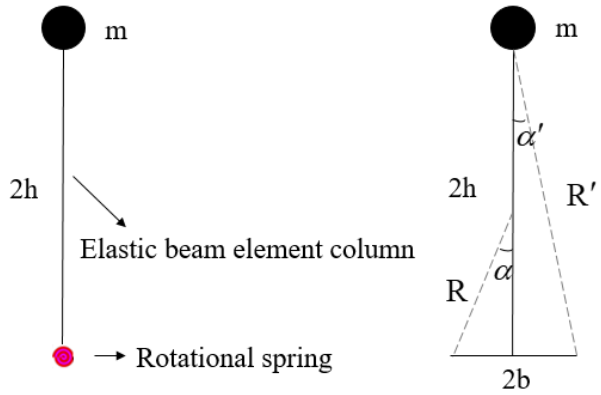

Figure 4.27. FE models with mass concentrated on the top

It is noted that the additional rotational moment of inertia ΔI_o of SM is changed. As shown in Figure 4.27, the moment of inertia of the experimental column rotating around the corner point of the foundation is $I_o = mR'^2 = m\left((2h)^2 + b^2\right)$, which is the same as that of DRB and augmented DRB model with mass concentrated on the top node. While for the SM, the moment of inertia refers to rotating around the endpoint of the rotational spring is $I_o = m(2h)^2$. Therefore, the difference $\Delta I_o = mb^2 = mR^2 \sin^2\alpha$ is added to the rotational degree of freedom of the top node. The E_s of rotational spring for SM is 30e6 kPa, the E_f of zero-length fiber section of DRBs is 30e9

kN/m^3, $dt = 0.0001$s, soil density $\rho = 2.5$ton/m^3, $V_s = 7000m/s$ is needed to represent the stiff ground under the rocking surface for the rigid structure, $V_s = 1000m/s$ is sufficiently large for the flexible structure.

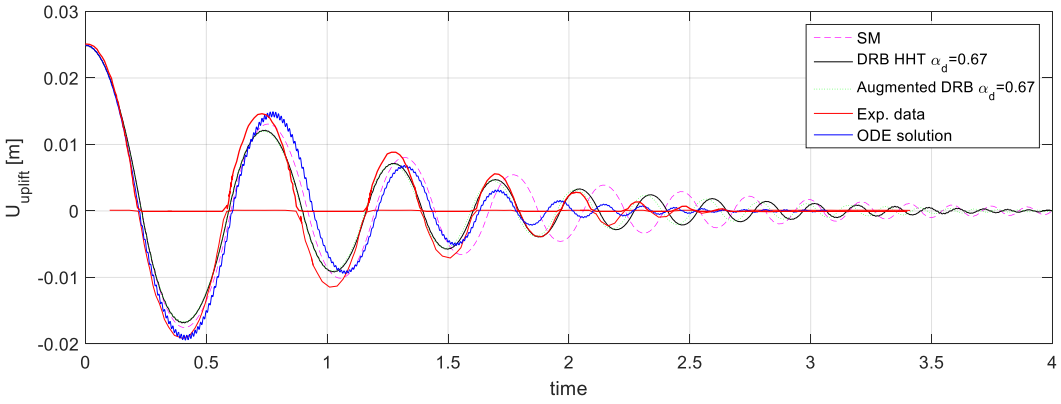

Figure 4.28. Uplift of rigid structure during free vibrations initiated by 25 mm

As shown in Figure 4.28, analytical and FE models work well for the rigid structure. Results reveal that:

(1) DRB and augmented DRB work better than the SM after 1.5sec. There is a phase shift for SM after 1 sec due to the slenderness $\tan\alpha = 1.6/3.32 = 0.48$. Since the equation for the damping coefficient is derived base on the data of $\tan\alpha < 0.3$, the SM is not as good in the less slender case because of the highly nonlinear nature of the rocking problem.

(2) The amplitudes of the uplift of FE models are slightly smaller than the experiment. Besides, there is no uplift after 2.6sec in experimental data. However, there is still a very small uplift in FE models but these differences within 5 mm seem acceptable.

Additionally, to validated the rocking behavior under forced vibration, the proposed analytical model, existing SM, DRB, and augmented DRB models (Vassiliou et al., 2014, 2017) are performed to simulate the rigid and deformable rocking bodies under the type-A pulse excitation and earthquake excitation, respectively. The responses of a rigid model, which is

identical to the model used in the reference (Zhang et al., 2019), and a deformable model, which is identical to the model in Chen's test (Chen, 2017), are calculated respectively.

The response of rigid block for type-A pulse excitation is plotted in Figure 4.29. It is observed that the results of FE models match well with the analytical model. Although only the results of the Newmark algorithm are shown here, the HHT algorithm also works when $\alpha_d = 0.67$.

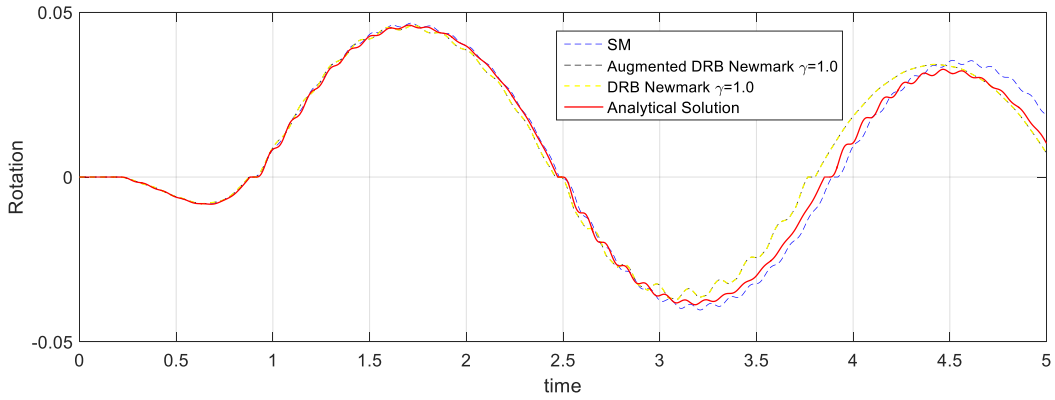

Figure 4.29. Comparison of rocking rotation subjected to type-A pulse excitation for $a_p/(g\tan\alpha)=1.30$, $w_n/p=11.9$, $w/p=5.1$, $\alpha=0.2$ and $\xi=0.005$ (a_p refers to the peak ground acceleration)

The responses of deformable column-foundation for an earthquake excitation, the same Takatori 090 ground motion from the 1995 Kobe earthquake shown in Figure 4.18, is plotted in Figure 4.30. It is observed that:

(1) All the results of all FE models match well with the analytical model. Although the rotation peak value around 7sec of DRB and augmented DRB is slightly larger than the analytical value (difference within 0.05), the peak value of the complete time history is well captured.

(2) Both SM and DRB models have a slight response fluctuation after 20 sec. However, the most critical part of response time history, i.e., from 5sec to 15sec, is well captured by all three models.

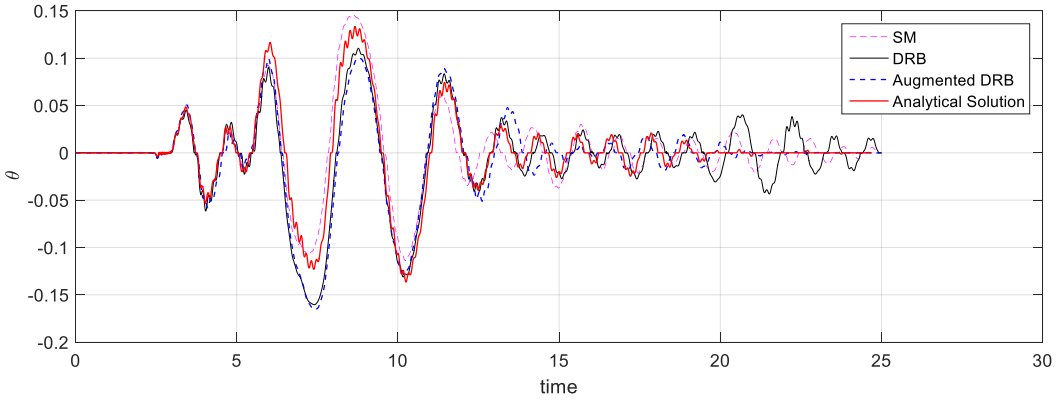

Figure 4.30. Comparison of rocking rotation subjected to earthquake excitation (Takatori 090, Kobe 1995)

As shown in Figure 4.31, the drifts of the column, u, defined in Figure 4.3 of different models are compared. u of FE models is computed using $u = u_{top} - H\sin\theta$, where u_{top} is the recorded total displacement of top node, $H\sin\theta$ represents the displacement due to rigid rotation caused by rocking. It is observed that:

(1) A high frequency fluctuation due to the elastic deformation of the flexible structure can be seen after each impact, especially in those episodes with large amplitudes. This vibration subsequently decays to near zero before the initiation of the next uplift phase. The drift fluctuation will disappear when the rocking rotation is near zero.

(2) The vibration of the drift of FE models decays faster than the analytical model. This may be due to the Rayleigh damping in the structure, which may cause the energy dissipation during the uplift phase of the structure to grossly increase, according to the experiments presented in Truniger et al. (2015).

(3) Although the drift is occasionally more or less overestimated or underestimated when using FE models, the peak value of drift is well captured.

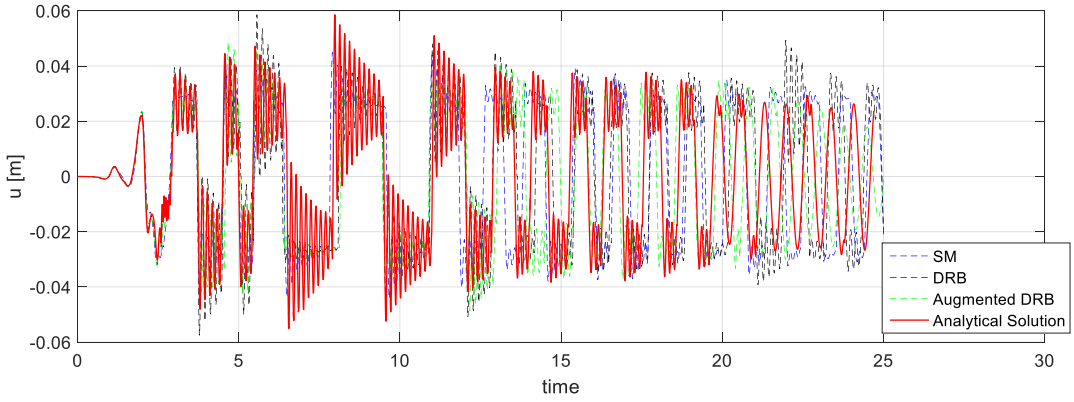

Figure 4.31. Comparison of the column's top drift u subjected to earthquake excitation (Takatori 090, Kobe 1995)

4.3.3 Zero-length Impact Rocking Model

According to the observation from previous comparison results, the modeling of flexible rocking behaviors using existing FE models is not accurate and sometimes not stable. This is mainly caused by the impact mechanism is not directly modeled, namely, viscous damping or numerical damping is used to approximate the energy dissipation during the impact. Besides, modeling energy dissipation is difficult if the deformation of the superstructure needs to be considered. Therefore, a better finite element model of rocking needs more intuitive modeling of the impact mechanism. To do so, a finite element based rocking model is implemented in OpenSees, consisting of a zero-length rocking element with a modified Dirac-delta type impact model.

The so-called "zero-length impact rocking element" is developed based on a modification of an earlier work (Acikgoz & DeJong, 2016). To improve the stability and convergency issue, modifications are derived in this study: (1) a complete energy dissipation cycle is adopted to capture the energy dissipation during impact, and to avoid dramatically changing of stiffness matrix which causes numerical issues; (2) The "zero-length impact element" is engaged with

rotational zero-length spring to model the uplift condition and rocking behavior. The modified Dirac-delta type impact model and implementation of the finite element model are introduced herein.

In finite element modeling in OpenSees, it is assumed that the rocking movement and phase transition can be captured by the modeling of rocking surface and structure components. Therefore, the zero-length impact element works to generate the impact force F_i and stiffness matrix K_i. In the Dirac-delta type impact model, as the structure approaches $\theta = 0$, an impact force F_i will act on the rigid foundation beam at the impending pivot point P′. This force applies moments counteracting the rocking, resulting in rotational decelerations that influence the elastic motion of the structure during the impact. After the phase transition at $\theta = 0$, the force is terminated as any forcing from the pivot point will no longer influence the moment equilibrium. This process is schematically illustrated in Figure 4.32. To maintain the numerical stability, the original model is modified that the impact force will gradually go to zero within a short time instead of a sudden drop to zero, thus the zero-stiffness matrix issue can be avoided.

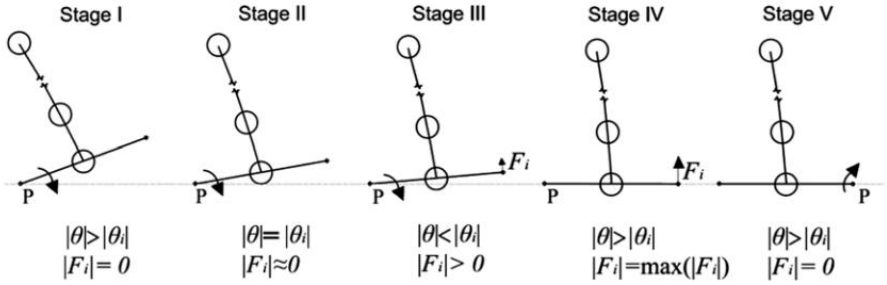

Figure 4.32. Schematic illustration of the applied impact forces for the modified Dirac-delta type impact model (Acikgoz & DeJong, 2016)

The impact force F_i is approximated by an amplitude scaled Gaussian function of the rocking angle θ. The Gaussian function is defined by a zero mean and a standard deviation of $n/\sqrt{2}$, where n is a width parameter of the Gaussian function that influences the sharpness of the

impact force. Independent of the value of n, when the unscaled Gaussian function is integrated over values of θ in the domain (-∞, +∞), a value of 1 is obtained. Using this property, the amplitude of the Gaussian function can be scaled to deliver an energy loss of $E_{ini}(1-r^2)$, where E_{ini} is the initial energy when impact happens, r is the coefficient of restitution. Then the impact force F_i has the following expression:

$$F_i(\theta) = \pm \frac{E_{ini}(1-r^2)}{2bn\sqrt{\pi}} e^{-\theta^2/n^2} \tag{4.32}$$

where b is half of rocking base width. A physically motivated approach is necessary for determining the width parameter n. It is assumed that the maximum impact force would be proportional to the angular velocity of the structure when impact forces are activated, which is denoted by $\dot{\theta}_i$. Additionally, considering the limit case of zero angular velocity, the maximum impact force on the corner can be considered bound by the static support force at rest position, $m_t g/2$, where m_t denotes the total mass of superstructure. These assumptions result in the following expression:

$$n = \frac{E_{ini}(1-r^2)}{2b\sqrt{\pi}(\frac{m_t g}{2} + C_p|\dot{\theta}_i|)} \tag{4.33}$$

where C_p is a proportionality constant that describes the relationship between $\dot{\theta}_i$ and F_i. Because this term relates to the mass and stiffness of the specific impacting surfaces, an empirical value for C_p needs to be determined to produce the best fit with the experimental results. Equation (4.33) depends on the system state at the moment of initiation of impact forces, as described by parameters E_{ini} and $\dot{\theta}_i$. Therefore, at each time step during the simulation of a rocking phase, conditions governing the initiation of the impact force need to be checked:

$$|\theta| < \theta_i = 2.576\left(\frac{n}{\sqrt{2}}\right), \quad \dot{\theta} < 0, \quad \dot{\theta}_i > \dot{\theta}_{min} \tag{4.34}$$

The first two conditions in Equations (4.34) ensures that the impact forces are only

activated at small rocking angles when the structure approaches impact. As a result, the impact forces do not interfere with large rocking motion. In particular, the coefficient 2.576 in the first condition describes the 99.5% confidence interval of the Gaussian function. This coefficient ensures that the specified amount of energy can be dissipated during the impact. The last condition sets a minimum angular velocity $\dot{\theta}_{min}$ to ensure numerical stability.

At every time step, n and θ_i are recalculated using the current system state, and conditions in Equations (4.34) are evaluated. When the rocking initiation conditions are not met, the impact forces will not be activated. When these conditions are satisfied at a particular time step, the specific values of E_{ini}, θ_i, $\dot{\theta}_i$ and n are fixed. Until the impact force is deactivated, these constant parameters are used alongside the current value of θ in the calculation of F_i with Equation (4.32). At each time step during the simulation of an impact phase, conditions governing the deactivation of the impact force needs to be checked:

$$|\theta| > 1.1\theta_i \tag{4.35}$$

The condition deactivates two phenomena: (1) The first phenomenon describes the system moves away from impact shortly after the initiation of forces. A constant coefficient of 1.1 has been arbitrarily specified to define this phenomenon. With reference to Figure 4.33, this case implies that impact forces are activated at Stage 2, but then the structure moves back towards Stage 1. (2) The second phenomenon describes the end of a complete rocking cycle. Then transition to a new full contact or rocking phase is automatically determined in the OpenSees model.

The effect of changing the value of modeling parameters on the function form of Equation (4.32) is illustrated in Figure 4.33. It can be observed that: A smaller r value or larger E_{ini} results in more energy dissipation; A smaller values of n are obtained for smaller rocking motion, resulting in sharper impact forces and smaller values for $\dot{\theta}_i$. A larger value of C_p results in a smaller value

of n and sharper impact forces. The parameters r and C_p can be designed to provide specific energy dissipation amount and impact force shape.

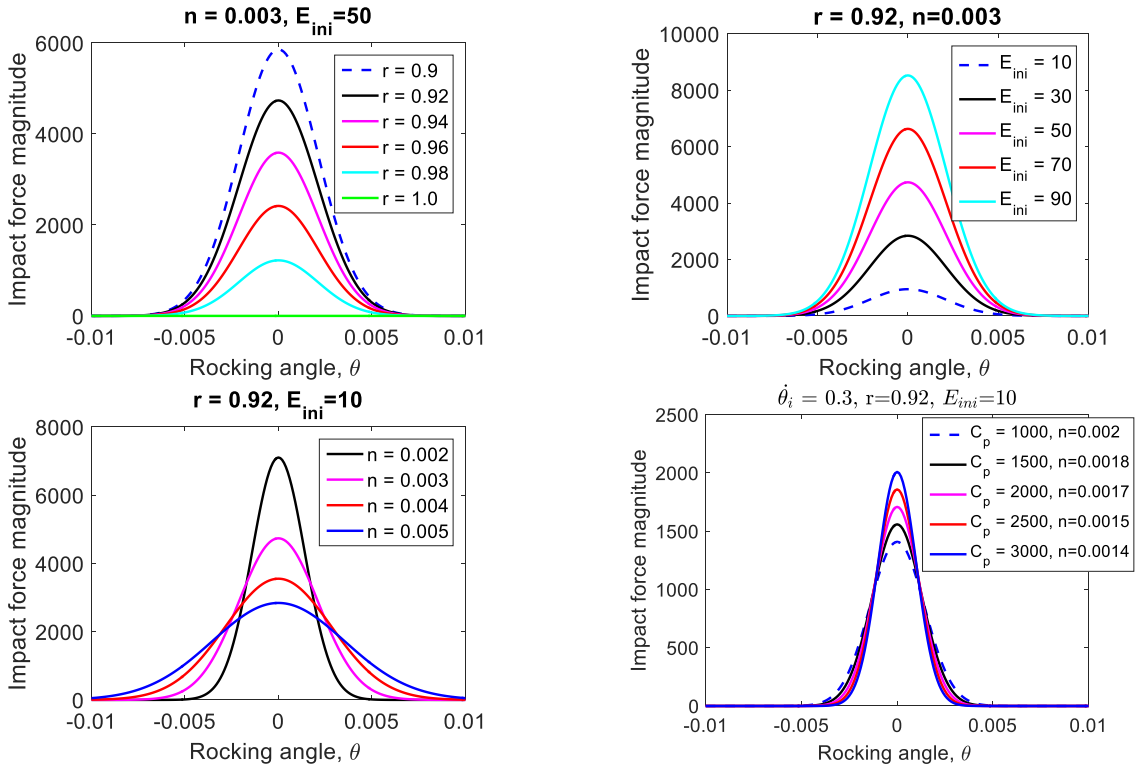

Figure 4.33. The effect of parameters on the shape of impact force

The following Figure 4.34 demonstrates the implementation of the zero-length element into OpenSees framework. The FE rocking element gets information from the nodal level, generates force and stiffness matrices, then passes the element resistance force and stiffness back to the structural level to form the residual force and solve the equation of motion. By directly taking the derivative of impact force to rocking angle θ in Equation (4.32), the rotational stiffness term can be determined by:

$$K_i = \frac{dF_i}{d\theta} = \frac{E_{ini}(1-r^2)}{2bn\sqrt{\pi}} e^{-\theta^2/n^2} \cdot \frac{-2\theta}{n^2} \tag{4.36}$$

Then the tangent stiffness needed in the zero-length element can be obtained by $K_i \frac{d\theta}{du}$, where u is the deformation of the rocking element that generates impact force.

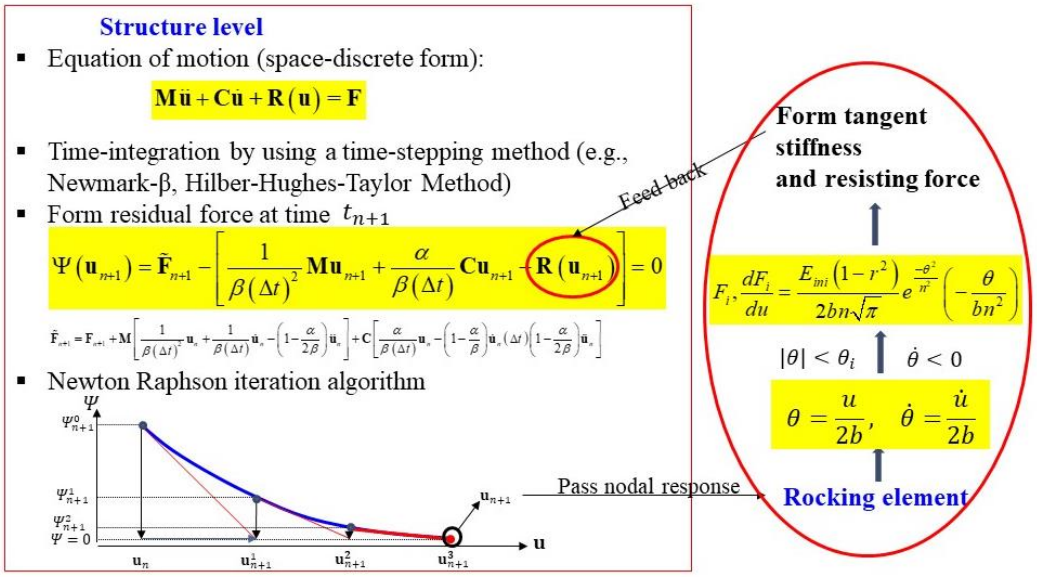

Figure 4.34. Implementation of FE rocking element

To model the rocking initiation of the structure, the implemented rocking element is engaged in a zero-length rotational spring, as shown in Figure 4.35. The uplift and close of the rocking gap are modeled by the elongation and shortening of the zero-length impact rocking element. The rocking initiation condition is the same as that of the SM model. Namely, a rotational moment and angle relation, as shown in Figure 4.6, is modeled by the zero-length rotational spring. Since the rocking about two pivot points is simulated by rocking about central rotational spring, the deformation u of the rocking element equals relative displacement between two pivot points. Then, the rotational angle θ is calculated by $\frac{u}{2b}$. Besides, a rotational mass equal to $\frac{\Delta I_o}{nnod}$ is added to the rotational DOF of each node along with the rocking component in the finite element model. For column-foundation type rocking component with lumped mass at top and base, such as bridge pier, $\Delta I_o = mb^2 = mR^2\sin^2\alpha$. For rectangular rocking components, such as a rocking shear wall, $\Delta I_o = \frac{4}{3}mR^2\left(1-\cos^2\alpha\right)$.

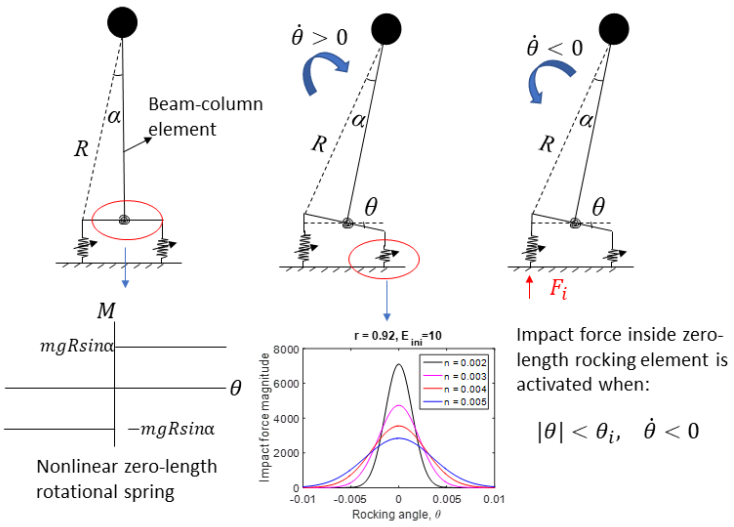

Figure 4.35. Modeling of rocking behavior in structural level

The user command of the zero-length impact rocking element is:

"ZeroLengthImpactRocking $tag $cNd $rNd $pNd $m_b $m_r $b $h $r_er $r_el $Cp $thetadot_min". The detailed explanation of each variable is shown below.

$tag	Unique element object tag
$tNd	Constrained node tag
$bNd	Retained node tag
$pNd	Pivot point tag
$m_b	Mass of foundation
$m_r	Mass of superstructure
$b	Half of rocking base width
$h	Height of rocking component. (Total height for column foundation system, half height for rectangular block)
$r_er	Restitution factor when impact happens at right pivot point
$r_el	Restitution factor when impact happens at left pivot point
$Cp	Cp value of impact force model
$thetadot_min	$\dot{\theta}_{min}$ of impact force model

The modified zero-length impact rocking model is also implemented in MATLAB and solved by ODE solver as a comparison in verifying the implementation of zero-length impact

rocking element in OpenSees. The stiff nature of the equations of motion resulted in the use of maximum time step limits. For computational efficiency, a minimum value of min(n) = 0.0001 was additionally specified. The phase transition conditions of the MATLAB model are the same as what were introduced in Dejong's model (Acikgoz & DeJong, 2016). A rigid column foundation model with b= 1.7m, h = 6.8m, m_r = 10kg, m_b = 0kg, r_er = r_el = 0.75, Cp = 1300kg*m/(rad*s), $\dot{\theta}_{min} = 0.01$ is obtained by using MATLAB model and OpenSees model. The rocking responses under type-A excitation with T = 1sec, ap = 0.4514g are shown in Figure 4.36. The same rocking responses obtained from the ODE solver and OpenSees model verified the assumption that the rocking initiation and rocking phase transition can be automatically captured in the OpenSees model by accurately model the moment rotation relationship of the rotational spring element, as well as mass and geometry properties of rocking components. Besides, it is observed that the impact force generated is also well captured. A slight difference may be due to different timestep used between the MATLAB model and the OpenSees model. The impact force of the MATLAB model has positive and negative value because the rocking angle can be positive or negative when directly solving the EOM using ODE solver. In the OpenSees model, the impact force always points up to dissipate energy.

The previous experiment of deformable cantilevers rocking on a rigid surface from Truniger (Truniger et al., 2015) is adopted hereby to verify the implemented "ZeroLengthImpactRocking" element. As shown in Figure 4.37, the rocking response of case "1HZ Short Base (10)" obtained by using the OpenSees model matches well with the shaking table test. In the OpenSees model, r_er=0.95, r_el = 0.97 and Cp=150kg*m/(rad*s) are selected so that the difference between FE response and test data can be minimized. The restitution factor r of rigid rocking with the same α as 1HZ short base case is 0.987, which can be used as a maximum

reference value for r_er and r_el.

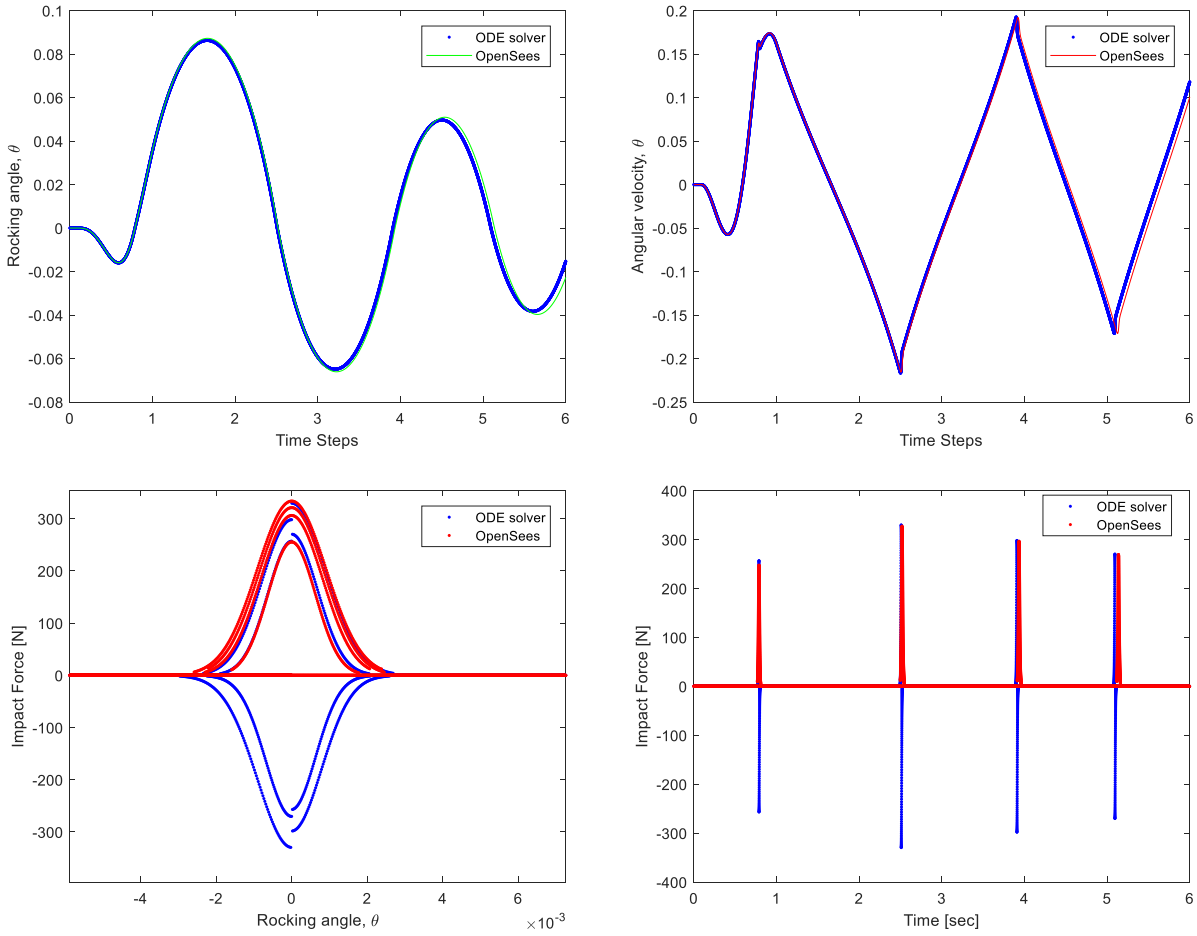

Figure 4.36. Validation of rocking phase transition in OpenSees model

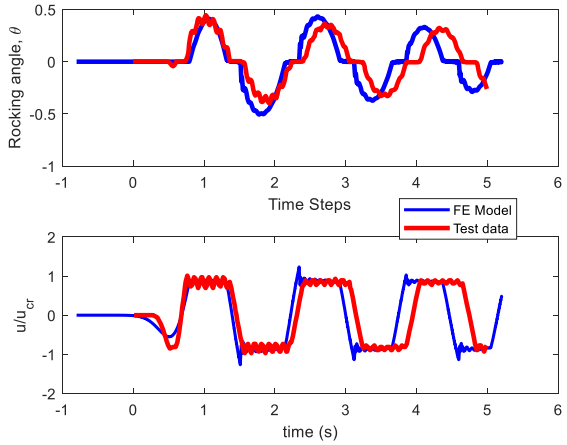

Figure 4.37. Comparison of flexible rocking case

4.4 PROBABILISTIC SEISMIC DEMAND MODEL (PSDM)

4.4.1 Background

Response results from previous studies revealed substantial sensitivities in rocking responses with respect to structural flexibility, treatment of rocking impact, and consideration of boundary conditions at the rocking interface. To capture the uncertainties in predictions from numerical models, the probabilistic seismic demand model (PSDM) can be an alternative way. This study is in response to the PEER blind prediction contest of shaking table tests for the seismic response of a rocking podium structure. Two different modeling schemes have been developed to predict the rocking responses of the test specimen under various earthquake ground motions. First, a 3D wobbling and rocking model based on Vassilou (2018) was implemented in MATLAB using a slightly different numerical treatment of solution when the uplift angle approaches zero. The second model is a high-fidelity finite element model developed in ABAQUS with all constitutive components being realistically modeled. In particular, responses from the ABAQUS model when subjected to small motions are found to be dominated by the sliding mode, resulting in unrealistic predictions that are sensitive to the assigned friction coefficients at the interface.

To capture the uncertainties in predictions from numerical models, the probabilistic seismic demand model (PSDM) was developed by evaluating the responses from the 3D MATLAB model under 800 scaled earthquake ground motions. The PSDM analysis demonstrates a reasonable correlation of the displacement response with the earthquake intensity, PGA, although noticeable variation can be observed. Based on PSDM results, the responses for 200 testing ground motions are re-predicted with randomly introduced variation and the mean response from PSDM. Additionally, the average response is taken between the responses from the ABAQUS model under large motions with that of the responses of the 3D MATLAB model. The cumulative distribution

functions (CDFs) are generated and compared using the predictions from PSDM and the average responses, which show very similar trends. Finally, the predictions from the PSDM are selected as the final results for test predictions.

4.4.2 PEER Center Shaking Table Tests

Seismic performance of rocking structures has long attracted the attention of the research community (Makris, 2014). Rocking isolations have shown great promise of improving the seismic resilience of civil structures by limiting forces, permanent displacements, damage, and cost. In this regard, the PEER center at the University of California, Berkeley is organizing a blind prediction contest to predict the peak bi-directional seismic responses of a four-column rocking podium excited by artificially generated ground motions applied by a shaking table. Such a blind prediction contest would allow the research community to be aware of the existence of public data on shaking table tests of three-dimensional rocking structures. It also enables different research teams to verify their analytical and/or numerical modeling techniques in simulating rocking behaviors under a wide range of ground motions, and to understand and capture the salient features associated with rocking dynamics.

The shaking table tests feature a rocking podium that was excited through the 6-dof shaking table located at the Earthquake and Large Structures (EQUALS) Laboratory of the University of Bristol. The rocking podium structure was designed by the ETH Zurich team, as shown in Figure 4.38. The tested model consists of four hollow circular steel columns with height, diameter and thickness of 1000, 244.5, and 8mm, respectively. Each of the columns was placed on the restrainer with conical end to limit the columns from wobbling out of their original position. 200 sets of 3D ground motions, correspond to tests EC1-EC100 (EC: El Centro) and tests CC1-CC100 (CC: Chi-Chi), measured on the shaking table surface were used here to investigate the seismic responses

("PEER Blind Prediction Contest," 2019). Each group has x-y-z entries, and the time interval and duration are 2.0×10^{-3}s and 45s, respectively.

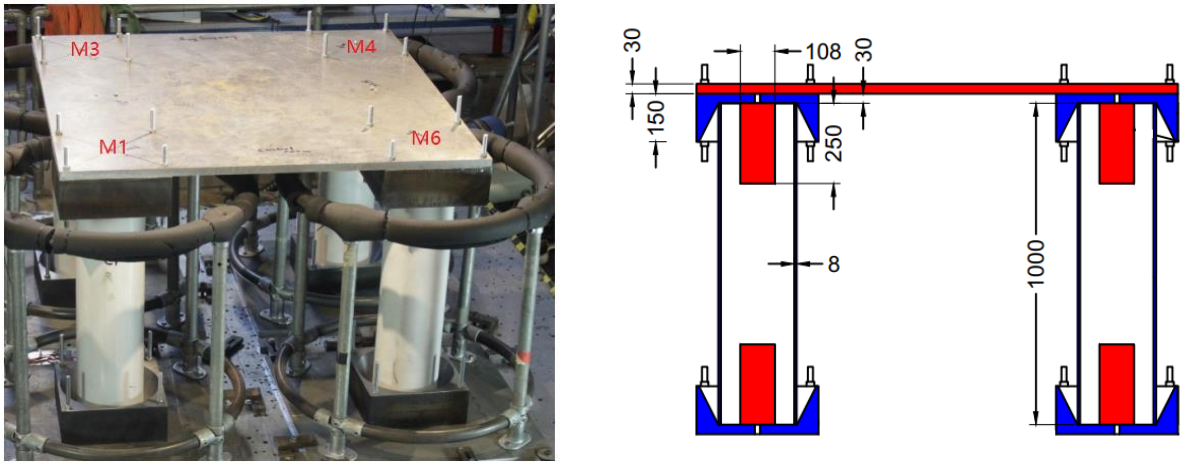

(a) Specimen (b) Section view

Figure 4.38. Specimen and section view of specimen

The displacement prediction of the vertical projection of each column center to the top surface for each of the 200 conducted tests are provided in the blind test:

$$\mathrm{M}_{ave} = \max_{t}\left[abs\left(\frac{\mathrm{M}_1(t)+\mathrm{M}_3(t)+\mathrm{M}_4(t)+\mathrm{M}_6(t)}{4} \right) \right] \tag{4.37}$$

where M1 to M6 are the displacements of the points marked in Figure 4.38(a) in the horizontal plan.

4.4.3 Numerical Models of the Rocking Podium

Considerable modeling efforts have been made in previous studies to investigate the rocking behaviors for various types of rocking structures, including free-standing rocking blocks (Zhang & Makris, 2001), two-dimensional (2D) rocking frames (Makris & Vassiliou, 2013), three-dimensional (3D) rocking bodies (Vassiliou et al., 2017), flexible rocking structures (Vassiliou et al., 2017), as well as rocking elements coupled with other structural components (Palermo et al., 2005). A comprehensive literature survey has been conducted herein, indicating that the analytical

model developed by (Vassiliou, 2018) for the 3D rocking podium is consistent with the shaking table test setup (as shown in Figure 4.39). Therefore, this model was adopted and implemented in MATLAB. However, as will be discussed later, modifications have been made on this model in dealing with the rocking impact (i.e. when uplift angle approaches zero). In addition, a high-fidelity 3D ABAQUS model with brick elements and surface-to-surface contact was also developed as the second case. The use of multiple models results from the fact that seismic rocking behavior is extremely sensitive to the imperfection of the specimen, the variation in initial conditions, as well as different modeling considerations (Bachmann et al., 2018).

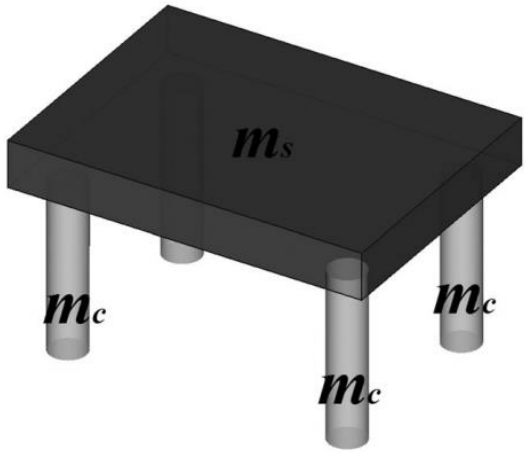

Figure 4.39. Illustration of the 3D podium structure (Vassiliou, 2018)

(1) 3D rocking podium model

Equations of motion for the 3D rocking podium under ground motion excitation was proposed by Vassiliou (Vassiliou, 2018). Based on several analytical assumptions in the 3D model of a free-standing rigid cylinder (Vassiliou et al., 2017), the model has two degrees of freedom: the tilt angle, θ, and the rolling angle, φ, which determines the location of the contact point between the cylinder and the supporting plane. The parameter $\gamma = m_s/(Nm_c)$ is introduced to normalize the mass between the rigid slab and N rocking columns, where m_s and m_c are the mass of the slab and one rocking column, respectively. The position vector of the center of mass, S, is given by:

$$\mathbf{r}_{O'S} = \begin{bmatrix} u_{gx} \\ u_{gy} \\ 0 \end{bmatrix}_{XYZ} + b \cdot \begin{bmatrix} (1-\cos\theta)\cdot\cos\varphi \\ (1-\cos\theta)\cdot\sin\varphi \\ \sin\theta \end{bmatrix}_{XYZ} + h \cdot \begin{bmatrix} \cos\varphi\sin\theta \\ \sin\varphi\sin\theta \\ \cos\theta \end{bmatrix}_{XYZ} \tag{4.38}$$

where u_{gx} and u_{gy} are the two horizontal components of the ground motion. Using Lagrange's energy method, the equations of motion for the 3D rocking podium can be derived as (Vassiliou, 2018):

$$\ddot{\theta} = -\hat{p}^2\left(\sin(\alpha-\theta)+\cos(\alpha-\theta)\left(\frac{\ddot{u}_{gx}}{g}\cos\varphi+\frac{\ddot{u}_{gy}}{g}\sin\varphi\right)\right) + \dot{\varphi}\begin{pmatrix} \sin\theta\sin^2\alpha\left(4\gamma+\frac{3}{2}\right)+\cos\alpha\sin\alpha\,(4\gamma+1)\left(1+\cos\theta-2\cos^2\theta\right) \\ +\sin\theta\cos\theta\left(\frac{4}{3}\cos^2\alpha-\frac{5}{4}\sin^2\alpha+4\gamma\left(\cos^2\alpha-\sin^2\alpha\right)\right) \end{pmatrix}\frac{12}{48\gamma+15+\cos^2\alpha} \tag{4.39}$$

$$\begin{pmatrix} \left(\frac{4}{3}\cos^2\alpha-\frac{5}{4}\sin^2\alpha+4\gamma\left(\cos^2\alpha-\sin^2\alpha\right)\right)\cdot\sin^2\theta+ \\ (3+8\gamma)(1-\cos\theta)\sin^2\alpha+2\sin\alpha\cos\alpha\sin\theta(1+4\gamma)(1-\cos\theta) \end{pmatrix}\cdot\ddot{\varphi}$$

$$+\begin{pmatrix} (3+8\gamma)\sin^2\alpha\sin\theta+\left(\frac{8}{3}\cos^2\alpha-\frac{5}{2}\sin^2\alpha+8\gamma\left(\cos^2\alpha-\sin^2\alpha\right)\right)\sin\theta\cos\theta \\ +2\cos\alpha\sin\alpha\,(1+4\gamma)\left(2\sin^2\theta+\cos\theta-1\right) \end{pmatrix}\cdot\dot{\varphi}\cdot\dot{\theta} \tag{4.40}$$

$$=(2\gamma+1)\left(\sin\alpha+\sin(\theta-\alpha)\right)\frac{\left(\ddot{u}_{gx}\sin\varphi-\ddot{u}_{gy}\cos\varphi\right)}{R}$$

where R and α are semi-diagonal and slenderness of the rocking column; $\hat{p}^2 = \frac{12(2\gamma+1)}{48\gamma+15+\cos^2\alpha}\frac{g}{R}$;

It is worth mentioning that Equation (4.40) cannot deal with the condition when θ approaches 0, such as the initial condition and the rocking impact. To deal with this issue without manually forcing any discontinuity on the equations of motion, an asymptotic equation is derived by applying the limit conditions of $\sin\theta\approx\theta$ and $\cos\theta\approx1$ when $\theta\to0$. As such, Equation (4.40)

can be updated as:

$$\begin{aligned}&\left(\left(3+8\gamma\right)\sin^2\alpha+\frac{8}{3}\cos^2\alpha-\frac{5}{2}\sin^2\alpha+8\gamma\left(\cos^2\alpha-\sin^2\alpha\right)\right)\cdot\dot{\varphi}\cdot\dot{\theta}\\&=\left(2\gamma+1\right)\cos\alpha\frac{\left(\ddot{u}_{gx}\sin\varphi-\ddot{u}_{gy}\cos\varphi\right)}{R}\end{aligned}\tag{4.41}$$

Equation (4.41) provides a new form of equation that can effectively substitute the original Equation (4.40) when θ approaches 0. Essentially, Equation (4.41) is theoretically sound as it provides a limit condition-based formula to quantify the system behavior without contradicting the mechanics that was initially held. Furthermore, it does not require any manual interruption on the system's equations of motion every time when θ approaches 0 during the numerical implementation.

Although few impact may occurs, a conservative coefficient of restitution approach by Housner (Housner, 1963) is used to consider the energy dissipation:

$$\sqrt{r}=\frac{\dot{\theta}_2}{\dot{\theta}_1}=1-\frac{\sin^2\alpha}{\frac{5}{8}+\frac{1}{24}\cos^2\alpha}\tag{4.42}$$

where $\dot{\theta}_1$ and $\dot{\theta}_2$ are angular velocities right before and after impact. This 3D rocking model is implemented in MATLAB and solved using ODE solver. This model is termed as the MATLAB model in this study.

(2) ABAQUS Model

A second 3D finite element model was built in ABAQUS to represent the testing rocking structure, as shown in Figure 4.40. The credit of modeling and analysis of the ABAQUS model should go to Zhenlei Jia, one of the team members from Beijing University of Technology for this PEER blind prediction contest. 3D linear brick elements with reduced integration (C3D8R) were used to model all constitutive parts. Table 4.1 lists the parameters for the elastic materials used in

the model. To bear a proper balance between computational efficiency and model accuracy, local mesh size of the rocking interfaces was set finer than the other parts, as is shown in Figure 4.40.

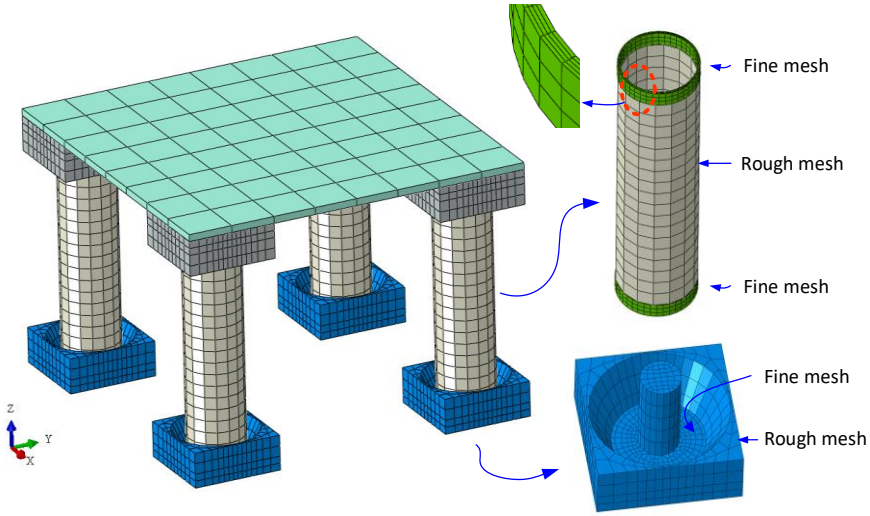

Figure 4.40. Finite element model in ABAQUS

Table 4.1. Property of the Materials Considered in the ABAQUS Model

Materials	Density (ton/mm^3)	Young's Modulus (MPa)	Poisson ratio
Steel	7.8e-9	200000	0.3
Aluminum	2.7e-9	69000	0.34

To simulate the rocking behavior between columns and steel footings, contact pairs were modeled by a surface-to-surface contact algorithm. The contact pair definition in ABAQUS consists of two parts: behavior in the normal direction and the tangential direction. The hard contact algorithm, which is based on the classical Lagrange multiplier method of constraint enforcement, was adopted in the normal direction. The penalty friction was used to simulate the tangential effect with a coefficient of 0.15. Gravity was first applied on the model, and then dynamic-implicit procedure in ABAQUS was utilized to calculate the dynamic response of the specimen. Acceleration on the three direction was applied on the bottom of the steel footings.

(3) Simulation results

According to the structural drawings of plan and section view of specimen, modeling parameters used in 3D MATLAB model are base radius $b = 122.25\text{mm}$, height $2h = 1000\text{mm}$, size $R = \sqrt{b^2 + h^2} = 514.7\text{mm}$, slenderness $\alpha = \tan^{-1}(b/h) = 0.24$ and mass ratio $\gamma = 3.214$. Ground accelerations in *x* and *y* direction are applied simultaneously in the 3D MATLAB model. The bi-axial displacement is obtained by $u = \sqrt{u_x^2 + u_y^2}$, where u_x and u_y can be obtained by using Equation (4.38). In 3D MATLAB model, since all columns are considered to be moving identically and they are assumed to be always in contact with the support and no sliding is allowed, it is determined that there is no rotation coupled with the horizontal translation. Therefore, all columns and the slab undergo identical motion, thus, $\mathrm{M}_{ave} = \max_t \left[abs(u) \right]$.

Figure 4.41 shows ABAQUS model results for the displacement time history responses at M1, M3, M4, and M6. It can be seen that displacements at M1, M3, M4, M6 are almost the same, namely columns are under identical movement and yaw of cap slab is not observed. Note that this phenomenon actually contradicts to the test results, which have shown some levels of slab torsion in the recorded movie. As previously mentioned, such discrepancy comes from the inherent significant sensitivities of the dynamic rocking behaviors. Specific actions will be proposed in this study to tackle such sensitivity and randomness associated with the rocking podium.

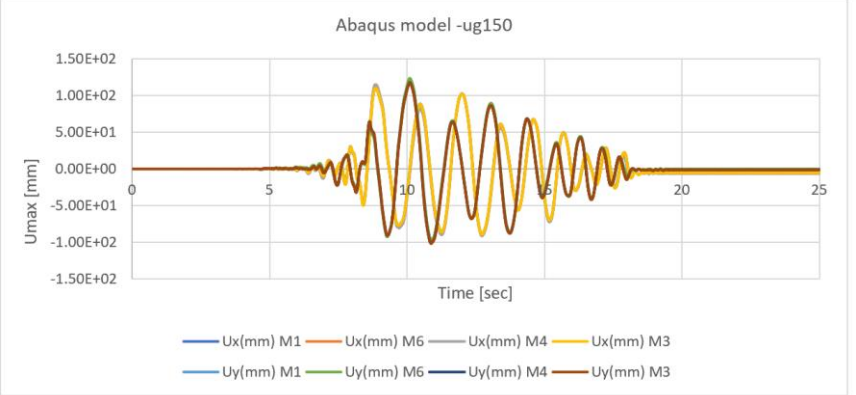

Figure 4.41. Displacement history of ABAQUS model under ground motion 150 excitation

Figure 4.42 compares the responses between ABAQUS and MATLAB 3D models for the testing structure under ground motion #120. It is observed that the 3D MATLAB model yields larger displacement than that of the ABAQUS model in this case. However, there are plenty other cases that the trends are reversed. The results demonstrated the sensitivity of responses due to different modeling methods.

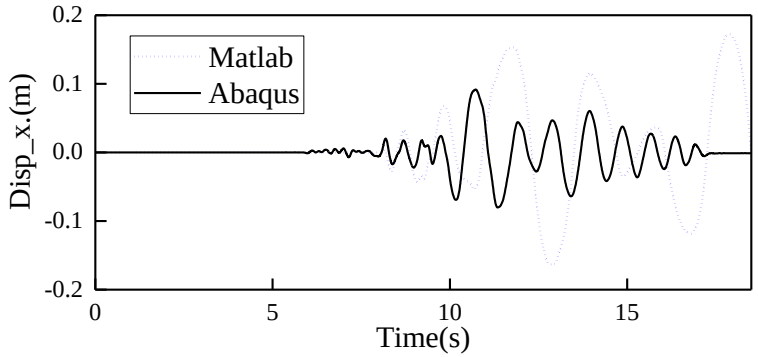

(a) X-direction

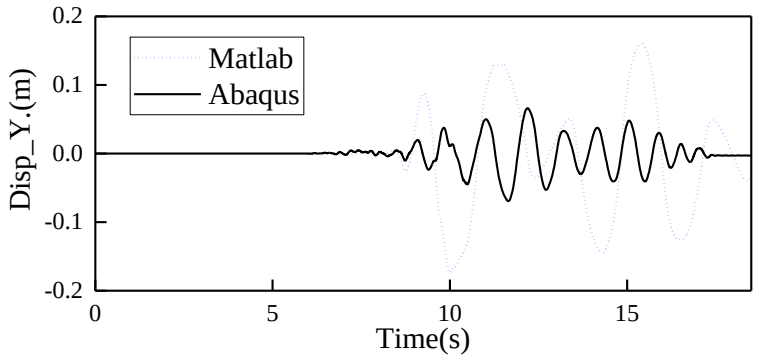

(a) Y-direction

Figure 4.42. Comparison of ABAQUS model and MATLAB model under ground motion 120

4.4.4 Probabilistic Seismic Demand Analyses

Both the MATLAB and ABAQUS models are used to simulate the rocking responses when subjected to the given 200 ground motions. However, due to the required long running time of simulation, only 98 simulations have been completed using the ABAQUS model. To compensate

this limitation, the 98 cases in ABAQUS were randomly selected to cover a similar level of variances embedded in ground motions. Results of M_{ave} from both the MATLAB and ABAQUS models are provided in the appendix. Note that based on the geometry, an upper bound displacement of 315mm is assigned on the MATLAB model when columns hit the restrainer.

As reflected from the simulation results, rocking responses can hardly be the same should a different modeling scheme is used. Rocking dynamics are substantially affected by several modeling considerations, including rocking impact, boundary conditions, response solvers, etc. Moreover, as revealed in the testing movie, the same rocking columns cannot yield consistent responses under the same set of ground motions. In other words, repeatability can be a significant challenge for shaking table tests of rocking structures (Bachmann et al., 2018). To this end, this study will tackle the very sensitive rocking responses in a probabilistic manner.

First, it has been observed that the given 200 ground motions mainly come from two earthquake records with discrete levels of intensity measures. As such, 600 additional ground motions are generated by scaling the original set of 200 motions. In particular, 300 ground motions were obtained by scaling up 1.5, 2.0, and 2.5 times of the original El-Centro records, whereas the remaining 300 ground motions were generated by scaling down 1.5, 2.0, 2.5 times of the original Chi-Chi records.

800 sets of time history analyses have been conducted using the 3D MATLAB model. For the purpose of revealing the physical trend between the rocking demand and the ground motion intensity measure, probabilistic seismic demand model (PSDM) have been developed using the following form:

$$S_D = a\ IM^{\ b} \text{ or } \ln S_D = \ln a + b \cdot \ln IM \tag{4.43}$$

where a and b are the regression coefficients; S_D is the median value of the seismic demand for the specific intensity measure (IM). The dispersion of the seismic demand σ is determined by:

$$\sigma = \sqrt{\frac{\sum_{i=1}^{N} \ln S_D - \ln\left[a \ IM^{\ b}\right]}{N-2}} \tag{4.44}$$

Figure 4.43 presents the PSDMs with respect to two commonly used intensity measures, peak ground acceleration (PGA) and peak ground velocity (PGV). It can be found that the coefficient of determination (R^2) of PGA is much larger than that of PGV. Therefore, in this study, the PGA is taken as the intensity measure, and the corresponding PSDM was used to predict the displacement of the slab.

One key consideration of using the PSDM lies in that it provides a viable way to effectively deal with the very sensitive rocking responses. To be specific, at each PGA level, the dispersion σ provide a potential solution space for rocking demand predictions. Namely, rocking responses can be anywhere within the two-sigma range away from the median values. Such probabilistic nature of the responses enables the extraction of the most reasonable set of data by comparing them with the results from other models, such as the ABAQUS model in this study.

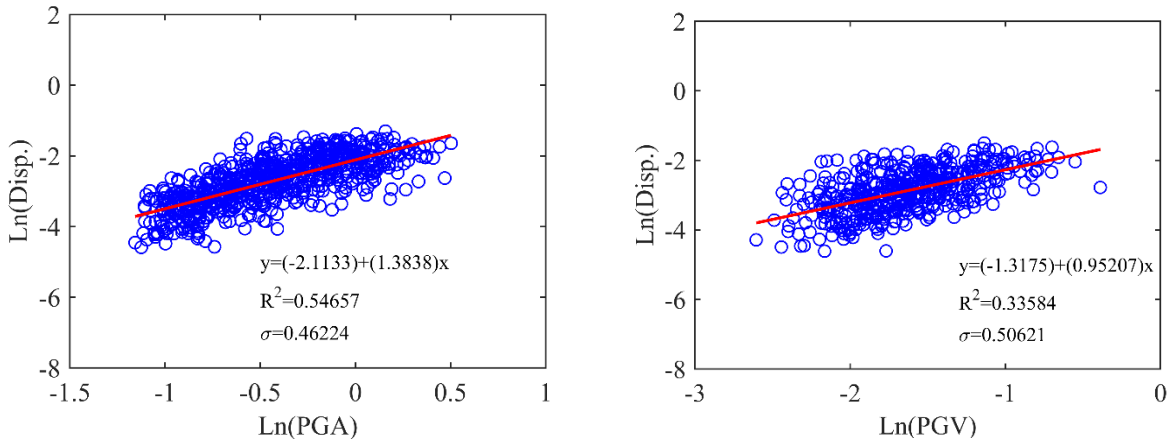

(a) PGA (b) PGV

Figure 4.43. Probabilistic seismic demand model of the displacement for different intensity measures

Four sets of results have been obtained by using two models, one in MATLAB and the other in ABAQUS. Figure 4.44 presents the cumulative distribution functions (CDFs) for these four sets of results. As is depicted, the first CDF illustrates the distribution of 98 rocking demand calculated from the ABAQUS model. An evident change of CDF slope can be found between the 35% small responses and the remaining 65% large responses. Such sudden change of slope results from the dominant sliding motions in ABAQUS when the model is subjected to the El-Centro motions with small PGAs. Under these cases, rocking was not initiated, and the response motions are very sensitive to the friction coefficient considered for the model. Therefore, the 35% small responses in ABAQUS bear very limited information and are most likely inaccurate. Conversely, the 65% large response data are considered to be reasonable in this study. In particular, because the ABAQUS model was excited by ground motions in three directions, which is consistent with the shaking table tests, realistic movements occur by observing both sliding motions and detachments at rocking column ends (as illustrated in Figure 4.45).

The second CDF curve is for the rocking responses from the MATLAB model when subjected to the given 200 testing motions. Using this model, about 10 cases (5%) have the rocking columns touch their end restrainers, leading to constant displacement values of 0.315m for the CDF range between 95% and 100%. The 3D MATLAB model can yield deterministic and repeatable results if same initial conditions were assigned. However, a small change in the initial conditions can often lead to different responses. As such, this CDF curve is considered to be partially accurate in predicting the test results.

The third CDF curve comes from the PSDM prediction that was developed by using 800 analysis results from the 3D MATLAB model. The curve covers a wider range of ground motion inputs and a level of uncertainty in rocking responses. The PSDM prediction was generated by

resampling the responses using 200 testing motions, where the embedded dispersion has been successfully considered in this process. In particular, a random number within the two-sigma range away from the median value was generated at each PGA level using the PSDM shown in Figure 4.43. As such, this curve has dealt with both the un-repeatability and randomness in association of the rocking responses. The PSDM predicted CDF curve is close to the CDF curve obtained by the 3D MATLAB model under small motions, and is in the middle of the ABAQUS and MATLAB results under large motions.

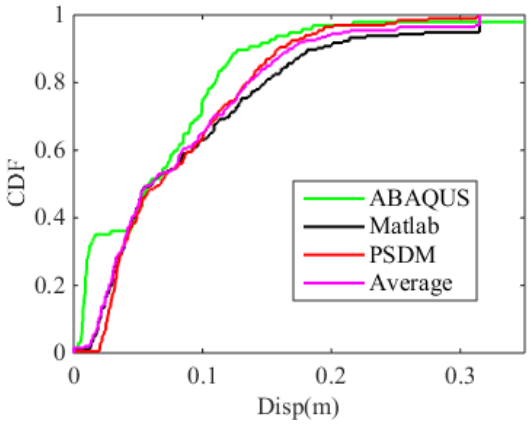

Figure 4.44. Cumulative distribution functions of the ABAQUS, analytical, and prediction results

The last case takes into account the perceived higher reliability of the ABAQUS results under large motions, as shown in Figure 4.45. Hence, the CDF curve is developed by taking the average between ABAQUS and MATLAB model results for the data that are larger than 0.05m and smaller than 0.315m. It can be observed that the PSDM and average curves yield very similar CDF outcomes. Finally, the prediction from the PSDM method is selected for final submission as the predicted test results.

The comparison between test results and predicted results are also compared. As shown in Figure 4.46. It is observed that the PSDM prediction matches very well with the experimental CDF

curve under Chi-Chi motions, but does not match well with the experimental CDF under EI Centro motions. It means that the PSDM is weighted toward larger earthquakes. PSDM should performs better if the modeling was conducted separately for large and small earthquakes.

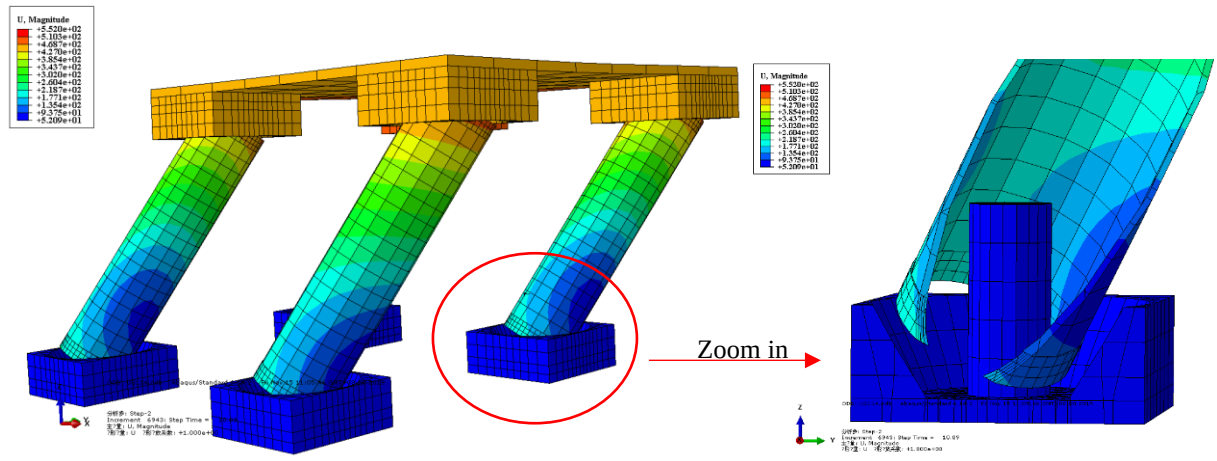

Figure 4.45. Large response caused by un-idealized motion in ABAQUS model

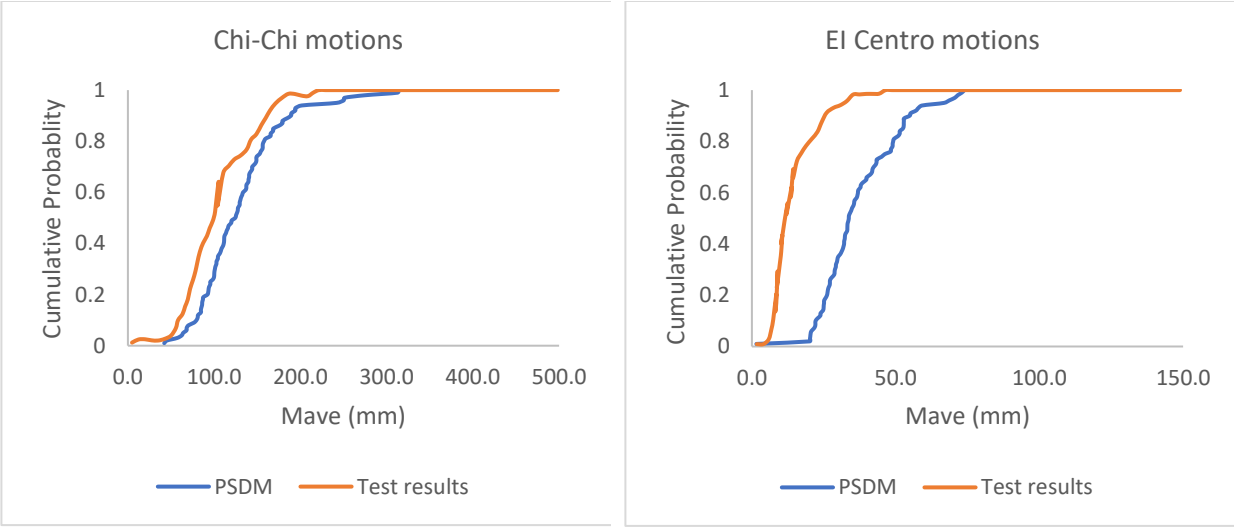

Figure 4.46. Comparison between empirical cumulative distribution and predicted cumulative distribution

4.5 CONCLUDING REMARKS

Both analytical models, FE models and probabilistic seismic demand models are used to

study the modeling of individual rocking response and CDF curves in this chapter. First, an analytical model of the rocking flexible column-foundation model is proposed. Comparing analytical rocking responses with shaking table results shows that the rocking behavior is sensitive to different energy dissipation mechanisms during impact. Moreover, this analytical model can be used to verify the FE models' accuracy in modeling rocking behavior of the flexible structures.

Second, three existing FE rocking models are evaluated by comparing them with analytical model and experimental results. It is observed that the existing FE models can accurately model the rigid rocking behavior, while they are not accurate when modeling the rocking behavior of flexible structures. The discrepancies are mainly caused by inappropriate modeling of the impact mechanism. Namely, viscous damping or numerical damping is used to approximate the energy dissipation during the impact.

To better model the instantaneous energy dissipation during impact, a finite element based rocking model is implemented in OpenSees, which consists of a zero-length rocking element with a modified Dirac-delta type impact model. A new user element, "ZeroLengthImpactRocking", is implemented in OpenSees and verified by comparing with shaking table tests. This new user element is useful when modeling the seismic performance of structures with rocking components in OpenSees.

Finally, the PEER Center shaking table tests of a four-column rocking podium are studied to reveal the sensitivities and uncertainties in rocking responses. A PSDM-based model is proposed to predict the rocking behavior through probabilistic seismic demand analyses. To generate the PSDM model, two different modeling schemes are presented in predicting the test results: one is the MATLAB model modified from a previous analytical study, and the second is the finite element model developed in ABAQUS. By addressing the significant uncertainty of the

rocking dynamics, four sets of response data are obtained. The following conclusions can be drawn from this study: (1) Seismic responses of the 3D rocking podium are sensitive to the variations in initial conditions, rocking impact treatment, and boundary conditions at the rocking interface. Rocking responses for individual testing cases are often difficult to predict. (2) PSDM-based model can successfully tackle the uncertainty issue embedded in the rocking responses.

5. CASE STUDY: SEISMIC PERFORMANCE OF 9-STORY ROCKING SHEAR WALL BUILDING

5.1 INTRODUCTION

Reinforced concrete (RC) walls are commonly used in mid-rise and high-rise buildings as the primary lateral force-resisting system. From extensive experimental results, it has been found that relatively slender RC walls, whose height-to-length ratio is about three or larger, are generally dominated by flexural behavior. In contrast, stout RC walls are essentially impacted by the interaction between flexure and shear (Wallace, 2007). A wide range of modeling approaches has been used to simulate the behavior of RC walls, e.g., lumped plasticity, distributed plasticity, and continuum elements. The model evaluation indicated that the most viable option to achieve accuracy and efficiency was using beam-column line elements with fiber-type cross-section models at integrated points (Pugh et al., 2015). A force-based beam-column is chosen in this study because displacement-based beam elements resulted in inaccurate axial force distribution and need a larger number of elements per story (Pugh et al., 2015).

Previous studies show that structures with partly rocking components, particularly a moment-resisting frame structure coupled with a rocking wall, have a better seismic performance than fixed base structures. For example, using nonlinear analysis in ABAQUS, Qu et al. (2012) found that the rocking wall associated with the energy dissipation devices effectively avoids weak story failure and reduces damages in other components. Shake table tests on four single rocking walls shows that although the walls were expected to have limited energy dissipation capacity, they showed satisfactory performance without experiencing visible damage up to the design-level earthquakes (Nazari et al., 2017). The seismic response of one-third-scale three-story steel frames

with columns allowed to uplift reveals that (Midorikawa et al., 2009): the maximum base shears of the rocking frames are effectively reduced; the maximum column tensile forces for the rocking frames are limited to a relatively constant value less than those for the fixed-base frames after the uplift motion occurs, whereas the maximum compressive forces are almost equal to or less than those for the fixed-base frames.

However, most available nonlinear analysis methods, shake table tests and design methodologies are for rocking components with tendons or restrainers, even though free-standing rocking might be more appealing when the lower cost is desired since it does not require anchoring to both wall and foundation. Namely, much emphasis is placed on the energy dissipation by the supplemental protective devices, yield steel plate, anchorages, and self-centering by tendons, while few comments are offered to what extent the mobilization of the rotational inertia of shear walls is modifying the dynamic response of the coupled reinforced concrete structure. In this chapter, nonlinear analyses of a moment-resisting frame structure coupled with a free-standing rocking wall are conducted to illustrate the effects of rocking components on the dynamic response of the structure.

5.2 FE MODEL OF SHEAR WALL

In this study, the force-based distributed-plasticity fiber beam-column element (Spacone et al., 1996) implemented in the OpenSees is utilized to model the slender shear wall. Figure 5.1 illustrates the procedure to establish the computational model of a shear wall specimen with fiber beam-column elements aggregating with an uncoupled equivalent linear shear spring (Pugh et al., 2015).

For the fiber sections, 1D concrete and steel response models are used to define the nonlinear material response, as shown in Figure 5.1. The concrete material response was

determined using the uniaxial Kent-Scott-Park model with linear tension softening, i.e., concrete02 model in OpenSees (Yassin, 1994). Steel material response was defined using the uniaxial Giuffré-Menegotto-Pinto model with isotropic strain hardening, i.e., steel02 model in OpenSees (Filippou et al., 1983). The model parameters to define the nonlinear behavior of material need to be calibrated from the material test data.

Since the fiber-type section model does not simulate the deformation due to shear, an equivalent shear spring was incorporated into the fiber section to provide an indirect way to consider the flexure-shear interaction. For the force-based beam-column element, a shear-response model can be integrated at the section level using section aggregation function (Marini & Spacone, 2006). The shear response of the wall was defined by the $V-\gamma$ relationship:

$$V = \gamma G_{eff} \kappa_s A_{cv} \tag{5.1}$$

where V is the shear force on the section, γ is the shear strain on the section, κ_s is the shear form factor taken as 5/6 for rectangular walls, A_{cv} is the shear area of the section. For the current study, $G_{eff} = 0.1G_c = 0.04E_c$ is used considering the cracking of section, and E_c is the elastic modulus of concrete.

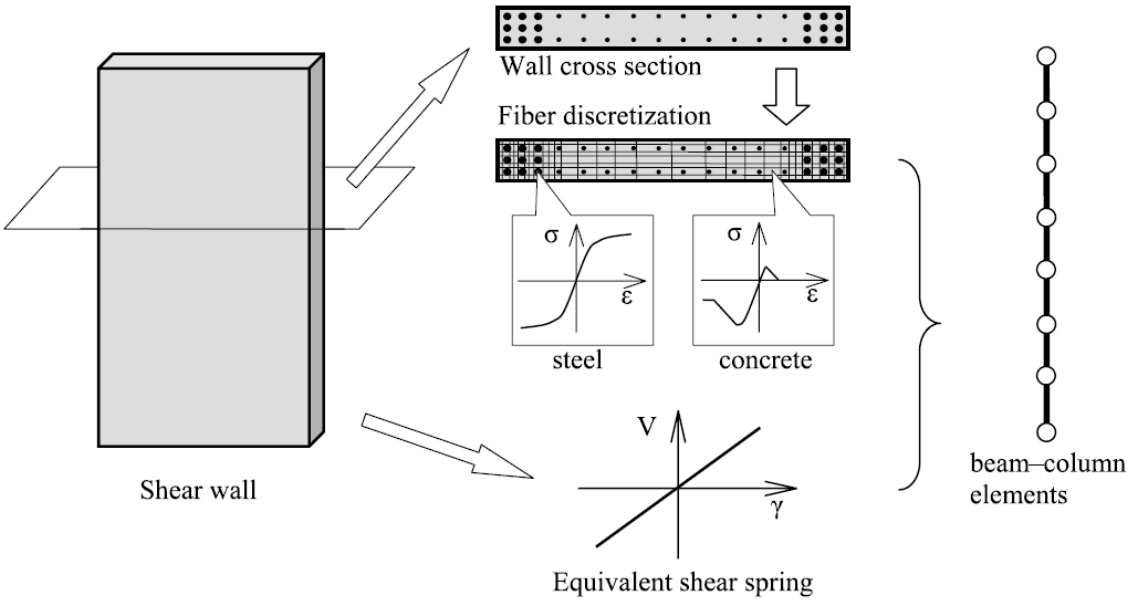

Figure 5.1. Scheme to establish the computational model of a shear wall using fiber beam-column element and an uncoupled equivalent shear spring (Tang & Zhang, 2011)

As shown in Figure 5.2, left, the modeling scheme described above is validated by simulation of cyclic test of an experimental shear wall, PW1 specimen with a height of 12ft, 6in by 120in in plan. The design details of the PW1 specimen can be found in Birely et al. (2008). Three nonlinear beam-column elements with five integration points in each element are used for the OpenSees model. The model parameters to define the nonlinear behavior of material were calibrated in the reference (Tang & Zhang, 2011). Figure 5.2, right, shows the comparison between the numerical analysis results from OpenSees and the measured cyclic behavior of the PW1 specimen. It can be seen that the nonlinear hysteretic behavior of the wall can be well captured using fiber beam-column elements in OpenSees. The generally good agreement between the numerical and experimental responses indicates that the outlined modeling technique is adequate to simulate the nonlinear force-displacement behavior of slender RC shear walls, furthermore, made it possible to use the force-based distributed-plasticity fiber beam-column element to simulate the rocking behavior of slender shear wall by combining with rocking models.

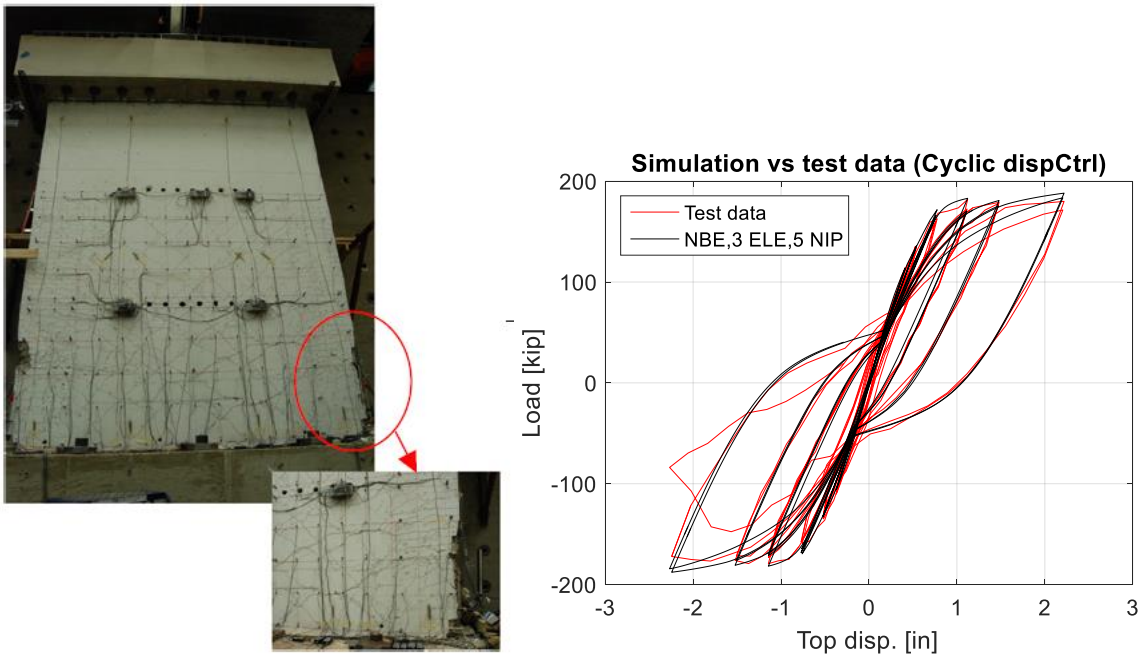

Figure 5.2. Simulation of the PW1 shear wall: PW1 specimen in laboratory (left) and simulation results against test data (right)

5.3 VALIDATION OF 9-STORY ROCKING SHEAR WALL

A 9-story shear wall with a height of 108ft, 20ft by 1.5ft in the plane, is shown in Figure 5.3. The model parameters are shown in Tables 5.1 and 5.2. First, the convergence of nonlinear response is checked by using different mesh sizes, as shown in Figure 5.4. The nonlinear force-displacement behavior of the 9-story RC shear wall can be well captured by using nine elements, i.e., 1 element per story, which will save much more computation costs while using this shear wall into a whole building model.

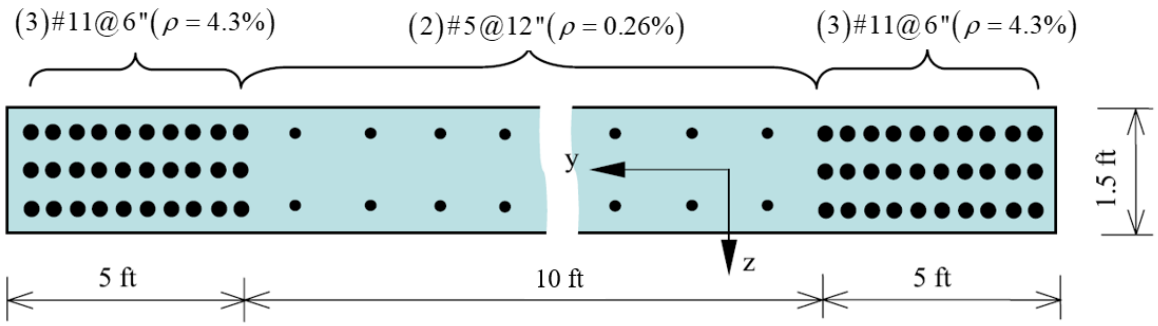

Figure 5.3. Reinforcement and geometric details of the planar RC shear wall

Table 5.1. Reinforcement material model and parameters used in numerical analysis

Material	Model in OpenSees	Model Parameters					
		f_y (ksi)	E (ksi)	b	R	c_{R1}	c_{R2}
#5 rebar	Steel02	65	29000	0.01	15	0.925	0.15
#11 rebar	Steel02	70	29000	0.01	18	0.925	0.15

Table 5.2. Concrete material model and parameters used in numerical analysis

Material	Model in OpenSees	Model Parameters						
		f'_c (ksi)	ε_0 (ksi)	f_{cu} (psi)	ε_u	λ	f_t (psi)	E_{ts} (psi)
Confined Concrete	Concrete02	-7500	-0.00372	-1500	-0.0186	0.1	500	416667
Unconfined Concrete	Concrete02	-5000	-0.00248	-1000	-0.00496	0.1	500	416667

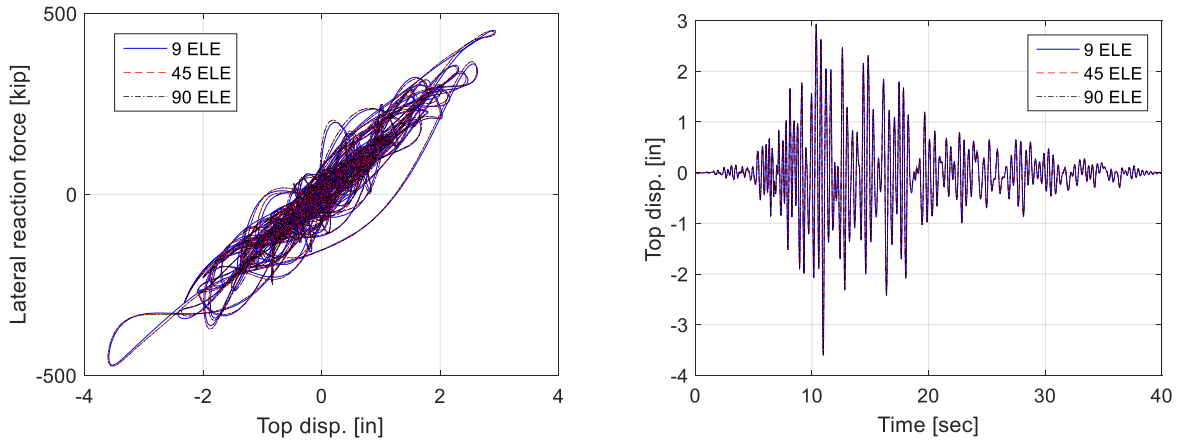

Figure 5.4. Demonstration of convergence of modeling for different mesh size under a recorded ground motion excitation (Takatori 090, the 1995 Kobe earthquake)

After verification of mesh sensitivity, this 9-story shear wall is combined with three existing FE rocking models introduced in Chapter 4 to model the rocking behavior of a free-standing shear wall. The outlined modeling technique is augmented by adding rigid arms on each floor to simulate the geometry of the shear wall, as shown in Figure 5.5. Since the shear wall model is a distributed-plasticity model with mass distributed along with the element, the analytical solution of the deformable rocking column-foundation model cannot be used as a comparison here. Therefore, the analytical model for the rigid rocking body (Zhang & Makris, 2001) is used to check the accuracy of rocking response of the augmented rocking shear wall model when the shear wall has sufficiently large stiffness, such as $E_b = 30e^7 \text{kPa}$. The rocking responses is evaluated under the same PEER strong motion database record used in Chapter 4, El Centro array #12, 140 (USGS station 931) with a scale factor of 5.

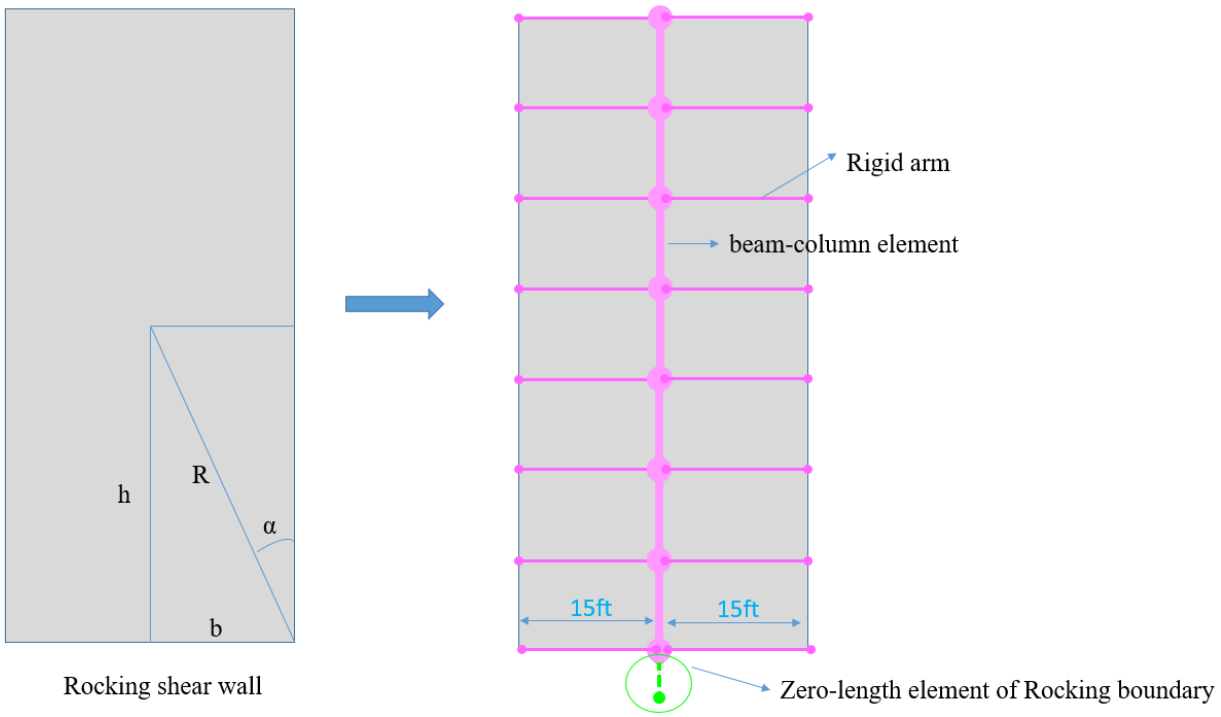

Figure 5.5. The finite element model of a rocking shear wall with geometry

The response time histories of SM using different time-stepping algorithms are shown in Figures 5.6 and 5.7. Note, there is no numerical damping in the SM model according to Vassiliou et al. (2014). However, for the SM model without numerical damping, the time history of both rotational and angular velocity cannot match well with the analytical solution, as shown in curves of "HHT $\alpha = 0.99$" and "Newmark $\gamma = 0.5$". A good agreement of response time history is attained if we use the numerical damping incorporate with the viscous damping in the rotational spring, as shown in curves of "HHT $\alpha = 0.67$" and "Newmark $\gamma = 1.0$". There is no convergence problem if a relatively softer pre-yield stiffness of rotational spring is used.

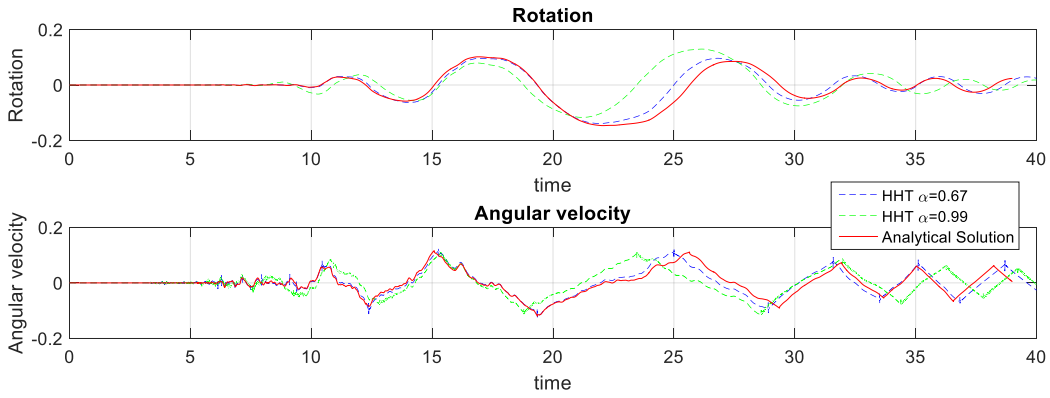

Figure 5.6. The time history of SM model using HHT time-stepping method with different damping factor

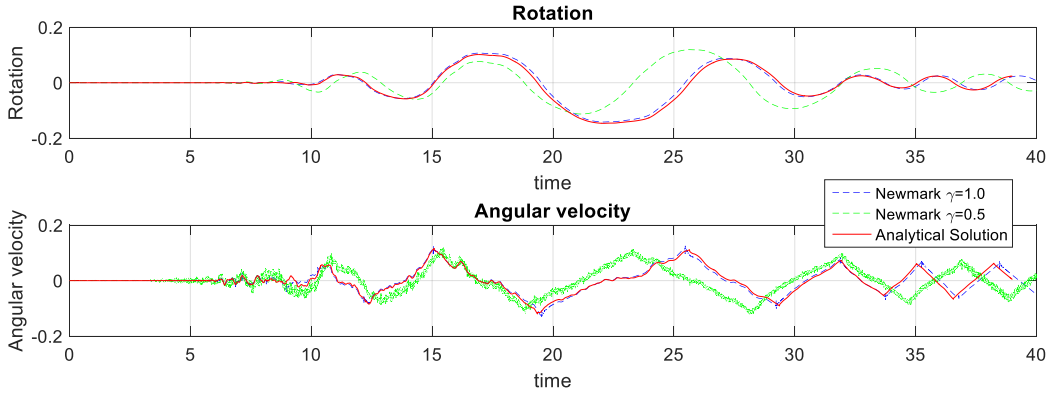

Figure 5.7. The time history of SM model using Newmark time-stepping method with different damping factor

The response time histories of the DRB model using the Newmark time-stepping algorithm are shown in Figures 5.8 and 5.9. The time step $dt = 0.005\text{sec}$, the tolerances at each step are $\text{Tol} = 10e^{-8}$ (in Figure 5.8) and $\text{Tol} = 10e^{-16}$ (in Figure 5.9). As shown in Figure 5.8, no further appreciable changes in the computed response are observed if $E_f > 30e^{7}\text{kip/in}^3$, therefore, E_f is selected as $30e^{9}\text{kip/in}^3$. It's observed that the time histories don't match well with analytical solution after 30sec, as shown in Figure 5.8. In comparison, a better agreement can be achieved by setting $\text{Tol} = 10e^{-16}$, as shown in Figure 5.9. There is also no convergence problem using the DRB

model when the Newmark algorithm is used.

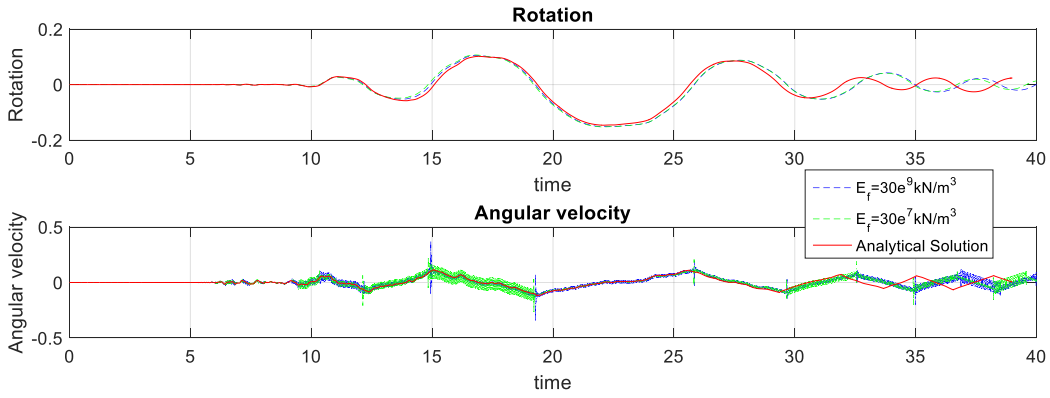

Figure 5.8. The time history of DRB model using Newmark time-stepping method with different stiffness of fiber section

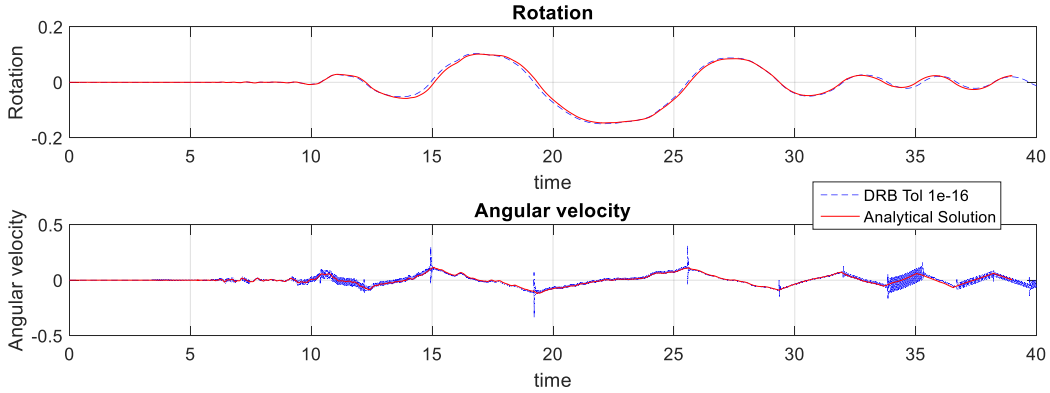

Figure 5.9. The time history of DRB model using Newmark time-stepping method with $\mathrm{dt} = 10e^{-16}$

However, it took some effort to make the DRB model converge if the HHT algorithm is used. The DRB model failed to converge when using the same time step $dt = 0.005\mathrm{sec}$. Although the response time histories can be obtained by using smaller $dt = 0.0001\mathrm{sec}$, as shown in Figure 5.10, it does not match well with the analytical solution. Even if changing the numerical damping α_d of the HHT algorithm cannot improve the accuracy. Moreover, the computation costs rapidly increase if a smaller $dt = 0.0001\mathrm{sec}$ is used. Therefore, the Newmark algorithm works better than

the HHT algorithm in this case.

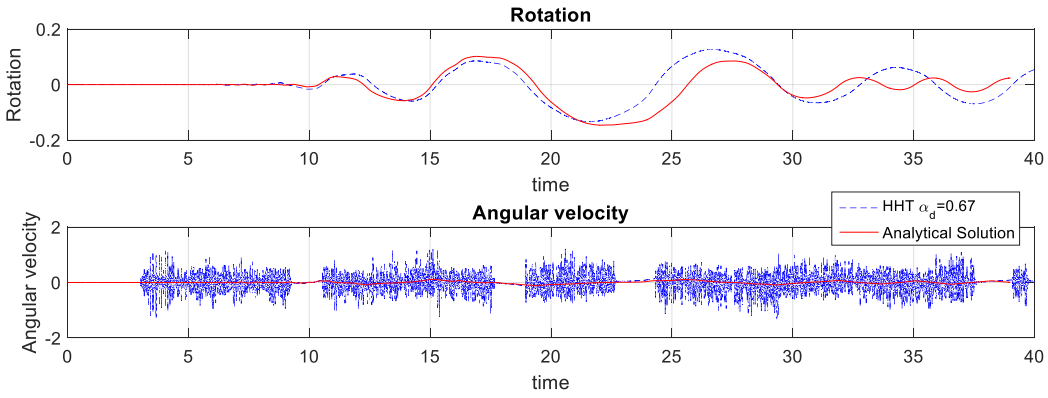

Figure 5.10. The time history of DRB model using HHT time-stepping method with $\mathrm{dt} = 10e^{-4}$

The comparison of response time histories of different FE models for both rigid and flexible cases is shown in Figures 5.11 and 5.12. As shown in Figure 5.11, for rigid case, the SM and DRB model with Newmark numerical damping $\gamma = 1.0$ have good agreement with the analytical solution. For the response of flexible case as shown in Figure 5.12, although there is no analytical solution to compare with, some conclusions can be observed as follows:

(1) For SM, the existence of numerical damping changes the response time history a lot. Besides, the results will diverge when using the SM model. Therefore, the SM model is not applicable when rocking structures become more flexible.

(2) The results of DRB model also diverge. As the rocking body becomes softer, the amount of energy numerically dissipated by the dissipative time-stepping integration algorithms diminishes, then the solution will diverge due to the presence of the undamped high-frequency components of motion. This behavior agrees with the observation in Vassiliou et al. (2017).

(3) For the augmented DRB model, results converge when using both Newmark and HHT algorithms. Because the augmented DRB model creating an alternate energy dissipation path, namely, considering the energy radiated into the ground under the rocking surface. However,

although the augmented DRB leads to convergence of the rotation time history, the same does not hold for the time history of the base moment response, and its ability to accurately predict the internal forces in deformable rocking frames has not been proven.

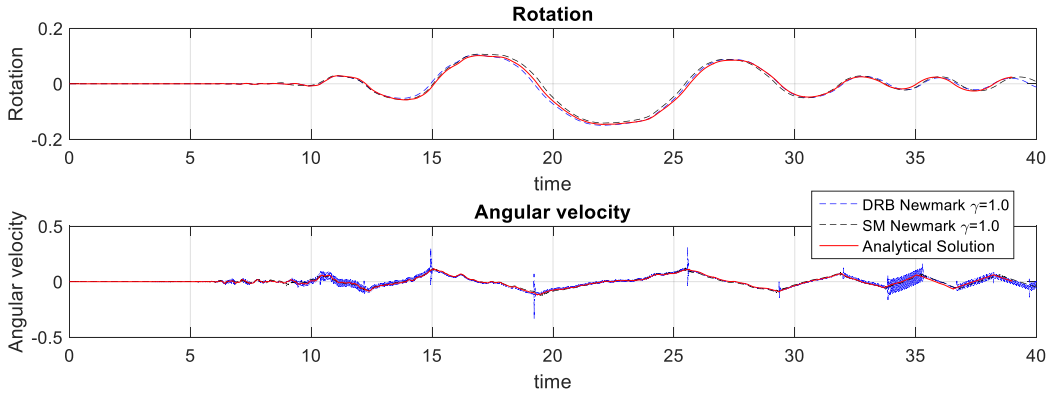

Figure 5.11. The comparison of response time histories of different FE models for rigid case

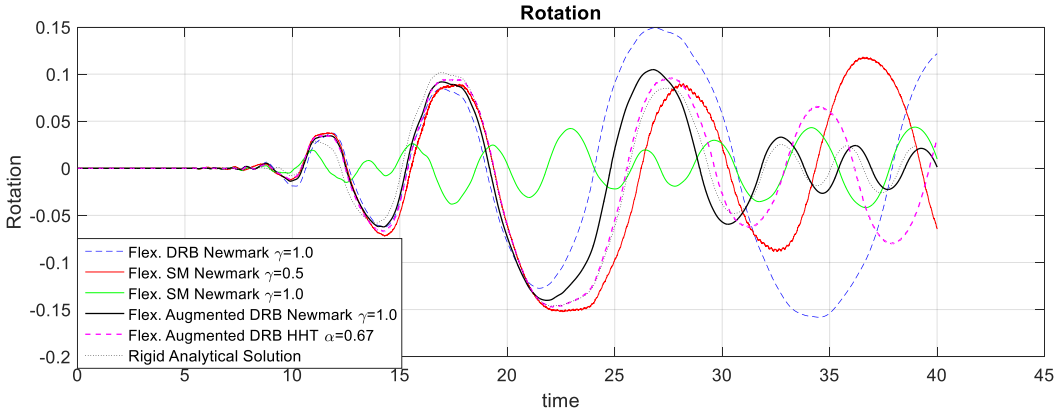

Figure 5.12. The comparison of response time histories of different FE models for flexible case

Due to the observed shortcomings in using three existing FE models, the implemented zero-length impact rocking element is used hereby to predict the seismic responses of the 9-story rocking shear wall and 9-story building equipped with the rocking shear wall. As shown in Figure 5.13, the rocking surface is modeled by using two zero-length impact rocking elements at two pivot points and one rotational spring with nonlinear moment-rotation behavior at the base center. The modeling of shear wall elements remains the same as described earlier.

Figure 5.14 plots the rocking responses (rotation and angular velocity in (a)) of the rigid 9-story shear wall using the zero-length impact rocking elements, where the realized impact forces are shown in Figure 5.14 (b) and (c). As shown in Figure 5.14, the predicted rigid rocking responses using the new FE model match well with the analytical solution when r=0.9 and Cp = 850 k*in/(rad*s) are used. Since the complete energy dissipation cycle is used, the impact force generated is gradually decreased to zero, thus maintaining the stability of the FE model.

Similarly, Figure 5.15 plots the rocking responses (rotation and angular velocity in (a)) of the flexible 9-story shear wall using the zero-length impact rocking elements, where the realized impact forces are shown in Figure 5.15 (b) and (c). As shown in Figure 5.15, the flexible rocking responses become much more stable and seem reasonable when compared with rigid rocking responses: the rocking period becomes larger while the impact force becomes smaller.

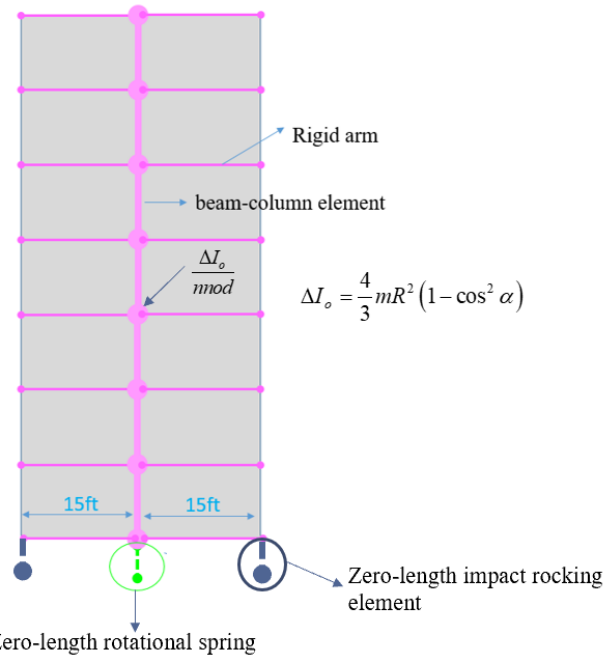

Figure 5.13. The FE model of a rocking shear wall using zero-length impact rocking element

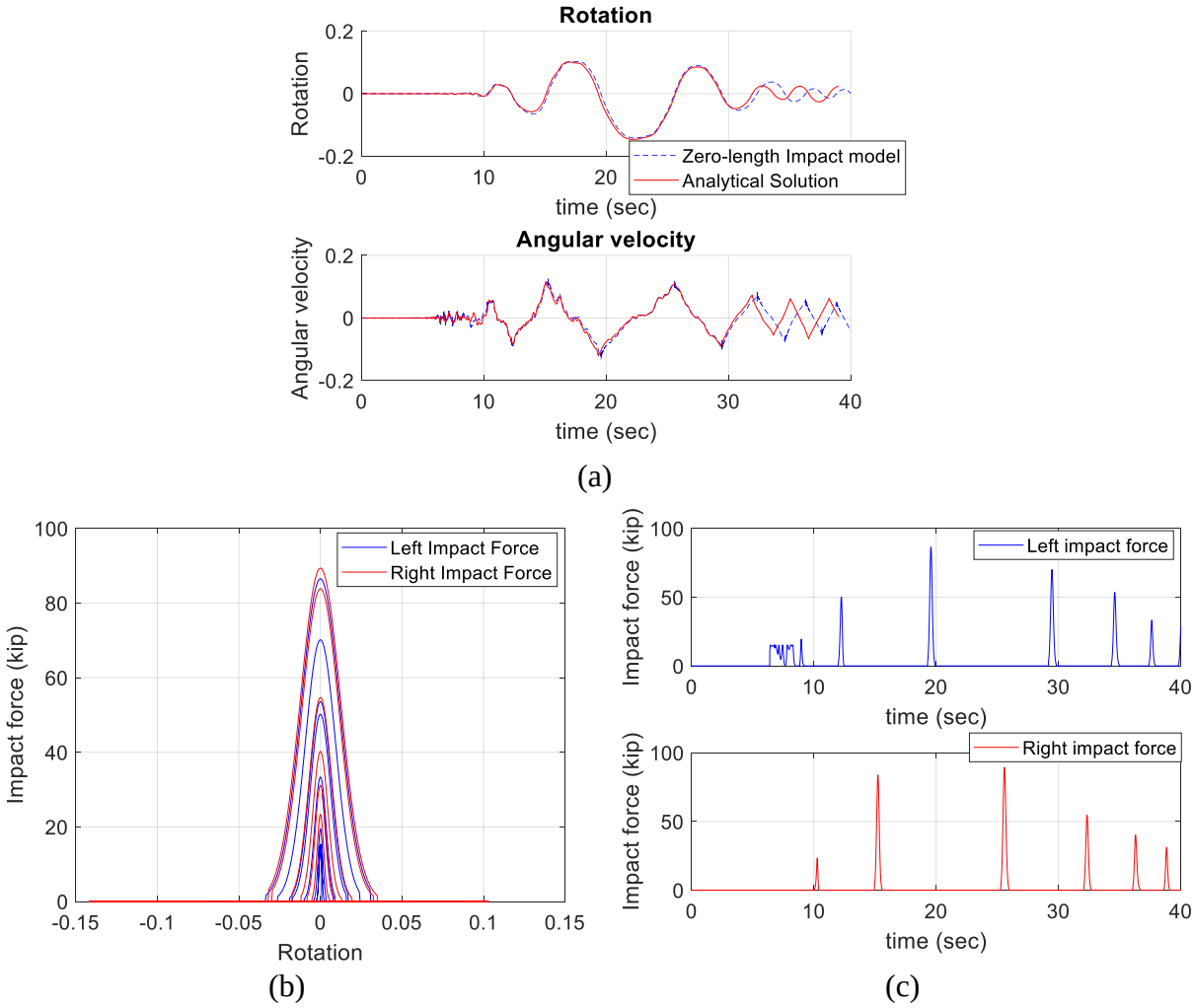

Figure 5.14. Rocking responses of rigid 9-story shear wall using “ZeroLengthImpactRocking” FE element

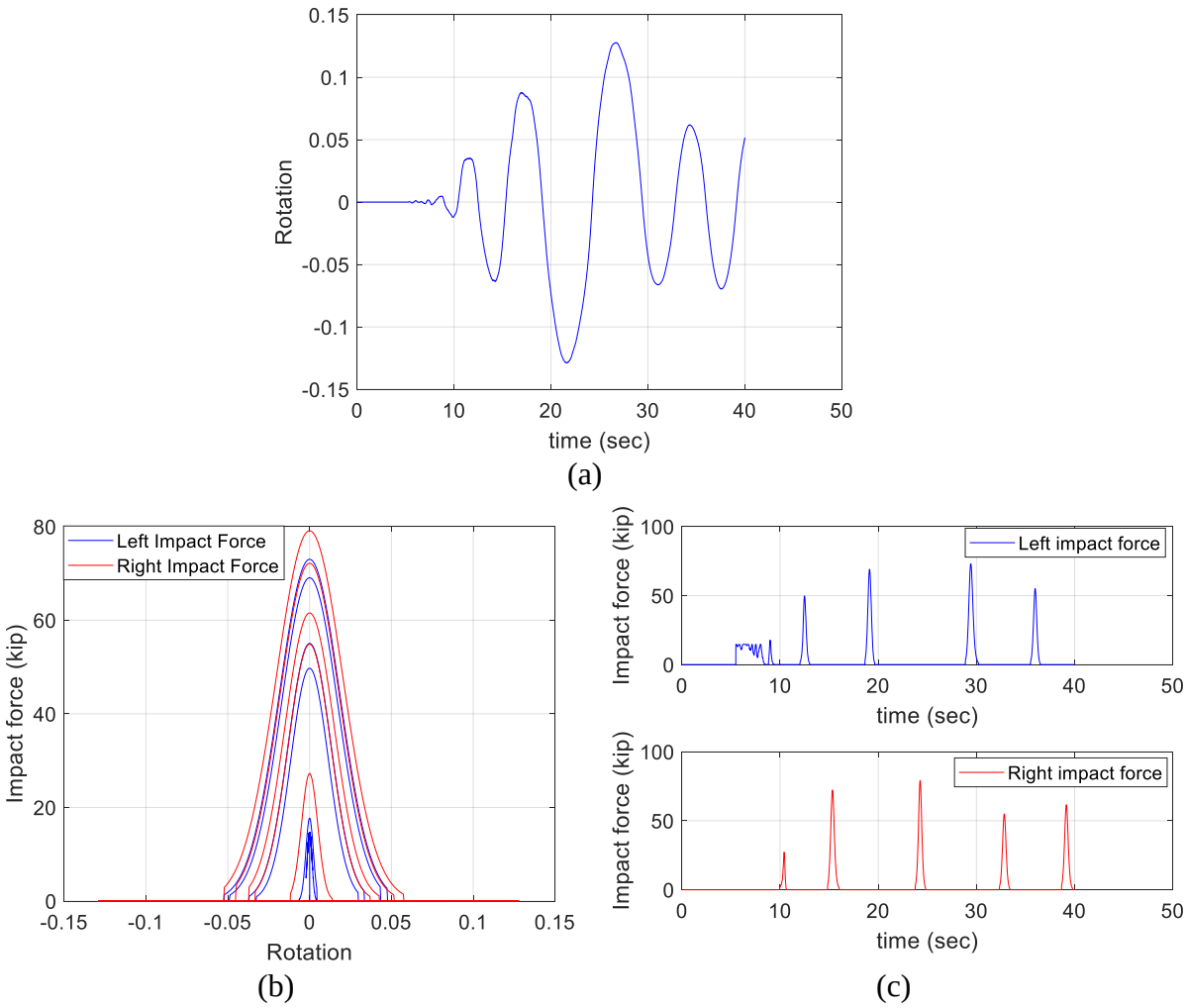

Figure 5.15. Rocking responses of flexible 9-story shear wall using "ZeroLengthImpactRocking" FE element

5.4 SEISMIC PERFORMANCE ASSESSMENT OF THE 9-STORY BUILDING

5.4.1 Numerical Model of 9-story Building

The 9-story office building is designed based on a seven-story office building described in Tang and Zhang (2011). The slenderness of the shear wall is increased by adding two stories and decreasing the length of the planar shear. The schematic sketch of the 9-story building is shown in Figure 5.16. It uses a dual system, consists of 5 RC planar shear walls and special moment frames,

for lateral loading resisting in the short-side direction. The seismic design in the long-side direction is not considered here because only the in-plane behavior of one bay in the short-side direction is of interest in this study. This building is assumed to be located at a Class-D NEHRP site in Bell, California, the same site as the benchmark building in the PEER report 2007/12 (Haselton et al., 2008).

The planar shear wall is expected to be dominated by its flexural behavior under lateral loads because its height-to-length ratio is 5.4. The planar 9-story shear wall, which is the same as the shear wall shown in Figure 5.3, is designed using the equivalent lateral force procedure and load combinations (dead load = 135psf, live load = 50psf) for strength design in ASCE 7-10 (ACI, 2011) and ACI 318-11. As shown in Figure 5.17 and Figure 5.18, the beams and columns are designed using the SAP2000 version 19 (SAP2000, 2017), an integrated software for structural analysis and design. The detailed design calculation of the shear wall can be found in the Appendix.

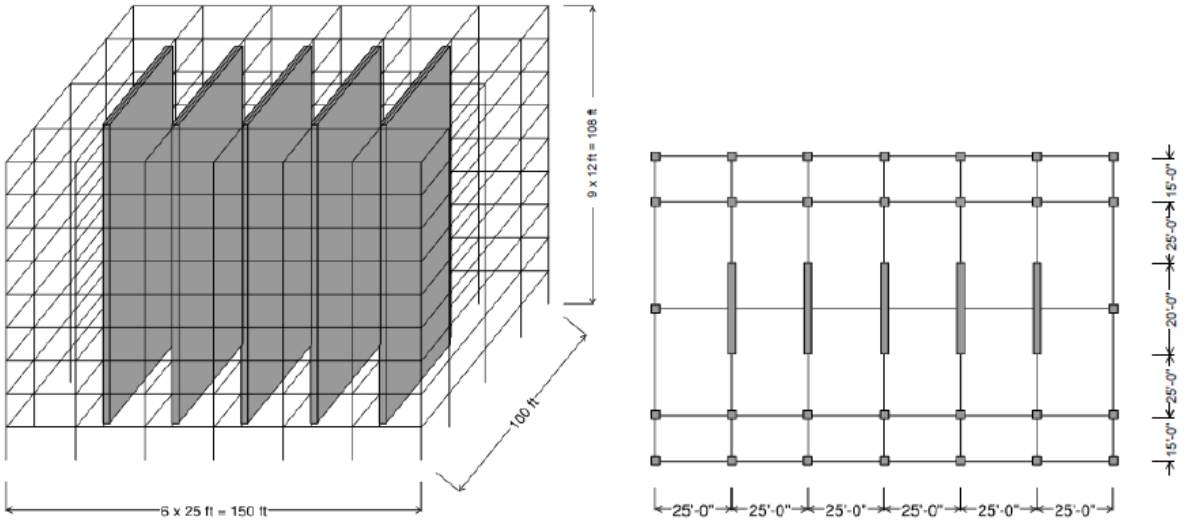

(a) (b)

Figure 5.16. The schematic sketch of the 9-story building: prospective view (a) and plan view (b)

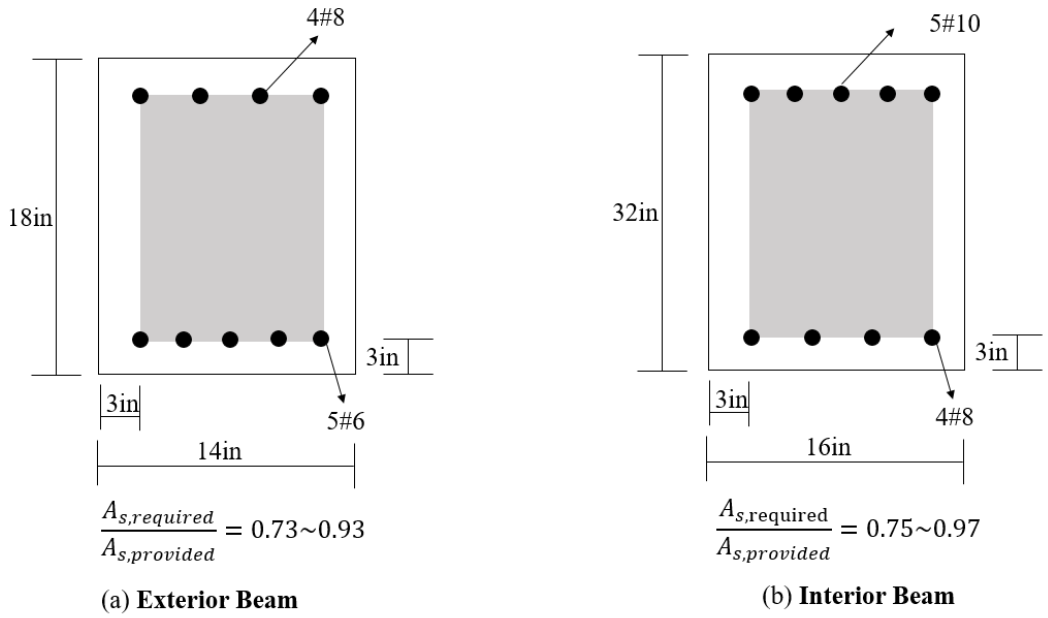

Figure 5.17. Reinforcement and geometric details of the exterior beams and interior beams

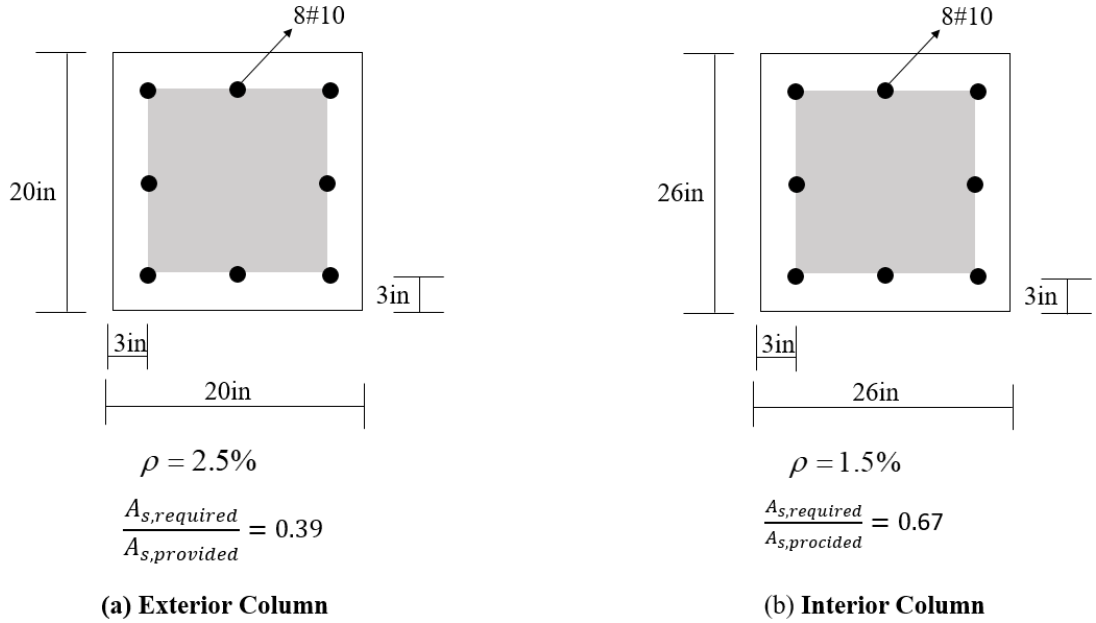

Figure 5.18. Reinforcement and geometric details of the exterior columns and interior columns

One interior bay in the long-side direction is modeled by a 2D four-bay plane frame with a shear wall along the short-side direction. Dynamic response of the 9-story building with two different support conditions, i.e., fixed base and free to rock, are evaluated through nonlinear

dynamic analysis in OpenSees. Once the rocking of the shear wall is activated, unique beam and column connections will be formed, as shown in Figure 5.19, to allow for the uplifting and rotating motion of the structure. The force-based distributed-plasticity fiber beam-column element (Spacone et al., 1996) implemented in the OpenSees is utilized to model the beams, columns, and slender shear wall. The model parameters of the element in OpenSees are shown in Tables 5.3 and 5.4. A Rayleigh damping model with a 5% damping ratio is assigned for the 1st and 9th modes. Using the modeling parameters r and C_p of previous 9-story rocking shear wall as a reference, a trial-and-error process is conducted to determine that r=0.8~0.9 and Cp = 850~1500 k*in/(rad*s) to make sure the impact force amplitude is reasonable compared with the total weight loaded on the shear wall.

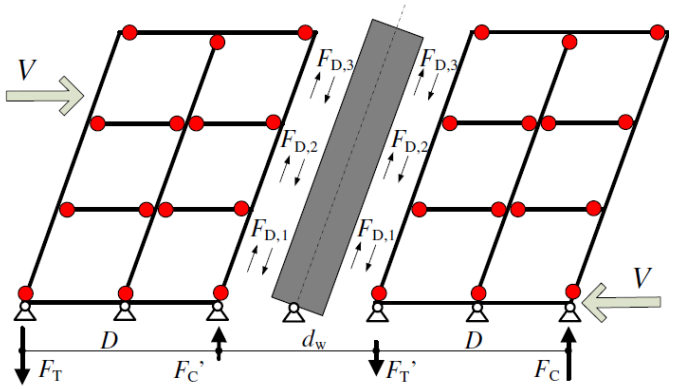

Figure 5.19. The 2D model of rocking wall-frame system (Qu et al., 2012)

Table 5.3. Reinforcement material model and parameters used in numerical analysis

Material	Model in OpenSees	Model Parameters					
		f_y (ksi)	E (ksi)	b	R	c_{R1}	c_{R2}
#5 rebar	Steel02	65	29000	0.01	15	0.925	0.15
#6 rebar	Steel02	65	29000	0.01	16	0.925	0.15
#8 rebar	Steel02	65	29000	0.01	17	0.925	0.15
#11 rebar	Steel02	70	29000	0.01	18	0.925	0.15

Table 5.4. Concrete material model and parameters used in numerical analysis

Material	Model in OpenSees	Model Parameters						
		f'_c (ksi)	ε_0 (ksi)	f_{cu} (psi)	ε_u	λ	f_t (psi)	E_{ts} (psi)
Confined Concrete	Concrete02	-7500	-0.00372	-1500	-0.0186	0.1	500	416667
Unconfined Concrete	Concrete02	-5000	-0.00248	-1000	-0.00496	0.1	500	416667

5.4.2 Results and Discussion

Seismic responses of the 9-story building are simulated when subject to the fault normal component of Newhall motion record under the 1994 Northridge earthquake with scale factor of 0.5. The time history of rocking angle, top displacement, and top acceleration of the fixed base model and rocking model are shown from Figure 5.20 to Figure 5.26. It is observed that:

(1) The rocking angle of the shear wall inside the building is smaller than that of the single rocking shear wall. This is expected since the moment frames connected with the rocking shear wall provide additional restraint after rocking is initiated.

(2) For top displacement: a) The displacement time history of the rocking shear wall and columns are similar because the pinned connection is triggered when rocking motion is activated. b) The peak value of the top displacement of the rocking model is two times that of the fixed base model due to the rigid motion caused by rotation during rocking. In contrast, the top displacements of the fixed base model and rocking model are very close when the rocking rotation is small. Although the total displacement of the rocking model is larger than that of the fixed base model, later it will be demonstrated that a large portion of this displacement is due to the rigid body motion, thus, will not lead to damage in the structural components. c) Note that, even though there are no post-tensioned tendons in the shear wall, the re-centering force provided by the wall gravity can bring the whole system back to the original position, while there is visible residual displacement

in fixed-base case. It validates the self-centering ability of a free-standing shear wall.

(3) For top acceleration: a) The top acceleration of the rocking model is smaller than the fixed base model during the time history -- the acceleration amplitude is reduced nearly 55% after rocking motion is initiated. Therefore, the structure with a rocking shear wall has a smaller acceleration demand. b) The acceleration is damped out after 25 sec for structure with the fixed base shear wall, while the acceleration is damped slower for structure with rocking shear wall due to the rocking motion. But the acceleration after 25sec is small enough not to cause any problem.

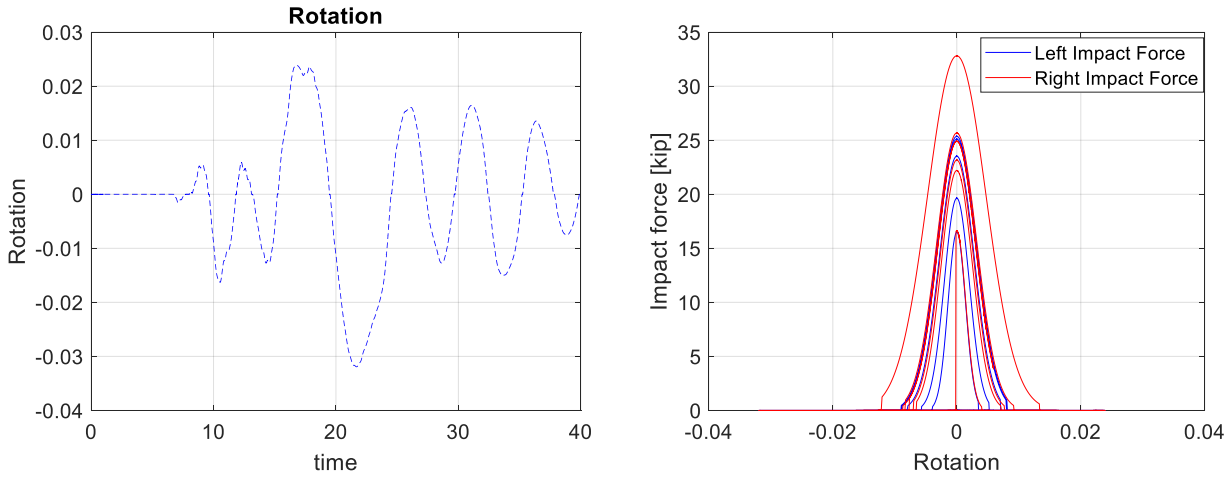

Figure 5.20. The rocking response of shear wall

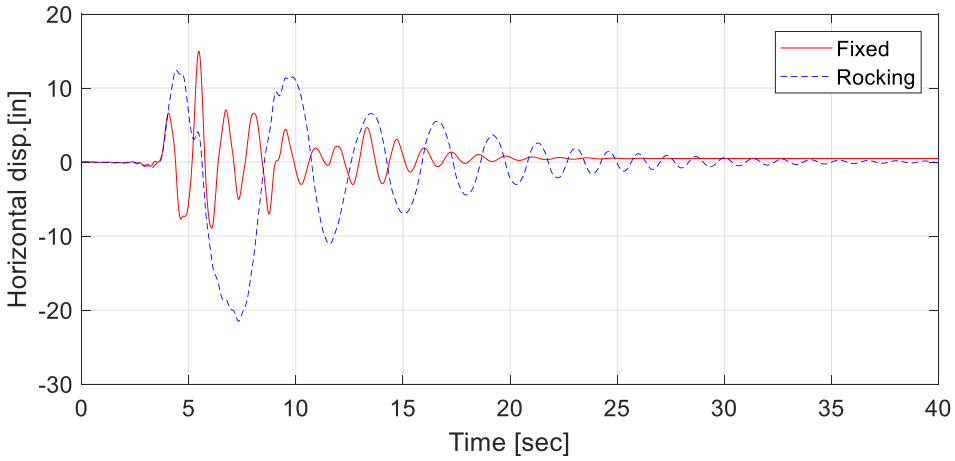

Figure 5.21. The top displacement time history of shear wall

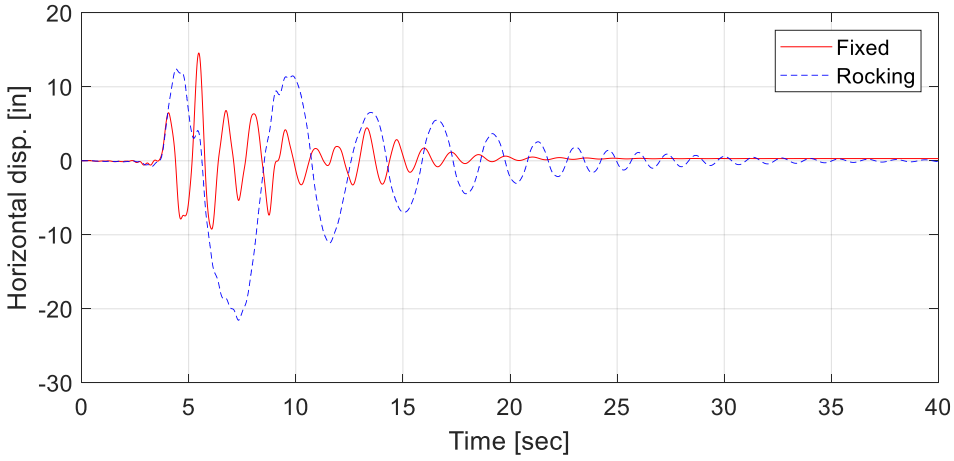

Figure 5.22. The top displacement time history of exterior column

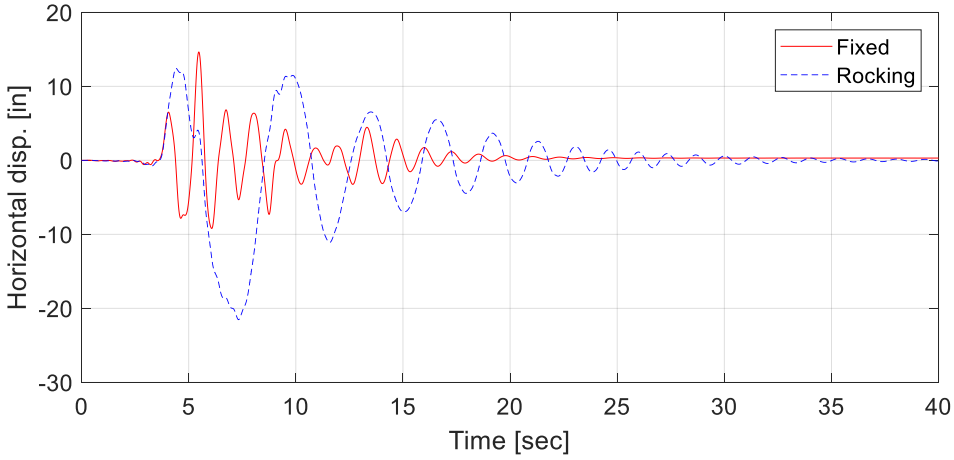

Figure 5.23. The top displacement time history of interior column

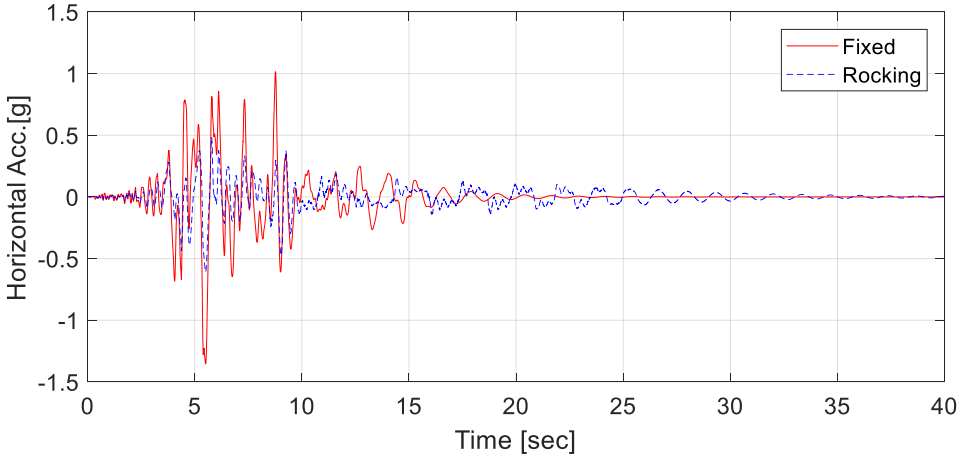

Figure 5.24. The top acceleration time history of shear wall

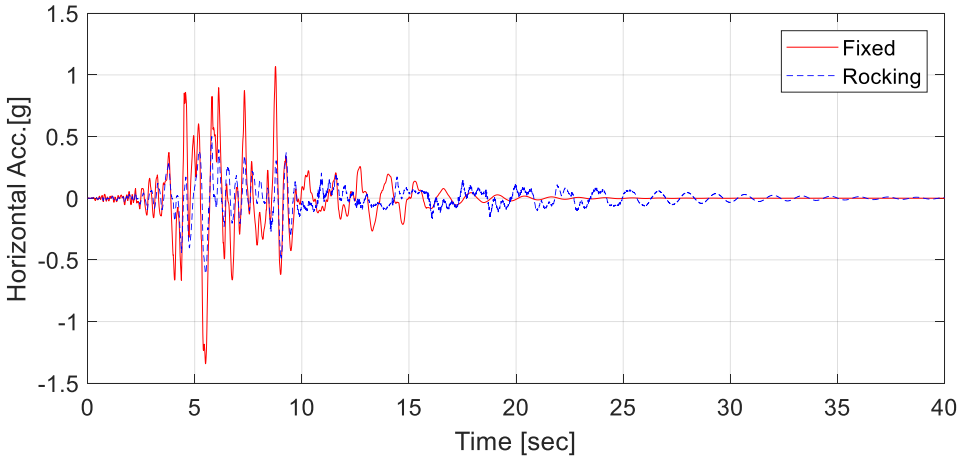

Figure 5.25. The top acceleration time history of exterior column

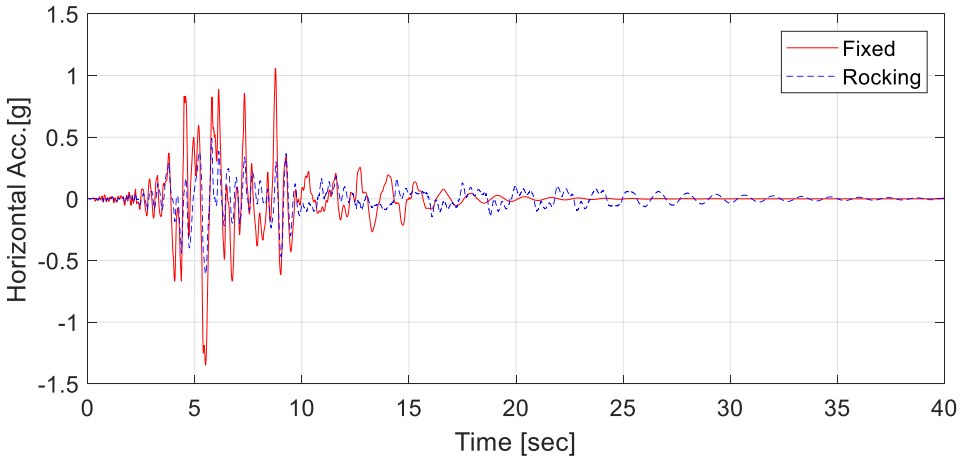

Figure 5.26. The top acceleration time history of interior column

Additionally, interstory drift ratio is commonly used as a measure of damage in assessing the seismic performance of multistory building structures. Figure 5.27 plots the interstory drift ratio of exterior column in the 9-story building computed by different FE models. The interstory drift ratio for rocking model is the elastic deformation interstory drift ratio obtained by subtract the rigid deformation from the total deformation. Interstory drift ratio of rocking structure is smaller than that of fixed base structure along each story. The maximum interstory drift is reduced from 1.52% to 0.35% by using the rocking shear wall. Besides, a much more uniform distribution of interstory drift ratio, which usually be treated as a benefit of using rocking shear wall in

retrofitting, is observed in upper floors. Note, the rocking behavior in this study is obtained by setting the existing shear wall to rocking. For the case of adding additional rocking shear wall as a retrofit (Qu et al., 2012), the benefit of uniform distribution of interstory drift ratio will be more significant since it brings in additional translational resistance.

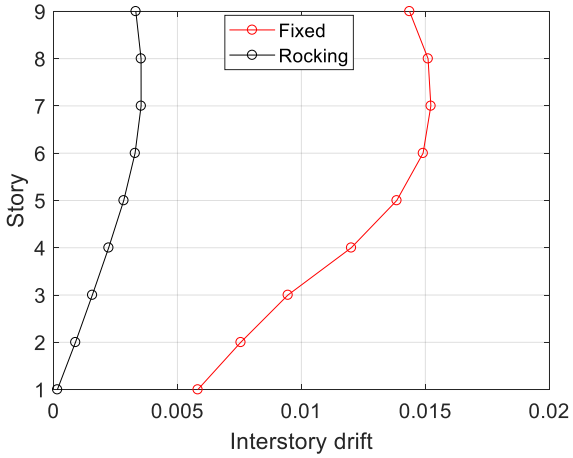

Figure 5.27. Interstory drift ratio of the exterior column in 9-story building

As shown in Figure 5.28 and Figure 5.29, the performance enhancement of flexural resistance is evaluated by comparing the moment-curvature plots of the fixed-base model and the rocking model. It is observed that the base of the rocking shear wall and other critical locations have almost linear behavior, while those of the fixed-based structure go further into the nonlinear state. Once the uplift mechanism is mobilized, the seismic demand on other critical locations of the structure will be reduced. Meanwhile, seismic resistance of rocking structures originates primarily from the mobilization of the rotational inertia of its members. Therefore, the structure survives with negligible or repairable damage.

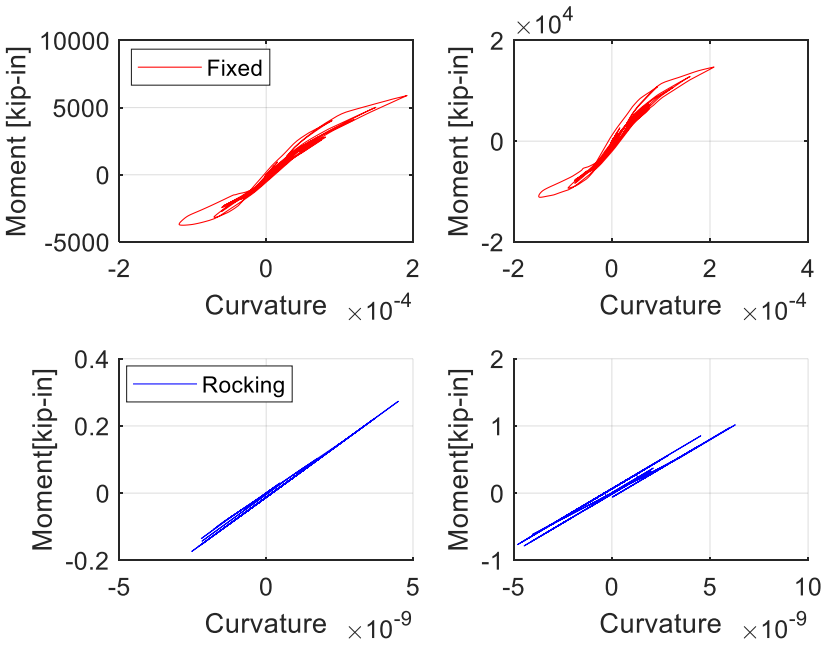

Figure 5.28. Moment-curvature relationship at the base of exterior column (left) and interior column (right) in 9-story building

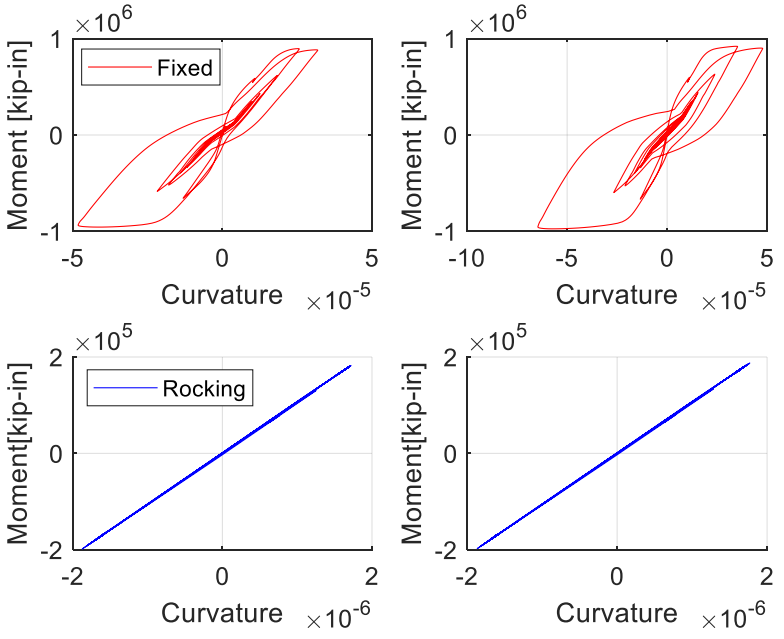

Figure 5.29. Moment-curvature relationship near the base (second integration point of the first element) of shear wall (left) and at the base of shear wall (right) in 9-story building

The 9-story building is analyzed under the excitation of a set of broad-band ground motions, which are selected from the PEER Strong Motion Database (http://ngawest2.berkely.edu/) by Baker et al. (2011). The mean and variance of their logarithmic response spectra match that predicted for a 'generic earthquake scenario' typical of high-seismicity sites in California. The ground motions were selected to match a magnitude 7 strike-slip earthquake at a distance of 10k for a soil site (shown in Table 5.5). The fault normal components of these ground motions are used as input ground motions. The normalized maximum responses of structure with rocking shear wall are presented in Table 5.6. It is observed that:

(1) Notable rocking motion, i.e., $\frac{\theta}{\alpha} > 5\%$, only happens under specific ground motion cases, which are highlighted in bold font in Table 5.5. For other case, $0.1\% < \frac{\theta}{\alpha} < 5\%$.

(2) The general benefit of using rocking components is observed. For large rocking cases, the drift reduction is 42%, the reduction of shear wall's base moment is 59%, the reduction of column's base shear is 14%, the reduction of top floor acceleration is 27%. At the same time, for small rocking cases, the drift reduction is 30%, the reduction of shear wall's base moment is 56%, the reduction of column's base shear is 13%, the reduction of top floor acceleration is 29%.

(3) By comparing the performance enhancement between large and small rocking cases, it can be concluded that the energy dissipation during impact is just a small portion of the seismic resistance of rocking structures. The mobilization of the rotational inertia and gravity of rocking structures provide sufficient seismic resistance in reducing the dynamic response.

(4) More research needs to be done to improve the proposed FE model. First, the rocking initiation condition, rotational moment of inertia, and energy computation are approximated by those of rigid rectangular block. An accurate value of the restitution factor and C_p value are still relying on the experimental test. The shear wall's slenderness and size remain to be optimized to

improve the rocking performance.

Table 5.5. Selected 14 soil motion inputs (M=7, R=10 KM) (Baker et al., 2011)

No.	Earthquake, Year	Station	Mag-nitude	Peak acceleration(g)
1	Mammoth Lakes,1980	Long Valley Dam	6.06	0.24
2	**Chi-Chi, Taiwan,1999**	**CHY036**	**7.62**	**0.32**
3	Cape Mendocino,1992	Rio Dell Overpass - FF	7.01	0.42
4	Imperial Valley-06,1979	Delta	6.53	0.24
5	**Kocaeli, Turkey, 1999**	**Yarimca**	**7.51**	**0.28**
6	Imperial Valley-06,1979	Calipatria Fire Station	6.53	0.13
7	Chi-Chi, Taiwan,1999	CHY034	7.62	0.29
8	Chi-Chi, Taiwan,1999	NST	7.62	0.37
9	**Kocaeli, Turkey, 1999**	**Duzce**	**7.51**	**0.28**
10	Spitak, Armenia,1988	Gukasian	6.77	0.22
11	**Loma Prieta,1989**	**Gilroy Array #4**	**6.93**	**0.36**
12	**Chi-Chi, Taiwan,1999**	**TCU060**	**7.62**	**0.21**
13	**Victoria, Mexico,1980**	**Chihuahua**	**6.33**	**0.11**
14	**Chi-Chi, Taiwan,1999**	**TCU118**	**7.62**	**0.11**

Table 5.6. Normalized maximum responses of structure with rocking shear wall

No.	θ/α (%)	R,rocking/R,fixed-base*			
		Drift ratio	Wall base moment	Column base shear	top floor acceleration
1	0.5	1.02	0.65	0.92	0.71
2	11.6	0.49	0.31	0.84	0.78
3	3	0.47	0.23	0.81	0.70
4	4.5	0.78	0.39	0.87	0.76
5	18.1	0.38	0.26	0.85	0.62
6	0.9	0.89	0.84	0.98	0.51
7	2.6	0.43	0.28	0.82	0.67
8	2.0	0.79	0.42	0.88	0.83
9	12.9	0.58	0.28	0.83	0.76
10	1.5	0.54	0.31	0.85	0.81
11	6.8	0.59	0.31	0.83	0.72
12	6.9	0.54	0.35	0.85	0.67
13	7.7	0.86	0.76	0.94	0.71
14	9.9	0.65	0.62	0.92	0.88

* R,rocking/R,fixed-base is the maximum responses of rocking structure normalized by maximum responses of fixed-base structure.

5.5 CONCLUDING REMARKS

First, a slender shear wall modeling technique of using force-based distributed-plasticity fiber beam-column element is verified. Then three existing FE models and one new FE model with zero-length impact rocking element are added into this slender shear wall model to predict the dynamic response of a rocking shear wall. All FE models can provide a good prediction for the rocking response of the rigid shear wall. However, the existing FE models are not applicable for modeling flexible rocking shear walls. In contrast, the proposed zero-length impact rocking model shows good numerical stability and prediction of both rigid and flexible rocking behavior.

Subsequently, the dynamic responses of a 9-story building with a fixed base shear wall and rocking wall are evaluated through nonlinear dynamic analysis in OpenSees by using the proposed zero-length impact rocking model only. The general benefit of improving the dynamic responses related to the design demand and damage, such as floor acceleration, interstory drift, base moment, base shear, and moment-curvature relationship, is observed under the excitation of a set of broad-band ground motions. Comparing the performance enhancement of large rocking and small rocking cases shows that the energy dissipation during impact is a small portion of the seismic resistance of rocking structures. The mobilization of the rotational inertia and gravity of the rocking structure provides sufficient seismic resistance in reducing the dynamic responses.

It should be noticed that more research needs to be done to improve the proposed FE zero-length impact rocking model. First, modeling parameters are still approximated by properties of rigid rectangular block and relying on the experimental test. Second, the shear wall's size and slenderness remain to be optimized to improve the rocking performance.

6. CONCLUSION AND FUTURE WORK

6.1 CONCLUSION

To investigate the performance enhancement of seismically protected structures, this research explores numerical simulation and nonlinear response analysis of two structural systems: one is inelastic structures and bridges with seismic protective devices, the other is structures with rocking components.

In the first half of the research, an equivalent passive control design procedure is proposed and verified for optimal design of inelastic structures and bridges with protective devices. An existing hybrid simulation software (UI-SIMCOR) is adopted and modified to enable the integration algorithm to include nonlinear seismic protective devices (such as base isolation, various dampers), different active control schemes (such as classical linear optimal control and nonlinear sliding mode control) and multi-support excitation scheme. While the realistic behavior of nonlinear structures is modeled separately in current finite element analysis software package (OpenSees), the nonlinear seismic protective devices and active structural control algorithms can be modeled in MATLAB and pieced together through hybrid simulation to produce the most realistic overall structural responses.

Then, the optimal design of equivalent passive control devices can be identified from the overall structural responses and active control forces. By applying the proposed passive control design procedure to an eight-story inelastic structure and a benchmark highway bridge with base isolation and nonlinear dampers, the following conclusions can be drawn: (1) The developed hybrid simulation framework can accurately assess the seismic behavior of inelastic structure and bridge with protective devices and active control schemes. (2) The optimal passive control design

are able to provide same seismic performance for the structures with various protective devices and various active control schemes. (3) The optimal passive design offers an appealing way to improve the seismic performance in general, namely, such performance enhancement stays when the structure has a different isolation design and subjects to different ground motion inputs.

Additionally, both analytical and numerical modeling, as well as probabilistic modeling of rocking behavior are studied in order to provide effective ways to evaluate the performance enhancement of structure using rocking components. After studying the existing models and an analytical model of the rocking flexible column-foundation model, a zero-length impact rocking model is proposed and implemented in OpenSees. All models are verified by comparing with analytical solutions and shaking table tests. It is found that the rocking responses are very sensitive to initial conditions, impact mechanism and structural flexibility. Therefore, a PSDM-based model is proposed to predict the 3D rocking behavior through probabilistic seismic demand analyses.

Finally, the reduction of strength demand and deformation demand, as well as the damage control by using rocking shear wall in a multi-story frame building are evaluated through a case study of 9-story rocking shear wall building. First, a slender shear wall modeling technique of using force-based distributed-plasticity fiber beam-column element is verified. Then the FE rocking models validated before are added into this slender shear wall model to predict the dynamic response of a rocking shear wall. Afterwards, the dynamic responses of a 9-story building with fixed-base shear wall or rocking shear wall are evaluated through nonlinear dynamic analysis in OpenSees. The dynamic response related to the design demand and damage, such as top displacement, top acceleration, interstory drift and moment-curvature relationship, are evaluated and it is observed that: (1) the interstory drift is reduced and uniformed by using rocking shear wall. (2) the edge elements of rocking model stay in the linear state while the elements of fixed

based model go further into the nonlinear state. (3) the moment demand of columns, beams and shear wall is significantly decreased by using the rocking shear wall.

In summary, this study provides an effective hybrid simulation scheme to evaluate the seismic performance of buildings with protective devices and structural controllers; provides efficient ways to find optimal design of protective devices which can improve the structural performance and mitigate earthquake hazards; provides accurate model to quantify the rocking responses and verify that the strength demand and deformation demand, as well as the damage can be well controlled by using rocking components.

6.2 FUTURE WORK

This research implemented seismic protective devises and active control algorithms into a hybrid simulation framework that could work for comprehensive numerical models of inelastic structure and benchmark highway bridge. The optimal passive control design can be derived by using active control responses and model identification methods. The method showed great promises in effectively improving structural performances with protective devices. Recommendations for future research and directions are as follows:

(1) Models of other seismic protective devices and different active control methods can be implemented in the hybrid simulation scheme.

(2) Other accurate model identification methods should be applied to identify equivalent passive control design.

(3) The choices of performance index when evaluating the control effects can be modified based on the needs. Besides, we can go one step further, which is relating the response quantities to the repair cost to provide more direct indication about the performance at the system level.

(4) In this study, after finding the optimized passive design using the proposed procedure,

the performance enhancement can be seen for this specific structure. However, this kind of benefit could be evaluated under the lifecycle assessment framework to give a big picture. For example, assessing whether it will significantly cut the lifecycle cost for the structures on a regional scale using the knowledge that is learned from this study.

For modeling and analysis of structure using rocking components, more study should be applied to understand the influence of impact mechanism and the uncertainty of FE rocking simulation. Furthermore, recommendations for future research using the implemented zero-length impact rocking element are as follows:

(1) Consider the soil flexibility to include the damage of the soil and SSI effects when rocking is initiated, as observed in real cases.

(2) Consider the vertical ground motion effects on the rocking behavior and structural responses, as vertical ground motion can be significant and impact the uplift of rocking components.

(3) The real rocking would be a 3D movement. More research should be done to improve the analytical and numerical modeling of the 3D rocking behavior and quantify the 3D motion.

.

APPENDIX

A.1 CALCULATION OF SLIDING SURFACE FOR SMC

Consider an n-DOF nonlinear building with the number of r controllers installed, for the determination of the $\mathbf{P}$ matrix, first convert the state equation of motion into the regular form by the transformation (Utkin, 2013):

$$\mathbf{Y} = \mathbf{D}\mathbf{z} \tag{a.1}$$

where $\mathbf{D}$ is a transformation matrix defined by:

$$\mathbf{D} = \begin{bmatrix} \mathbf{I}_{2n-r} & -\mathbf{B}_1\mathbf{B}_2^{-1} \\ \mathbf{0} & \mathbf{I}_r \end{bmatrix};\ \mathbf{B} = \begin{bmatrix} \mathbf{B}_1 \\ \mathbf{B}_2 \end{bmatrix} \tag{a.2}$$

where $\mathbf{I}_{2n-r}$ and $\mathbf{I}_r$ are $(2n-r)\times(2n-r)$ and $(r\times r)$ identity matrices respectively; $\mathbf{B}_1$ and $\mathbf{B}_2$ are $(2n-r)\times r$ and $(r\times r)$ submatrices obtained from the partition of the $\mathbf{B}$ matrix. In terms of transformed state vector $\mathbf{Y}$, the performance index J becomes $J = \int_0^\infty \mathbf{Y}^{\mathrm{T}}(t)\mathbf{T}\mathbf{Y}(t)\mathrm{d}t$, where

$$\mathbf{T} = \left(\mathbf{D}^{-1}\right)' \mathbf{Q}\mathbf{D}^{-1};\ \mathbf{T} = \begin{bmatrix} \mathbf{T}_{11} & \mathbf{T}_{12} \\ \mathbf{T}_{21} & \mathbf{T}_{22} \end{bmatrix} \tag{a.3}$$

where $\mathbf{T}_{11}$ and $\mathbf{T}_{22}$ are $(2n-r)\times(2n-r)$ and $(r\times r)$ submatrices obtained from the partition of the $\mathbf{T}$ matrix. $\mathbf{Q}$ is a $(2n\times 2n)$ positive definite weighting matrix. Minimizing the performance index J one obtains (Yang et al., 1995):

$$\mathbf{Y}_2 = -0.5\mathbf{T}_{22}^{-1}\left(\bar{\mathbf{A}}_{12}'\hat{\mathbf{P}} + 2\mathbf{T}_{21}\right)\mathbf{Y}_1 \tag{a.4}$$

where $\mathbf{Y}_1$ and $\mathbf{Y}_2$ are $(2n-r)$ and (r) vectors obtained from the partition of the vector $\mathbf{Y}$. $\bar{\mathbf{A}} = \mathbf{D}\mathbf{A}\mathbf{D}^{-1}$. $\hat{\mathbf{P}}$ is a $(2n-r)\times(2n-r)$ matrix satisfying the following Riccati equation:

$$\hat{\mathbf{A}}'\hat{\mathbf{P}} + \hat{\mathbf{P}}\hat{\mathbf{A}} - 0.5\hat{\mathbf{P}}\bar{\mathbf{A}}_{12}\mathbf{T}_{22}^{-1}\bar{\mathbf{A}}_{12}'\hat{\mathbf{P}} = -2\left(\mathbf{T}_{11} - \mathbf{T}_{12}\mathbf{T}_{22}^{-1}\mathbf{T}_{12}'\right) \tag{a.5}$$

Where $\hat{\mathbf{A}} = \bar{\mathbf{A}}_{11} - \bar{\mathbf{A}}_{12}\mathbf{T}_{22}^{-1}\mathbf{T}_{21}$, $\bar{\mathbf{A}}_{11}$ and $\bar{\mathbf{A}}_{22}$ are $(2n-r)\times(2n-r)$ and $(r\times r)$ submatrices obtained from the partition of the matrix $\bar{\mathbf{A}}$. Finally, the design matrix $\mathbf{P}$ of the sliding surface $\mathbf{S} = \mathbf{PZ} = 0$ is obtained as:

$$\mathbf{P} = \bar{\mathbf{P}}\mathbf{D} = \left[\bar{\mathbf{P}}_1 \vdots \mathbf{I}_r\right]\mathbf{D} \tag{a.6}$$

where $\bar{\mathbf{P}}_1 = 0.5\mathbf{T}_{22}^{-1}\left(\bar{\mathbf{A}}_{12}'\hat{\mathbf{P}} + 2\mathbf{T}_{21}\right)$.

A.2 3D ROCKING RESPONSES DATA FOR PSDM

Table A.1. Predicted M_{ave} using different methods

GM #	Maximum displacement M_{ave} [mm]			
	ABAQUS Model	3D MATLAB model	PSDM	Average
EC1	3.1	25.6	25.1	25.6
EC2		27.6	39.8	27.6
EC3	3.1	0.0	1.5	0.0
EC4		15.1	34.1	15.1
EC5	9.0	24.0	41.1	24.0
EC6		51.0	71.6	51.0
EC7		37.4	29.6	37.4
EC8		30.4	28.6	30.4
EC9	6.6	50.2	29.7	50.2
EC10		24.2	48.4	24.2
EC11	10.1	51.0	27.1	51.0
EC12	8.0	31.3	28.9	31.3
EC13		63.6	57.9	63.6
EC14	9.1	41.8	52.9	41.8
EC15	8.2	18.8	36.7	18.8
EC16	9.1	52.5	66.7	52.5
EC17		30.5	57.1	30.5
EC18	7.1	39.2	31.6	39.2
EC19	28.7	31.2	50.7	31.2
EC20		35.8	45.1	35.8
EC21		20.4	25.7	20.4
EC22	6.3	32.6	30.7	32.6
EC23		121.7	53.0	121.7
EC24		38.2	51.5	38.2

EC25		28.9	26.1	28.9
EC26		12.6	22.9	12.6
EC27		21.1	52.5	21.1
EC28	11.1	19.7	33.2	19.7
EC29		50.7	37.7	50.7
EC30		30.4	24.9	30.4
EC31		48.2	41.8	48.2
EC32		29.6	22.1	29.6
EC33		14.7	32.6	14.7
EC34		15.1	43.1	15.1
EC35	10.2	59.3	68.7	59.3
EC36		34.2	36.9	34.2
EC37		21.4	43.5	21.4
EC38		30.2	49.1	30.2
EC39		41.9	37.0	41.9
EC40		18.0	33.5	18.0
EC41	12.3	32.9	48.9	32.9
EC42		39.2	51.4	39.2
EC43	12.1	45.4	25.1	45.4
EC44		32.7	20.4	32.7
EC45		84.8	27.8	84.8
EC46		43.6	29.2	43.6
EC47	9.7	54.1	22.0	54.1
EC48		27.1	34.8	27.1
EC49		24.2	30.0	24.2
EC50	13.9	61.2	39.9	61.2
EC51	7.1	47.7	48.9	47.7
EC52		17.3	37.9	17.3
EC53	9.9	18.9	24.7	18.9
EC54		21.8	43.4	21.8
EC55		40.6	20.2	40.6
EC56	15.1	21.5	52.8	21.5
EC57		31.2	34.5	31.2
EC58		21.2	33.3	21.2
EC59		13.1	49.4	13.1
EC60		18.9	33.1	18.9
EC61		19.6	41.9	19.6
EC62		47.4	42.4	47.4
EC63		21.2	33.7	21.2
EC64		68.6	48.2	68.6
EC65		52.3	35.7	52.3
EC66		27.8	38.6	27.8
EC67		24.4	23.9	24.4
EC68		39.6	29.2	39.6
EC69	16.4	48.5	21.5	48.5

EC70	7.2	34.7	31.2	34.7
EC71		27.4	27.2	27.4
EC72		37.6	73.0	37.6
EC73	6.7	18.9	28.8	18.9
EC74		39.3	52.8	39.3
EC75		13.6	32.1	13.6
EC76		24.5	55.2	24.5
EC77		39.6	35.6	39.6
EC78	5.9	41.5	26.4	41.5
EC79		65.3	25.0	65.3
EC80		0.0	26.3	0.0
EC81	8.5	29.6	23.8	29.6
EC82	7.3	13.7	32.3	13.7
EC83		54.5	33.2	54.5
EC84		48.4	73.9	48.4
EC85		45.1	70.6	45.1
EC86		30.0	59.2	30.0
EC87		25.6	20.7	25.6
EC88		62.6	46.2	62.6
EC89		17.8	32.1	17.8
EC90	9.1	32.4	22.1	32.4
EC91		0.0	27.1	0.0
EC92		78.3	33.7	78.3
EC93		41.2	36.4	41.2
EC94		32.3	54.9	32.3
EC95	7.7	40.2	20.3	40.2
EC96	10.1	24.5	35.3	24.5
EC97	9.0	42.4	26.7	42.4
EC98	11.7	44.2	31.9	44.2
EC99		8.2	32.4	8.2
EC100	3.6	25.9	20.1	25.9
CC1		156.5	104.4	156.5
CC2		153.2	132.6	153.2
CC3	68.6	135.1	111.6	101.9
CC4	99.4	101.8	56.9	100.6
CC5		140.7	136.7	140.7
CC6	50.3	112.8	93.5	81.6
CC7		65.4	148.8	65.4
CC8	166.9	209.4	85.2	188.2
CC9		44.0	45.1	44.0
CC10	47.8	105.5	76.5	105.5
CC11	136.1	172.0	81.4	154.1
CC12	74.9	271.7	189.1	173.3
CC13		108.9	129.6	108.9
CC14	475.0	148.0	106.4	311.5

CC15		130.5	102.7	130.5
CC16	77.6	315.0	104.3	196.3
CC17	112.4	72.2	312.6	92.3
CC18		50.2	79.5	50.2
CC19		118.2	144.1	118.2
CC20	104.4	193.8	102.7	149.1
CC21		315.0	140.6	315.0
CC22	216.5	69.1	93.2	142.8
CC23	96.4	137.1	124.5	116.7
CC24	99.5	112.2	114.5	105.9
CC25	111.8	98.4	64.1	105.1
CC26	111.0	128.8	157.8	119.9
CC27		315.0	179.1	315.0
CC28		135.9	194.1	135.9
CC29	85.2	188.7	131.2	137.0
CC30		61.4	144.1	61.4
CC31		315.0	156.3	315.0
CC32	60.2	52.2	168.4	56.2
CC33	90.5	176.4	241.9	133.5
CC34		96.7	140.6	96.7
CC35	68.9	315.0	100.3	192.0
CC36	185.3	315.0	70.4	250.2
CC37	109.5	96.4	133.5	102.9
CC38		96.8	120.3	96.8
CC39	99.1	180.9	189.7	140.0
CC40	44.7	82.5	87.5	82.5
CC41		252.2	108.6	252.2
CC42	54.3	108.9	130.4	81.6
CC43	71.9	226.9	111.6	149.4
CC44	123.5	109.0	250.3	116.2
CC45	67.0	91.2	149.3	79.1
CC46		315.0	168.7	315.0
CC47	126.5	181.2	137.3	153.8
CC48	156.7	161.0	86.2	158.9
CC49		44.6	110.3	44.6
CC50	89.5	107.6	107.7	98.5
CC51		94.0	95.6	94.0
CC52		170.3	68.2	170.3
CC53		171.2	127.4	171.2
CC54		126.0	149.0	126.0
CC55	80.7	110.8	113.6	95.8
CC56		144.1	129.6	144.1
CC57	145.1	214.5	126.5	179.8
CC58		214.5	139.6	214.5
CC59		88.2	116.0	88.2

CC60		163.1	125.4	163.1
CC61		161.3	84.6	161.3
CC62	5.7	16.5	42.1	16.5
CC63		159.6	165.5	159.6
CC64		315.0	165.3	315.0
CC65	85.0	108.9	154.0	96.9
CC66		175.3	314.1	175.3
CC67		81.1	100.1	81.1
CC68		315.0	156.5	315.0
CC69	48.4	83.7	251.2	83.7
CC70	120.1	148.9	111.2	134.5
CC71	53.2	201.2	152.7	127.2
CC72		92.1	67.9	92.1
CC73	75.3	84.3	159.6	79.8
CC74	85.0	178.9	116.8	131.9
CC75		84.0	142.1	84.0
CC76		74.6	194.4	74.6
CC77	53.2	153.9	95.5	103.5
CC78	55.7	47.4	139.8	51.5
CC79		52.3	94.1	52.3
CC80	121.6	144.8	147.0	133.2
CC81		81.3	92.2	81.3
CC82		129.8	156.0	129.8
CC83	6.7	126.3	98.7	126.3
CC84	115.4	137.9	86.9	126.7
CC85	44.5	128.0	184.6	128.0
CC86		52.8	174.8	52.8
CC87		106.0	112.0	106.0
CC88	73.3	80.5	100.9	76.9
CC89	102.0	315.0	62.3	208.5
CC90	90.1	128.5	274.9	109.3
CC91	58.4	103.6	201.7	81.0
CC92		166.2	86.0	166.2
CC93		145.6	127.6	145.6
CC94		120.9	137.5	120.9
CC95	107.4	125.2	101.5	116.3
CC96		199.7	84.6	199.7
CC97	93.3	121.1	80.9	107.2
CC98	99.4	149.5	119.7	124.4
CC99		166.4	179.3	166.4
CC100	152.2	138.0	99.9	145.1

A.3 SHEAR WALL DESIGN OF 9-STORY OFFICE BUILDING

A nine-story residential building with five shear walls of 20ft (length)×1.5ft (thickness)×108ft (height)

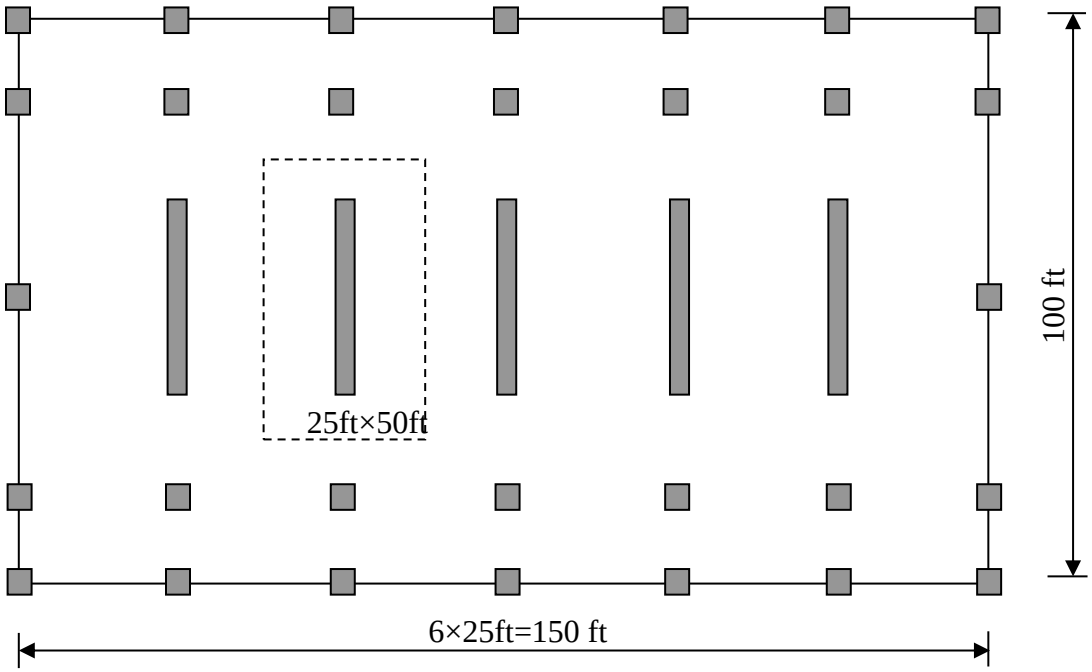

Dead load: 135 psf on each floor;

Live load (office use): 50 psf on each floor

Reduction in live loads per ASCE 7-05 4.8.1: $50\,psf\left(0.25+\frac{15}{\sqrt{4\times1250}}\right)=23.1\,psf$

Self-weight of a wall: $150\,pcf\times20\,ft\times1.5\,ft\times108\,ft=486kips$

Self-weight of beams: $150\,pcf\times(20/12)\,ft\times(16/12)\,ft\times25\,ft=8.3kips$

Self-weight of slab: $150\,pcf\times25\,ft\times45\,ft\times(6/12)\,ft=84.375kips$

Seismic weight of each floor: $w_i=135psf\times150\,ft\times100\,ft=2025kips$

Effective seismic weight for each wall: $W=9\times2025/5+486+8.3\times9+84.375\times9=4965kips$

Estimate the period of the structure by rule of thumb: $T_a=0.02\times(108)^{0.75}=0.67\sec$

Assume the building locates in Bell, Los Angeles, site class D:

$S_s = 1.5g, \quad S_1 = 0.9g,$

$S_{MS} = 1.5g, \quad S_{M1} = 1.35g$

$S_{DS} = (2/3)S_{MS} = 1.0g$

$S_{D1} = (2/3)S_{M1} = 0.9g$

$T_s = S_{D1} / S_{DS} = 0.9\,\text{sec}$

$T_0 = 0.2S_{D1} / S_{DS} = 0.18\,\text{sec}$

$T_L = 8\,\text{sec}$

Occupancy category, II

Importance factor I=1.0

Seismic design category E ← $S_1 > 0.75g$

For dual systems with special moment frames capable of resisting at least 25% of prescribed seismic forces with special reinforced concrete shear walls, R=7

Following equivalent lateral force procedure,

$$C_s = \frac{S_{DS}}{(R/I)} = \frac{1.0}{7} = 0.143$$

Check the maximum and minimum limits on Cs,

$$C_s \le \frac{S_{D1}}{T(R/I)} = \frac{0.9}{0.67 \times 7} = 0.192 \text{ , OK!}$$

$C_S \ge 0.01$, OK!

$$C_s \ge \frac{0.5S_1}{(R/I)} = \frac{0.5 \times 0.9}{7} = 0.064 \text{ , OK!}$$

Therefore, $C_s = 0.143$

Design base shear due to equivalent seismic load: $V = C_S W = 0.143 \times 4965 kips = 710 kips$

Linear distribution of equivalent seismic force according to

Floor #	F_x (kip)	$F_x h_x$ (kip-ft)
1	14	163
2	29	691

3	45	1610
4	61	2933
5	78	4671
6	95	6831
7	112	9420
8	130	12444
9	147	15908
$\sum$	710	54671

Equivalent earthquake loads applied at the base of the shear wall:

$V_{EQ} = 710 kips$

$M_{EQ} = \sum_{x=1}^{7} M_x = 54671 kip - ft$

The deal load and live load within the tributary area (dashed rectangle in the figure at beginning) at each floor:

$DL = 135 psf \times 25 ft \times 50 ft = 169 kips$

$LL = 23.1 psf \times 25 ft \times 50 ft = 29 kips$

The total dead load at the base of the shear wall:

$P_{DL} = 9 \times 169 kips + 486 kips$ (self-weight of wall)$+9 \times 8.3 + 9 \times 84.375 = 2841 kips$

The total live load at the base of the shear wall:

$P_{LL} = 9 \times 29 kips = 261 kips$

Summary of Loads at the base of a central shear wall:

$P_{DL} = 2841 kips$

$P_{LL} = 261 kips$

$V_{EQ} = 710 kips$

$M_{EQ} = 54671 kip - ft$

Load combinations for Strength Design (ASCE 7-05 12.4.2.3):

(1) $U=(1.2+0.2S_{DS})D+\rho Q_E+0.5L=1.4D+Q_E+0.5L$

$P_u = 1.4P_{DL} + 0.5P_{LL} = 4108kips$

$V_u = V_{EQ} = 710kips$

$M_u = M_{EQ} = 54671kip - ft$

(2) $U=(0.9-0.2S_{DS})D+\rho Q_E=0.7D+Q_E$

$P_u = 0.7P_{DL} = 1989kips$

$V_u = V_{EQ} = 710kips$

$M_u = M_{EQ} = 54671kip - ft$

Design of boundary vertical reinforcement:

Load combination (2) is critical because of the smaller axial force

$$T_u = \frac{M_u - P_u(0.4l_w)}{0.8l_w} = \frac{54671 - 1989 \times (0.4 \times 20)}{0.8 \times 20} = 2422kips$$

$$A_{sb} \geq \frac{T_u}{\phi f_y} = \frac{2422kips}{0.9 \times 60ksi} = 44.85in^2$$

30 #11 bars, $A_s = 46.8in^2$

REFERENCES

ACI. (2011). *Building code requirements for structural concrete and commentary (ACI318-11)*: American Concrete Institute.

Acikgoz, S., & DeJong, M. J. (2012). The interaction of elasticity and rocking in flexible structures allowed to uplift. *Earthquake Engineering & Structural Dynamics, 41*(15), 2177-2194. doi:10.1002/eqe.2181

Acikgoz, S., & DeJong, M. J. (2016). Analytical modelling of multi-mass flexible rocking structures. *Earthquake Engineering & Structural Dynamics, 45*(13), 2103-2122. doi:10.1002/eqe.2735

Agrawal, A. K., Tan, P., Nagarajaiah, S., & Zhang, J. (2009). Benchmark Structural Control Problem for A Seismically Excited Highway Bridge-Part I: Phase I Problem Definition. *Structural Control and Health Monitoring, 16*(5), 509-529.

Ajrab, J. J., Pekcan, G., & Mander, J. B. (2004). Rocking wall-frame structures with supplemental tendon systems. *Journal of Structural Engineering-Asce, 130*(6), 895-903.

Ali, S. F., & Ramaswamy, A. (2009). Optimal dynamic inversion ‐ based semi ‐ active control of benchmark bridge using MR dampers. *Structural Control and Health Monitoring: The Official Journal of the International Association for Structural Control and Monitoring and of the European Association for the Control of Structures, 16*(5), 564-585.

Anastasopoulos, I., Gelagoti, F., Spyridaki, A., Sideri, J., & Gazetas, G. (2014). Seismic Rocking Isolation of an Asymmetric Frame on Spread Footings. *Journal of Geotechnical and Geoenvironmental Engineering, 140*(1), 133-151. doi:10.1061/(Asce)Gt.1943-5606.0001012

Argyris, J. H., Kelsey, S., & Kamel, H. (1964). *Matrix methods of structural analysis: a precis of recent developments*: Pergamon Press: Oxford.

ASCE. (2010). *Minimum Design Loads for Buildings and Other Structures (ASCE/SEI 7-10)*: American Society of Civil Engineerings.

Bachmann, J., Strand, M., Vassiliou, M., Broccardo, M., & Stojadinović, B. (2018). Is rocking motion predictable? *Earthquake Engineering & Structural Dynamics, 47*(2), 535-552.

Baker, J. W., Lin, T., Shahi, S. K., & Jayaram, N. (2011). New ground motion selection procedures and selected motions for the PEER transportation research program. *PEER report, 3*.

Barthes, C. B. (2012). *Design of earthquake resistant bridges using rocking columns.* (PhD), University of California, Berkeley,

Birely, A., Lehman, D., Lowes, L., Kuchma, D., Hart, C., & Marley, K. (2008). *Investigation of the seismic behavior and analysis of reinforced concrete structural walls*. Paper presented at the 14th world conference on earthquake engineering, Beijing, China.

Broyden, C. G. (1965). A class of methods for solving nonlinear simultaneous equations. *Mathematics of computation, 19*(92), 577-593.

Chang, K. C., Chang, D. W., Tsai, M. H., & Sung, Y. C. (2000). Seismic Performance of Highway Bridges. *Earthquake Engineering and Engineering Seismology, 2*(1), 55-77.

Chen, Y. (2017). *Effect of near-fault ground motion characteristics on bridges with footing uplift.* (PhD), University of Auckland,

Chopra, A. K., & McKenna, F. (2016). Modeling viscous damping in nonlinear response history analysis of buildings for earthquake excitation. *Earthquake Engineering & Structural Dynamics, 45*(2), 193-211. doi:10.1002/eqe.2622

Chopra, A. K., & Yim, S. C. S. (1985). Simplified Earthquake Analysis of Structures with Foundation Uplift. *Journal of Structural Engineering-Asce, 111*(4), 906-930.

Christopoulos, C., Filiatrault, A., & Bertero, V. V. (2006). *Principles of passive supplemental damping and seismic isolation*: Iuss press.

Cimellaro, G. P., & Retamales, R. (2007). Optimal softening and damping design for buildings. *Structural Control and Health Monitoring: The Official Journal of the International Association for Structural Control and Monitoring and of the European Association for the Control of Structures, 14*(6), 831-857.

Constantinou, M. C., Soong, T. T., & Dargush, G. F. (1998). Passive energy dissipation systems for structural design and retrofit.

Deng, L. J., Kutter, B. L., & Kunnath, S. K. (2012). Centrifuge Modeling of Bridge Systems Designed for Rocking Foundations. *Journal of Geotechnical and Geoenvironmental Engineering, 138*(3), 335-344. doi:10.1061/(Asce)Gt.1943-5606.0000605

DesRoches, R., & Delemont, M. (2002). Seismic retrofit of simply supported bridges using shape memory alloys. *Engineering Structures, 24*(3), 325-332.

Dimitrakopoulos, E. G., & DeJong, M. J. (2012). Overturning of Retrofitted Rocking Structures under Pulse-Type Excitations. *Journal of Engineering Mechanics-Asce, 138*(8), 963-972. doi:10.1061/(Asce)Em.1943-7889.0000410

Dyke, S., Spencer , B., Sain, M., & Carlson, J. (1996). Modeling and control of magnetorheological dampers for seismic response reduction. *Smart materials and structures, 5*(5), 565.

Filippou, F. C., Popov, E. P., & Bertero, V. V. (1983). *Effects of Bond Deterioration on Hysteretic Behavior of Reinforced Concrete Joints*. Retrieved from Report EERC 83-19, Earthquake Engineering Research Center, University of California, Berkerley:

Gajan, S., & Kutter, B. L. (2008). Capacity, settlement, and energy dissipation of shallow footings subjected to rocking. *Journal of Geotechnical and Geoenvironmental Engineering, 134*(8), 1129-1141. doi:10.1061/(Asce)1090-0241(2008)134:8(1129)

Gazetas, G. (1983). Analysis of machine foundation vibrations: state of art. *International Journal of Soil Dynamics and Earthquake Engineering, 2*(1), 2-42.

Gelagoti, F., Kourkoulis, R., Anastasopoulos, I., & Gazetas, G. (2012). Rocking isolation of low-rise frame structures founded on isolated footings. *Earthquake Engineering & Structural Dynamics, 41*(7), 1177-1197. doi:10.1002/eqe.1182

Gluck, N., Reinhorn, A., Gluck, J., & Levy, R. (1996). Design of supplemental dampers for control of structures. *Journal of Structural Engineering, 122*(12), 1394-1399.

Hajjar, J. F., Sesen, A. H., Jampole, E., & Wetherbee, A. (2013). *A synopsis of sustainable structural systems with rocking, self-centering, and articulated energy-dissipating fuses* (NEU-CEE-2013-01). Retrieved from Department of Civil and Environmental Engineering, Northeastern University, Boston:

Hall, J. F. (2006). Problems encountered from the use (or misuse) of Rayleigh damping. *Earthquake Engineering & Structural Dynamics, 35*(5), 525-545. doi:10.1002/eqe.541

Han, Q., Du, X. L., Liu, J. B., Li, Z. X., Li, L. Y., & Zhao, J. F. (2009). Seismic Damage of Highway Bridges during the 2008 Wenchuan Earthquake. *Earthquake engineering and engineering vibration, 8*(2), 263-273.

Harden, C., Hutchinson, T., & Moore, M. (2006). Investigation into the effects of foundation uplift on simplified seismic design procedures. *Earthquake Spectra, 22*(3), 663-692. doi:10.1193/1.2217757

Haselton, C. B., Goulet, C. A., Mitrani-Reiser, J., Beck, J. L., Deierlein, G. G., & Prorter, K. A. (2008). *An assessment to Benchmark the seismic performance of a code-conforming reinforced concrete moment-frame building* Retrieved from PEER Report 2007/12, Pacific Earthquake Engineerng Research Center, University of California, Berkeley:

Hilber, H. M., Hughes, T. J. R., & Taylor, R. L. (1977). Improved Numerical Dissipation for Time Integration Algorithms in Structural Dynamics. *Earthquake Engineering & Structural Dynamics, 5*(3), 283-292. doi:DOI 10.1002/eqe.4290050306

Housner, G. W. (1963). The behavior of inverted pendulum structures during earthquakes. *Bulletin of the Seismological Society of America, 53(2)*, 404-417.

Housner, G. W., Bergman, L. A., Caughey, T. K., Chassiakos, A. G., Claus, R. O., Masri, S. F., . . . Yao, J. T. (1997). Structural control: past, present, and future. *Journal of Engineering Mechanics, 123*(9), 897-971.

Hung, H. H., Liu, K. Y., Ho, T. H., & Chang, K. C. (2011). An experimental study on the rocking response of bridge piers with spread footing foundations. *Earthquake Engineering & Structural Dynamics, 40*(7), 749-769. doi:10.1002/eqe.1057

Ikegami, R., & Kishinouye, F. (1947). A study on the overturning of rectangular columns in the case of the Nankai earthquake on December 21, 1946. *Bulletin of the Seismological Society of America, 40*, 749-769.

Jennings, P. C., & Wood, J. H. (1971). *Earthquake damage to freeway structures*. Retrieved from Engineering Features of the San Fernando Earthquake, February 9, 1971, chapter 6, Report EERL 71-02, California Institute of Technology, Earthquake Engineering Research Laboratory, Pasadena, California.:

Kaynia, A. M., & Kausel, E. (1980). *Dynamic stiffness and seismic response of sleeved piles*. Retrieved from

Kim, S.-H., & Shinozuka, M. (2004). Development of fragility curves of bridges retrofitted by column jacketing. *Probabilistic Engineering Mechanics, 19*(1-2), 105-112.

Kirkpatrick, p. (1927). Seismic measurements by the overthrow of columns. *Bulletin of the Seismological Society of America, 17*, 95-109.

Konstantinidis, D., & Makris, N. (2007). *The dynamics of a rocking block in three dimensions* Paper presented at the 8th HSTAM International Congress on Mechanics, Patras, Greece.

Kunde, M., & Jangid, R. (2003). Seismic behavior of isolated bridges: A-state-of-the-art review. *Electronic Journal of Structural Engineering, 3*(2), 140-169.

Kwon, O.-S., Elnashai, A. S., & Spencer, B. F. (2008). A framework for distributed analytical and hybrid simulations. *Structural Engineering and Mechanics, 30*(3), 331-350.

Kwon, O.-S., Nakata, N., Elnashai, A., & Spencer, B. (2005). A framework for multi-site distributed simulation and application to complex structural systems. *Journal of Earthquake Engineering, 9*(05), 741-753.

Kwon, O.-S., Nakata, N., Park, K.-S., Elnashai, A., & Spencer, B. (2007). User manual and examples for UI-SIMCOR v2. 6. *Department of Civil and Environmental Engineering, University of Illinois at Urbana-Champaign. Urbana, IL*.

Lavan, O., Cimellaro, G. P., & Reinhorn, A. M. (2008). Noniterative Optimization Procedure for Seismic Weakening and Damping of Inelastic Structures. *Journal of Structural Engineering, 134*(10), 1638-1648. doi:doi:10.1061/(ASCE)0733-9445(2008)134:10(1638)

Li, J., Spencer, B. F., Elnashai, A. S., & Phillips, B. M. (2012). Substructure hybrid simulation with multiple-support excitation. *Journal of Engineering Mechanics, 138*(7), 867-876.

Ma, Q. T., Butterworth, J. W., & Davidson, B. J. (2005). *Modelling rocking structures using standard finite elements* Paper presented at the 2005 NZSEE Conference, Wairakei Resort, Taupo, New Zealand.

Makris, N. (2014). A half-century of rocking isolation. *Earthquakes and Structures, 7*(6), 1187-1221.

Makris, N., & Konstantinidis, D. (2003). The rocking spectrum and the limitations of practical design methodologies. *Earthquake Engineering & Structural Dynamics, 32*(2), 265-289. doi:10.1002/eqe.223

Makris, N., & Roussos, Y. S. (2000). Rocking response of rigid blocks under near-source ground motions. *Geotechnique, 50*(3), 243-262.

Makris, N., & Vassiliou, M. F. (2013). Planar rocking response and stability analysis of an array of free-standing columns capped with a freely supported rigid beam. *Earthquake Engineering & Structural Dynamics, 42*(3), 431-449. doi:10.1002/eqe.2222

Makris, N., & Zhang, J. (2001). Rocking response of anchored blocks under pulse-type motions. *Journal of Engineering Mechanics-Asce, 127*(5), 484-493. doi:Doi 10.1061/(Asce)0733-9399(2001)127:5(484)

Makris, N., & Zhang, J. (2004). Seismic response analysis of a highway overcrossing equipped with elastomeric bearings and fluid dampers. *Journal of Structural Engineering, 130*(6), 830-845.

Marini, A., & Spacone, E. (2006). Analysis of reinforced concrete elements including shear effects. *Aci Structural Journal, 103*(5), 645-655.

Maroney, B., Romstad, K., & Chajes, M. (1990). *Interpretation of Rio Dell freeway response during six recorded earthquake events.* Paper presented at the Procs. of the 4th US National Conference on Earthquake Eng., Palm springs, CA.

Mazzoni, S., McKenna, F., Scott, M. H., & Fenves, G. L. (2006). OpenSees command language manual. *Pacific Earthquake Engineering Research (PEER) Center, 264*.

Midorikawa, M., Ishihara, T., Azuhata, T., Hori, H., Kusakari, T., & ASari, T. (2009). *Three-dimensional shaking table tests on seismic response of reduced-scale steel rocking frames.* . Paper presented at the Proceedings of the 3rd International Conference on Advances in Experimental Structural Engineering.

Milne, J. (1885). Seismic experiments. *Trans. Seismol. Soc. Jpn., 8*, 1-82.

Nagarajaiah, S., Narasimhan, S., Agrawal, A., & Tan, P. (2009). Benchmark structural control problem for a seismically excited highway bridge—Part III: Phase II Sample controller for the fully base‐isolated case. *Structural Control and Health Monitoring: The Official Journal of the International Association for Structural Control and Monitoring and of the European Association for the Control of Structures, 16*(5), 549-563.

Nakashima, M. (1990). *Integration techniques for substructure pseudo-dynamic test.* Paper presented at the 4th US National Conference on Earthquake Engineering, 1990. 5.

Nazari, M., Sritharan, S., & Aaleti, S. (2017). Single precast concrete rocking walls as earthquake force-resisting elements. *Earthquake Engineering & Structural Dynamics, 46*(5), 753-769. doi:10.1002/eqe.2829

Ohtori, Y., Christenson, R. E., Spencer, B., & Dyke, S. (2004). Benchmark Control Problems for Seismically Excited Nonlinear Buildings. *Journal of Engineering Mechanics, 130*(4), 366-385.

Oliveto, G., Calio, N., & Greco, A. (2003). Large displacement behaviour of a structural model with foundation uplift under impulsive and earthquake excitations. *Earthquake Engineering & Structural Dynamics, 32*(3), 369-393.

OpenSees. (2017). (Open System for Earthquake Engineering Simulation). *opensees.berkeley.edu*.

Padgett, J. E., & DesRoches, R. (2008). Methodology for the development of analytical fragility curves for retrofitted bridges. *Earthquake Engineering & Structural Dynamics, 37*(8), 1157-1174.

Palermo, A., Pampanin, S., & Calvi, G. M. (2005). Concept and development of hybrid solutions for seismic resistant bridge systems. *Journal of Earthquake Engineering, 9*(06), 899-921.

Palermo, A., Pampanin, S., & Marriott, D. (2007). Design, modeling, and experimental response of seismic resistant bridge piers with posttensioned dissipating connections. *Journal of Structural Engineering, 133*(11), 1648-1661.

Palermo, M., Silvestri, S., Trombetti, T., & Landi, L. (2013). Force reduction factor for building structures equipped with added viscous dampers. *Bulletin of Earthquake Engineering, 11*(5), 1661-1681.

Parcianello, E., Chisari, C., & Amadio, C. (2017). Optimal design of nonlinear viscous dampers for frame structures. *Soil Dynamics and Earthquake Engineering, 100*, 257-260.

PEER Blind Prediction Contest. (2019). *https://peer.berkeley.edu/2019-blind-prediction-contest*.

PEER Ground Motion Database. http://ngawest2.berkely.edu/.

Peng, Y., Zhang, J., Xi, W. (2021a). Structural control of inelastic structures with energy dissipation devices through hybrid simulation. In preparation.

Peng, Y., Xie, Y., Xi, W., Dyke, S., Zhang, J. (2021b). Optimal passive control design of the benchmark highway bridge based on hybrid simulation. In preparation.

Petrini, L., Maggi, C., Priestley, M. J. N., & Calvi, G. M. (2008). Experimental verification of viscous damping modeling for inelastic time history analyzes. *Journal of Earthquake Engineering, 12*, 125-145. doi:10.1080/13632460801925822

Poulos, H. (1968). Analysis of the settlement of pile groups. *Geotechnique, 18*(4), 449-471.

Psycharis, I. N., & Jennings, P. C. (1983). Rocking of Slender Rigid Bodies Allowed to Uplift. *Earthquake Engineering & Structural Dynamics, 11*(1), 57-76. doi:DOI 10.1002/eqe.4290110106

Pugh, J. S., Lowes, L. N., & Lehman, D. E. (2015). Nonlinear line-element modeling of flexural reinforced concrete walls. *Engineering Structures*, *104*, 174-192. doi:10.1016/j.engstruct.2015.08.037

Qu, Z., Wada, A., Motoyui, S., Sakata, H., & Kishiki, S. (2012). Pin-supported walls for enhancing the seismic performance of building structures. *Earthquake Engineering & Structural Dynamics*, *41*(14), 2075-2091. doi:10.1002/eqe.2175

Rahmani, A., Taiebat, M., Finn, W. L., & Ventura, C. E. (2016). Evaluation of substructuring method for seismic soil-structure interaction analysis of bridges. *Soil Dynamics and Earthquake Engineering*, *90*, 112-127.

Reinhorn, A. M., Li, C., & Constantinou, M. C. (1995). Experimental & analytical investigation of seismic retrofit of structures with supplemental damping, Part 1: fluid viscous damping devices.

Ricker, N. (1943). Further developments in the wavelet theory of seismogram structure. *Bulletin of the Seismological Society of America*, *33*(3), 197-228.

Roesset, J. M. (1984). *Dynamic stiffness of pile groups.* Paper presented at the Analysis and design of pile foundations.

Saouma, V., & Sivaselvan, M. (2008). *Hybrid Simulation Theory, Implementation and Applications* (1st Edition ed.). London: CRC Press.

SAP2000. (2017). *https://www.csiamerica.com/products/sap2000*.

Schellenberg, A., & Mahin, S. (2006). *Integration of hybrid simulation within the general-purpose computational framework OpenSees.* Paper presented at the Eighth US National Conference on Earthquake Engineering.

Soong, T. T., & Costantinou, M. C. (2014). *Passive and active structural vibration control in civil engineering* (Vol. 345): Springer.

Soong, T. T., & Dargush, G. F. (1997). Passive energy dissipation systems in structural engineering.

Soong, T. T., & Spencer, B. F. (2002). Supplemental energy dissipation: state-of-the-art and state-of-the-practice. *Engineering Structures*, *24*(3), 243-259. doi:https://doi.org/10.1016/S0141-0296(01)00092-X

Spacone, E., Filippou, F. C., & Taucer, F. F. (1996). Fiber beam-column model for non-linear analysis of R/C frames .1. Formulation. *Earthquake Engineering & Structural Dynamics*, *25*(7), 711-725. doi:Doi 10.1002/(Sici)1096-9845(199607)25:7<711::Aid-Eqe576>3.0.Co;2-9

Spencer, B., Dyke, S., Sain, M., & Carlson, J. (1997). Phenomenological model for magnetorheological dampers. *Journal of Engineering Mechanics*, *123*(3), 230-238.

Spencer, B., & Nagarajaiah, S. (2003). State of the art of structural control. *Journal of Structural Engineering, 129*(7), 845-856.

Symans, M., Charney, F., Whittaker, A., Constantinou, M., Kircher, C., Johnson, M., & McNamara, R. (2008). Energy dissipation systems for seismic applications: current practice and recent developments. *Journal of Structural Engineering, 134*(1), 3-21.

Tan, P., & Agrawal, A. K. (2009). Benchmark structural control problem for a seismically excited highway bridge—part II: phase I sample control designs. *Structural Control and Health Monitoring: The Official Journal of the International Association for Structural Control and Monitoring and of the European Association for the Control of Structures, 16*(5), 530-548.

Tang, Y. C., & Zhang, J. (2011). Probabilistic seismic demand analysis of a slender RC shear wall considering soil-structure interaction effects. *Engineering Structures, 33*(1), 218-229. doi:10.1016/j.engstruct.2010.10.011

Tarakji, G. (1997). Lessons Not Learned from 1989 Loma Prieta Earthquake. *Journal of Professional Issues in Engineering Education and Practice, 118*(2), 132-138.

Truniger, R., Vassiliou, M. F., & Stojadinovic, B. (2015). An analytical model of a deformable cantilever structure rocking on a rigid surface: experimental validation. *Earthquake Engineering & Structural Dynamics, 44*(15), 2795-2815. doi:10.1002/eqe.2609

Tubaldi, E., & Kougioumtzoglou, I. A. (2015). Nonstationary stochastic response of structural systems equipped with nonlinear viscous dampers under seismic excitation. *Earthquake Engineering & Structural Dynamics, 44*(1), 121-138.

Utkin, V. I. (2013). *Sliding modes in control and optimization*: Springer Science & Business Media.

Vassiliou, M. F. (2018). Seismic response of a wobbling 3D frame. *Earthquake Engineering & Structural Dynamics, 47*, 1212-1228.

Vassiliou, M. F., Burger, S., Egger, M., Bachmann, J. A., Broccardo, M., & Stojadinovic, B. (2017). The three-dimensional behavior of inverted pendulum cylindrical structures during earthquakes. *Earthquake Engineering & Structural Dynamics, 46*, 2261-2280.

Vassiliou, M. F., Mackie, K. R., & Stojadinovic, B. (2014). Dynamic response analysis of solitary flexible rocking bodies: modeling and behavior under pulse-like ground excitation. *Earthquake Engineering & Structural Dynamics, 43*(10), 1463-1481. doi:10.1002/eqe.2406

Vassiliou, M. F., Mackie, K. R., & Stojadinovic, B. (2017). A finite element model for seismic response analysis of deformable rocking frames. *Earthquake Engineering & Structural Dynamics, 46*(3), 447-466.

Vassiliou, M. F., & Makris, N. (2012). Analysis of the rocking response of rigid blocks standing free on a seismically isolated base. *Earthquake Engineering & Structural Dynamics, 41*(2), 177-196. doi:10.1002/eqe.1124

Vassiliou, M. F., & Makris, N. (2015). Dynamics of the Vertically Restrained Rocking Column. *Journal of Engineering Mechanics, 141*(12).

Vassiliou, M. F., Truniger, R., & Stojadinovic, B. (2015). An analytical model of a deformable cantilever structure rocking on a rigid surface: development and verification. *Earthquake Engineering & Structural Dynamics, 44*(15), 2775-2794. doi:10.1002/eqe.2608

Wallace, J. W. (2007). Modelling issues for tall reinforced concrete core wall buildings. *The Structural Design of Tall and Special Buildings, 16*, 615-632.

Wang, Z. (2008). A preliminary report on the Great Wenchuan Earthquake. *Earthquake engineering and engineering vibration, 7*, 225-234.

Wen, Y. (1976). Method for random vibration of hysteretic systems. *Journal of the engineering mechanics division, 102*(2), 249-263.

Wiebe, L., Christopoulos, C., Tremblay, R., & Leclerc, M. (2012). *Modelling inherent damping for rocking systems: results of large-scale shake table testing*. Paper presented at the In proceedings of the 15th World Conference on Earthquake Engineering.

Xi, W. (2014). *Performance Based Implementation of Seismic Protective Devices for Structures.* PhD Dissertation. University of California, Los Angeles.

Xie, Y. (2017). *Seismic Modeling, Quantifying and Protection of Highway Bridges Considering Shaking and Lateral Spreading.* (10261035 Ph.D.), University of California, Los Angeles,

Xie, Y., Huo, Y., & Zhang, J. (2017). Development and validation of p‐y modeling approach for seismic response predictions of highway bridges. *Earthquake Engineering & Structural Dynamics, 46*(4), 585-604.

Xie, Y., & Zhang, J. (2017). Optimal design of seismic protective devices for highway bridges using performance-based methodology and multiobjective genetic optimization. *Journal of Bridge Engineering, 22*(3), 04016129.

Xie, Y., & Zhang, J. (2018). Design and optimization of seismic isolation and damping devices for highway bridges based on probabilistic repair cost ratio. *Journal of Structural Engineering, 144*(8), 04018125.

Xie, Y., Zhang, J., & Huo, Y. (2018). Simplified drift demand prediction of bridges under liquefaction-induced lateral spreading. *Journal of Bridge Engineering, 23*(8), 04018053.

Xie, Y., Zhang, J., & Xi, W. (2018). Effectiveness evaluation and optimal design of nonlinear viscous dampers for inelastic structures under pulse-type ground motions. *Earthquake Engineering & Structural Dynamics, 47*(14), 2802-2820. doi:10.1002/eqe.3109

Yang, G., Wu, B., Ou, G., Wang, Z., & Dyke, S. (2017). HyTest: platform for structural hybrid simulations with finite element model updating. *Advances in Engineering Software, 112*, 200-210.

Yang, J. N., Li, Z., & Liu, S. C. (1992). Stable controllers for instantaneous optimal control. *Journal of Engineering Mechanics, 118*(8), 1612-1630.

Yang, J. N., Wu, J. C., & Agrawal, A. K. (1995). Sliding Mode Control for Nonlinear and Hysteretic Structures. *Journal of Engineering Mechanics, 121*(12), 1330-1339. doi:10.1061/(ASCE)0733-9399(1995)121:12(1330)

Yassin, M. (1994). *Nonlinear analysis of prestressed concrete structures under monotonic and cyclic loads.* (PhD), University of California, Berkeley,

Young, K.-K. D. (1993). *Variable structure control for robotics and aerospace applications*: Elsevier Science Inc.

Zhang, J. (2002). *Seismic Response Analysis and Protection of Highway Overcrossings Including Soil-Structure Interaction.* PhD Dissertation. University of California, Berkeley.

Zhang, J., & Huo, Y. (2009). Evaluating effectiveness and optimum design of isolation devices for highway bridges using the fragility function method. *Engineering Structures, 31*(8), 1648-1660.

Zhang, J., & Makris, N. (2001). Rocking response of free-standing blocks under cycloidal pulses. *Journal of Engineering Mechanics-Asce, 127*(5), 473-483. doi:Doi 10.1061/(Asce)0733-9399(2001)127:5(473)

Zhang, J., & Makris, N. (2002a). Kinematic response functions and dynamic stiffnesses of bridge embankments. *Earthquake Engineering & Structural Dynamics, 31*(11), 1933-1966.

Zhang, J., & Makris, N. (2002b). Seismic response analysis of highway overcrossings including soil–structure interaction. *Earthquake Engineering & Structural Dynamics, 31*(11), 1967-1991.

Zhang, J., Makris, N., & Delis, T. (2004). Structural characterization of modern highway overcrossings—case study. *Journal of Structural Engineering, 130*(6), 846-860.

Zhang, J., Xie, Y. Z., & Wu, G. (2019). Seismic response predictions of bridges with rocking column-foundation. *Earthquake Engineering & Structural Dynamics, 48*(1), 152-170, (http:doi.org/10.1002/eqe.3129)

Zhou, F., & Fisher, D. G. (1992). Continuous sliding mode control. *International Journal of Control, 55*(2), 313-327.